UiT The Arctic University of Norway

Faculty of Science and Technology, Department of Geosciences

Holocene precipitation seasonality on Svalbard and in Northern Fennoscandia

Reconstructed using organic geochemical and stable isotope proxies

Sofia Elisabeth Kjellman

A dissertation for the degree of Philosophiae Doctor

July 2022

Holocene precipitation seasonality on Svalbard and in Northern Fennoscandia

Reconstructed using organic geochemical and stable isotope proxies

Sofia Elisabeth Kjellman

A dissertation for the degree of Philosophiae Doctor

UiT The Arctic University of Norway

Faculty of Science and Technology

Department of Geosciences

July 2022

Supervisors:

Professor Anders Schomacker
Department of Geosciences
UiT The Arctic University of Norway

Assistant Professor Elizabeth K. Thomas
Department of Geology
University at Buffalo, The State University of New York

Associate Professor Lena Håkansson
Department of Arctic Geology
The University Centre in Svalbard

Front page image: Ringhorndalen on northern Spitsbergen, Svalbard, seen from helicopter in July 2018. Jodavannet, one of the studied lakes, is seen in the left of the photo.
(Photo: Sofia Elisabeth Kjellman)

Abstract

The high latitudes are experiencing faster climate change than the global average. Feedback mechanisms between the atmosphere, cryosphere and the oceans amplify the warming, and intensify the water cycle. Arctic precipitation is projected to increase because of enhanced winter evaporation due to diminishing sea ice, increased poleward moisture transport in summer, and increased atmospheric moisture content in summer and early fall. Large model uncertainties and different seasonal expressions of these processes emphasize the need to improve our understanding of long-term spatial and temporal variability in the water cycle.

Stable isotopes of oxygen and hydrogen ($\delta^{18}O$ and $\delta^{2}H$) in precipitation are sensitive to the conditions at the moisture source, atmospheric temperature, and the moisture travel history, and are therefore widely used tracers of past and current changes in the water cycle. This study focuses on two aspects of water isotope proxies: 1) reconstructing Holocene precipitation seasonality on Svalbard using $\delta^{2}H$ of leaf wax *n*-alkanoic acids from lake sediments (Papers I and III), and 2) exploring the variable influence of inflow (precipitation) seasonality and evaporation on the modern isotopic variability of lake waters in northern Fennoscandia (Paper II). Seasonal distribution of precipitation is important for example because winter precipitation is one of the main controls on glacier mass balance. Understanding the seasonal distribution of precipitation in the past might, therefore, help decipher the drivers of glacier variations.

On Svalbard, we targeted four lakes along a climatic gradient from the relatively warm and humid west coast to the relatively cold and arid Nordaustlandet. We focused on the C_{22} and C_{28} *n*-alkanoic acids, interpreted to reflect lake and soil water, respectively. Our results suggest that Early and Middle Holocene summers were warm with high evapotranspiration, and/or received more proximal moisture. On northern Spitsbergen, the proportion of winter relative to summer precipitation increased in the Early Holocene, as the oceans warmed, and the sea ice retreated. After *c*. 6 cal. kyr BP, summers became cooler with less evapotranspiration, and/or more distally derived moisture. The proportion of winter precipitation decreased as the ocean surface cooled, and the sea-ice cover increased, but periods of increased winter precipitation still occurred. Varying lake hydrology impacted the seasonality reflected in the aquatic leaf waxes; therefore, a good understanding of the individual lake systems is crucial for robust proxy interpretations.

In northern Fennoscandia, surface water was sampled from 135 lakes, from the Norwegian Sea to the Bothnian Bay. We find that both coastal and inland lakes are sensitive to distillation during moisture transport, and that lakes farther from the Norwegian Sea additionally are affected by evaporation. We estimated the inflow isotopic composition for evapo-concentrated lakes using a Bayesian method and compared the values for lakes sampled in both 2019 and 2020. It is suggested that more ^{2}H-depleted values in 2020 reflect that the lakes received relatively more winter precipitation in 2020, related to strong westerlies bringing greater-than-average amounts of North Atlantic moisture. This implies that evapo-concentrated lakes experience isotopic variability due to both evaporative enrichment and variable inflow isotopic composition, and that coastal lakes are better targets for precipitation reconstructions.

We find that summer precipitation variability across Svalbard follows changes in summer insolation and temperature, whereas the seasonal distribution of precipitation on northern Svalbard is controlled by regional ocean surface conditions, with more winter precipitation during periods of strong Atlantic water advection and reduced sea-ice cover. The inflow isotopic composition to Fennoscandian lakes is influenced by variable strength of the westerlies, by affecting the relative proportion of winter and summer precipitation entering the lake. These results highlight the impact of North Atlantic conditions on the seasonal precipitation patterns on Svalbard and in northern Fennoscandia.

Plain language summary

As the Arctic warms, it is also getting wetter. Exactly why, and by how much is difficult to predict due to lack of long-term observations and complex interactions between the atmosphere, cryosphere (e.g., sea ice and glaciers), and the oceans. The main reason for Arctic precipitation increases is retreating sea ice. The sea ice acts as a lid that prevents evaporation from the ocean surface. In a warmer climate, more winter sea ice will disappear, resulting in more available moisture, and more winter precipitation. Furthermore, the Arctic receives moisture from the mid-latitudes, and this transport is projected to increase, mostly in summer. Additionally, the moisture content in the atmosphere will increase, as warm air can hold more water vapor.

To better understand the climate system, we can use modern and geological data. Stable oxygen and hydrogen isotopes ($\delta^{18}O$ and $\delta^{2}H$) in precipitation are sensitive to changes in the conditions at the moisture source and in atmospheric temperature and circulation patterns and can therefore provide information about various processes in the water cycle. Lakes are excellent climate archives since sediments (e.g., organic mud, silt, sand) accumulate on the lake floor over time, and hold information about the environmental conditions at the time of deposition. Plants living in and around the lake use lake and soil water when they produce leaf wax – a fatty coating to protect against water loss – which incorporates the hydrogen isotopic signal of the source water.

In this thesis, lake sediments are combined with modern lake water and precipitation measurements to study water cycle changes on Svalbard and in northern Fennoscandia (i.e., northern Norway, Finland, and Sweden), with a focus on precipitation seasonality. This is an important aspect for the mass balance of glaciers since the amount of winter precipitation together with the summer temperature decide if a glacier grows or shrinks.

Our results suggest that Holocene variability in summer precipitation on Svalbard follows changes in summer insolation and temperature. Northern Svalbard received more winter precipitation during times of increased inflow of Atlantic water, reduced sea-ice extent, and more available moisture. Modern lake water isotope data from northern Fennoscandia suggest that the lake water isotopic composition changes in response to varying proportion of summer and winter precipitation, which partly depends on the atmospheric circulation patterns over the North Atlantic, and due to evaporative enrichment. This thesis highlights the potential of using organic geochemical and stable isotope proxies to study seasonal changes in precipitation.

Acknowledgements

First and foremost, I would like to thank my supervisors Anders Schomacker and Elizabeth Thomas for their guidance, encouragement, and support. Anders, in addition to being a dedicated and enthusiastic supervisor, you have invested a lot in me and my career development. Thank you for always taking your time to listen and offer advice, countless cups of coffee, and for often believing more in me than I believe in myself. Elizabeth (or my 'leaf wax guru', as I sometimes like to refer to you as): learning a new and quite complex climate proxy has been challenging, but you have always been there with your expertise, passion, and patience to guide me. Our weekly Zoom dates have been invaluable, and whenever I have felt stuck, you have helped me to find a way forward. Thank you!

I would like to thank Lena Håkansson for being part of the supervision team and UNIS for having me as a guest PhD student in the beginning of the project. I would also like to acknowledge the co-authors on the scientific papers presented in this thesis: Sandrine Duboscq, Allison Cluett, and Owen Cowling for sample and data processing; Nick McKay for LiPD support and troubleshooting; Wes Farnsworth, Lis Allaart, Skafti Brynjólfsson, and Ólafur Ingólfsson for the many hours spent in the field and for commenting on Paper I and III. I am also grateful to Mike Retelle and others who participating in fieldwork during lake sediment coring, and to John Arne Opheim, Marie Bulínová, and the rest who helped me collect precipitation and lake water samples. Thank you to Owen for training and help in the lab, and for answering questions about lab procedures and data. Thanks to Katie Lovell and Kayla Hollister for sample processing, and the rest of the UB Stable Isotope and Biogeochemistry Lab (Allison, Meg, Devon, and others) for welcoming me into the group during my stay at UB, for sharing code, and for discussing methodology and data.

All the long days at the UiT Department of Geosciences would not have been the same without the people. A special thanks to the early career researchers, and to the JEDI group for wanting to make a difference. The people in the 'Ice Girls' office (Ingrid, Lis, Vårin, and Christine): thanks for sharing experiences, supporting each other, and all the fun we had in our office. Ingrid, thank you also for being the older and wiser PhD student when I first started, for introducing me to knitting, and for many great outdoor memories. People in the blue barrack (Louise, Carly, Amicia, Marie, Harald, Marina, Paul, Carmen, and others): thank you for being

part of my bubble during the pandemic, and for your company and encouragement during the last months of writing.

Marie and Alex, thanks for joining me and Anders in the lake group (and doubling it in size!). It has been great discussing lakes with you, to have your support, and to join you in the field. Naima and Lis, thank you for being inspiring and caring early career researchers and friends, and for sharing the ups and downs of the PhD journey and life. Louise, thank you for seeing when I needed a hug, and for adopting me to your Tromsø family. All the hikes, skiing and cabin trips with you, Ellery, Albus, and others have become an important part of my Tromsø life. An extra thanks to Naima and Lou for being there for me during the stressful final weeks of this work. Thanks also to the 'Strikk og Drikk' groups (in Tromsø and on Zoom) for being great places to meet, relax, and stay in touch. To my friends in Tromsø, Stockholm and elsewhere in the world: thank you for your encouragement and support.

Finally, I would thank my family for their endless love and care. Thank you for always believing in me, helping me, and bearing with the me – like for example when I (at least partly) turned our northern Norway holiday into a lake water sampling campaign. Thanks to my brother Lelle for driving, and the others for patiently waiting or assisting. To my twin sister Ulrika: one of the hardest things with doing this PhD was moving away from you. Thank you for the many hours spent with me over the phone, whenever I needed cheering up, help with decision-making, or just wanted company on my weekend walks. Mamma och pappa, tack för att ni alltid finns där!

Preface

This thesis is the result of a PhD project carried out at UiT The Arctic University of Norway between February 2018 and July 2022. The four-year doctoral position was funded by the Faculty of Science and Technology at UiT. Additional funding for fieldwork, laboratory analyses, conference attendance, and mobility was granted by the Svalbard Environmental Protection Fund (17/101 to Schomacker and 20/36 to Schomacker and Kjellman), Olle Engkvists Stiftelse (204-0129 to Schomacker and Kjellman), Helge Ax:son Johnsons Stiftelse (to Kjellman), Nansenfondet (to Schomacker), and the National Science Foundation (EAR-IF 1652274 to Thomas).

The primary tools used in this project are organic geochemical and stable isotope proxies. Sediment cores were collected within other projects between 2015 and 2019, and lake water and precipitation sampling were initiated in 2018 and 2019 as part of this study. In 2018, I spent two months in the University at Buffalo (UB) Organic and Stable Isotope Biogeochemistry Laboratory (OSIBL), learning techniques for extracting and analyzing lipid biomarkers from lake sediments. A second, four-months long, stay at UB was planned in 2020 but cancelled due to the Covid-19 pandemic. The remaining organic geochemical analyses were carried out by technical staff and students in Dr. Thomas's lab at UB. Water samples were analyzed at OSIBL and at the Facility for advanced isotopic research and monitoring of weather, climate, and biogeochemical cycling (FARLAB), University of Bergen.

To fulfil the 25% department and teaching duties, I taught exercises, instructed during field excursions, and provided feedback on student reports on bachelor course GEO-2003 Quaternary Geology (2019-2021) and graduate course GEO-3136/8136 Practical geochronological methods in marine, terrestrial Quaternary Geology and geohazards (2019-2022). I also co-supervised two master students in 2019 and 2020. Part of the duty work included organizing the department's Friday Seminar series (2019-2020), and science communication through establishment of the department's Instagram account (2018-2020), giving presentations to high school students and organizing Geology Day in Tromsø (2020).

To complete the instruction component equivalent to 30 ECTS, I attended GEO-8136 Practical geochronological methods in marine, terrestrial Quaternary Geology and geohazards at UiT, INTPART Arctic Field Summer School 2018: Arctic Coastal Environments in Rapid Transition, in Utqiaġvik, Alaska (organized by University of Alaska Fairbanks in collaboration

with UiT and University of Calgary, funded by the Research Council of Norway), and AG-848 Arctic Late Quaternary Glacial and Marine Environmental History at UNIS in 2018. In 2019, I took the mandatory course SVF-8600 Philosophy of Science and Ethics at UiT. Based on the essay I wrote for the ethics course, I later that year published a career column in the world-leading journal Nature (Kjellman, 2019).

Over the course of my PhD education, I participated and presented results related to the thesis work at the following international conferences: Joint International Paleolimnology Association and the International Association of Limnogeology (IPA-IAL) Meeting 2018 in Stockholm; 49th International Arctic Workshop in Stockholm, 2019; American Geophysical Union (AGU) Fall Meeting 2020, online; 2nd International Processes and Palaeo-Environmental changes in the Arctic: From Past to Present (PalaeoArc) Conference 2021, online; 35th Nordic Geological Winter Meeting in Reykjavík, 2022. Additionally, I have presented my work at the UiT Geoscience Research Academy of Tromsø (GReAT) Annual Meetings in 2019, 2020, and 2021, and at the Norwegian Research school on changing climates in the coupled earth system (CHESS) Annual Meeting in 2020.

Beyond the thesis work, I have over the course of my PhD program published one additional research paper as a first author (based on my master's thesis; Kjellman et al., 2018) and contributed to seven publications as a co-author (Schomacker et al., 2019; Allaart et al., 2020; Voldstad et al., 2020; Allaart et al., 2021a; Allaart et al., 2021b; Alsos et al., 2021; Vick et al., 2022), whereof two were associated with master's thesis projects that I co-supervised.

The PhD project resulted in three first-authored scientific articles, contributing new knowledge about Arctic precipitation. In this work, we generated seasonal Holocene precipitation isotope records from four lake sediment sequences from Svalbard and investigated modern lake water isotope systematics in northern Fennoscandia.

This thesis consists of an introduction and a summary of the three following research articles:

I. **Kjellman, S. E.**, Schomacker, A., Thomas, E. K., Håkansson, L., Duboscq, S., Cluett, A. A., Farnsworth, W. R., Allaart, L., Cowling, O. C., McKay, N. P., Brynjólfsson, S., & Ingólfsson, Ó., 2020. Holocene precipitation seasonality in northern Svalbard: influence of sea ice and regional ocean surface conditions. *Quaternary Science Reviews*, *240*, 1063882. https://doi.org/10.1016/j.quascirev.2020.106388.

Data related to **Paper I** are freely available at the NOAA/World Data Service for Paleoclimatology website: https://www.ncdc.noaa.gov/paleo/study/29852.

II. **Kjellman, S. E.**, Thomas, E. K., & Schomacker, A., 2022. Arctic and sub-Arctic lake water δ^2H and $\delta^{18}O$ along a coastal-inland transect: implications for interpreting water isotope proxy records. *Journal of Hydrology*, *67*, 127556. https://doi.org/10.1016/j.jhydrol.2022.127556.

Data related to **Paper II** are freely available in the Supplementary Information and in the Water Isotopes Database at www.waterisotopes.org (Project IDs 00292 (surface waters) and 00293 (precipitation)).

III. **Kjellman, S. E.**, Thomas, E. K., Schomacker, A., Farnsworth, W.R., Cowling, O.C., Allaart, L., & Brynjólfsson, S. Holocene precipitation seasonality along a climatic gradient from western Spitsbergen to Nordaustlandet, Svalbard. In review for *Palaeogeography, Palaeoclimatology, Palaeoecology.*

Data related to **Paper III** will be freely available at the NOAA/World Data Service for Paleoclimatology website and in the Water Isotopes Database.

Contents

Abbreviations

ACL	average chain length
AMS	accelerator mass spectrometry
AO	Arctic Oscillation
cal. kyr BP	calibrated thousand years before present (BP = 1950)
CRediT	Contributor Roles Taxonomy
DCM	dichloromethane
DEM	digital elevation model
d-excess or dxs	deuterium excess
ELA	equilibrium line altitude
ECTS	European Credit Transfer and Accumulation System
FAME	fatty acid methyl ester
FARLAB	Facility for advanced isotopic research and monitoring of weather, climate, and biogeochemical cycling
FID	flame ionization detector
GC	gas chromatograph
GMWL	Global Meteoric Water Line
GNIP	Global Network of Isotopes in Precipitation
IRMS	isotope ratio mass spectrometer
LEL	local evaporation line
LIA	Little Ice Age
LiPD	Linked PaleoData
LMWL	Local Meteoric Water Line
LOI	loss on ignition
MAAT	mean annual air temperature
MAP	mean annual precipitation
m a.s.l.	meters above sea level
MeOH	methanol
NAO	North Atlantic Oscillation
OSIBL	The University at Buffalo Organic and Stable Isotope Biogeochemistry Laboratory
OIPC	Online Isotopes in Precipitation Calculator

RCP8.5	Representative Concentration Pathway 8.5 W/m^2 radiative forcing in 2100 = emission scenario “business as usual”
*sed*aDNA	sedimentary ancient DNA
SEM	standard error of the mean
TLE	total lipid extract
UB	University at Buffalo
UiT	UiT The Arctic University of Norway
UNIS	The University Centre in Svalbard
VSMOW	Vienna Standard Mean Ocean Water
WS-CRDS	Wavelength Scanned Cavity Ring Down Spectrometer
XRF	X-ray fluorescence
δ^2H	stable hydrogen isotope ratio (subscript letters indicate the source: aq = aquatic plant waxes; I = lake water inflow; lake = lake water; precip = precipitation; terr = terrestrial plant waxes)
$\delta^{18}O$	stable oxygen isotope ratio
^{14}C	radiocarbon

1. Introduction

1.1. Arctic precipitation changes

The Arctic region is experiencing rapid and vast climate changes. The near-surface temperature change over the Arctic is enhanced compared to the global average – a phenomenon called Arctic amplification. This concept was hypothesized already in 1896 by the Swedish scientist Svante Arrhenius, arguing that the effect of changes in the atmospheric carbon dioxide concentration on Earth's surface temperature will be larger by the poles (Arrhenius, 1896). A key driver of Arctic amplification is the albedo feedback. When snow and ice (high albedo) melts, darker surfaces (low albedo) are exposed, and more solar energy is absorbed. Diminishing sea ice lowers the albedo as well as enhances the heat flux to the atmosphere (Serreze et al., 2009; Screen & Simmonds, 2010).

The amplified Arctic warming has huge impacts on the hydrological cycle. Increased evaporation from ice-free seas results in increased precipitation amounts (Bintanja & Selten, 2014; Kopec et al., 2016). A wetter Arctic also results from increased poleward moisture transport (Dufour et al., 2016; Singh et al., 2017; Bintanja et al., 2020), and increased atmospheric moisture content (Screen & Simmonds, 2010; Swann et al., 2010). These processes have different seasonal expression, with meridional moisture transport being more important in summer, atmospheric water vapor content increasing most in summer and early fall, and enhanced evaporation being most prominent in fall and winter. Furthermore, the interannual variability in precipitation is projected to increase (Bintanja et al., 2020), and a greater fraction of the precipitation is expected to fall as rain (Bintanja & Andry, 2017; Førland et al., 2020; McCrystall et al., 2021). Future precipitation increases are projected to be heterogenous, with the greatest annual precipitation increases over the Barents Sea, western Scandinavia, eastern Eurasia, and western North America (Linderholm et al., 2018).

Modeled projections of changes in Arctic precipitation seasonality and humidity are associated with large uncertainties, due to inadequate knowledge of natural climate variations, future anthropogenic greenhouse gas emissions, feedback mechanisms, and model uncertainties (Rawlins et al., 2010; Hanssen-Bauer et al., 2019). To improve our understanding of spatial and temporal variations in precipitation amounts and seasonality over longer timescales, we need paleoclimatic proxy records. Many proxies provide information about temperature, ocean

circulation, and sea ice (e.g., Risebrobakken et al., 2003; de Vernal et al., 2013; Sundqvist et al., 2014; Kaufman et al., 2020). However, our understanding of hydrological changes is still limited, partly because individual proxies often are sensitive to multiple aspects of the water cycle (Konecky et al., 2020). Annual precipitation amounts have been reconstructed using Greenland ice cores (e.g., Dahl-Jensen et al., 1993) and pollen (e.g., Seppä & Birks, 2001; Bjune et al., 2004), but few proxies reflect precipitation seasonality.

In this study, we aim to improve our knowledge about precipitation seasonality on Svalbard and in northern Fennoscandia, two regions projected to experience great and spatially variable precipitation increases (Eklund et al., 2015; Ruosteenoja et al., 2016; Hanssen-Bauer et al., 2017; Hanssen-Bauer et al., 2019). We evaluate precipitation changes across two different timescales: Holocene variability on Svalbard and modern variability in northern Fennoscandia.

One of the reasons we focus on precipitation seasonality is its importance for glacier mass balance. A key question in Holocene climate reconstructions on Svalbard that remains to be answered is why some glaciers re-advanced during the Early Holocene, which was a period characterized by warming and unfavorable conditions for glacier growth (Farnsworth et al., 2020). It has been suggested that warmer oceans and decreasing sea ice – similar mechanisms as are projected to affect precipitation in the future – caused increased winter precipitation amounts in the Late Holocene (D'Andrea et al., 2012; Müller et al., 2012; Røthe et al., 2015). If similar processes acted in the Early Holocene, winter precipitation might have counterbalanced summer temperature-induced glacier ablation.

Stable isotope ratios of oxygen and hydrogen ($\delta^{18}O$ and $\delta^{2}H$) in precipitation are powerful tools for understanding modern-day and past hydrological processes due to their sensitivity to moisture source conditions, atmospheric temperature, and circulation (Dansgaard, 1964; Rozanski et al., 1993; Gat, 1996). In the following sections, I provide an overview of stable water isotopes and the processes influencing the precipitation isotopic composition (section 1.2), and an introduction to the use of leaf wax hydrogen isotopes as a paleo-precipitation proxy (section 1.3).

1.2. Stable water isotopes: basic concepts

Stable isotopes are atoms of the same element with the same number of protons and electrons, but different numbers of neutrons. Stable hydrogen isotopes have 0 or 1 neutrons (^{1}H and ^{2}H, the latter also called deuterium), and stable oxygen isotopes have 8, 9, or 10 neutrons (^{16}O, ^{17}O, and ^{18}O). The various isotopes have different mass: the more neutrons, the heavier isotopes, and therefore different physical and chemical properties. Heavy isotopes have higher binding energies and are less volatile than light isotopes, and thus react more slowly. During phase changes (e.g., evaporation and condensation), stable isotopes become enriched in one phase and depleted in the other. This separation is called isotopic fractionation.

Due to the considerably lower abundance of the heavy isotopes, stable isotopes are expressed as the ratio (R) between the rare (heavy) and common (light) isotopes ($^{2}H/^{1}H$ or $^{18}O/^{16}O$), compared to the same ratio in an international standard. Isotope ratios are reported using delta notation (δ) in per mil (‰) relative to Vienna Standard Mean Ocean Water (VSMOW):

$$\delta = 1000 \times \left(\frac{R_{sample}}{R_{VSMOW}} - 1\right) ‰ \qquad \text{(Equation 1)}$$

Stable isotopes are separated from each other through two types of fractionation processes: equilibrium fractionation and kinetic fractionation. Equilibrium fractionation is highly temperature-dependent and occurs during changes between phases in equilibrium. For example, when standard mean ocean water (by definition $\delta^{2}H$ = 0‰ and $\delta^{18}O$ = 0‰) evaporates, isotopically lighter isotopes are preferentially evaporated, and form depleted atmospheric vapor. The ocean surface water, on the other hand, gets isotopically enriched. When the atmospheric water vapor condenses, the resulting precipitation will be enriched relative to the vapor, leaving the remaining vapor depleted (Fig. 1). This process, which results in partitioning of isotopes between two reservoirs as one of the reservoirs decreases in size, is called Rayleigh distillation (Fig. 1). In short, the isotope ratios in the cloud vapor and the condensate are a function of the fraction of remaining water vapor in the cloud (which is a function of temperature), meaning that the precipitation gets more and more depleted as the fraction of water vapor in the cloud gets smaller and smaller.

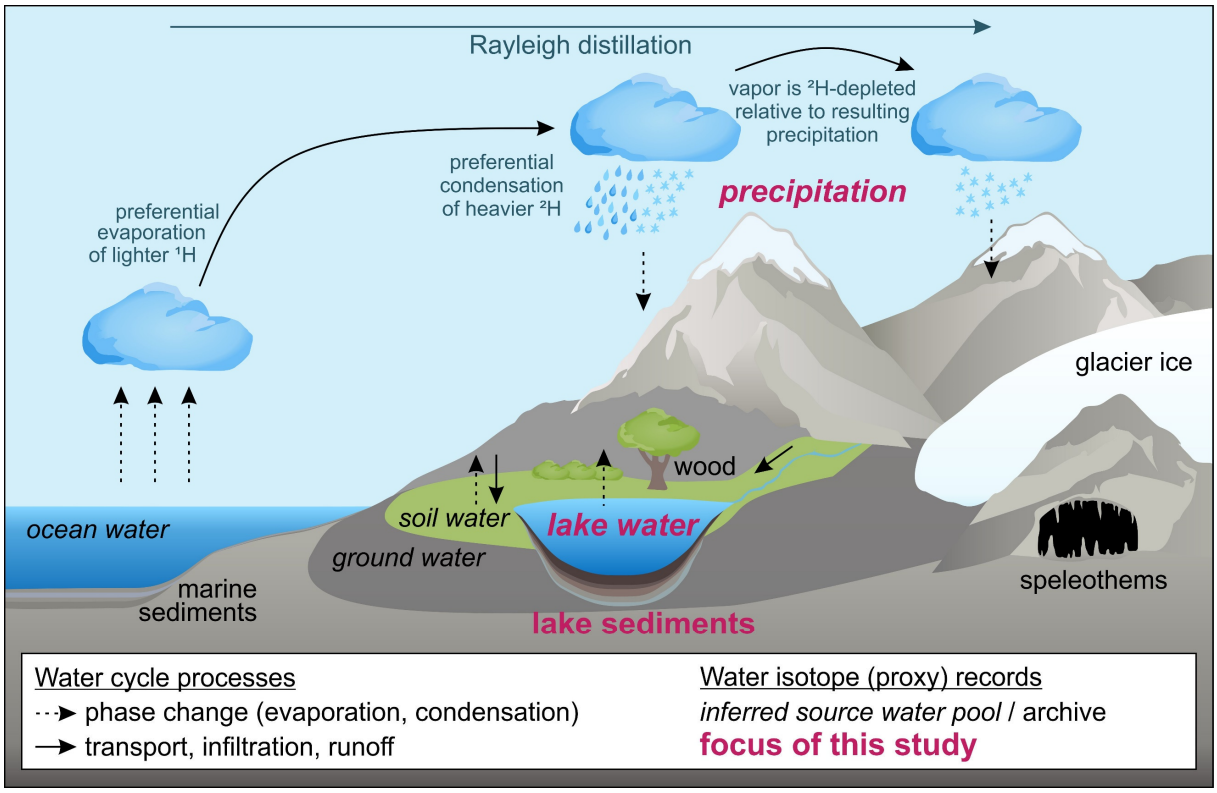

Fig. 1. Conceptual model of the global water cycle, with environmental water pools and archives that can be used to study water isotope proxies. The water pools/proxy records focused on in this study are displayed in red. Arrows show water cycle processes (phase changes and transport). Evaporation of sea water leads to cloud formation and progressive rainout and isotopic fractionation as temperature decreases (Rayleigh distillation). Modified after Konecky et al. (2020).

The spatial and temporal patterns of precipitation δ^2H and $\delta^{18}O$ (hereafter also referred to as precipitation isotopes) are controlled by several mechanisms, including the temperature dependence of equilibrium fractionation, progressive rainout during transport, and fraction of solid precipitation. Due to the mass-dependent fractionation of hydrogen and oxygen isotopes, there is a linear correlation between δ^2H and $\delta^{18}O$. The global average relationship between δ^2H and $\delta^{18}O$ in meteoric waters is described by the Global Meteoric Water Line (GMWL; Craig, 1961):

$$\delta^2H = 8 \times \delta^{18}O + 10 \qquad \text{(Equation 2)}$$

When a phase reaction cannot reach equilibrium, kinetic fractionation processes can occur. These processes are unidirectional, caused by slower diffusion speed of the heavy isotopes. When water molecules diffuse during evaporation, there is an "excess" of deuterium relative to ^{18}O in vapor (Dansgaard, 1964), causing a deviation from the expected 1:8 ratio. This non-

equilibrium fractionation can be quantified by the so-called deuterium excess (also referred to as d-excess or dxs), which can be calculated as:

$$d - excess = \delta^2H - 8 \times \delta^{18}O \quad \text{(Equation 3)}$$

The extent of non-equilibrium fractionation during evaporation (and hence the d-excess value) depends on the air and water temperature, relative humidity above the water surface, and evaporative surface cooling (Merlivat & Jouzel, 1979; Cappa et al., 2003). Furthermore, kinetic fractionation effects can occur during snow formation in mixed-phase clouds (Jouzel & Merlivat, 1984).

Since precipitation isotopes are affected by transport and fractionation processes in the global hydrological cycle, they are widely employed hydrological tracers. As direct measurements of precipitation δ^2H and $\delta^{18}O$ are not available over longer timescales, information about past precipitation isotope variability must be obtained indirectly using paleoclimate proxies. Stable isotopes of hydrogen and oxygen get preserved in various geological records and are therefore commonly applied to understand the paleoenvironment. Some of the most common applications are temperature reconstructions from ice cores (e.g., Dansgaard et al., 1969; Johnsen et al., 2001; Divine et al., 2011), and from foraminifera tests preserved in marine sediments (e.g., Emiliani, 1955; Rasmussen & Thomsen, 2004; Lisiecki & Raymo, 2005). In lake sediments, $\delta^{18}O$ from authigenic carbonates, chironomids (non-biting midges), and diatoms reflects the isotopic composition of the lake water when they formed. As lakes are mainly recharged by meteoric water, these proxies can indirectly archive the isotopic composition of past precipitation, and be used to reconstruct atmospheric circulation, humidity, precipitation seasonality etc. (e.g., Anderson et al., 2001; Hammarlund et al., 2002; Rosqvist et al., 2013; Arppe et al., 2017).

An increasingly popular proxy for high-latitude paleo-precipitation isotopes is δ^2H of sedimentary leaf waxes (e.g., Thomas et al., 2012; Balascio et al., 2013; Thomas et al., 2016; Keisling et al., 2017; Balascio et al., 2018b; Thomas et al., 2018; Thienemann et al., 2019; Thomas et al., 2020; Cowling et al., 2021; Gorbey et al., 2021; Katrantsiotis et al., 2021). This proxy is introduced in the following section and the focus of **Papers I & III**. The key to accurate climate interpretations using water isotope proxies from lacustrine sediments is to understand the processes affecting the lake water isotopic composition (Leng & Marshall, 2004; Jonsson

et al., 2009; Cluett & Thomas, 2020). Therefore, **Paper II** explores the modern water isotopic composition of Arctic and sub-Arctic lakes to evaluate the impact of variable precipitation isotopic composition and seasonality, as well as evaporative enrichment, on the lake water δ^2H and $\delta^{18}O$.

1.3. The leaf wax δ^2H paleo-precipitation proxy

Biomarkers are organic molecules that record past environmental and climate conditions. Compound-specific lipid biomarkers are widely used in paleoenvironmental studies due to their persistence to degradation over long geological timescales and their abundance in sedimentary settings (Eglinton & Eglinton, 2008). A variety of lipid biomarkers can be extracted from lake sediments and used to reconstruct different paleoenvironmental conditions within and around the lake basin. Plants produce superficial waxes to keep their moisture balance and protect the leaves (Eglinton & Hamilton, 1967). Here we focus on the leaf wax hydrogen isotopic composition (δ^2H_{wax}) of *n*-alkanoic acids, which are straight-chain fatty acids produced by bacteria, algae, and higher plants. δ^2H_{wax} is a useful tool for paleoclimatologists, as it is highly correlated to the δ^2H of the source water used by the organism (Sachse et al., 2004; Sachse et al., 2012; McFarlin et al., 2019). There is an offset between δ^2H_{wax} and the δ^2H of soil water or lake water (apparent fractionation, ε_{app}), e.g., due to biosynthetic fractionation (ε_{bio}) occurring during leaf wax generation (Fig. 2; Sessions et al., 1999; Sachse et al., 2012). Different plant types can have different ε_{bio} (Daniels et al., 2017; Berke et al., 2019), but it is relatively constant for specific compounds (Sachse et al., 2012; McFarlin et al., 2019).

The environmental water pool used as the hydrogen source differs between organisms, with aquatic plants using lake water and terrestrial plants using soil water during the growing season (Ficken et al., 2000; Aichner et al., 2010b; Shanahan et al., 2013; Wilkie et al., 2013; Thomas et al., 2016; Daniels et al., 2017). Since the hydrogen isotopic composition of aquatic leaf waxes (δ^2H_{aq}) reflects the δ^2H of lake water (δ^2H_{lake}), it will indirectly reflect precipitation δ^2H (δ^2H_{precip}) in precipitation-fed systems. Additionally, in arid regions where evaporation exceeds precipitation, the lake water δ^2H may be overprinted by evaporative δ^2H enrichment (Fig. 2; Gibson et al., 2002; Tondu et al., 2013; Cluett & Thomas, 2020). Precipitation is also the ultimate source of soil water used by terrestrial plants. Soil water can be evaporatively enriched,

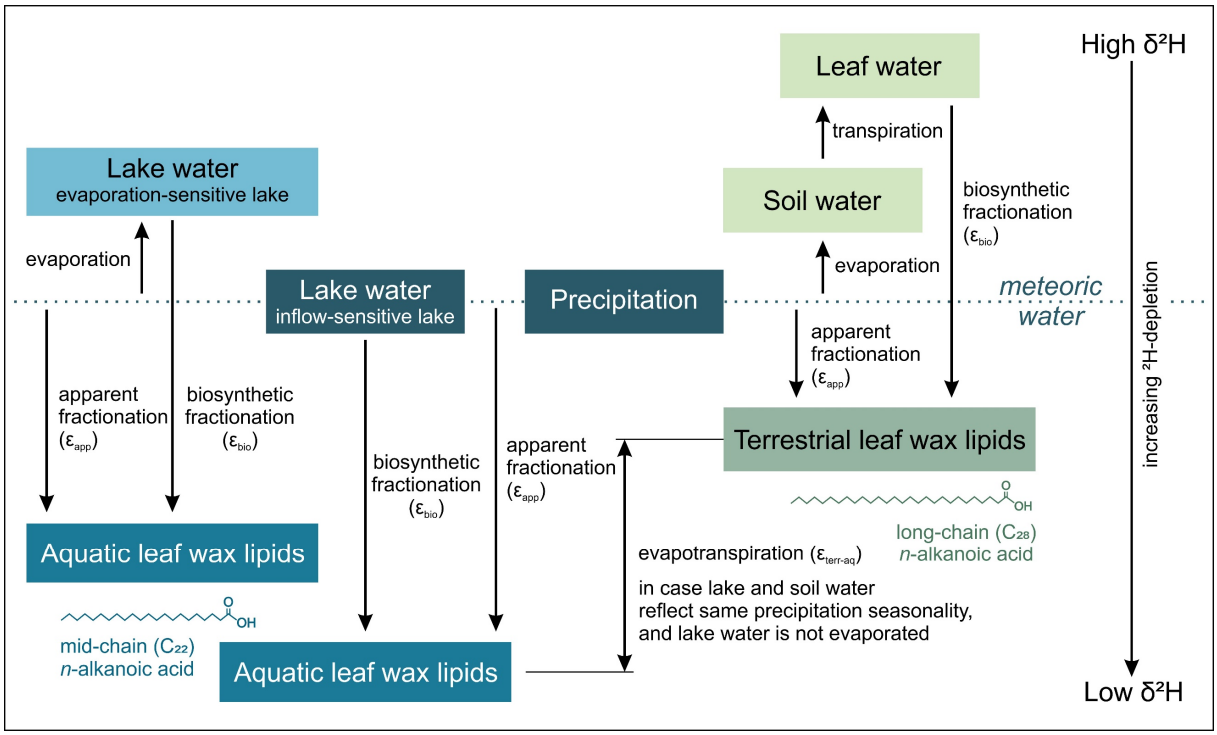

Fig. 2. Isotopic relationships and processes between source water and aquatic and terrestrial leaf waxes (not to scale). Adapted and modified from Sachse et al. (2006) and Aichner (2009).

which means that δ^2H of terrestrial plants (δ^2H_{terr}) reflects growing season soil water δ^2H, which is possibly influenced by evapotranspiration (Fig. 2; Kahmen et al., 2013).

The growing season lake and soil water δ^2H can reflect different precipitation seasonality. δ^2H_{lake} can reflect summer δ^2H_{precip} if the lake has a short residence time and the water is exchanged throughout summer, mean annual δ^2H_{precip} if the lake has a long residence time and the lake water consists of a mix of summer and winter precipitation, or winter δ^2H_{precip} if the lake receives a higher proportion of the annual precipitation as snow and/or late snowmelt (e.g., Katrantsiotis et al., 2021). Growing season soil water is often assumed to mainly be recharged by summer precipitation (Throckmorton et al., 2016).

In addition to δ^2H_{wax}, the following two parameters are useful for leaf wax interpretations. To quantify the isotopic difference between long-chain (C_{28}) and mid-chain (C_{22}) waxes, assuming that the compounds have similar ε_{app} (Thomas et al., 2020), we can calculate $\varepsilon_{28\text{-}22}$, using the equation:

$$\varepsilon_{28-22} = 1000 \times \left(\frac{\delta^2H_{C28}+1000}{\delta^2H_{C22}+1000} - 1\right) \quad \text{(Equation 4)}$$

This index can be interpreted as the isotopic difference between the source water pools, i.e., soil and lake water (Fig. 2). Changes in $\varepsilon_{28\text{-}22}$ can reflect changes in relative humidity (Rach et al., 2017) or precipitation seasonality (Thomas et al., 2020), depending on the hydrology of the lake. The average chain length distribution (ACL) for even-chain C_{20} to C_{30} *n*-alkanoic acids is calculated as:

$$ACL_{22-30} = \frac{\sum(n \times C_n)}{\sum(C_n)} \quad \text{(Equation 5)}$$

where C_n is the concentration (µg/g sediment) of each *n*-alkanoic acid with *n* carbon atoms. The ACL can give indications of likely source attributions since different plant types preferentially produce different leaf wax homologues.

1.4. Regional setting

The work in this thesis is focused to two research areas: the high-Arctic Svalbard archipelago (**Papers I & III**) and northern Fennoscandia (i.e., northern Norway, Finland, and Sweden; **Paper II**; Fig. 3). Both areas are located in the dynamic Nordic Seas region, where water and air masses originating from low and high latitudes meet, and atmospheric-ocean energy transfer results in varying seasonal climate (Drange et al., 2005). Temperatures in the Nordic Seas (the Norwegian Sea, Greenland Sea, and Iceland Sea) and surrounding areas are higher than at other locations at similar latitudes, mainly due to two mechanisms: 1) meridional heat transport by the North Atlantic Current, and 2) prevailing westerly and southwesterly maritime winds (Årthun et al., 2017). The North Atlantic Current brings warm waters northward along the Norwegian coast, before splitting into the Barents Sea Current and the West Spitsbergen Current, continuing this transport up along the west coast of Spitsbergen (Fig. 3; Skagseth et al., 2008).

In winter, temperature and precipitation variability in the region are strongly associated with the North Atlantic Oscillation (NAO) and intense cyclone activity. The NAO index is defined as the normalized air-pressure difference between the Icelandic Low and the Azores High in winter (Rogers, 1984). The NAO is closely related to the Arctic Oscillation (AO), which is associated with the polar vortex, and causes similar local temperature and precipitation signals (Thompson & Wallace, 1998; Dickson et al., 2000). During positive NAO (or AO) conditions, the pressure gradient between Iceland and the Azores (or between the Arctic and the northern Atlantic and Pacific Oceans) is greater than normal, causing stronger-than-normal westerlies,

(Hurrell, 1995; Uvo, 2003; Lawrence et al., 2020). The NAO also influences the glacier mass balance in northern Fennoscandia and to a lesser extent Svalbard, by regulating the amount of winter accumulation (Pohjola & Rogers, 1997; Bonan et al., 2019). Strong winter cyclones are common over the Norwegian Sea and between Svalbard and Fennoscandia and associated with strong winds and high precipitation amounts (Serreze et al., 1993; Rogers et al., 2005; Wickström et al., 2020).

Summer precipitation is not as strongly related to atmospheric circulation. Cyclones are common also in summer, but they are weaker and more spatially variable (Serreze et al., 1993; Zhang et al., 2004; Wickström et al., 2020). Summer rainfall over Scandinavia is often caused by local convection due to surface heating (Jaagus, 2009; Dyrrdal et al., 2015). On Svalbard, low summer temperatures make local convective precipitation less likely to occur. Precipitation amounts are low due to stable, stratified air masses containing low amounts of water vapor (Førland et al., 2009).

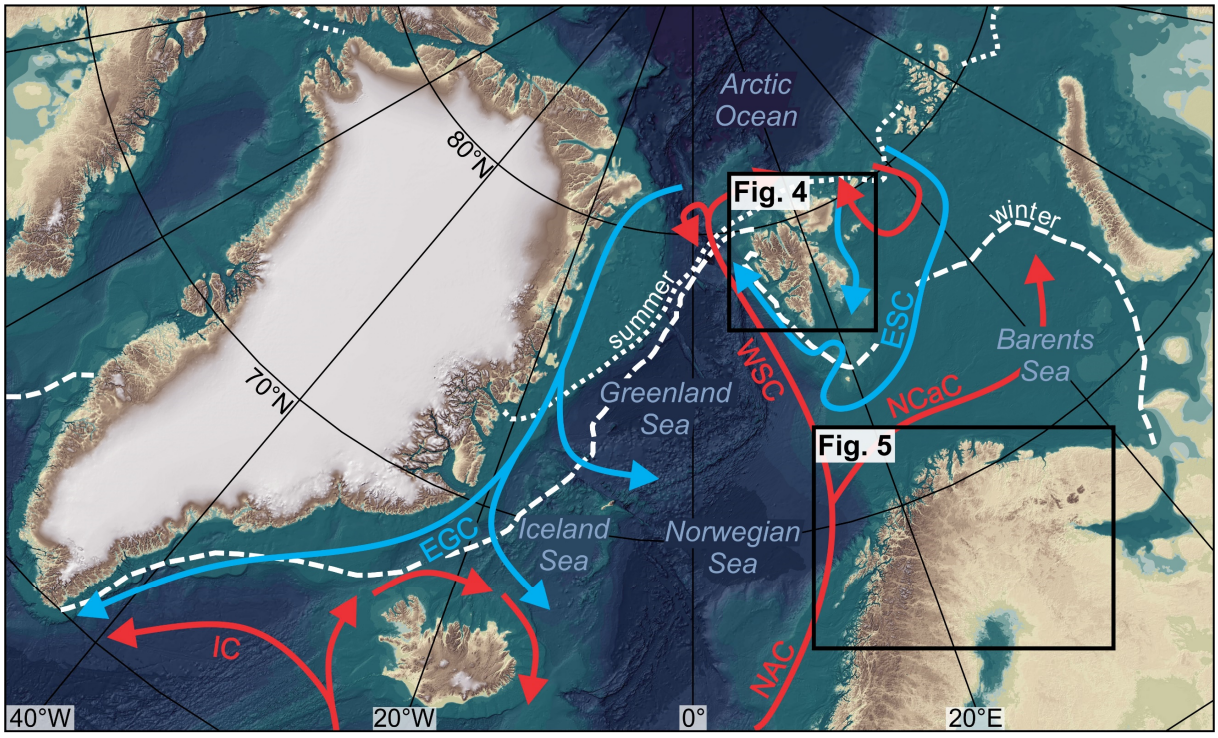

Fig. 3. Overview map of the North Atlantic region. Major ocean surface currents are indicated in red (warm: NAC = North Atlantic Current; NCaC = North Cape Current; WSC = West Spitsbergen Current; IC = Irminger Current) and blue (cold: ESC = East Spitsbergen Current; EGC = East Greenland Current), and median winter and summer sea-ice extent 1981–2010 are shown with white dashed and dotted lines (National Snow and Ice Data Center, 2019). Black boxes mark the two study areas. Background map from IBCAO (Jakobsson et al., 2012).

1.4.1. Svalbard

Svalbard (74–81°N and 10–35°E) is located at the end of the North Atlantic cyclone track and experiences warmer and wetter conditions than other areas at similar latitude (Eckerstorfer & Christiansen, 2011; Serreze & Barry, 2014). The archipelago spans large climate gradients, due to the influence of Arctic and Atlantic air masses and variable ocean heat flux, further influencing the distribution of sea ice (Fig. 4; Hisdal, 1998; Walczowski & Piechura, 2011). The Fram Strait is the world's northernmost ocean area with essentially ice-free conditions all year round (Fig. 4; Haugan, 1999). The West Spitsbergen Current transports warm, saline water in the east of the strait, along the west coast of Spitsbergen (Skagseth et al., 2008). Svalbard is dominated by southwesterly winds bringing mild Atlantic air, and northeasterly winds bringing dry polar air (Hagen et al., 1993). Easterly moisture from the Barents Sea cause high precipitation amounts over the east coast glaciers (Hagen et al., 1993), whereas extreme precipitation events are favored by south-southwesterly flow (Dobler et al., 2019). Precipitation amounts are highest over the mountains on the west coast and the southeastern islands, whereas the central and northeastern parts are relatively arid (Østby et al., 2017). In addition to these large-scale patterns, Svalbard experiences large local variability (Humlum, 2002; Førland & Hanssen-Bauer, 2003).

Fig. 4. Overview map of Svalbard. Studied lakes are marked with red stars, meteorological stations with large white circles, and other place names mentioned in the text with small white (terrestrial) and blue (marine) circles. Background map from IBCAO (Jakobsson et al., 2012).

A homogenized, composite monthly mean air temperature time series for Svalbard Airport shows a warming rate of 0.32 °C per decade from 1898 to 2018 (Nordli et al., 2020). After 1991, the rate is 1.7 °C per decade, which is twice the Arctic average and approximately seven times the global average (0.8 and 0.2 °C per decade, respectively; Nordli et al., 2020). From 1971–2000 to 2071–2100, Svalbard is projected to see a temperature increase of almost 10 °C (for emission scenario RCP8.5 = "business as usual"; Hanssen-Bauer et al., 2019). The amplified warming also has an immense impact on the hydrological cycle, through shorter ice-cover seasons in the fjords on the west coast, reduced glacier net mass balance, permafrost warming, and increased moisture transport (Hanssen-Bauer et al., 2019).

In an Arctic context, Svalbard has a unique precipitation record, comprising a number of 50-100-year-long time series of precipitation measurements (Førland et al., 1997; Hanssen-Bauer, 2002; Førland et al., 2011; Hanssen-Bauer et al., 2019). At the four long-term stations (Svalbard Airport, Ny-Ålesund, Bjørnøya, and Hopen), the precipitation amounts have increased by 20–35% over the last 50 years (Førland et al., 2020). There are no long-term precipitation measurements from northeastern Svalbard, but snow accumulation measurements suggest that southern Spitsbergen receives twice as much snow (in water equivalent) compared to central and northern Spitsbergen, and that the east coast receives 40% more snow than the west coast (Sand et al., 2003). From 1971–2000 to 2071–2100, precipitation amounts are projected to increase by 65% (for RCP8.5; Hanssen-Bauer et al., 2019). The largest relative increases are predicted to occur in winter and in the northeast. The heterogenous pattern of snow accumulation has impact on the equilibrium line altitude (ELA) of glaciers, being lower in coastal, and higher in inland settings (Hagen et al., 1993; van Pelt et al., 2016). Furthermore, heavy precipitation events have become more frequent and intense (Hanssen-Bauer et al., 2019), and are projected to continue to do so towards the end of the 21st century (Isaksen et al., 2017).

Our understanding of precipitation isotope variability on Svalbard is limited. Monthly precipitation isotopes have been measured at Isfjord Radio (78.07°N, 13.63°E; 6 m a.s.l.) between 1961–1965 and 1972–1975, and Ny-Ålesund (78.92°N, 11.93°E; 7 m a.s.l.) in 1990–2016, as part of the Global Network of Isotopes in Precipitation (GNIP; IAEA/WMO, 2019). Additionally, precipitation isotope values were monitored at the Hornsund Polish Polar Station in 2013–2014 (Arppe et al., 2017) and in Barentsburg in 1975–1981 and 2016–2017 (Skakun et al., 2020). All these sites are located on the west coast of Spitsbergen, and none of the data

series show a significant seasonal trend in δ^2H or $\delta^{18}O$. The isotopic seasonality is expected to be higher in central and northeastern Svalbard, because of larger contrast in climate between winter and summer.

To reconstruct Holocene climate on Svalbard beyond the instrumental record, we can use paleoclimate records. Many studies have focused on temperature and sea-ice history, but little is known about precipitation. The Early Holocene was characterized by peak summer insolation (Laskar et al., 2004), and high ocean surface and subsurface temperatures due to increased Atlantic heat flux (e.g., Hald et al., 2007; Werner et al., 2016; Mangerud & Svendsen, 2018). This led to reduced sea-ice cover in the eastern Fram Strait (Werner et al., 2016) and in many Svalbard fjords (e.g., Forwick & Vorren, 2009; Bartels et al., 2018; Allaart et al., 2020). Warmer-than-present temperatures have also been suggested by alkenones (van der Bilt et al., 2019) and sedimentary ancient DNA (*sed*aDNA) of vascular plants (Voldstad et al., 2020) from lacustrine sediments. Furthermore, the glacier cover on Svalbard was substantially reduced (Fjeldskaar et al., 2018; Farnsworth et al., 2020). However, glacier re-advances still occurred, and it has been speculated that increased winter precipitation might have been one of the drivers (Farnsworth et al., 2020). Glaciers were absent or much smaller during the Middle Holocene (e.g., Svendsen & Mangerud, 1997; Allaart et al., 2021b), and warm and dry conditions are suggested from lake sediment records (Balascio et al., 2018b; Voldstad et al., 2020). Sea surface temperatures remained high (e.g., Werner et al., 2016; Mangerud & Svendsen, 2018), and sea-ice concentrations low (Werner et al., 2016) until *c*. 6–5 cal. kyr BP. The Late Holocene was characterized by Neoglacial cooling, with declining summer insolation (Laskar et al., 2004), and lower temperatures inferred from alkenones (van der Bilt et al., 2018), plant macrofossils (Birks, 1991), and *sed*aDNA (Voldstad et al., 2020). The sea-ice cover in the Fram Strait and Svalbard fjords increased with weakened Atlantic water advection (Forwick & Vorren, 2009; Werner et al., 2016; Bartels et al., 2018), and many glaciers re-advanced between 4–0.5 cal. kyr BP (Farnsworth et al., 2020). Some of the Neoglacial and Little Ice Age (LIA) glacier advances have been suggested to be driven by increased winter precipitation (D'Andrea et al., 2012; Røthe et al., 2015), possibly due to occasional northward shifts of the sea-ice edge, and increased evaporation (Müller et al., 2012).

Precipitation reconstruction on Svalbard is hampered by the lack of available climate archives reflecting precipitation changes. The dating of ice cores is challenging due to surface melting in summer altering the original ice core records, and the oldest ice core records to date go back

only *c*. 1,200 years (Isaksson et al., 2003; Isaksson et al., 2005; Divine et al., 2011). Furthermore, local pollen production is low, and the long-distance component is high (van der Knaap, 1987; Birks, 1991), limiting the suitability of pollen studies. To better constrain the seasonal variability in precipitation throughout the Holocene on Svalbard, we analyze sedimentary leaf waxes, presented in **Papers I & III**.

1.4.2. Northern Fennoscandia

The second region of interest and focus of **Paper II** is northern Fennoscandia, where we investigate surface water samples from Norway, Finland, and Sweden. The study area spans from the Norwegian Sea in the northwest to Bothnian Bay in the southeast, between 65.74°N to 71.11°N and 18.39°E to 30.06°E (Fig. 5). The northwestern side of the Scandinavian Mountains is characterized by alpine topography shaped by Quaternary glaciations, with steep mountains, U-shaped valleys, and fjords. The highest mountains are the *c*. 1800-meter-high Lyngen Alps (Fig. 5). Towards southeast the mountains become gradually lower, forming a more gently undulating landscape, and reaching sea level by the Bothnian Bay.

The topography has a great impact on the climate in the area. The western side of the mountains has a maritime climate (cool summers and mild winters), whereas the interior parts are more continental (warm summers and cold winters; Førland et al., 2009). Most of the moisture is brought by dynamic low-pressure systems from the North Atlantic and prevailing westerly winds. When the warm humid air reaches land, the steep topography causes orographic lift, and precipitation falls on the windward side of the mountains (Hanssen-Bauer & Førland, 2000). The leeward side is in rain shadow and receives much lower precipitation amounts (Uvo, 2003). The NAO has a large impact on winter precipitation by regulating the strength of the westerlies (Hurrell, 1995; Uvo, 2003; Irannezhad et al., 2014). During NAO+ conditions, Scandinavia receives more precipitation due to a northward shift of the North Atlantic storm track. Also AO+ conditions can result in higher precipitation amounts (Lawrence et al., 2020). Furthermore, winters with mild Arctic weather, low sea-ice concentrations and strongly negative NAO and AO conditions can result in extreme snowfall over northern Europe (Cohen et al., 2013; Bailey et al., 2021). During cold air outbreaks, dry polar air exposed to warm ocean water surfaces creates high heat and moisture flux (Shapiro et al., 1987; Papritz & Sodemann, 2018).

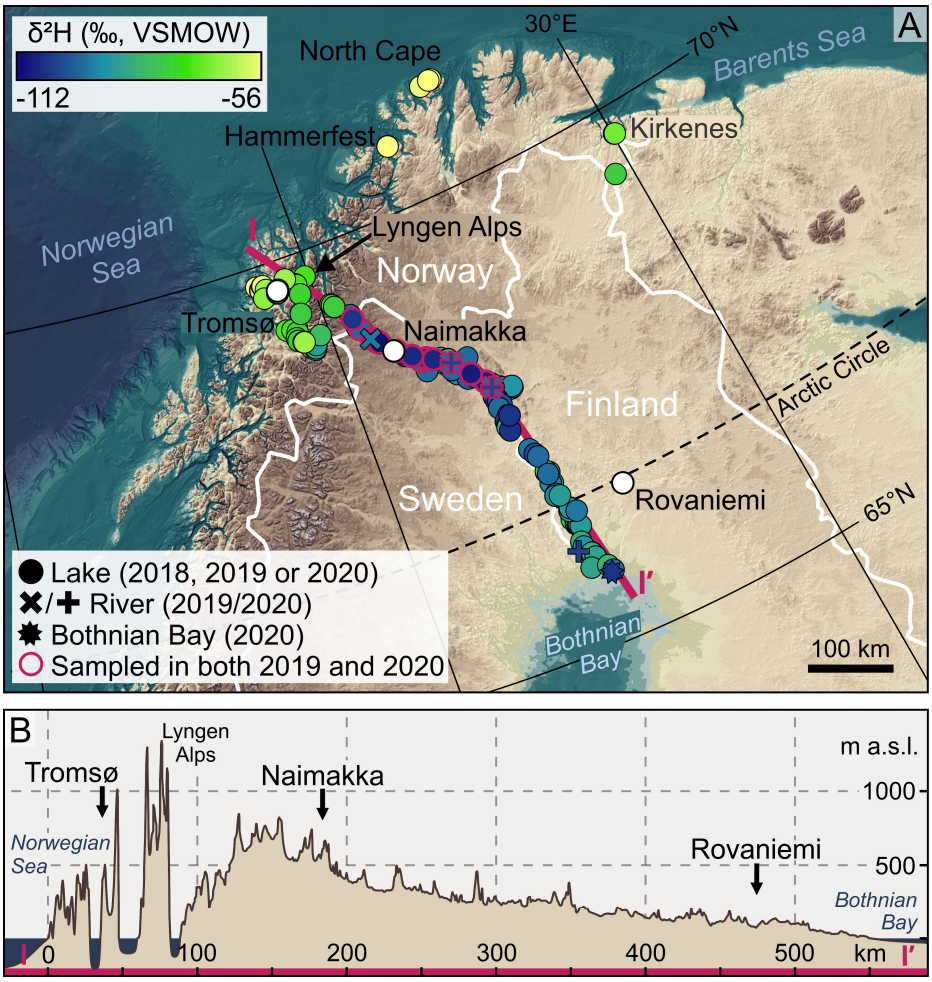

Fig. 5. (a) Map of northern Fennoscandia, showing surface water δ^2H from 135 lakes, two rivers and the Bothnian Bay (colored by δ^2H value), locations of meteorological stations (white circles), and the extent of the elevation profile in (b) (red line). Background map from IBCAO (Jakobsson et al., 2012). (b) Elevation profile from the Norwegian Sea to the Bothnian Bay.

In northern Norway, the mean annual air temperature (MAAT) has increased by 0.08–0.11 °C per decade from 1900 to 2014 (Hanssen-Bauer et al., 2017). The increase is greatest (0.14–0.15 °C per decade) in spring, and lowest (and not statistically significant) in winter. For emission scenario RCP8.5, MAAT is projected to increase by 5.0–6.1 °C from 1971–2000 to 2071–2100, and the increase is predicted to be largest in winter (Hanssen-Bauer et al., 2017). Finland has experienced a long-term (1847–2013) mean warming of 0.14 °C per decade (Mikkonen et al., 2015), and in northern Finland, the MAAT has increased by 0.3–0.4 °C per decade between 1961–2010 (Aalto et al., 2016). For emission scenario RCP8.5, Ruosteenoja et al. (2016) projected an increase of mean winter air temperature by 6–8 °C and mean summer air temperature by 4–5 °C from 1981–2010 to 2070–2099 in northern Finland and northern

Sweden. This corroborates with data from Sweden (Eklund et al., 2015), predicting similar values for RCP8.5, and the largest increase in winter.

Mean annual precipitation (MAP) amounts have increased by 0.2–1.7% per decade from 1900 to 2014 in northern Norway (Hanssen-Bauer et al., 2017). Also northern Sweden has experienced a wetting trend since 1900, in particular after 1950, and especially in winter (Chen et al., 2021). From 1971–2000 to 2071–2100, MAP amounts over northern Norway are projected to increase by 17–22 % (RPC8.5; Hanssen-Bauer et al., 2017). The increase is projected to occur during all seasons, but there is no consistency between models and scenarios in terms of seasonal trends. For northern Finland and northern Sweden, the precipitation amounts are projected to increase by 20–30% in winter and *c*. 10% in summer from 1981–2010 to 2070–2099 (RCP8.5; Ruosteenoja et al., 2016).

Monthly precipitation δ^2H and $\delta^{18}O$ have been measured at two GNIP stations in our study area: Naimakka (68.68°N, 21.53°E; 403 m a.s.l.) in 1990–1995 and Rovaniemi (66.50°N, 25.75°E; 107 m a.s.l.) in 2003–2014 (Fig. 5; IAEA/WMO, 2019). To monitor the precipitation isotope seasonality at a more coastal site, we installed a precipitation gauge in Tromsø (69.68°N, 18.96°E; 73 m a.s.l.; Fig. 5) in 2019 (see section 2.2.1). Naimakka is the most continental site, located on the eastern side of the Scandinavian Mountains, and displays the most depleted values and the strongest seasonality. Tromsø precipitation δ^2H and $\delta^{18}O$ are relatively enriched and do not show a strong seasonality. Rovaniemi falls in between, having a stronger seasonal variability than Tromsø, but less depleted values than Naimakka.

1.5. Aims and research objectives

Arctic precipitation changes in response to warming during earlier periods in Earth's history can serve as an analogue for the future. However, the Holocene history of Arctic precipitation changes is largely unknown, due to the absence of long instrumental records and lack of robust proxies. In the light of future projections (i.e., variable precipitation increases between different seasons and different locations), we need to increase the spatial distribution of long-term paleo-precipitation records, which requires thoughtful consideration of how lake water proxies record variable seasonal distribution of precipitation. The overall aim of this PhD project is to increase our understanding of the Arctic water cycle, and how changes in time and space are reflected in stable water isotope proxies.

More specifically, the research objectives are to:

- Generate Holocene precipitation records across the understudied Svalbard based on terrestrial and aquatic leaf wax δ^2H, with a focus on precipitation seasonality (**Papers I & III**).
- Identify Holocene variations in winter precipitation on Svalbard, one of the main controls on glacier mass balance (**Papers I & III**).
- Explore modern controls on lake water δ^2H by evaluating variable impact of precipitation δ^2H and evaporation on lake water δ^2H across northern Fennoscandia (**Paper II**).

2. Scientific approach

In this thesis, I use lipid biomarkers from lacustrine sediment cores from Svalbard to investigate Holocene variability in Arctic precipitation seasonality (**Papers I & III**), and lake surface water samples from northern Fennoscandia to investigate modern controls on lake water δ^2H (**Paper II**). The motivation behind the use of two different study areas was mainly practicality. From Svalbard, we had access to a large collection of lake sediment cores that we could use for the Holocene precipitation reconstruction, but few modern data. Getting good spatial coverage of lakes from Svalbard for a lake water study as presented in **Paper II** would require massive logistical support because of the remote location. By targeting northern Fennoscandia, an area with a well-developed road system and easy access to lakes, we could cover a large area and sample many lakes within a few days. It was also feasible to repeat the sampling over several years. Additionally, we could compare the isotopic composition of the lake water to precipitation isotope data from stations along our targeted transect.

Although our southernmost lake on Svalbard is located *c*. 800 km north of the Norwegian mainland and influenced by a range of different processes (e.g., variable sea-ice extent, Arctic air and water masses), there are parallels between the two study regions. Both regions experience climate gradients related to the dominance of North Atlantic moisture and alpine topography, with humid maritime climate on the west coast and drier more continental climate towards the (north/south)east. Furthermore, the west coast (i.e., Isfjord Radio and Ny-Ålesund on Svalbard; Tromsø on the mainland) experiences similar amplitude of seasonal temperature variability (although Svalbard is generally 5–10 °C colder) and receives most precipitation in

fall and winter. In the following sections, I present the scientific approach used in this study, starting with the Holocene sedimentary leaf waxes from lakes on Svalbard, followed by the modern lake water isotopes from northern Fennoscandia.

2.1. Svalbard lakes

For the Holocene precipitation reconstructions, we targeted four lakes on Svalbard to explore spatial and temporal differences in precipitation seasonality (Figs 4 and 6). The lakes were chosen based on their location and estimated residence time (i.e., the average time a given molecule of water remains in the lake). By utilizing sediment cores analyzed in other studies (Schomacker et al., 2019; Voldstad et al., 2020; Farnsworth et al., 2022), we could target sedimentary records that have already been scanned and logged, and which have a good chronological control. A pilot study of one core from Austre Nevlingen was performed at UB in 2018, which together with analyses of a second core generated data for **Paper I**. Heftyevatnet, Jodavannet and Kløverbladvatna are introduced in **Paper III**. Details on the locations of the lakes, and lake and catchment morphometry are given in Table 1.

Table 1. Lake data for Austre Nevlingen, Heftyevatnet, Jodavannet and Kløverbladvatna, Svalbard.

Lake	Latitude (°N)	Longitude (°E)	Lake elevation (m a.s.l.)	Maximum water depth (m)	Lake surface area (km^2)	Catchment area (km^2)	Spring Melt Residence Time (months)	Ice-free Season Residence Time (months)
Austre Nevlingen	79.783	15.786	41	18	0.12	0.48	28.3	156.7
Heftyevatnet	77.998	14.149	43	6.5	0.015	0.15	2.1	15.4
Jodavannet	79.338	16.017	140	6.4	0.020	1.31	0.8	4.2
Kløverbladvatna	79.765	21.715	8	17.5	0.23	1.64	19.0	105.4

2.1.1. Sediment cores

The lacustrine sediment cores presented in **Papers I & III** were collected between 2015 and 2019. The coring, core splitting, logging, and a range of standard bulk sediment analyses are described for Kløverbladvatna, Jodavannet, and Heftyevatnet by Schomacker et al. (2019), Voldstad et al. (2020), and Farnsworth et al. (2022). The Austre Nevlingen cores are presented for the first time in **Paper I**.

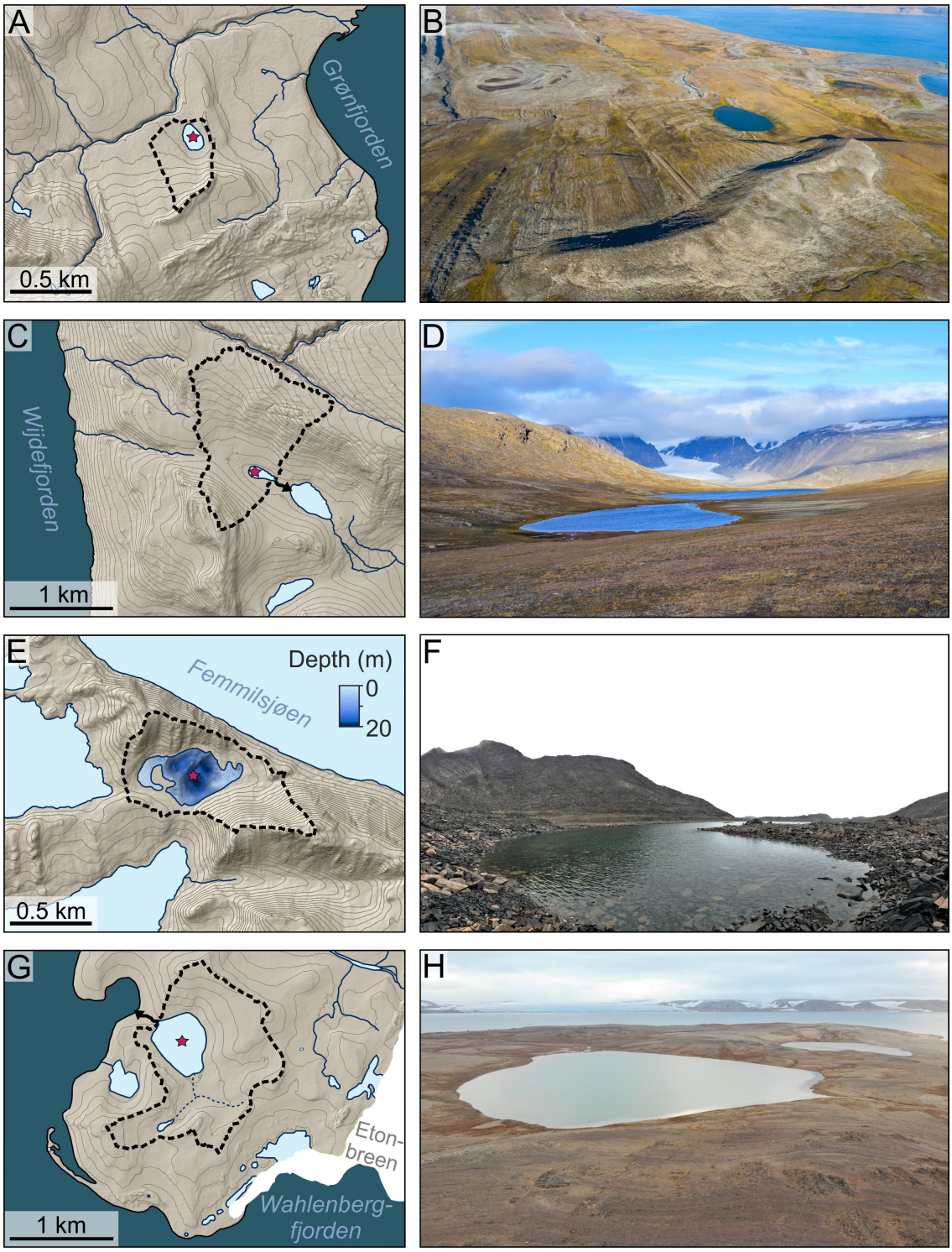

Fig. 6. Catchment overviews of Heftyevatnet, western Spitsbergen (a-b), Jodavannet, northern Spitsbergen (c-d), Austre Nevlingen, northern Spitsbergen (e-f), and Kløverbladvatna, Nordaustlandet (g-h). Background maps in (a), (c), (e), and (g) based on 5x5 m DEM from Norwegian Polar Institute (2014) with 10-m contour lines. The photographs were taken in August 2017 (Erik S. Mannerfelt; Farnsworth et al., 2022), August 2016 (Anders Schomacker), August 2018 (Sofia E. Kjellman), and August 2021 (Sara M. Cohen), respectively.

From all lakes, overlapping cores were collected using a Universal surface corer (120 cm long and Ø68 mm coring tubes) and a hand-held lightweight piston corer (200 cm long and Ø60 mm coring tubes). Coring was performed through a hole in the floor of a small Zodiac in summer, or from the spring lake ice. To identify the deepest basin in each lake, the bathymetry of all lakes was surveyed using a Hondex PS-7 Transducer LCD Digital Sounder for point measurements, and for Austre Nevlingen with a Garmin ECHOMAP™ Plus 73SV with a CV52HW-TM transducer and a 5 Hz receiver, using the Quick Draw contour function.

All lake sediment cores were split open, logged and analyzed in an ITRAX core scanner (Croudace et al., 2006) to record variations in the element-geochemical properties. The ITRAX provides high-resolution X-ray fluorescence (XRF) data, magnetic susceptibility (MS), and optical and radiographic images. We used the titanium (Ti) signal and the calcium-to-iron (Ca/Fe) ratio to identify variations in the minerogenic input, as these can be used to detect lake basin isolation (Larsen et al., 2017) and glacial meltwater input (Kylander et al., 2011). Ti was normalized against the incoherent (inc) and coherent (coh) Rh scatter (Ti/(inc + coh) to remove instrumental effects (Kylander et al., 2011). The XRF data were also used for core correlation (section 2.1.2). To determine the organic matter content, we performed loss on ignition (LOI; Heiri et al., 2001) on 1–2 cm^3 samples, that were dried at 110 °C for 24 h and ignited at 550 °C for 4 h. Core descriptions and lithostratigraphy are presented in full in by Schomacker et al. (2019), Voldstad et al. (2020), Farnsworth et al. (2022), and in **Paper I.** An overview of all sediment cores, including core photographs, X-ray images, lithology, and depths for leaf wax and radiocarbon samples is given in **Paper III**.

2.1.2. Core chronologies and composite core construction

To determine the timing of changes in the sedimentary records and interpret variability over time, it is crucial to have a good age control. Radiocarbon (^{14}C) dating is a widely used method to determine the age of late Quaternary sediments, but can be problematic on Svalbard due to lack of organic material, and the presence of coal or carbonate rocks. To avoid potential lake reservoir effects and minimize the risk of getting too old ages, we targeted lakes with little or no coal and carbonates in the catchment, and preferentially dated terrestrial plant remains, since terrestrial plants uptake carbon directly from the atmosphere (Hajdas, 2008). In regions with crystalline bedrock, autochthonous aquatic macrofossils can be used for dating since the ^{14}C in lake water and atmosphere is often in equilibrium (Wolfe et al., 2004). The radiocarbon ages

presented in **Papers I & III** are mainly measured on *Salix polaris* leaves or aquatic bryophytes. Another advancing dating method is tephrochronology, using the chemical fingerprint of discrete layers of volcanic ash (tephra) to identify volcanic eruptions of known age. Cryptotephra (non-visible volcanic ash) can travel far from the volcanic source before being deposited and has been found in Svalbard lake sediments (D'Andrea et al., 2012; van der Bilt et al., 2017; Farnsworth et al., 2022). In **Paper III**, the Vedde Ash, identified by Farnsworth et al. (2022), is used as an age constraint in the Heftyevatnet age-depth model.

All core chronologies in this study are based on accelerator mass spectrometry (AMS) radiocarbon dating on handpicked plant macrofossils, identified and isolated through sieving. The samples were dated at the Ångström Laboratory, Uppsala University, Sweden, and Lund University Radiocarbon Dating Laboratory, Sweden. Age-depth models for the sediment cores are presented in **Paper I** (Austre Nevlingen), and by Schomacker et al. (2019; Kløverbladvatna), Voldstad et al. (2020; Jodavannet), and Farnsworth et al. (2022; Heftyevatnet). Three new age-depth models were generated in **Paper III**, to include seven additional ages for Heftyevatnet, three new ages for Jodavannet, and to establish a composite age-depth model for Kløverbladvatna. Since we used multiple cores from all lakes, a composite sequence was constructed for each of the lakes. The overlapping cores were aligned in AnalySeries (v. 2.0.8; Paillard et al., 1996) and correlated using tie points in the XRF data, looking at several different elemental ratios (e.g., Ca/Fe, Fe/Ti, and Ti/(inc+coh)).

To allow us to present proxy data with age model uncertainty, all proxy and chronological data were entered into Linked PaleoData (LiPD) files (McKay & Emile-Geay, 2016). Age-depth models were generated in R (v. 4.1.3; R Core Team, 2021) using Bacon (v. 2.5.7; Blaauw & Christen, 2011) and the IntCal13 (**Paper I**; Reimer et al., 2013) or IntCal20 dataset (**Paper III**; Reimer et al., 2020) within the geoChronR package (v. 1.1.5; McKay et al., 2021). The lower depth (d.max) for each record was set to the lowermost leaf wax or radiocarbon sample depth, and the upper depth (d.min) to the uppermost leaf wax sample. To account for changes in sedimentation rate (as indicated by a major change in the lithology), boundaries were added and the prior mean accumulation rate (bacon.acc.mean) adjusted. All radiocarbon ages are presented in calibrated kiloyears before present (cal. kyr BP; BP = 1950).

2.1.3. Lipid biomarker extraction and analysis

Biogeochemical and isotopic analyses were performed in the Organic and Stable Isotope Biogeochemistry Laboratory at the University at Buffalo, using previously published methods (Thomas et al., 2012). In short, the *n*-alkanoic acids were 1) extracted, 2) purified, and 3) analyzed (Fig. 7). A simplified flowchart summarizing the methodological approach and analytical procedures used for the lacustrine sediment records and modern plant samples, focusing on the *n*-alkanoic acid extraction and analysis, is shown in Figure 8.

In the first step, the samples were freeze-dried, homogenized, and mixed with diatomaceous earth. The total lipid extract (TLE) was extracted with a Dionex 200 Accelerated Solvent Extractor (ASE) using dichloromethane (DCM):methanol 9:1 (v:v), flushed three times for 10 minutes each. The ASE uses high temperature (120 °C) and pressure (1200 psi) to extract the free lipids from the sediments. An internal standard ($C_{20:1}$ *n*-alkanoic acid) was added to allow biomarker quantification. Subsequently, the acid fraction was separated from the neutral fraction using flash columns with an aminopropyl silica gel solid phase. The aminopropyl group acts as a base and forms a strong bond to the acid functional group of the fatty acids. Therefore, when the neutral fraction was eluted in DCM:isopropanol 2:1, the fatty acids stuck to the solid phase. To collect the acid fraction, we used 4% acetic acid in DCM. This stronger acid bonds stronger to the solid phase and the fatty acids are therefore released. After extraction, the fatty

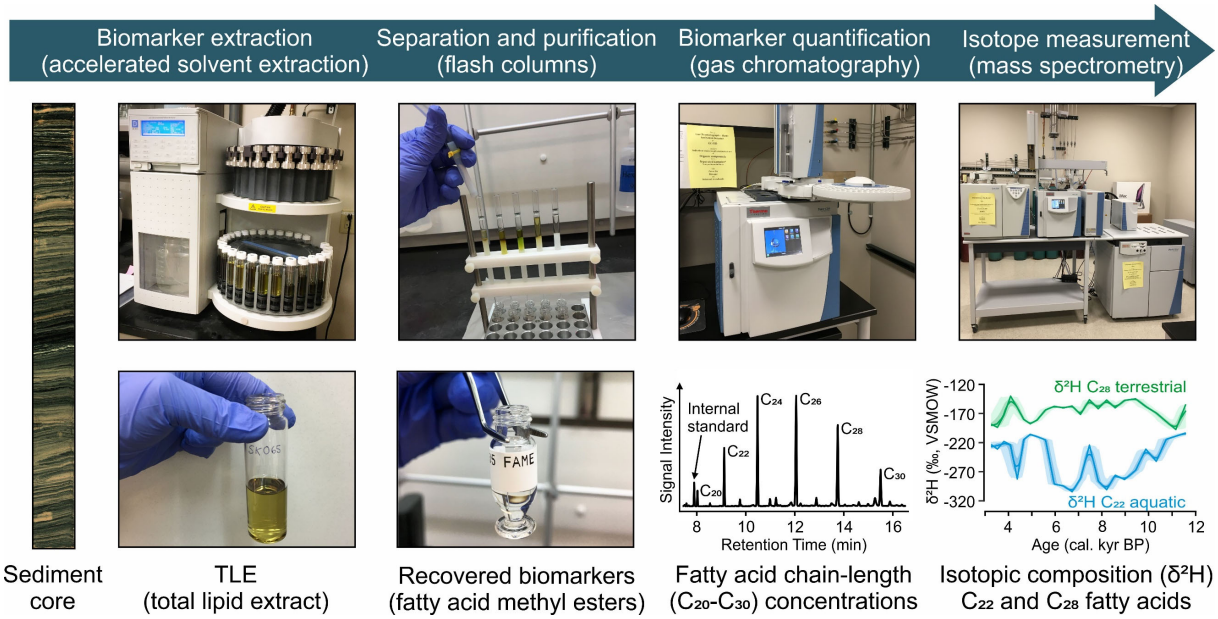

Fig. 7. Simplified methodology for generating leaf wax *n*-alkanoic acid data, from lipid extraction to δ^2H analysis.

acids need to be derivatized to be sufficiently volatile to be analyzed on the gas chromatograph. The acid fraction was methylated in acidified methanol with a known isotopic composition at 60 °C overnight, converting the fatty acids into less polar fatty acid methyl esters (FAMEs). After extraction, the FAMEs were purified before quantification and δ^2H measurement. The FAMEs were extracted in hexane three times from a hexane-salt water mixture. A final clean-up was done using flash columns with a silica gel solid phase, eluting FAMEs in DCM, after first eluting apolar compounds (e.g., alkanes and hydroxy fatty acids) in hexane.

We quantified the relative abundance of *n*-alkanoic acids on a Thermo Trace 1310 Gas Chromatograph (GC) with two flame ionization detectors operated in parallel and AI1310 autosamplers and two split/splitless injectors. Details on the GC conditions and programs are given in Table 2. Compound peaks were identified using the retention time of the added internal standard as a reference. To convert peak areas into concentrations, we used external calibration curves determined for a C_{28} FAME standard. The FAME masses were normalized to the dry mass of extracted sample and the recovery of the standard.

FAME δ^2H was measured on a Thermo Scientific Delta V Plus isotope ratio mass spectrometer (IRMS) coupled to a Trace 1310 GC via an Isolink II and Conflo IV. The FAME concentrations were used to dilute and inject target amounts of compounds. We used the same GC conditions as during FAME quantification, except for the final flow rate and the carrier gas (Table 2). The H_3^+ factor was determined at the beginning of every sequence, and samples were run in triplicates (or duplicates or singles for small samples) along with FAME standards of known composition to account for drift, linearity and normalize to the VSMOW scale (Table 2). The FAME values were also corrected for hydrogens added during methylation. We injected C_{20} and C_{28} FAME standards at a range of masses to constrain the peak-size effects on the measured isotopic composition. Peaks that were below a threshold (*c*. 2-4 V·s for each sequence) were excluded. For sequences without clear linearity and small peaks (C_{20} and/or C_{30}), all peaks for that chain length were discarded. For details, see **Paper III**. The total uncertainty of measured δ^2H values is given as the Standard Error of the Mean (SEM), i.e., the square root of the sum of the squares of total measurement uncertainty for each sample, divided by the square root of the number of measurements.

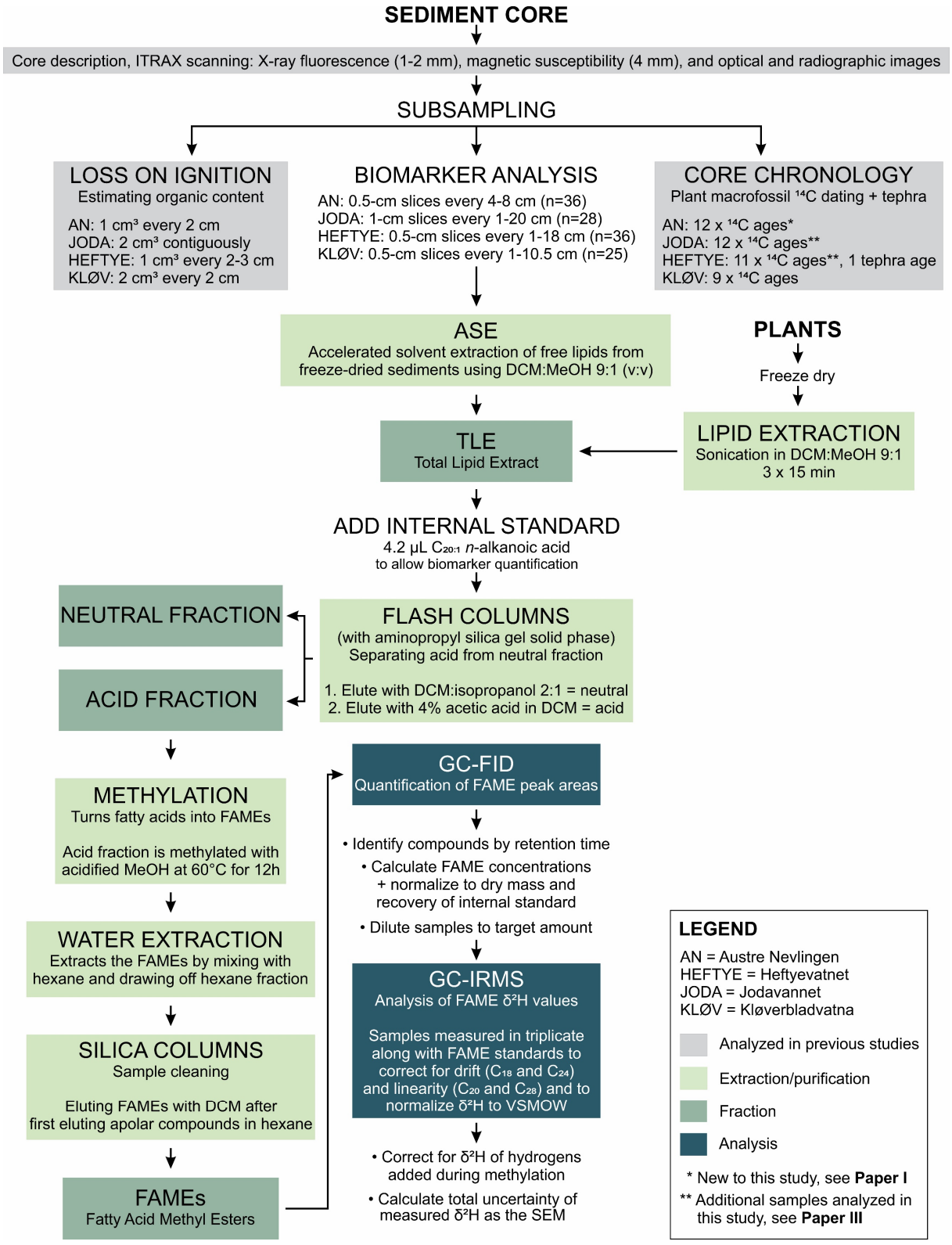

Fig. 8. Flowchart summarizing the methodological approach and geochemical analyses performed in this study, producing data for **Papers I & III**. Abbreviations are listed on pages x–xi.

Table 2. Instrumentation and settings for FAME quantification using gas chromatography with flame ionization detection (GC-FID) and δ^2H analysis using gas chromatography-isotope ratio mass spectrometry (GC-IRMS).

	GC-FID	**GC-IRMS**
Analyzer	Thermo Trace 1310 GC with two FIDs operated in parallel with AI1310 autosamplers and two split/splitless injectors	Thermo Scientific Delta V Plus IRMS coupled via Isolink II and Conflo IV to a Trace 1310 GC
Inlet and flow conditions	Inlets held at 250 °C and operated in splitless mode for 45 s, after which split flow was turned on at 14 mL min^{-1}, followed by constant column flow of 3.6 mL min^{-1} using hydrogen carrier gas	Inlets held at 250 °C and operated in splitless mode for 45 s, after which split flow was turned on at 14 mL min^{-1}, followed by constant column flow of 1.5 mL min^{-1} using helium carrier gas
Oven program	Initial temperature of 70 °C for 1 min, then ramped to 230 °C at 27 °C min^{-1}, followed by a final ramp to 315 °C at 6 °C min^{-1}, and held for 10 min	Initial temperature of 70 °C for 1 min, then ramped to 230 °C at 27 °C min^{-1}, followed by a final ramp to 315 °C at 6 °C min^{-1}, and held for 10 min
H_3^+ factor	–	Between 2.19 ± 0.02 and 5.00 ± 0.04 ppm/nA
FAME standards	C_{28} (Fisher Scientific)	C_{18} and C_{24} (drift), C_{20} and C_{28} (linearity) (A. Schimmelman, University of Indiana)

2.1.4. Chain-length distribution of leaf wax *n*-alkanoic acids

To interpret sedimentary leaf wax δ^2H, we need knowledge about the plants producing the waxes, and their dominating chain lengths. The classical framework for interpreting leaf wax δ^2H is based on studies from low- and mid-latitudes, finding that terrestrial plants produce high concentrations of long-chain waxes and aquatic plants predominantly produce mid-chain waxes (e.g., Ficken et al., 2000; Aichner et al., 2010a; Bush & McInerney, 2013; Diefendorf & Freimuth, 2017). Constraints on modern Arctic vegetation are sparse, but there is an increasing number of studies investigating modern leaf wax *n*-alkanoic acids and *n*-alkanes (e.g., Daniels et al., 2017; Berke et al., 2019; Dion-Kirschner et al., 2020).

In our sedimentary δ^2H records, there is a clear separation between mid- and long-chain waxes (except after 3.6 cal. kyr BP in Kløverbladvatna). The isotope values and trends are similar for homologues within each group but differ between the groups. This suggests that mid- and long-chain waxes come from two different sources. In July 2018, we collected a selection of the most common plants growing in the northern Wijdefjorden area (close to Austre Nevlingen). The relative *n*-alkanoic chain-length distribution of plants from four plant groups (dwarf shrubs: *Salix polaris*; rushes: *Luzula confusa*; terrestrial mosses: *Polytrichum* sp. and aquatic mosses:

unidentified) are presented in **Paper I**. The total lipid extract was extracted from freeze-dried plant material using sonication in DCM:methanol 9:1, after which the samples were treated and processed the same way as the sedimentary lipid samples (Fig. 8). *Luzula confusa* and *Salix polaris* had the highest relative C_{28} concentrations and the lowest concentrations of mid-chain waxes, whereas the mosses contained relatively higher C_{20} and C_{22} waxes. Thus, we interpret the mid-chain waxes to mainly be produced by aquatic bryophytes and long-chain waxes by terrestrial plants, in agreement with previous studies (e.g., Thomas et al., 2016; Daniels et al., 2017; Berke et al., 2019).

2.1.5. Precipitation isotope seasonality reflected in the lake water

When interpreting proxy data from a sedimentary record, it is important to know the drivers of modern isotope variability. In this study, we focus on seasonal changes in precipitation, which means that it is crucial to understand what precipitation isotope seasonality is reflected in δ^2H_{terr} and δ^2H_{aq}. To help guide our leaf wax δ^2H interpretations, we calculated seasonal residence times and collected surface water samples from the lakes. The residence time was calculated based on the lake volume and catchment size, together with the seasonal precipitation amount from the most representative meteorological station (for details, see **Paper III**). Water samples were collected from the lakes in August 2018 (Austre Nevlingen), August 2019 (Jodavannet), and August 2021 (Heftyevatnet and Kløverbladvatna) (Fig. 9). In addition, 21 lakes were sampled on northern Spitsbergen in July-August 2018 (Fig. 9b), three lakes on Sjuøyane in August 2018, three lakes on western Spitsbergen in April 2018, two lakes on northern Spitsbergen in August 2019, three lakes on western Spitsbergen and one lake on Nordaustlandet in August 2021 (Fig. 9a). These samples were collected using an opportunistic approach, i.e., collected during various field trips by me, co-authors, or others, and give a rough idea of the spatial lake water isotopic variability on Svalbard. The lake water isotopes were measured on a Picarro L2130-i WS-CRDS at OSIBL (for instrumentation and procedures, see Table 3). To get indications of the precipitation seasonality reflected by the lake water, we compared the lake isotopes to measured precipitation isotopes on Svalbard and to precipitation isotope values modeled using the Online Isotopes in Precipitation Calculator (OIPC; Bowen et al., 2005; IAEA/WMO, 2019; Bowen, 2021).

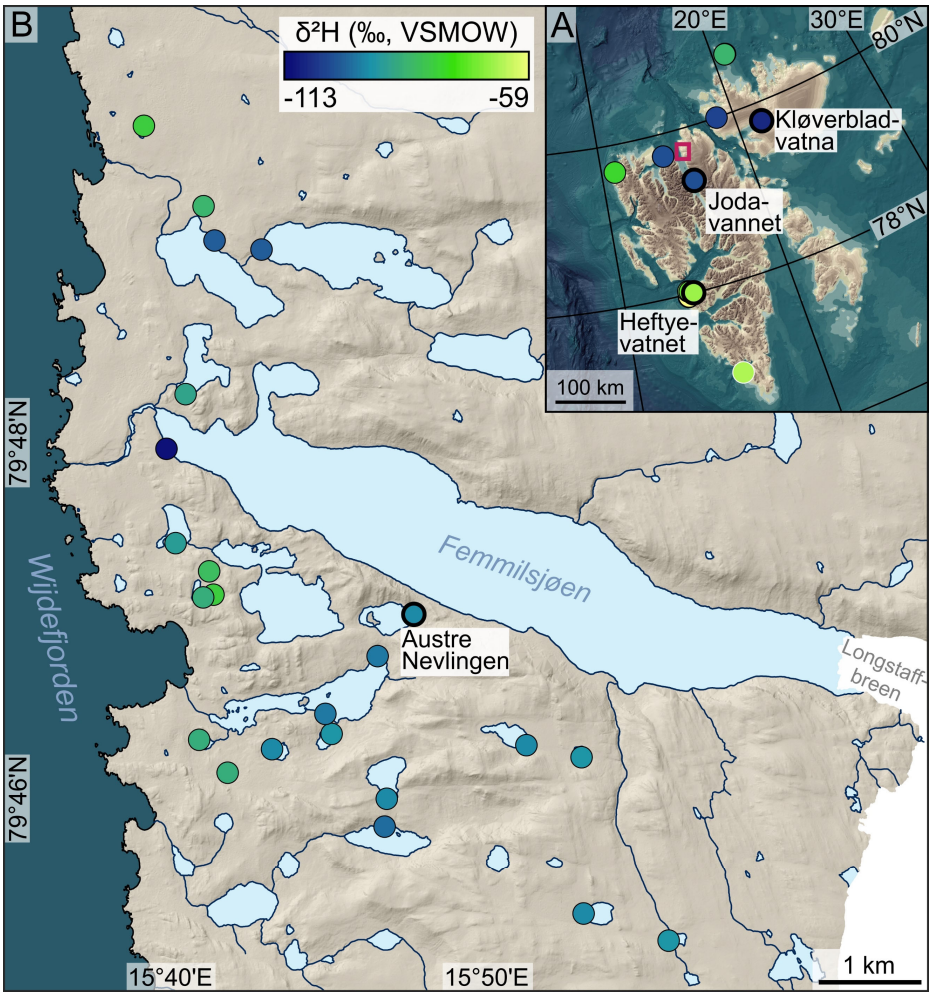

Fig. 9. Spatial summer (July–August) lake water δ^2H variability on Svalbard (a) and zoomed in to an area on northern Spitsbergen (b). Lakes analyzed for sedimentary leaf wax δ^2H in this study are labelled and outlined with a bold black line. The red box in (a) shows the extent of (b). The southernmost sample in (a) is from Arppe et al. (2017), outlined in white. Background maps in (a) from IBCAO (Jakobsson et al., 2012) and in (b) based on 5x5 m DEM from the Norwegian Polar Institute (2014).

Heftyevatnet is located on the western flank of Grønfjorden, on the humid west coast of Spitsbergen (Figs 4 and 6a-b). The lake is fed by catchment runoff and has a large catchment-to-lake ratio suggesting a short residence time. This was supported by δ^2H_{lake} close to summer δ^2H_{precip} at Isfjord Radio (14 km southwest of the lake). We therefore interpret both δ^2H_{terr} and δ^2H_{aq} from Heftyevatnet to reflect summer δ^2H_{precip} and use the difference between the two to reconstruct evapotranspiration.

Jodavannet is a small lake on the eastern flank of Wijdefjorden, northern Spitsbergen (Figs 4 and 6c-d). The lake receives surface runoff from the surrounding slopes and drains into a larger lake in the southeast. The lake has a large catchment-to-lake ratio, indicating a short residence

time. We targeted Jodavannet because we wanted a summer-biased δ^2H_{aq} record from northern Spitsbergen. However, ^2H-depleted modern δ^2H_{lake} suggested that the lake water is reflecting mean annual to winter precipitation. This could be a result of the exceptionally dry summers in this area (Elvebakk & Nilsen, 2002; Østby et al., 2017), and summer precipitation contributing a relatively small portion of the annual precipitation. Thus, we use Jodavannet δ^2H_{aq} to reconstruct changes in the seasonal distribution of precipitation (for further discussion, see **Paper III**). δ^2H_{terr} is interpreted in terms of summer precipitation δ^2H but might also incorporate some winter precipitation due to more winter-biased soil water.

Austre Nevlingen is located *c*. 50 km north of Jodavannet, close to the mouth of Wijdefjorden (Figs 4 and 6e-f). This area is slightly less arid (Østby et al., 2017). The lake has a small catchment-to-lake ratio and ^2H-depleted δ^2H_{lake}, indicating a long residence time. δ^2H_{terr} and δ^2H_{aq} are interpreted to reflect the same precipitation δ^2H seasonality as in Jodavannet, i.e., seasonal distribution of precipitation and summer precipitation δ^2H.

Kløverbladvatna is a threshold lake on Oxfordhalvøya, Nordaustlandet (Figs 4 and 6g-h). The peninsula sits between three ice caps, resulting in a relatively dry climate. A dry channel on the southeastern side indicates that the lake has previously received meltwater from Etonbreen, but the lake has no active inlet today. Kløverbladvatna has a small catchment-to- lake ratio and ^2H-depleted δ^2H_{lake} indicating a long residence time. We interpret δ^2H_{terr} to reflect summer δ^2H_{precip} (possibly incorporating some winter δ^2H_{precip}), and δ^2H_{aq} to reflect mean annual δ^2H_{precip}.

Ideally, we would have precipitation δ^2H data from the lake locations to quantify how strong the precipitation isotope seasonality is at present. The only available δ^2H_{precip} are from the humid west coast of Spitsbergen. In August 2019, we installed a 4-inch diameter RG202 Stratus All-Weather Rain Gauge in Adventdalen (*c*. 9 km southeast of Longyearbyen; Fig. 4) to record δ^2H_{precip} at a more arid location. For logistical reasons, the gauge was moved to Longyearbyen and later to Nybyen (2.5 km farther inside Longyeardalen), where UNIS students could help us to collect the samples. There were several issues with the sampling: 1) long periods without precipitation, 2) low precipitation amounts and strong winds resulted in undercatch and very small samples, 3) polar bear presence prevented collection of the samples some days, and 4) the gauge was unattended in periods when we did not have anyone that could collect the samples. Additionally, varying local conditions at the different gauge locations and sampling

by different persons add uncertainty to the measurements. Ultimately, we decided to stop the sample collection in June 2020, since we were not able to generate a coherent dataset. Thus, the Adventdalen/Longyearbyen samples (n = 45) have not been analyzed and are not presented in this thesis.

2.2. Northern Fennoscandian lakes

2.2.1. Water sample collection

For **Paper II**, we collected surface water samples from 135 lakes in the summers of 2018, 2019, and 2020 (Figs 5 and 10). The lakes varied in size from <0.01 km^2 to >10 km^2, and lake elevation from sea level to *c.* 700 m a.s.l. The water sampling was mainly focused to the first week in July each year to facilitate interannual comparison. In July 2018, the sampling was concentrated to a 5 km^2 area around Tromsø, coastal Norway (n = 30). In the end of June 2019, we collected samples along the north Norwegian coast (n = 9), and the July 2019 and 2020 campaigns targeted lakes along a coastal-to-inland transect (Fig. 5). The transect comprises easy-accessible lakes along the European route E8, from the Lyngen Alps (Norway) close to the Norwegian Sea in northwest, to Kemi (Finland) by the Bothnian Bay in the southeast, i.e., between 69.4°N, 20.3°E and 65.7°N, 24.6°E. In 2019, the transect reached 230 km inland (n = 35), and in 2020 the transect was extended farther southeast, to a total of 460 km (n = 68). The transect spans elevations from close to sea level up to *c*. 560 m a.s.l., with the highest elevation close to the tripoint between Norway, Finland, and Sweden (Fig. 5). Eleven of the transect lakes were sampled in 2013 by Balascio et al. (2018a), and twelve of them were sampled in both 2019 and 2020. We also sampled two locations on the Muonio River in both years, as well as resampled some of the coastal lakes (n = 2 and n = 4 in 2019 and 2020, respectively). The samples were collected from the shoreline, *c*. 10 cm below the surface to avoid evaporatively enriched surface water. The samples were stored in 4 mL glass vials with no headspace, sealed with Parafilm, and kept cold until analysis.

To infer the seasonality of the lake water, we compared the δ^2H_{lake} to δ^2H_{precip} from Naimakka and Rovaniemi (Fig. 5; IAEA/WMO, 2019). Naimakka is located on the eastern side of the Scandinavian Mountains, and Rovaniemi farther southeast, just south of the Arctic Circle. To record the variability in precipitation isotopes closer to the Norwegian Sea, we installed a 4-inch diameter RG202 Stratus All-Weather Rain Gauge on the roof of the UiT Geoscience

Fig. 10. Photographs of a selection of sampled lakes in northern Norway, Finland, and Sweden. Codes refer to Site IDs in the Supplementary data for **Paper II**.

building (69.68°N, 18.96°E; 73 m a.s.l.) in September 2019. Precipitation samples used to calculate amount-weighted mean monthly values presented in **Paper II** were collected every morning between September 6, 2019, and September 5, 2021 (n = 407). Solid precipitation was collected directly from the 4-inch cylinder, whereas liquid samples were collected using a funnel and an inner 1-inch cylinder. Frozen samples were melted in a sealed container at room temperature. Temperature and precipitation amount (or snow water equivalent) was recorded at every sample collection. All samples were transferred to 4 mL glass vials, sealed with Parafilm, and kept cold until analysis.

2.2.2. Water isotope analysis and inflow δ^2H inference

All lake water and precipitation samples were filtered through a 0.2-µm PTFE filter before being analyzed for their δ^2H and $\delta^{18}O$ isotopic composition. Lake water samples collected in 2018–2019 were analyzed at UB, whereas the 2020 lake water samples and 2019–2021 precipitation samples were measured at FARLAB. Information on instrumentation, number of injections per sample, standards, corrections, calibrations, and uncertainties are presented in **Paper II** and in Table 3.

In **Paper II**, we present lake water and precipitation δ^2H and $\delta^{18}O$, as well as d-excess calculated using Equation 3 (section 1.2). To facilitate comparison between our new

Table 3. Instrumentation and procedures used for water δ^2H and $\delta^{18}O$ measurements at the University at Buffalo Organic and Stable Isotope Biogeochemistry Laboratory (OSIBL) and the Facility for advanced isotopic research and monitoring of weather, climate, and biogeochemical cycling (FARLAB), University of Bergen.

	OSIBL 2018–2019 lake water	**FARLAB** 2020 lake water 2019–2021 precipitation
Analyzer	Picarro L2130-i WS-CRDS	Picarro L2140-i WS-CRDS
Vaporization module	V1102-i	A0211
Autosampler	CTC PAL	A0325
Total no. of injections per sample	4	12
No. of injections per sample used to get reported value (average)	3	4–6
Range of in-house standards (calibrated against primary standards GISP, VSMOW2, and SLAP2)	–265.86 to +21.43‰ (δ^2H) –33.62 to +12.41‰ ($\delta^{18}O$)	–
Range of drift standard and two laboratory standards (calibrated against VSMOW2 and SLAP2)	–	–308.14 to +9.2‰ (δ^2H) –40.06 to +1.77‰ ($\delta^{18}O$)
Memory correction	van Geldern and Barth (2012)	Gröning (2011)
Average standard deviation of replicate measurements	0.08‰ (δ^2H) 0.02‰ ($\delta^{18}O$)	–
Average standard uncertainties for calibrated measurement values (provided according to Gröning (2018))	–	0.43‰ (δ^2H) 0.06‰ ($\delta^{18}O$)

precipitation dataset and published precipitation δ^2H data, we converted the daily precipitation data into monthly amount weighted (aw) mean values using the equation:

$$\delta_{aw} = \frac{1}{P} \times \sum_{i=1}^{n} (p_i \times \delta_i) \quad \text{(Equation 6)}$$

where P and p_i are the monthly and daily precipitation amounts in mm, δ_i is δ^2H or $\delta^{18}O$, and n is the number of sampling days.

When using water isotope proxies to infer precipitation δ^2H, it is important to quantify the possible influence of evaporation. Based on the assumption that isotope values of partially evaporated water will evolve along an evaporation line (EL), a widely used approach is to estimate the isotopic composition of the source water by back-correction to the EL-MWL intersection (Clark & Fritz, 1997). This assumes that all δ^2H_{lake} variation results from evaporation, and that all lakes in a region have the same source water (i.e., precipitation) isotopic composition. At high latitudes and in systems with strong seasonality, the source isotopic composition can vary between years due to changing relative proportion of isotopically depleted snowfall and isotopically enriched rainfall (Tondu et al., 2013). To estimate the source water δ^2H for evapo-concentrated lakes, we applied the Bayesian 'MWL source implementation' method by Bowen et al. (2018). This approach to estimate source water values includes uncertainty in the MWL and the LEL, thus providing a more rigid estimate of source water δ^2H uncertainty. To run the model, the user supplies a MWL equation and a hypothesized LEL slope (both with confidence intervals), lake water δ^2H and $\delta^{18}O$ with uncertainties and covariance (0.95), and the number of iterations (10,000). We used a re-calibrated GMWL ($\delta^2H = 8.01 \times \delta^{18}O + 9.57$; n = 80,672; Bowen et al., 2018) for the MWL equation, having much less uncertainty than the LMWLs, and applied different LEL slopes for samples collected in 2019 and 2020 (4.82 and 5.18, respectively). These LEL slopes were based on linear regression for the isotopic composition of lakes sampled in both years (n = 12), providing a reasonable starting estimate. The modeled mean source water isotope values, referred to as inferred inflow δ^2H (δ^2H_I) were used to compare the seasonality of inflow along the transect and to non-evaporated coastal lakes.

3. Summary of research papers

In this thesis, I present two studies of sedimentary leaf wax δ^2H from lakes on Svalbard, and one study of lake water δ^2H and $\delta^{18}O$ from northern Fennoscandia. **Paper I** presents a case study from Austre Nevlingen, reconstructing Holocene precipitation seasonality on northern Spitsbergen. In **Paper III**, Austre Nevlingen is complemented by records from three additional lakes: Heftyevatnet, Jodavannet and Kløverbladvatna. The four lakes are located along a climatic gradient across Svalbard and reflect different precipitation seasonality, allowing us to investigate Holocene seasonal precipitation changes in both time and space. **Paper II** focuses on the modern isotopic composition of 135 lakes in northern Fennoscandia, sampled from 2018 to 2020 and spanning a coastal-to-inland transect from the Norwegian Sea to the Bothnian Bay.

3.1. Paper I

Kjellman, S. E., Schomacker, A., Thomas, E. K., Håkansson, L., Duboscq, S., Cluett, A. A., Farnsworth, W. R., Allaart, L., Cowling, O. C., McKay, N. P., Brynjólfsson, S., & Ingólfsson, Ó., 2020. **Holocene precipitation seasonality in northern Svalbard: influence of sea ice and regional ocean surface conditions**. *Quaternary Science Reviews*, *240*, 1063882. https://doi.org/10.1016/j.quascirev.2020.106388.

A critical knowledge gap in the Svalbard climate reconstructions is the lack of robust records of Holocene precipitation changes. In **Paper I**, we present sedimentary leaf wax δ^2H data from Austre Nevlingen, northern Spitsbergen. We targeted a lake with a long residence time (i.e., with δ^2H_{lake} reflecting mean annual δ^2H_{precip}) to allow us to extract information about seasonal variability. The hydrogen isotopic composition of C_{22} and C_{28} *n*-alkanoic acids (mainly derived from aquatic and terrestrial plants, respectively) were used to infer past lake and soil water δ^2H, interpreted to reflect mean annual and summer precipitation. Our results suggest that northern Spitsbergen experienced large variability in precipitation seasonality throughout the Holocene. ^2H-enriched δ^2H_{terr} in the Early and Middle Holocene (until *c*. 5.6 cal. kyr BP) suggests enhanced summer evaporation and/or ^2H-enriched summer precipitation, indicating warm and stable summer conditions. Decreasing δ^2H_{aq} in the Early Holocene and ^2H-depleted values until *c*. 6 cal. kyr BP likely reflect prominent increase in winter precipitation amounts. We propose that Early Holocene warming had a strong effect on the moisture availability. High summer insolation and increased Atlantic heat flux warmed the waters around Svalbard and caused

reduction in sea-ice cover. More open water promoted evaporation and greater winter precipitation amounts. After *c.* 5.6 cal. kyr BP, decreasing δ^2H_{terr} suggests gradual summer cooling, with less evaporative enrichment and/or more ^2H-depleted summer precipitation. The δ^2H_{aq} trend is not as clear after 6 cal. kyr BP, which we attribute to changes in lake hydrology resulting in large shifts in δ^2H_{aq}. We propose that the duration of lake-ice cover might have varied with variable climate, affecting the amount of snowmelt bypass and thus the relative proportion of summer and winter precipitation entering the lake. The Austre Nevlingen record suggests that the Holocene precipitation seasonality on northern Spitsbergen is strongly linked to regional ocean surface conditions and sea-ice cover, which is in agreement with modern observations and future projections.

3.2. Paper II

Kjellman, S. E., Thomas, E. K., & Schomacker, A., 2022. **Arctic and sub-Arctic lake water δ^2H and $\delta^{18}O$ along a coastal-inland transect: implications for interpreting water isotope proxy records**. *Journal of Hydrology*, *67*, 127556. https://doi.org/10.1016/j.jhydrol.2022.127556.

Stable isotope proxies that indirectly archive the isotopic composition of hydrogen and oxygen in past precipitation are widely used to reconstruct various aspects of the water cycle. A common approach is to assume a single control on the lake water isotope variability for a given record. One of the outcomes of **Paper I** is that the precipitation seasonality reflected in δ^2H_{lake} can vary through time because of changes in the lake dynamics. Another crucial part of interpreting water isotope proxy records is to separate the precipitation isotope signal from evaporation. In **Paper II**, we measured δ^2H and $\delta^{18}O$ of surface water from 135 lakes in northern Fennoscandia over three years, to study how their isotopic composition varies in time and space. We targeted easy-accessible lakes along a 460-km-long transect from the Norwegian Sea in northwest, to the Bothnian Bay in the southeast. This is a region with strong contrasts in climate, with prevailing westerly winds bringing Atlantic moisture ashore, and the Scandinavian Mountains shielding the leeward side from precipitation. To estimate the source isotopic composition (i.e., the lake water inflow values; δ^2H_I) for evapo-concentrated transect lakes, we used a Bayesian method. Our results show that there is spatial and temporal variation in δ^2H_{lake} in this region. Both coastal and inland lakes are sensitive to distillation during atmospheric moisture transport, controlling the inflow isotopic composition. In addition, lakes

farther from the Norwegian Sea are more sensitive to evaporation. We suggest that more ^{2}H-depleted δ^2H_I in 2020 than in 2019 is a result of a snow-rich winter 2020, attributed to extreme AO+ conditions and increased moisture supply from the North Atlantic. The large snow amounts resulted in more inflow of ^{2}H-depleted winter precipitation to the lakes. We conclude that the lake water isotopic variability in northern Fennoscandia reflects seasonal precipitation changes associated with atmospheric circulation changes, as well as catchment-integrated evaporation. Through-flowing coastal lakes are most suited for precipitation reconstructions, whereas δ^2H_{lake} variability in more inland lake is likely to incorporate both changes in inflow variability and evaporation.

3.3. Paper III

Kjellman, S. E., Thomas, E. K., Schomacker, A., Farnsworth, W. R., Cowling, O. C., Allaart, L., & Brynjólfsson, S. **Holocene precipitation seasonality along a climatic gradient from western Spitsbergen to Nordaustlandet, Svalbard**. In review for *Palaeogeography, Palaeoclimatology, Palaeoecology.*

The Svalbard archipelago spans large climate gradients due to complex feedback mechanisms in the atmosphere-ocean-ice system. Climate models project that Svalbard will experience heterogeneous precipitation changes in the future, with largest increase in northeast and during the winter months. In **Paper I**, we suggested that northern Spitsbergen experienced increased winter precipitation during the warm Early Holocene. In **Paper III**, we apply the same method to three additional lakes across Svalbard to explore regional differences in Holocene water cycle changes. From Heftyevatnet, on the relatively warm and humid west coast of Spitsbergen, we interpret δ^2H_{terr} and δ^2H_{aq} to reflect summer precipitation δ^2H. We use the difference between the two (ε_{28-22}) to infer changes in evapotranspiration. The other three lake records are from the relatively cold and arid northeastern Svalbard: Jodavannet and Austre Nevlingen on northern Spitsbergen, and Kløverbladvatna on Nordaustlandet. We interpret δ^2H_{terr} from these three lakes to mainly reflect summer precipitation, but with some incorporation of winter precipitation due to more winter-biased soil water. δ^2H_{aq} reflects variable seasonal distribution of precipitation due to varying lake hydrology. In the Early and Middle Holocene, relatively ^{2}H-enriched δ^2H_{terr} suggests dry summer conditions and/or more proximal summer moisture across Svalbard, and high ε_{28-22} suggests high evapotranspiration. We interpret an Early Holocene decrease in δ^2H_{aq} in both Austre Nevlingen and Jodavannet to reflect an increase in

winter relative to summer precipitation, associated with increased moisture supply as the sea-ice cover decreased with regional warming. Winter precipitation likely stayed high until *c*. 6 cal. kyr BP. After 6–5.5 cal. kyr BP, ^{2}H-depleted $\delta^{2}H_{terr}$ and lower ε_{28-22} indicate cooler summer, less evapotranspiration, and/or more distal moisture. Intermittent ^{2}H-depleted $\delta^{2}H_{aq}$ suggests periodic increases in winter precipitation or decreases in summer precipitation inflow to the lakes on northern Spitsbergen. Our results show the potential of the leaf wax $\delta^{2}H$ proxy to reconstruct seasonal distribution of precipitation, summer precipitation $\delta^{2}H$, and/or evapotranspiration, depending on the hydrology of the lake.

3.4. Author contributions

The papers and manuscript in this thesis are the result of collaboration between researchers from different institutions, contributing to various parts of each study. All co-authors and individual contributions are listed in Table 4.

Table 4. Overview of author contributions to each of the research articles (**Papers I–III**). The contributor roles have been defined according to the CRediT (Contributor Roles Taxonomy) criteria (https://casrai.org/credit/). AAC = Allison A. Cluett; AS =Anders Schomacker; EKT = Elizabeth K. Thomas; LA = Lis Allaart; LH = Lena Håkansson; NPM = Nicholas P. McKay; OCC = Owen C. Cowling; ÓI = Ólafur Ingólfsson; SB = Skafti Brynjólfsson; SD = Sandrine Duboscq; SEK = Sofia E. Kjellman; WRF = Wesley R. Farnsworth.

Contribution	Paper I	Paper II	Paper III
Conceptualization	SEK, AS, EKT, LH	SEK, AS, EKT	SEK, AS, EKT
Data curation	SEK	SEK	SEK
Formal analysis	SEK, EKT, OCC	SEK, AS, EKT	SEK, EKT, OCC
Funding acquisition	AS, LA, ÓI, EKT, SD	AS, SEK, EKT	AS, SEK, EKT, WRF
Investigation [1] Data collection (fieldwork) [2] Laboratory work [3] Data interpretation	SEK[1,2,3], AS[1,2,3], EKT[2,3], LH[2], SD[2,3], AAC[2,3], WRF[1,2], LA[1], OCC[2], SB[1], ÓI[1]	SEK[1,3], EKT[3], AS[1,3]	SEK[1,2,3], EKT[2,3], AS[1,2,3], WRF[1,2], OCC[2], LA[1], SB[1]
Project administration	SEK, AS	SEK, AS	SEK, AS
Software	SEK, EKT, NPM	SEK	SEK
Supervision	AS, EKT, LH	AS, EKT	AS, EKT
Visualization	SEK	SEK	SEK
Writing – original draft	SEK	SEK	SEK
Writing – review & editing	SEK, AS, EKT, LH, SD, AAC, WRF, LA, OCC, NPM, SB, ÓI	SEK, EKT, AS	SEK, EKT, AS, WRF, OCC, LA, SB

4. Discussion

4.1. Source and seasonality of *n*-alkanoic acids

Robust proxy interpretations rely on a well-grounded understanding of the environmental factors driving the isotopic variation. Leaf wax δ^2H is a useful tool to infer past hydrological changes because of the strong linear relationship with precipitation δ^2H (Sachse et al., 2004; Hou et al., 2008; McFarlin et al., 2019). However, the translation from source water to leaf wax δ^2H involves a series of isotopic fractionation processes related to both plant physiology and environmental factors (Sachse et al., 2012). Furthermore, to interpret leaf wax δ^2H in terms of seasonal precipitation variability, we need to consider the seasonality of the source (soil or lake water) pools. In this section, I discuss some of the challenges of making accurate leaf wax source attribution and inferring the source water seasonality.

The first step in leaf wax δ^2H interpretation is to consider the source of the leaf wax homologues. In **Papers I & III**, the δ^2H of all even-chain length *n*-alkanoic acids in our four lakes, except for part of the Kløverbladvatna record, show different trends for the mid- and long-chain homologues. This indicates that they come from two different plant groups. Globally, studies have shown that terrestrial plants primarily produce long-chain waxes (Sachse et al., 2012; Diefendorf & Freimuth, 2017), whereas aquatic plants produce relatively higher concentrations of mid-chain waxes (Ficken et al., 2000; Aichner et al., 2010b). Also in the Arctic, terrestrial plants produce high relative concentrations of long-chain waxes (e.g., Wilkie et al., 2013; Daniels et al., 2017; Berke et al., 2019). The few Arctic studies that examine aquatic plants suggest that they produce higher concentrations of mid-chain than long-chain homologues (Thomas et al., 2016; Berke et al., 2019; Gorbey et al., 2021). On Svalbard, there are almost no aquatic vascular plants, but submerged bryophytes are abundant in some lakes (Balascio et al., 2018b; Voldstad et al., 2020; **Papers I & III**). Aquatic bryophytes from western Greenland (n = 1; Thomas et al., 2016) and Baffin Island (n = 4; Gorbey et al., 2021) are dominated by C_{24} *n*-alkanoic acids, followed by C_{22} and C_{26}. Balascio et al. (2018b) measured the concentrations of C_{19}–C_{33} *n*-alkanes in one aquatic bryophyte sample from Amsterdamøya, northwestern Svalbard, with C_{27}, C_{25} and C_{21} being the most abundant homologues.

In **Paper I**, we present the average chain-length distribution of aquatic bryophytes (n = 2) from northern Spitsbergen, displaying similar concentration of C_{24}, C_{26} and C_{28} *n*-alkanoic acids,

which are the most abundant waxes in the bryophytes (Fig. 11). *Salix polaris* has a similar distribution as the aquatic mosses, whereas *Luzula confusa* is dominated by C_{28}, and *Polytrichum* sp. is dominated by C_{20} and C_{22} (Fig. 11). In absolute concentrations (µg *n*-alkanoic acids per g dry biomass), *Salix polaris* and *Luzula confusa* produce the greatest amount of the long-chain waxes per g biomass and *Polytrichum* the greatest amounts of C_{20} and C_{22}. *Salix polaris* produces higher amounts of all chain lengths compared to the aquatic bryophytes. Furthermore, the average distribution of *n*-alkanoic acids in the sediments vary between the lakes (Fig. 11), reflecting the different plant communities in the catchments. These chain-length observations highlight the importance of the δ^2H patterns for source attribution. From the chain-length distribution alone, it is difficult to separate terrestrial and aquatic plants, but the clear separation between mid- and long-chain δ^2H trends supports the canonical two-source interpretation. In Kløverbladvatna, all homologues show similar trends after 3.6 cal. kyr BP, which could indicate a source change (i.e., different sources before and same source after 3.6 cal. kyr BP), as the chain-length distribution in the sediments changes (Fig. 11). Another possibility is that the dominant wax producers changed, but more details on the leaf wax sources at this site are needed to confirm the reason for the shift in δ^2H.

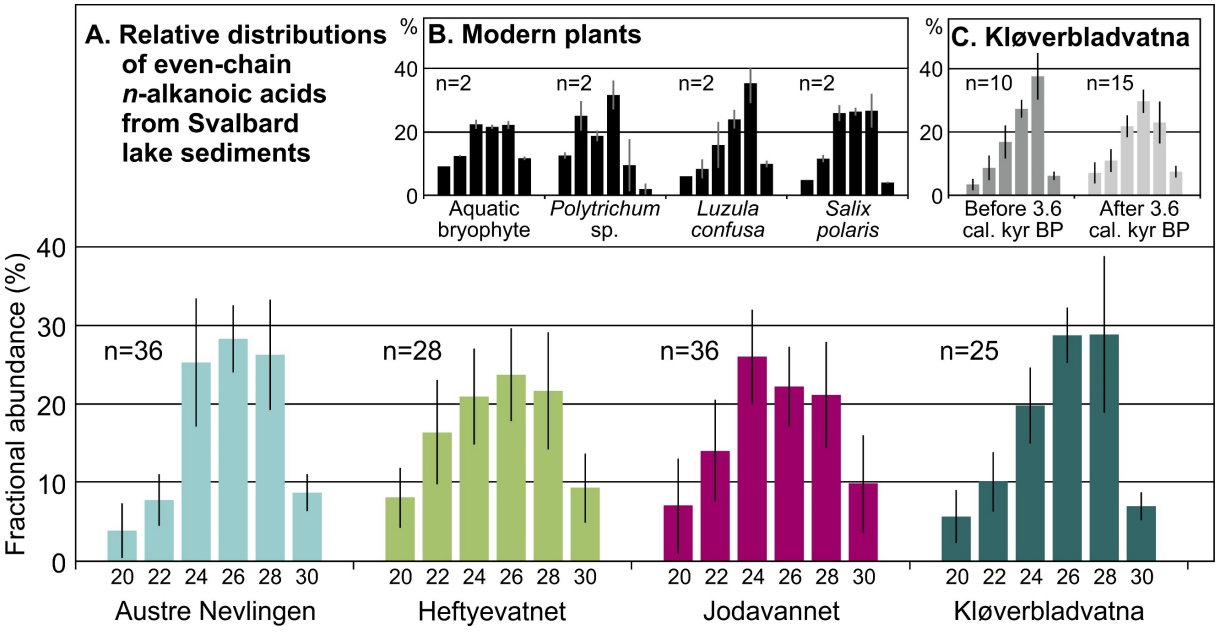

Fig. 11. Distribution of even-chain *n*-alkanoic acids between C_{20} and C_{30} from (a) Svalbard lake sediments (**Papers I & III**), (b) modern plants from northern Spitsbergen (**Paper I**), and (c) in Kløverbladvatna sediments before and after 3.6 cal. kyr BP (**Paper III**). Error bars show one standard deviation.

To extract information of seasonal precipitation changes from leaf wax δ^2H, we need to assess the seasonality reflected in the source water pools used by the plants. In previous Arctic studies, terrestrial leaf wax δ^2H is interpreted to reflect summer precipitation δ^2H and summer evaporative enrichment, assuming that the soil water during the growing season is mainly recharged by summer precipitation (Cooper et al., 1991; Thomas et al., 2016; Throckmorton et al., 2016; Thomas et al., 2020). In **Paper III**, we suggest that the soil water on northern Svalbard might reflect a mix of summer and winter precipitation. We base this argument on a few lines of evidence. Soil moisture measurements close to the Jodavannet catchment suggest that most of the summer soil moisture comes from snowmelt early in the season (Eidesen et al., 2018). Additionally, summer precipitation amounts on northeastern Svalbard are very low, and might not saturate the active layer by the end of summer, which therefore subsequently gets recharged by winter precipitation during the following snowmelt season. Furthermore, δ^2H_{terr} in the three northeastern lakes are ^2H-depleted compared to Heftyevatnet on the west coast. This could reflect a greater influence of ^2H-depleted winter precipitation on the soil water, and/or more Rayleigh distillation during moisture transport from the Atlantic Ocean.

Aquatic leaf wax δ^2H can reflect different precipitation seasonality depending on the residence time of the lake (e.g., Thomas et al., 2020). The residence time can be calculated based on the lake volume, catchment size, and runoff estimated from the precipitation amount (Jonsson et al., 2009). We lack good constraints on precipitation amounts falling over central and northeastern Svalbard, meaning that the calculated residence times are rough estimates. In **Paper III**, Jodavannet had unexpectedly ^2H-depleted δ^2H_{lake} considering the presumably short residence time (Table 1). We suggest three possible explanations for why Jodavannet may not reflect summer precipitation, including low summer precipitation amounts that do not flush the lake in summer, evaporation of summer precipitation before it reaches the lake, and inflow of winter-biased groundwater. Furthermore, the residence time might change through time. In **Papers I & III**, we observe large shifts in δ^2H_{aq} in Austre Nevlingen and Jodavannet, which we suggest reflect variable sensitivity of the lake basins to the seasonal distribution of precipitation. Processes influencing the relative proportion of summer and winter precipitation in the lake during the growing season and/or the residence time include the duration of lake-ice cover, degree of snowmelt bypass, and lake-level changes. In **Paper II**, we show that lake water δ^2H is sensitive to variable winter precipitation amounts from one year to the next. In

conclusion, it is important to evaluate temporal changes in lake and catchment processes influencing the precipitation seasonality reflected in lake and soil water isotope proxies.

4.2. Regional variability in paleo-precipitation seasonality

One of the main focuses of all three papers is seasonal changes in precipitation δ^2H. In **Paper II**, modern lake water δ^2H registered variable input of winter (^2H-depleted) relative to summer (^2H-enriched) precipitation from one year to the next, implying that lake water isotope proxies from carefully selected lakes can be interpreted in terms of seasonal distribution of precipitation. Paleoclimate records can provide information about how the hydrological cycle responded to past climate change, but depending on the hydrology of the lake, they may register different precipitation seasonality.

In modern studies it is easier to constrain the drivers behind δ^2H_{lake} (and therefore indirectly δ^2H_{precip}) changes because of available meteorological and hydrological data. We can monitor seasonal changes in real time and attribute variations in δ^2H_{lake} to observed processes. For instance, we observed more ^2H-depleted lake water isotopes in summer 2020 than in summer 2019. We interpret the ^2H-depleted values to reflect relatively higher winter input in 2020, supported by large snow amounts falling in winter and spring 2020. In paleo-precipitation studies, we cannot make direct observation of environmental changes during the time of proxy synthesis. This makes inference of the drivers of seasonal precipitation changes from proxy records more challenging. In **Paper I**, we targeted a lake which, based on the modern δ^2H_{lake} and residence time calculations, likely has δ^2H_{aq} reflecting mean annual precipitation δ^2H. Large shifts in the δ^2H_{aq} during the Middle and Late Holocene suggested that was not always the case, but that hydrological changes could alter the seasonality reflected by the lake.

Papers I & III suggested that northern Svalbard likely received a higher proportion of winter precipitation relative to the annual total in the Early and Middle Holocene, until *c*. 6 cal. kyr BP, and during shorter periods also in the Late Holocene. The Early Holocene increase coincided with high summer insolation and increased advection of warm Atlantic water to Svalbard, and we interpret the increased winter precipitation to be a response to enhanced evaporation from ice-free seas. Reconstructions of seasonal distribution of precipitation can also help assess the importance of lower summer temperature versus higher winter precipitation amounts on glacier activity on Svalbard. There are multiple lines of evidence for greater

precipitation amounts on northern Svalbard in the Early Holocene. ^{2}H-depleted $\delta^{2}H_{aq}$ in our sedimentary leaf wax records suggests an increasingly greater portion of winter precipitation from *c*. 11.7 to 6 cal. kyr BP (**Paper I & III**), and higher frequency of "snowmelt layers" in lake sediments from Vårfluesjøen (Fig. 4) from the beginning of the record at 10.2 cal. kyr BP to 7 cal. kyr BP (Røthe et al., 2018). The snowmelt layers are fining-upwards silt layers interpreted to reflect short-lived events of increased runoff from snowmelt in the catchment. Winter precipitation has also been suggested to be one of the drivers of Neoglacial (Müller et al., 2012; Røthe et al., 2015) and LIA glacier expansion (D'Andrea et al., 2012; Arppe et al., 2017; Røthe et al., 2018) on Svalbard.

To place our seasonal precipitation trends into a wider context, we can consider paleo-precipitation and glacier records from other Arctic and sub-Arctic regions. In northern Greenland and on northwestern Iceland, increased winter precipitation is suggested to have helped ice caps to survive the HTM (Schomacker et al., 2016; Larsen et al., 2019). Furthermore, asynchronous Middle to Late Holocene glacier expansion in the Arctic indicates that the Neoglacial is not only forced by cooler temperatures associated with declining insolation (McKay et al., 2018), but driven by multiple mechanisms (Solomina et al., 2015; Kjær et al., 2022; Larocca & Axford, 2022). In this context, the effect of precipitation amount and seasonality is poorly understood. Temperature appears to be the dominant long-term control of the size of the Greenland Ice Sheet, but precipitation may drive shorter regional and local events (Alley et al., 2010).

Badgeley et al. (2020) generated independent reconstructions of mean annual temperature and precipitation for the last 20,000 years on Greenland using paleoclimate data assimilation, combining ice-core $\delta^{18}O$ and accumulation rates with climate-model simulations. The results suggested that annual precipitation closely followed temperature, with low precipitation amounts in the Younger Dryas, followed by an increasing trend in the Early Holocene, and relatively stable precipitation after *c*. 8 cal. kyr BP (Badgeley et al., 2020). On coastal western Greenland, Thomas et al. (2016) interpreted 100‰ more negative sedimentary leaf wax $\delta^{2}H_{aq}$ from 6 to 4 cal. kyr BP than during the Early and Late Holocene to reflect increased winter snowfall, coinciding with high summer temperature, increased heat advection from the West Greenland Current, and decreased winter sea-ice cover in Baffin Bay and the Labrador Sea. Coastal areas were likely more sensitive to local sea-ice changes than the central parts of the

Greenland Ice Sheet. Holocene sea-ice reconstructions suggest different sea-ice dynamics between different Arctic regions (de Vernal et al., 2013), which could partly explain the different timing of ^{2}H-depleted $\delta^{2}H_{aq}$ in lakes on Svalbard and in Greenland. Periods of enhanced evaporation from seas with reduced ice cover occur at different times on northern Svalbard (Early and Middle Holocene until *c*. 6 cal. kyr BP; **Papers I & III**) and western Greenland (6 to 4 cal. kyr BP; Thomas et al., 2016), yet highlighting that reduced regional sea ice and warmer sea surface temperatures are important controls of the moisture source for Arctic winter precipitation.

4.3. Improvement of the leaf wax $\delta^{2}H$ proxy and other water isotope proxies

As discussed in section 4.1, the hydrogen isotopic composition of leaf waxes depends on several biological and environmental factors. Paleo-hydrological interpretations based on $\delta^{2}H_{wax}$ differ between studies due to differences in lake hydrology (e.g., influencing the seasonality reflected in the lake water $\delta^{2}H$), but also highlights our incomplete understanding of the factors influencing lipid $\delta^{2}H$ variability (Linderholm et al., 2018). There are many possible directions for how to improve water isotope proxy interpretations. In this section, I present some advances made, as well as approaches that might prove fruitful.

4.3.1. Modern water isotope monitoring

A requirement for making accurate proxy interpretation is a good understanding of modern water cycle processes. Monitoring of precipitation $\delta^{2}H$ and $\delta^{18}O$ (e.g., through GNIP; IAEA/WMO, 2019) provides a baseline for interpreting seasonal precipitation variability, but the spatial distribution of high-Arctic measurements remains sparse, and time series often span short and different periods. Furthermore, short-term variation in observational records spanning only one or two years might bias long-term estimates based on those observations (Bowen & Revenaugh, 2003). On Svalbard, all precipitation measurements are from the west coast of Spitsbergen (Arppe et al., 2017; IAEA/WMO, 2019; Skakun et al., 2020). As part of this study, we tried to monitor precipitation isotopes in the more arid Longyearbyen area, but it proved challenging (see section 2.1.5). Future monitoring programs could help constrain the precipitation seasonality across Svalbard, if logistically feasible. In 2018, the Pan-Arctic Precipitation Isotope Network (PAPIN) was established to coordinate precipitation isotope

sampling across key climate types in the Arctic (Mellat et al., 2021). Our precipitation gauge installed in Tromsø to generate data for **Paper II** is still in operation and included as the first coastal Fennoscandian station in the PAPIN network.

We also need better constraints on the seasonal moisture sources. One way to investigate how moisture source changes impact the precipitation at a specific location is to use backtracking modeling. A study from western Greenland demonstrates that moisture source changes can dampen the precipitation isotope seasonality (Cluett et al., 2021). Furthermore, Lagrangian moisture diagnostic and isotope-enabled general circulation models have identified seasonal and interannual variability in moisture sources to Greenland with changing atmospheric circulation patterns and sea-ice cover, subsequently controlling precipitation δ^2H and $\delta^{18}O$ (Werner et al., 2001; Sodemann et al., 2008a; Sodemann et al., 2008b; Nusbaumer et al., 2019). Seasonal moisture source changes have also been suggested to determine precipitation δ^2H and $\delta^{18}O$ in western Siberia, based on in situ water vapor isotope measurements and semi-Lagrangian backward trajectories (Bonne et al., 2020). Climate on Svalbard is tightly linked to atmospheric and oceanic circulation and sea ice and is therefore likely also experiencing moisture source variability on different timescales.

In **Paper II**, we explore lake water isotopic variability over three years. The data show that lake water δ^2H can display variable sensitivity to changes in precipitation δ^2H and evaporation through time. Proxy records of hydrological variation provide information about a combination of processes but are, for a given record, often interpreted to reflect changes in only one variable such as moisture balance, moisture source change, or precipitation seasonality. By monitoring δ^2H_{lake} changes from year to year and comparing to regional conditions, we can assess the main drivers of modern isotopic variability and target lakes that are sensitive to changes in the process we want to reconstruct. In addition to the samples from 2018–2020 included in **Paper II**, we have repeated the lake water sampling in the first week of July in 2021 and 2022, to continue monitoring the isotopic range and environmental factors controlling lake water isotopes in northern Fennoscandia. Similar efforts on Svalbard would be beneficial to find suitable lakes for future paleo-precipitation studies.

4.3.2. Modern leaf wax isotope monitoring

In addition to the processes determining δ^2H_{precip} and δ^2H_{lake}, we need to consider the transformation from source water δ^2H to wax δ^2H. In **Papers I & III**, we focus on qualitative assessment of past hydrological changes, by inferring relative changes in precipitation seasonality and changes in summer δ^2H_{precip}. If we want to isolate changes in precipitation δ^2H, we need to translate δ^2H_{wax} into δ^2H_{precip}. As presented in section 1.3, δ^2H_{wax} is depleted by a fractionation factor (ε_{app}) relative to δ^2H_{precip} due to climatic and/or plant physiological drivers (Fig. 2; Sessions et al., 1999; Kahmen et al., 2013). To convert δ^2H_{wax} into source water δ^2H, we need good constraints on ε_{app}. Few Arctic studies have investigated terrestrial plant ε_{app} (Wilkie et al., 2013; Daniels et al., 2017; Berke et al., 2019), and to our knowledge there are no quantifications of ε_{app} for aquatic bryophytes, which are abundant at some of our study sites. Furthermore, a global database of *n*-alkanoic acid ε_{app} measured in lake surface sediments, compiled by McFarlin et al. (2019), shows that the median *n*-alkanoic acid ε_{app} values are consistently around –100‰ to –110‰, independent of chain length and source (lake or precipitation) water (Thomas et al., 2020). Given that ε_{app} is not well quantified in the Arctic, the uncertainties are large, and ε_{app} is relatively constant (at least considering the catchment average for a given chain length), we do not convert δ^2H_{wax} to δ^2H_{precip}. More modern studies are needed to better constraints ε_{app} in the Arctic, especially for aquatic plants.

Modern studies monitoring wax transport and deposition could help us distinguish aquatic from terrestrial sources. By monitoring transport into and within the lake and separating the two sources, it may be possible to quantify their relative contribution to the sedimentary leaf waxes. Furthermore, their chain-length distribution and isotopic composition could be compared to the chain-length distribution and isotopic composition of modern lake and catchment vegetation to distinguish wax sources to the lake sediments, using a range of recently developed tools, e.g., the Stable Isotope Mixing Model (SIMM; Parnell & Inger, 2016). Additionally, these interpretations would benefit from detailed vegetation mapping to determine the most abundant modern plants.

4.3.3. Spatial and temporal resolution of paleo-precipitation records

A key to solid proxy interpretations is having sufficiently high temporal resolution. Ideally, we want to have enough data points to decipher the rate of change, in addition to the amplitude.

The leaf wax δ^2H records presented in **Papers I & III** have an average temporal resolution ranging from 220 to 450 years between subsamples for each lake record. This resolution allows interpretations of general long-term trends but reveals less about short-term variability and complicates comparison between records. Furthermore, each subsample integrates sediments deposited over multiple years. The sample resolution from Arctic lake sediments is commonly limited by low sedimentation rates and low organic content.

In an on-going project in collaboration with researchers from the University of Massachusetts Amherst and Bates College, we analyze leaf wax δ^2H from a laminated surface sediment core from Linnévatnet, western Spitsbergen. By high-resolution sampling of the sedimentary sequence covering the instrumental period, we aim to compare the leaf wax δ^2H record to precipitation measurements from Isfjord Radio, 3.5 km west of the lake. This new study will hopefully allow us to 1) generate a high-resolution Arctic leaf wax δ^2H record for the last *c*. 120 years, and 2) evaluate how well δ^2H_{wax} correlate to seasonal precipitation variability. A similar reconstruction was successfully performed using δ^2H_{wax} from varved proglacial lake sediments on Baffin Island (Thomas et al., 2012).

Since precipitation amounts and seasonality are highly variable in time and space, we need to increase the spatial distribution of long-term paleo-precipitation records. Ice-core records from ice sheets and ice caps, such as the Greenland Ice Sheet, provide information about annual precipitation amount (annual accumulation) (e.g., Dahl-Jensen et al., 1993). Annual precipitation amounts have also been reconstructed from pollen, with available Holocene records from northern Fennoscandia (e.g., Hammarlund et al., 2002; Bjune et al., 2004; Jones et al., 2004), northeast Russia (Melles et al., 2012), and Arctic Canada and Alaska (e.g., Viau & Gajewski, 2009), but few studies differentiate between summer and winter precipitation (Allen et al., 2007). Another popular proxy for investigating various aspects of the water cycle is $\delta^{18}O$ from diatom biogenic silica, lacustrine carbonates, lake sediment cellulose, and chironomids, studied in lakes in Canada (e.g., Edwards et al., 1996; Wolfe et al., 1996), Alaska (Anderson et al., 2001), Greenland (e.g., Anderson et al., 2004; Lasher et al., 2017), northern Fennoscandia (e.g., Hammarlund et al., 2002; Rosqvist et al., 2013), and Russia (Wolfe et al., 2000). These records span different time scales, and with different temporal resolution, in addition to coming from lakes influenced by different environmental conditions. Some studies interpret $\delta^{18}O$ variability in terms of moisture balance, whereas others focus on moisture source shifts caused by atmospheric circulation changes and/or seasonality. Precipitation seasonality

has been reconstructed from leaf wax δ^2H from lake sediments on Greenland (Thomas et al., 2016; Thomas et al., 2020) and Svalbard (**Papers I and III**), and from a north Norwegian peatland (Nichols et al., 2009). Although there is an increasing number of studies on precipitation seasonality, we still know little about the spatial variability, and need more and higher-resolution records.

4.3.4. Other tools to improve the leaf wax δ^2H interpretations

Another way to advance proxy-based paleoclimate interpretations is to use proxy system modeling (e.g., Evans et al., 2013; Dee et al., 2018; Morrill et al., 2019). Since water isotopes are impacted by a combination of factors, this approach could be an important key to constraining the sensitivity of a lake to e.g., changes in the seasonal distribution of precipitation. Proxy system models allow us to use our understanding of modern physical and biological processes affecting the proxy and use sensitivity testing to evaluate which factor, or combination of factors, that most likely caused the isotope variability in our record (Dee et al., 2018). We could for example assess the influence of climate parameters such as winter precipitation amount or relative humidity on aquatic plant leaf wax δ^2H. To set up lake-specific models and optimize the model performance, we need detailed field measurements of modern lake and catchment parameters, as outlined in sections 4.3.1 and 4.3.2.

Leaf wax δ^2H interpretations benefit from being combined with other proxies from the same lake. Plant *sed*aDNA can constrain plant community changes and their possible impact on δ^2H_{wax}, and bulk elemental and stable isotope measurements of carbon and nitrogen ($\delta^{13}C$, $\delta^{15}N$, and C:N) can be used to examine terrestrial and aquatic contributions to the sediments (Gorbey et al., 2021). Diatom and pollen data can aid δ^2H_{wax} interpretations by providing information about lake conditions and atmospheric temperature (Katrantsiotis et al., 2021). Useful proxies for lake water and air temperatures are alkenones (e.g., D'Andrea et al., 2012; Longo et al., 2020), branched glycerol dialkyl glycerol tetraethers (brGDGTs; e.g., Keisling; Thomas et al., 2018), and chironomids (e.g., Wooller et al., 2004; Arppe et al., 2017). A recent study combined leaf wax δ^2H with $\delta^{18}O$ from chironomids in the same sediment archive to reconstruct precipitation seasonality on western Greenland (Corcoran et al., 2021). However, direct comparison between δ^2H and $\delta^{18}O$ from different proxies requires good constraints on the apparent fractionation factor for each proxy to estimate lake water δ^2H. Ultimately, multi-proxy

investigations allow a thorough examination of various parameters. The more we know about the lake system, the better our understanding of the leaf wax δ^2H proxy becomes.

5. Concluding remarks

The main goal of this PhD project was to contribute to a better understanding of Arctic water cycle changes using stable isotope and organic geochemical proxies to investigate seasonal precipitation variability in time and space. More specifically, the aims were to provide Holocene records of precipitation seasonality from Svalbard, and to examine spatial and temporal variability in modern lake water isotopes and their drivers in northern Fennoscandia.

We present Holocene precipitation reconstructions from four lakes across Svalbard. Our results demonstrate that Svalbard experienced higher proportion of winter precipitation relative to the annual total during times of decreased sea-ice extent and emphasize the role of variable regional ocean surface condition on the seasonal distribution of precipitation on Svalbard. The specific outcomes from the Svalbard leaf wax studies are summaries of **Papers I & III**. The modern lake water study from northern Fennoscandia focused on spatial and interannual variability in lake water δ^2H, inferred inflow (precipitation) δ^2H, and evaporative enrichment. The results showed that the interannual variability is mainly controlled by the inflow isotopic composition, and that lakes farther from the Atlantic Ocean are more susceptible to evaporation. Furthermore, variable atmospheric circulation patterns over the North Atlantic influence the relative proportion of winter and summer precipitation entering the lakes. Details on these findings are given in **Paper II**.

Overall, the results presented in this dissertation highlight the potential of organic geochemical and stable isotope proxies to decipher past changes in precipitation seasonality, as well as emphasize the need for careful consideration of lake- and catchment-specific factors influencing lake and soil water δ^2H. Finally, this dissertation outlines potential future directions for how to advance the understanding and interpretations of organic geochemical and precipitation isotope proxies.

6. Future perspectives

Stable water isotope proxies are powerful tools to infer water cycle changes on different timescales. This study has demonstrated that interpretations require careful consideration, as proxy records provide indirect evidence of climate change and can additionally be affected by environmental processes. By improving our understanding of the processes influencing the isotopic composition of precipitation, lake water, soil water, and plants, we ca quantify the water cycle changes more confidently. Preferably, this is achieved through collaborative efforts across disciplines. To forward our interpretations of past water cycle changes on Svalbard, future studies should strive to:

- Improve our understanding of seasonal precipitation variability across Svalbard in modern times, by monitoring precipitation amounts and isotopes in the central, northern, and eastern parts of the archipelago. This requires a massive logistical effort in remote locations but would contribute valuable constraints on spatial variability in Arctic precipitation seasonality. Precipitation isotopes are a bellwether of water cycle change, with larger signal-to-noise ratios than precipitation amount, and greater ability to distinguish changes in moisture source and atmospheric circulation. Thus, having long-term and spatially detailed information about precipitation isotope change will benefit understanding of Arctic system change.

- Investigate modern moisture source variability and how it affects the isotopic composition of precipitation falling on Svalbard. This could be achieved by precipitation backtracking modeling and water-tagging experiments, determining where precipitation originally evaporated.

- Establish regional calibration of the leaf wax δ^2H proxy for Svalbard by measuring leaf wax homologue distributions and δ^2H values of modern plants, leaf water, soil water, and surface sediments to constrain the apparent fractionation.

- Develop techniques to monitor wax transport to and within the lake, to separate and quantify terrestrial and aquatic wax contribution to the lake sediments. Furthermore, detailed mapping of modern catchment vegetation can help evaluating the contribution of different plant types to the sedimentary leaf wax record.

- Increase the temporal resolution in future lipid biomarker studies. This could help assess whether changes occurred momentarily (possibly reflecting catchment processes altering the seasonality reflected in the lake) or gradually. Furthermore, it would enable more accurate correlations between records.

- Enhance the spatial resolution of Arctic paleo-precipitation records. Precipitation varies substantially on a regional and local scale, and the spatial coverage of proxy data, especially concerning precipitation seasonality, is inadequate to make meaningful comparison between regions.

- Explore proxy system modeling. This might prove to be a key tool to assess precipitation seasonality and to constrain the importance of a combination of processes explaining changes recorded in lake water isotope proxies. This modeling approach uses modern climate variables to simulate lake hydrologic and isotopic balance. Thus, proxy system modeling can help us excel the interpretation from lake water isotope proxies beyond describing relative trends.

- Combine leaf wax δ^2H with other proxies. A multi-proxy approach enables reconstruct of multiple climate aspects from the same sedimentary record and provide additional support for interpretations. For example, *sed*aDNA provides evidence of vegetation shifts in response to changes in climate and give indications about the plant wax sources. Moreover, $\delta^{13}C$ can help constrain the provenance of the waxes, and chironomids, alkenones, and brGDGTs can be used to infer past temperature anomalies.

7. References

Aalto, J., Pirinen, P., & Jylhä, K., 2016. New gridded daily climatology of Finland: permutation-based uncertainty estimates and temporal trends in climate. *Journal of Geophysical Research: Atmospheres, 121*(8), 3807-3823. https://doi.org/10.1002/2015JD024651

Aichner, B., 2009. Aquatic macrophyte-derived biomarkers as palaeolimnological proxies on the Tibetan Plateau. PhD thesis. University of Potsdam, Alfred Wegener Institute for Polar and Marine Research. 146 pp.

Aichner, B., Herzschuh, U., & Wilkes, H., 2010a. Influence of aquatic macrophytes on the stable carbon isotopic signatures of sedimentary organic matter in lakes on the Tibetan Plateau. *Organic Geochemistry, 41*(7), 706-718. https://doi.org/10.1016/j.orggeochem.2010.02.002

Aichner, B., Herzschuh, U., Wilkes, H., Vieth, A., & Böhner, J., 2010b. δD values of *n*-alkanes in Tibetan lake sediments and aquatic macrophytes – A surface sediment study and application to a 16 ka record from Lake Koucha. *Organic Geochemistry, 41*(8), 779-790. https://doi.org/10.1016/j.orggeochem.2010.05.010

Allen, J. R., Long, A. J., Ottley, C. J., Pearson, D. G., & Huntley, B., 2007. Holocene climate variability in northernmost Europe. *Quaternary Science Reviews, 26*(9-10), 1432-1453. https://doi.org/10.1016/j.quascirev.2007.02.009

Allaart, L., Müller, J., Schomacker, A., Rydningen, T. A., Håkansson, L., Kjellman, S. E., Mollenhauer, G., & Forwick, M., 2020. Late Quaternary glacier and sea-ice history of northern Wijdefjorden, Svalbard. *Boreas, 49*(3), 417-437. https://doi.org/10.1111/bor.12435

Allaart, L., Schomacker, A., Håkansson, L. M., Farnsworth, W. R., Brynjólfsson, S., Grumstad, A., & Kjellman, S. E., 2021a. Geomorphology and surficial geology of the Femmilsjøen area, northern Spitsbergen. *Geomorphology, 382*, 107693. https://doi.org/10.1016/j.geomorph.2021.107693

Allaart, L., Schomacker, A., Larsen, N. K., Nørmark, E., Rydningen, T. A., Farnsworth, W. R., Retelle, M., Brynjólfsson, S., Forwick, M., & Kjellman, S. E., 2021b. Glacial history of the Åsgardfonna Ice Cap, NE Spitsbergen, since the last glaciation. *Quaternary Science Reviews, 251*, 106717. https://doi.org/10.1016/j.quascirev.2020.106717

Alley, R. B., Andrews, J. T., Brigham-Grette, J., Clarke, G., Cuffey, K. M., Fitzpatrick, J., Funder, S., Marshall, S., Miller, G., & Mitrovica, J., 2010. History of the Greenland Ice Sheet: paleoclimatic insights. *Quaternary Science Reviews, 29*(15-16), 1728-1756. https://doi.org/10.1016/j.quascirev.2010.02.007

Alsos, I. G., Lammers, Y., Kjellman, S. E., Merkel, M. K. F., Bender, E. M., Rouillard, A., Erlendsson, E., Guðmundsdóttir, E. R., Benediktsson, Í. Ö., & Farnsworth, W. R., 2021. Ancient sedimentary DNA shows rapid post-glacial colonisation of Iceland followed by relatively stable vegetation until the Norse settlement (Landnám) AD 870. *Quaternary Science Reviews, 259*, 106903. https://doi.org/10.1016/j.quascirev.2021.106903

Anderson, L., Abbott, M. B., & Finney, B. P., 2001. Holocene climate inferred from oxygen isotope ratios in lake sediments, central Brooks Range, Alaska. *Quaternary Research, 55*(3), 313-321. https://doi.org/10.1006/qres.2001.2219

Anderson, N. J., & Leng, M. J., 2004. Increased aridity during the early Holocene in West Greenland inferred from stable isotopes in laminated-lake sediments. *Quaternary Science Reviews, 23*(7-8), 841-849. https://doi.org/10.1016/j.quascirev.2003.06.013

Arppe, L., Kurki, E., Wooller, M. J., Luoto, T. P., Zajączkowski, M., & Ojala, A. E., 2017. A 5500-year oxygen isotope record of high arctic environmental change from southern Spitsbergen. *The Holocene, 27*(12), 1948-1962. https://doi.org/10.1177/0959683617715698

Arrhenius, S., 1896. XXXI. On the influence of carbonic acid in the air upon the temperature of the ground. *The London, Edinburgh, and Dublin Philosophical Magazine and Journal of Science, 41*(251), 237-276. https://doi.org/10.1080/14786449608620846

Badgeley, J. A., Steig, E. J., Hakim, G. J., & Fudge, T. J., 2020. Greenland temperature and precipitation over the last 20 000 years using data assimilation. *Climate of the Past, 16*(4), 1325-1346. https://doi.org/10.5194/cp-16-1325-2020

Bailey, H., Hubbard, A., Klein, E. S., Mustonen, K.-R., Akers, P. D., Marttila, H., & Welker, J. M., 2021. Arctic sea-ice loss fuels extreme European snowfall. *Nature Geoscience*, 1-6. https://doi.org/10.1038/s41561-021-00719-y

Balascio, N. L., D'Andrea, W. J., Anderson, R. S., & Wickler, S., 2018a. Influence of vegetation type on n-alkane composition and hydrogen isotope values from a high latitude ombrotrophic bog. *Organic Geochemistry, 121*, 48-57. https://doi.org/10.1016/j.orggeochem.2018.03.008

Balascio, N. L., D'Andrea, W. J., Gjerde, M., & Bakke, J., 2018b. Hydroclimate variability of High Arctic Svalbard during the Holocene inferred from hydrogen isotopes of leaf waxes. *Quaternary Science Reviews, 183*, 177-187. https://doi.org/10.1016/j.quascirev.2016.11.036

Balascio, N. L., D'Andrea, W. J., Bradley, R. S., & Perren, B. B., 2013. Biogeochemical evidence for hydrologic changes during the Holocene in a lake sediment record from southeast Greenland. *The Holocene, 23*(10), 1428-1439. https://doi.org/10.1177/0959683613493938

Bartels, M., Titschack, J., Fahl, K., Stein, R., & Hebbeln, D., 2018. Wahlenbergfjord, eastern Svalbard: a glacier-surrounded fjord reflecting regional hydrographic variability during the Holocene? *Boreas, 47*(4), 1003-1021. https://doi.org/10.1111/bor.12325

Berke, M. A., Sierra, A. C., Bush, R., Cheah, D., & O'Connor, K., 2019. Controls on leaf wax fractionation and δ^2H values in tundra vascular plants from western Greenland. *Geochimica et Cosmochimica Acta, 244*, 565-583. https://doi.org/10.1016/j.gca.2018.10.020

Bintanja, R., & Andry, O., 2017. Towards a rain-dominated Arctic. *Nature Climate Change, 7*(4), 263. https://doi.org/10.1038/nclimate3240

Bintanja, R., & Selten, F. M., 2014. Future increases in Arctic precipitation linked to local evaporation and sea-ice retreat. *Nature, 509*(7501), 479-482. https://doi.org/10.1038/nature13259

Bintanja, R., van der Wiel, K., Van der Linden, E., Reusen, J., Bogerd, L., Krikken, F., & Selten, F., 2020. Strong future increases in Arctic precipitation variability linked to poleward moisture transport. *Science advances, 6*(7), eaax6869. https://doi.org/10.1126/sciadv.aax6869

Birks, H. H., 1991. Holocene vegetational history and climatic change in west Spitsbergen - plant macrofossils from Skardtjørna, an Arctic lake. *The Holocene, 1*(3), 209-218. https://doi.org/10.1177/095968369100100303

Bjune, A. E., Birks, H., & Seppä, H., 2004. Holocene vegetation and climate history on a continental-oceanic transect in northern Fennoscandia based on pollen and plant macrofossils. *Boreas, 33*(3), 211-223. https://doi.org/10.1111/j.1502-3885.2004.tb01142.x

Blaauw, M., & Christen, J. A., 2011. Flexible paleoclimate age-depth models using an autoregressive gamma process. *Bayesian analysis, 6*(3), 457-474. https://doi.org/10.1214/11-BA618

Bonan, D. B., Christian, J. E., & Christianson, K., 2019. Influence of North Atlantic climate variability on glacier mass balance in Norway, Sweden and Svalbard. *Journal of Glaciology, 65*(252), 580-594. https://doi.org/10.1017/jog.2019.35

Bonne, J.-L., Meyer, H., Behrens, M., Boike, J., Kipfstuhl, S., Rabe, B., Schmidt, T., Schönicke, L., Steen-Larsen, H. C., & Werner, M., 2020. Moisture origin as a driver of temporal variabilities of the water vapour isotopic composition in the Lena River Delta, Siberia. *Atmospheric Chemistry and Physics, 20*(17), 10493-10511. https://doi.org/10.5194/acp-20-10493-2020

Bowen, G. J., 2021. OIPC: The online isotopes in precipitation calculator, version 3.1. Available at http://www.waterisotopes.org

Bowen, G. J., Putman, A., Brooks, J. R., Bowling, D. R., Oerter, E. J., & Good, S. P., 2018. Inferring the source of evaporated waters using stable H and O isotopes. *Oecologia, 187*(4), 1025-1039. https://doi.org/10.1007/s00442-018-4192-5

Bowen, G. J., & Revenaugh, J., 2003. Interpolating the isotopic composition of modern meteoric precipitation. *Water Resources Research, 39*(10). https://doi.org/10.1029/2003WR002086

Bowen, G. J., Wassenaar, L. I., & Hobson, K. A., 2005. Global application of stable hydrogen and oxygen isotopes to wildlife forensics. *Oecologia, 143*(3), 337-348. https://doi.org/10.1007/s00442-004-1813-y

Bush, R. T., & McInerney, F. A., 2013. Leaf wax *n*-alkane distributions in and across modern plants: Implications for paleoecology and chemotaxonomy. *Geochimica et Cosmochimica Acta, 117*, 161-179. https://doi.org/10.1016/j.gca.2013.04.016

Cappa, C. D., Hendricks, M. B., DePaolo, D. J., & Cohen, R. C., 2003. Isotopic fractionation of water during evaporation. *Journal of Geophysical Research: Atmospheres, 108*(D16). https://doi.org/10.1029/2003JD003597

Clark, I. D., & Fritz, P., 1997. Environmental isotopes in hydrogeology. CRC press. 342 pp.

Cluett, A., Thomas, E., Evans, S., & Keys, P., 2021. Seasonal variations in moisture origin explain spatial contrast in precipitation isotope seasonality on coastal western Greenland. *Journal of Geophysical Research: Atmospheres, 126*(11), e2020JD033543. https://doi.org/10.1029/2020JD033543

Cluett, A. A., & Thomas, E. K., 2020. Resolving combined influences of inflow and evaporation on western Greenland lake water isotopes to inform paleoclimate inferences. *Journal of Paleolimnology, 63*, 251-268. https://doi.org/10.1007/s10933-020-00114-4

Cohen, J., Jones, J., Furtado, J. C., & Tziperman, E., 2013. Warm Arctic, cold continents: A common pattern related to Arctic sea ice melt, snow advance, and extreme winter weather. *Oceanography, 26*(4), 150-160. Retrieved from http://www.jstor.org/stable/24862104

Cooper, L., Olsen, C., Solomon, D., Larsen, I., Cook, R., & Grebmeier, J., 1991. Stable isotopes of oxygen and natural and fallout radionuclides used for tracing runoff during snowmelt in an Arctic watershed. *Water Resources Research, 27*(9), 2171-2179. https://doi.org/10.1029/91WR01243

Corcoran, M. C., Thomas, E. K., & Morrill, C., 2021. Using a paired chironomid δ18O and aquatic leaf wax δ2H approach to reconstruct seasonality on western Greenland during the Holocene. *Paleoceanography and Paleoclimatology, 36*(4), e2020PA004169. https://doi.org/10.1029/2020PA004169

Cowling, O. C., Thomas, E. K., Svendsen, J. I., Mangerud, J., Haflidason, H., Regnéll, C., & Brendryen, J., 2021. Western Siberia experienced rapid shifts in moisture source and summer water balance during the last deglaciation and early Holocene. *Journal of Quaternary Science*. https://doi.org/10.1002/jqs.3386

Craig, H., 1961. Isotopic variations in meteoric waters. *Science, 133*(3465), 1702-1703. https://doi.org/10.1126/science.133.3465.1702

Croudace, I. W., Rindby, A., & Rothwell, R. G., 2006. ITRAX: description and evaluation of a new multi-function X-ray core scanner. *Geological Society, London, Special Publications, 267*(1), 51-63. https://doi.org/10.1144/GSL.SP.2006.267.01.04

D'Andrea, W. J., Vaillencourt, D. A., Balascio, N. L., Werner, A., Roof, S. R., Retelle, M., & Bradley, R. S., 2012. Mild Little Ice Age and unprecedented recent warmth in an 1800 year lake sediment record from Svalbard. *Geology, 40*(11), 1007-1010. https://doi.org/10.1130/G33365.1

Dahl-Jensen, D., Johnsen, S., Hammer, C., Clausen, H., & Jouzel, J., 1993. Past accumulation rates derived from observed annual layers in the GRIP ice core from Summit, Central Greenland. In W. R. Peltier (Ed.), *Ice in the climate system* (pp. 517-532). Springer Berlin Heidelberg. Retrieved from http://link.springer.com/10.1007/978-3-642-85016-5

Daniels, W. C., Russell, J. M., Giblin, A. E., Welker, J. M., Klein, E. S., & Huang, Y., 2017. Hydrogen isotope fractionation in leaf waxes in the Alaskan Arctic tundra. *Geochimica et Cosmochimica Acta, 213*, 216-236. https://doi.org/10.1016/j.gca.2017.06.028

Dansgaard, W., 1964. Stable isotopes in precipitation. *Tellus, 16*(4), 436-468. https://doi.org/10.3402/tellusa.v16i4.8993

Dansgaard, W., Johnsen, S. J., Møller, J., & Langway Jr, C. C., 1969. One thousand centuries of climatic record from Camp Century on the Greenland ice sheet. *Science, 166*(3903), 377-381. https://doi.org/10.1126/science.166.3903.377

de Vernal, A., Hillaire-Marcel, C., Rochon, A., Fréchette, B., Henry, M., Solignac, S., & Bonnet, S., 2013. Dinocyst-based reconstructions of sea ice cover concentration during the Holocene in the Arctic Ocean, the northern North Atlantic Ocean and its adjacent seas. *Quaternary Science Reviews, 79*, 111-121. http://dx.doi.org/10.1016/j.quascirev.2013.07.006

Dee, S. G., Russell, J. M., Morrill, C., Chen, Z., & Neary, A., 2018. PRYSM v2. 0: A proxy system model for lacustrine archives. *Paleoceanography and Paleoclimatology, 33*(11), 1250-1269. https://doi.org/10.1029/2018PA003413

Dickson, R., Osborn, T., Hurrell, J., Meincke, J., Blindheim, J., Adlandsvik, B., Vinje, T., Alekseev, G., & Maslowski, W., 2000. The Arctic ocean response to the North Atlantic oscillation. *Journal of Climate, 13*(15), 2671-2696. https://doi.org/10.1175/1520-0442(2000)013<2671:TAORTT>2.0.CO;2

Diefendorf, A. F., & Freimuth, E. J., 2017. Extracting the most from terrestrial plant-derived *n*-alkyl lipids and their carbon isotopes from the sedimentary record: A review. *Organic Geochemistry, 103*, 1-21. https://doi.org/10.1016/j.orggeochem.2016.10.016

Dion-Kirschner, H., McFarlin, J. M., Masterson, A. L., Axford, Y., & Osburn, M. R., 2020. Modern constraints on the sources and climate signals recorded by sedimentary plant waxes in west Greenland. *Geochimica et Cosmochimica Acta, 286*, 336-354. https://doi.org/10.1016/j.gca.2020.07.027

Divine, D., Isaksson, E., Martma, T., Meijer, H. A., Moore, J., Pohjola, V., van de Wal, R. S., & Godtliebsen, F., 2011. Thousand years of winter surface air temperature variations

in Svalbard and northern Norway reconstructed from ice-core data. *Polar Research, 30*(1), 7379. https://doi.org/10.3402/polar.v30i0.7379
Dobler, A., Førland, E. J., & Isaksen, K., 2019. *Present and future heavy rainfall statistics for Svalbard - Background-report for Climate in Svalbard 2100*. Norwegian Centre for Climate Services (NCCS), NCCS report no. 3/2019, 29 pp.
Drange, H., Dokken, T., Furevik, T., Gerdes, R., Berger, W., Nesje, A., Orvik, K. A., Skagseth, O., Skjelvan, I., & Osterhus, S., 2005. The Nordic seas: an overview. *Geophysical Monograph-American Geophysical Union, 158*(1). https://doi.org/10.1029/158GM02
Dufour, A., Zolina, O., & Gulev, S. K., 2016. Atmospheric moisture transport to the Arctic: Assessment of reanalyses and analysis of transport components. *Journal of Climate, 29*(14), 5061-5081. https://doi.org/10.1175/JCLI-D-15-0559.1
Dyrrdal, A. V., Lenkoski, A., Thorarinsdottir, T. L., & Stordal, F., 2015. Bayesian hierarchical modeling of extreme hourly precipitation in Norway. *Environmetrics, 26*(2), 89-106. https://doi.org/10.1002/env.2301
Eckerstorfer, M., & Christiansen, H. H., 2011. The "High Arctic maritime snow climate" in central Svalbard. *Arctic, Antarctic, and Alpine Research, 43*(1), 11-21. https://doi.org/10.1657/1938-4246-43.1.11
Edwards, T. W., Wolfe, B. B., & Macdonald, G. M., 1996. Influence of changing atmospheric circulation on precipitation δ18O–temperature relations in Canada during the Holocene. *Quaternary Research, 46*(3), 211-218. https://doi.org/10.1006/qres.1996.0061
Eglinton, G., & Hamilton, R. J., 1967. Leaf Epicuticular Waxes: The waxy outer surfaces of most plants display a wide diversity of fine structure and chemical constituents. *Science, 156*(3780), 1322-1335. https://doi.org/10.1126/science.156.3780.1322
Eglinton, T. I., & Eglinton, G., 2008. Molecular proxies for paleoclimatology. *Earth and Planetary Science Letters, 275*(1-2), 1-16. https://doi.org/10.1016/j.epsl.2008.07.012
Eidesen, P. B., Arnesen, G., Elven, R., & Søli, G., 2018. *Kartlegging av Ringhorndalen, Wijdefjorden: en uutforsket arktisk oase.* Rapport til Sysselmannen på Svalbard, The University Centre in Svalbard, The University of Oslo, Ecofact Nord AS, 43 pp.
Eklund, A., Axén Mårtensson, J., Bergström, S., Björck, E., Dahné, J., Lindström, L., Olsson, J., Simonsson, L., & Sjökvist, E., 2015. *Sveriges framtida klimat: Underlag till Dricksvattenutredningen*. Swedish Meteorological and Hydrological Institute (SMHI), Klimatologi nr 14, 82 pp.
Elvebakk, A., & Nilsen, L., 2002. *Indre Wijdefjorden med sidefjordar: eit botanisk unikt steppeområde på Svalbard*. Rapport til Sysselmannen på Svalbard, University of Tromsø, Tromsø, 75 pp.
Emiliani, C., 1955. Pleistocene temperatures. *The Journal of Geology, 63*(6), 538-578. https://www.jstor.org/stable/30080906
Evans, M. N., Tolwinski-Ward, S. E., Thompson, D. M., & Anchukaitis, K. J., 2013. Applications of proxy system modeling in high resolution paleoclimatology. *Quaternary Science Reviews, 76*, 16-28. http://dx.doi.org/10.1016/j.quascirev.2013.05.024
Farnsworth, W. R., Allaart, L., Ingólfsson, Ó., Alexanderson, H., Forwick, M., Noormets, R., Retelle, M., & Schomacker, A., 2020. Holocene glacial history of Svalbard: Status, perspectives and challenges. *Earth-Science Reviews, 208*, 103249. https://doi.org/10.1016/j.earscirev.2020.103249
Farnsworth, W. R., Ingólfsson, Ó., Mannerfelt, E. S., Kalliokoski, M. H., Guðmundsdóttir, E. R., Retelle, M., Allaart, L., Brynjólfsson, S., Furze, M. F., & Hancock, H. J., 2022.

Vedde Ash constrains Younger Dryas glacier re-advance and rapid glacio-isostatic rebound on Svalbard. *Quaternary Science Advances, 5*, 100041. https://doi.org/10.1016/j.qsa.2021.100041

Ficken, K. J., Li, B., Swain, D., & Eglinton, G., 2000. An *n*-alkane proxy for the sedimentary input of submerged/floating freshwater aquatic macrophytes. *Organic Geochemistry, 31*(7-8), 745-749. https://doi.org/10.1016/S0146-6380(00)00081-4

Fjeldskaar, W., Bondevik, S., & Amantov, A., 2018. Glaciers on Svalbard survived the Holocene thermal optimum. *Quaternary Science Reviews, 199*, 18-29. https://doi.org/10.1016/j.quascirev.2018.09.003

Forwick, M., & Vorren, T. O., 2009. Late Weichselian and Holocene sedimentary environments and ice rafting in Isfjorden, Spitsbergen. *Palaeogeography, Palaeoclimatology, Palaeoecology, 280*(1-2), 258-274. https://doi.org/10.1016/j.palaeo.2009.06.026

Førland, E., Hanssen-Bauer, I., & Nordli, P., 1997. *Climate statistics and longterm series of temperature and precipitation at Svalbard and Jan Mayen*. Norwegian Meteorological Institute, MET Norway, Klima Report 21, 97 pp.

Førland, E. J., Benestad, R., Hanssen-Bauer, I., Haugen, J. E., & Skaugen, T. E., 2011. Temperature and Precipitation Development at Svalbard 1900–2100. *Advances in Meteorology, 2011*, 1-14. https://doi.org/10.1155/2011/893790

Førland, E. J., Flatøy, F., Hanssen-Bauer, I., Haugen, J. E., Isaksen, K., Sorteberg, A., Ådlandsvik, B., & Benestad, R. E., 2009. *Climate development in North Norway and the Svalbard region during 1900–2100.* Norwegian Polar Institute, Report series no. 128. 44 pp.

Førland, E. J., & Hanssen-Bauer, I., 2003. Past and future climate variations in the Norwegian Arctic: overview and novel analyses. *Polar Research, 22*(2), 113-124. https://doi.org/10.3402/polar.v22i2.6450

Førland, E. J., Isaksen, K., Lutz, J., Hanssen-Bauer, I., Schuler, T. V., Dobler, A., Gjelten, H. M., & Vikhamar-Schuler, D., 2020. Measured and Modeled Historical Precipitation Trends for Svalbard. *Journal of Hydrometeorology, 21*(6), 1279-1296. https://doi.org/10.1175/JHM-D-19-0252.1

Gat, J. R., 1996. Oxygen and hydrogen isotopes in the hydrologic cycle. *Annual Review of Earth and Planetary Sciences, 24*, 225-262. https://doi.org/10.1146/annurev.earth.24.1.225

Gibson, J., Prepas, E., & McEachern, P., 2002. Quantitative comparison of lake throughflow, residency, and catchment runoff using stable isotopes: modelling and results from a regional survey of Boreal lakes. *Journal of Hydrology, 262*(1-4), 128-144. https://doi.org/10.1016/S0022-1694(02)00022-7

Gorbey, D. B., Thomas, E. K., Crump, S. E., Hollister, K. V., Raynolds, M. K., Raberg, J. H., de Wet, G., Sepúlveda, J., & Miller, G. H., 2021. Southern Baffin Island mean annual precipitation isotopes modulated by summer and autumn moisture source changes during the past 5800 years. *Journal of Quaternary Science*. https://doi.org/10.1002/jqs.3390

Gröning, M., 2011. Improved water $\delta^{2}H$ and $\delta^{18}O$ calibration and calculation of measurement uncertainty using a simple software tool. *Rapid Communications in Mass Spectrometry, 25*(19), 2711-2720. https://doi.org/10.1002/rcm.5074

Gröning, M., 2018. SICalib User Manual (Stable Isotope Calibration for routine δ-scale measurements) Ver 2.16 j. Terrestrial Environment Laboratory (TEL) Technical Note No. 01. International Atomic Energy Agency, Vienna, Austria., 37 pp.

Hagen, J. O., Liestøl, O., Roland, E., & Jørgensen, T., 1993. *Glacier atlas of Svalbard and Jan Mayen*. Norwegian Polar Institute, Meddelelser 129, 141 pp.
Hajdas, I., 2008. Radiocarbon dating and its applications in Quaternary studies. *E&G Quaternary Science Journal, 57*(1/2), 2-24. https://doi.org/10.3285/eg.57.1-2.1
Hald, M., Andersson, C., Ebbesen, H., Jansen, E., Klitgaard-Kristensen, D., Risebrobakken, B., Salomonsen, G. R., Sarnthein, M., Sejrup, H. P., & Telford, R. J., 2007. Variations in temperature and extent of Atlantic Water in the northern North Atlantic during the Holocene. *Quaternary Science Reviews, 26*(25-28), 3423-3440. https://doi.org/10.1016/j.quascirev.2007.10.005
Hammarlund, D., Barnekow, L., Birks, H. J. B., Buchardt, B., & Edwards, T. W., 2002. Holocene changes in atmospheric circulation recorded in the oxygen-isotope stratigraphy of lacustrine carbonates from northern Sweden. *The Holocene, 12*(3), 339-351. https://doi.org/10.1191/0959683602hl548rp
Hanssen-Bauer, I., 2002. Temperature and precipitation in Svalbard 1912–2050: measurements and scenarios. *Polar Record, 38*(206), 225-232. https://doi.org/10.1017/S0032247400017757
Hanssen-Bauer, I., & Førland, E., 2000. Temperature and precipitation variations in Norway 1900–1994 and their links to atmospheric circulation. *International Journal of Climatology: A Journal of the Royal Meteorological Society, 20*(14), 1693-1708. https://doi.org/10.1002/1097-0088(20001130)20:14<1693::AID-JOC567>3.0.CO;2-7
Hanssen-Bauer, I., Førland, E., Haddeland, I., Hisdal, H., Mayer, S., Nesje, A., Nilsen, J., Sandven, S., Sandø, A., & Sorteberg, A., 2017. *Climate in Norway 2100 - A knowledge base for climate adaptation*. Norwegian Centre for Climate Services (NCCS) NCCS report no. 1/2017, 47 pp.
Hanssen-Bauer, I., Førland, E. J., Hisdal, H., Mayer, S., Sandø, A. B., & Sorteberg, A., 2019. *Climate in Svalbard 2100 - A knowledge base for climate adaptation* 2387-3027. Norwegian Centre for Climate Services (NCCS), NCCS report no. 1/2019, 207 pp.
Haugan, P. M., 1999. Structure and heat content of the West Spitsbergen Current. *Polar Research, 18*(2), 183-188. https://doi.org/10.3402/polar.v18i2.6572
Heiri, O., Lotter, A. F., & Lemcke, G., 2001. Loss on ignition as a method for estimating organic and carbonate content in sediments: reproducibility and comparability of results. *Journal of Paleolimnology, 25*(1), 101-110. https://doi.org/10.1023/A:1008119611481
Hisdal, V., 1998. *Svalbard: nature and history*. Norwegian Polar Institute, Polarhåndbok No. 12, 123 pp.
Hou, J., D'Andrea, W. J., & Huang, Y., 2008. Can sedimentary leaf waxes record D/H ratios of continental precipitation? Field, model, and experimental assessments. *Geochimica et Cosmochimica Acta, 72*(14), 3503-3517. https://doi.org/10.1016/j.gca.2008.04.030
Humlum, O., 2002. Modelling late 20th-century precipitation in Nordenskiold Land, Svalbard, by geomorphic means. *Norsk Geografisk Tidsskrift-Norwegian Journal of Geography, 56*(2), 96-103. https://doi.org/10.1080/002919502760056413
Hurrell, J. W., 1995. Decadal trends in the North Atlantic Oscillation: regional temperatures and precipitation. *Science, 269*(5224), 676-679. https://doi.org/10.1126/science.269.5224.676
IAEA/WMO. 2019. Global Network of Isotopes in Precipitation. The GNIP Database. Retrieved from https://nucleus.iaea.org/wiser
Irannezhad, M., Marttila, H., & Kløve, B., 2014. Long-term variations and trends in precipitation in Finland. *International Journal of Climatology, 34*(10), 3139-3153. https://doi.org/10.1002/joc.3902

Isaksen, K., Førland, E., Dobler, A., Benestad, R., Haugen, J., & Mezghani, A., 2017. *Klimascenarioer for Longyearbyen-området, Svalbard*. Norwegian Meteorological Institute, MET Norway Report No. 15/2017, 55 pp.

Isaksson, E., Hermanson, M., Hicks, S., Igarashi, M., Kamiyama, K., Moore, J., Motoyama, H., Muir, D., Pohjola, V., Vaikmäe, R., van de Wal, R. S. W., & Watanabe, O., 2003. Ice cores from Svalbard—useful archives of past climate and pollution history. *Physics and Chemistry of the Earth, Parts A/B/C, 28*(28-32), 1217-1228. https://doi.org/10.1016/j.pce.2003.08.053

Isaksson, E., Kohler, J., Pohjola, V., Moore, J., Igarashi, M., Karlöf, L., Martma, T., Meijer, H., Motoyama, H., & Vaikmäe, R., 2005. Two ice-core $\delta^{18}O$ records from Svalbard illustrating climate and sea-ice variability over the last 400 years. *The Holocene, 15*(4), 501-509.

Jakobsson, M., Mayer, L., Coakley, B., Dowdeswell, J. A., Forbes, S., Fridman, B., Hodnesdal, H., Noormets, R., Pedersen, R., & Rebesco, M., 2012. The international bathymetric chart of the Arctic Ocean (IBCAO) version 3.0. *Geophysical research letters, 39*(12). https://doi.org/10.1029/2012GL052219

Johnsen, S. J., Dahl-Jensen, D., Gundestrup, N., Steffensen, J. P., Clausen, H. B., Miller, H., Masson-Delmotte, V., Sveinbjörnsdottir, A. E., & White, J., 2001. Oxygen isotope and palaeotemperature records from six Greenland ice-core stations: Camp Century, Dye-3, GRIP, GISP2, Renland and NorthGRIP. *Journal of Quaternary Science: Published for the Quaternary Research Association, 16*(4), 299-307. https://doi.org/10.1002/jqs.622

Jones, V. J., Leng, M. J., Solovieva, N., Sloane, H. J., & Tarasov, P., 2004. Holocene climate of the Kola Peninsula; evidence from the oxygen isotope record of diatom silica. *Quaternary Science Reviews, 23*(7-8), 833-839. https://doi.org/10.1016/j.quascirev.2003.06.014

Jonsson, C. E., Leng, M. J., Rosqvist, G. C., Seibert, J., & Arrowsmith, C., 2009. Stable oxygen and hydrogen isotopes in sub-Arctic lake waters from northern Sweden. *Journal of Hydrology, 376*(1-2), 143-151. https://doi.org/10.1016/j.jhydrol.2009.07.021

Jouzel, J., & Merlivat, L., 1984. Deuterium and oxygen 18 in precipitation: Modeling of the isotopic effects during snow formation. *Journal of Geophysical Research: Atmospheres, 89*(D7), 11749-11757. https://doi.org/10.1029/JD089iD07p11749

Jaagus, J., 2009. Regionalisation of the precipitation pattern in the Baltic Sea drainage basin and its dependence on large-scale atmospheric circulation. *Boreal Environment Research, 14*, 31-44.

Kahmen, A., Schefuß, E., & Sachse, D., 2013. Leaf water deuterium enrichment shapes leaf wax *n*-alkane δD values of angiosperm plants I: Experimental evidence and mechanistic insights. *Geochimica et Cosmochimica Acta, 111*, 39-49. https://doi.org/10.1016/j.gca.2012.09.003

Katrantsiotis, C., Norström, E., Smittenberg, R. H., Salonen, J. S., Plikk, A., & Helmens, K., 2021. Seasonal variability in temperature trends and atmospheric circulation systems during the Eemian (Last Interglacial) based on *n*-alkanes hydrogen isotopes from Northern Finland. *Quaternary Science Reviews, 273*, 107250. https://doi.org/10.1016/j.quascirev.2021.107250

Kaufman, D., McKay, N., Routson, C., Erb, M., Davis, B., Heiri, O., Jaccard, S., Tierney, J., Dätwyler, C., & Axford, Y., 2020. A global database of Holocene paleotemperature records. *Scientific data, 7*(1), 1-34. https://doi.org/10.1038/s41597-020-0445-3

Keisling, B. A., Castañeda, I. S., & Brigham-Grette, J., 2017. Hydrological and temperature change in Arctic Siberia during the intensification of Northern Hemisphere Glaciation. *Earth and Planetary Science Letters, 457*, 136-148. https://doi.org/10.1016/j.epsl.2016.09.058

Kjellman, S. E., 2019. As a climate researcher, should I change my air-travel habits? *Nature, 571*(7766). https://doi.org/10.1038/d41586-019-01652-2

Kjellman, S. E., Axelsson, P. E., Etzelmüller, B., Westermann, S., & Sannel, A. B. K., 2018. Holocene development of subarctic permafrost peatlands in Finnmark, northern Norway. *The Holocene, 28*(12), 1855-1869. https://doi.org/10.1177/0959683618798126

Kjær, K. H., Bjørk, A. A., Kjeldsen, K. K., Hansen, E. S., Andresen, C. S., Siggaard-Andersen, M.-L., Khan, S. A., Søndergaard, A. S., Colgan, W., & Schomacker, A., 2022. Glacier response to the Little Ice Age during the Neoglacial cooling in Greenland. *Earth-Science Reviews, 227*, 103984. https://doi.org/10.1016/j.earscirev.2022.103984

Konecky, B. L., McKay, N. P., Comas-Bru, L., Dassié, E. P., DeLong, K. L., Falster, G. M., Fischer, M. J., Jones, M. D., Jonkers, L., & Kaufman, D. S., 2020. The Iso2k database: a global compilation of paleo-$\delta^{18}O$ and $\delta^{2}H$ records to aid understanding of Common Era climate. *Earth System Science Data, 12*(3), 2261-2288. https://doi.org/10.5194/essd-12-2261-2020

Kopec, B. G., Feng, X., Michel, F. A., & Posmentier, E. S., 2016. Influence of sea ice on Arctic precipitation. *Proc Natl Acad Sci U S A, 113*(1), 46-51. https://doi.org/10.1073/pnas.1504633113

Kylander, M. E., Ampel, L., Wohlfarth, B., & Veres, D., 2011. High-resolution X-ray fluorescence core scanning analysis of Les Echets (France) sedimentary sequence: new insights from chemical proxies. *Journal of Quaternary Science, 26*(1), 109-117. https://doi.org/10.1002/jqs.1438

Larocca, L. J., & Axford, Y., 2022. Arctic glaciers and ice caps through the Holocene: a circumpolar synthesis of lake-based reconstructions. *Climate of the Past, 18*(3), 579-606. https://doi.org/10.5194/cp-18-579-2022

Larsen, N. K., Levy, L. B., Strunk, A., Søndergaard, A. S., Olsen, J., & Lauridsen, T. L., 2019. Local ice caps in Finderup Land, North Greenland, survived the Holocene Thermal Maximum. *Boreas, 48*(3), 551-562. https://doi.org/10.1111/bor.12384

Larsen, N. K., Strunk, A., Levy, L. B., Olsen, J., Bjørk, A., Lauridsen, T. L., Jeppesen, E., & Davidson, T. A., 2017. Strong altitudinal control on the response of local glaciers to Holocene climate change in southwest Greenland. *Quaternary Science Reviews, 168*, 69-78. https://doi.org/10.1016/j.quascirev.2017.05.008

Lasher, G. E., Axford, Y., McFarlin, J. M., Kelly, M. A., Osterberg, E. C., & Berkelhammer, M. B., 2017. Holocene temperatures and isotopes of precipitation in Northwest Greenland recorded in lacustrine organic materials. *Quaternary Science Reviews, 170*, 45-55. https://doi.org/10.1016/j.quascirev.2017.06.016

Laskar, J., Robutel, P., Joutel, F., Gastineau, M., Correia, A., & Levrard, B., 2004. A long-term numerical solution for the insolation quantities of the Earth. *Astronomy & Astrophysics, 428*(1), 261-285. https://doi.org/10.1051/0004-6361:20041335

Lawrence, Z. D., Perlwitz, J., Butler, A. H., Manney, G. L., Newman, P. A., Lee, S. H., & Nash, E. R., 2020. The remarkably strong Arctic stratospheric polar vortex of winter 2020: Links to record-breaking Arctic oscillation and ozone loss. *Journal of Geophysical Research: Atmospheres, 125*(22), e2020JD033271. https://doi.org/10.1029/2020JD033271

Leng, M. J., & Marshall, J. D., 2004. Palaeoclimate interpretation of stable isotope data from lake sediment archives. *Quaternary Science Reviews, 23*(7-8), 811-831. https://doi.org/10.1016/j.quascirev.2003.06.012

Linderholm, H. W., Nicolle, M., Francus, P., Gajewski, K., Helama, S., Korhola, A., Solomina, O., Yu, Z., Zhang, P., & D'Andrea, W. J., 2018. Arctic hydroclimate variability during the last 2000 years. *Climate of the Past*. https://doi.org/10.5194/cp-14-473-2018

Lisiecki, L. E., & Raymo, M. E., 2005. A Pliocene-Pleistocene stack of 57 globally distributed benthic $\delta^{18}O$ records. *Paleoceanography, 20*(1). https://doi.org/10.1029/2004PA001071

Longo, W. M., Huang, Y., Russell, J. M., Morrill, C., Daniels, W. C., Giblin, A. E., & Crowther, J., 2020. Insolation and greenhouse gases drove Holocene winter and spring warming in Arctic Alaska. *Quaternary Science Reviews, 242*, 106438. https://doi.org/10.1016/j.quascirev.2020.106438

Mangerud, J., & Svendsen, J. I., 2018. The Holocene Thermal Maximum around Svalbard, Arctic North Atlantic; molluscs show early and exceptional warmth. *The Holocene, 28*(1), 65-83. https://doi.org/10.1177/0959683617715701

McCrystall, M. R., Stroeve, J., Serreze, M., Forbes, B. C., & Screen, J. A., 2021. New climate models reveal faster and larger increases in Arctic precipitation than previously projected. *Nature communications, 12*(1), 1-12. https://doi.org/10.1038/s41467-021-27031-y

McFarlin, J. M., Axford, Y., Masterson, A. L., & Osburn, M. R., 2019. Calibration of modern sedimentary $\delta^{2}H$ plant wax-water relationships in Greenland lakes. *Quaternary Science Reviews, 225*, 105978. https://doi.org/10.1016/j.quascirev.2019.105978

McKay, N., & Emile-Geay, J., 2016. Technical note: The Linked Paleo Data framework - a common tongue for paleoclimatology. *Climate of the Past, 12*, 1093–1100. https://doi.org/10.5194/cp-12-1093-2016

McKay, N. P., Emile-Geay, J., & Khider, D., 2021. geoChronR - an R package to model, analyze, and visualize age-uncertain data. *Geochronology, 3*(1), 149-169. https://doi.org/10.5194/gchron-3-149-2021

McKay, N. P., Kaufman, D. S., Routson, C. C., Erb, M. P., & Zander, P. D., 2018. The onset and rate of Holocene Neoglacial cooling in the Arctic. *Geophysical research letters, 45*(22), 12,487-412,496. https://doi.org/10.1029/2018GL079773

Mellat, M., Bailey, H., Mustonen, K.-R., Marttila, H., Klein, E. S., Gribanov, K., Bret-Harte, M. S., Chupakov, A. V., Divine, D. V., & Else, B., 2021. Hydroclimatic controls on the isotopic ($\delta^{18}O$, $\delta^{2}H$, *d-excess*) traits of pan-Arctic summer rainfall events. *Frontiers in Earth Science, 9*, 367. https://doi.org/10.3389/feart.2021.651731

Melles, M., Brigham-Grette, J., Minyuk, P. S., Nowaczyk, N. R., Wennrich, V., DeConto, R. M., Anderson, P. M., Andreev, A. A., Coletti, A., & Cook, T. L., 2012. 2.8 million years of Arctic climate change from Lake El'gygytgyn, NE Russia. *Science, 337*(6092), 315-320. https://doi.org/10.1126/science.1222135

Merlivat, L., & Jouzel, J., 1979. Global Climatic Interpretation of the Deuterium-Oxygen 18 Relationship for Precipitation. *Journal of Geophysical Research: Oceans, 84*(C8), 5029-5033. https://doi.org/10.1029/JC084iC08p05029

Mikkonen, S., Laine, M., Mäkelä, H., Gregow, H., Tuomenvirta, H., Lahtinen, M., & Laaksonen, A., 2015. Trends in the average temperature in Finland, 1847–2013. *Stochastic Environmental Research and Risk Assessment, 29*(6), 1521-1529. https://doi.org/10.1007/s00477-014-0992-2

Morrill, C., Meador, E., Livneh, B., Liefert, D. T., & Shuman, B. N., 2019. Quantitative model-data comparison of mid-Holocene lake-level change in the central Rocky Mountains. *Climate dynamics, 53*(1), 1077-1094. https://doi.org/10.1007/s00382-019-04633-3

Müller, J., Werner, K., Stein, R., Fahl, K., Moros, M., & Jansen, E., 2012. Holocene cooling culminates in sea ice oscillations in Fram Strait. *Quaternary Science Reviews, 47*, 1-14. https://doi.org/10.1016/j.quascirev.2012.04.024

National Snow and Ice Data Center. 2019. SOTC: Sea ice. Retrieved from http://nsidc.org/cryosphere/sotc/sea_ice.html

Nichols, J. E., Walcott, M., Bradley, R., Pilcher, J., & Huang, Y., 2009. Quantitative assessment of precipitation seasonality and summer surface wetness using ombrotrophic sediments from an Arctic Norwegian peatland. *Quaternary Research, 72*(3), 443-451. https://doi.org/10.1016/j.yqres.2009.07.007

Nordli, Ø., Wyszyński, P., Gjelten, H., Isaksen, K., Łupikasza, E., Niedźwiedź, T., & Przybylak, R., 2020. Revisiting the extended Svalbard Airport monthly temperature series, and the compiled corresponding daily series 1898–2018. https://doi.org/10.33265/polar.v39.3614

Norwegian Polar Institute, 2014. *Terrengmodell Svalbard (S0 Terrengmodell)*. Norwegian Polar Institute. https://doi.org/10.21334/npolar.2014.dce53a47

Nusbaumer, J., Alexander, P. M., LeGrande, A. N., & Tedesco, M., 2019. Spatial shift of Greenland moisture sources related to enhanced Arctic warming. *Geophysical research letters, 46*(24), 14723-14731. https://doi.org/10.1029/2019GL084633

Paillard, D., Labeyrie, L., & Yiou, P., 1996. AnalySeries 1.0: a Macintosh software for the analysis of geophysical time-series. *Eos, 77*, 379. https://doi.org/10.1029/96EO00259

Papritz, L., & Sodemann, H., 2018. Characterizing the local and intense water cycle during a cold air outbreak in the Nordic seas. *Monthly Weather Review, 146*(11), 3567-3588. https://doi.org/10.1175/MWR-D-18-0172.1

Parnell, A., & Inger, R., 2016. Simmr: a stable isotope mixing model. R package version 0.3. R. Available at https://CRAN.R-project.org/package=simmr

Pohjola, V. A., & Rogers, J. C., 1997. Atmospheric circulation and variations in Scandinavian glacier mass balance. *Quaternary Research, 47*(1), 29-36. https://doi.org/10.1006/qres.1996.1859

R Core Team. 2021. R: A language and environment for statistical computing. R Foundation for Statistical Computing, Vienna, Austria. 2016. Retrieved from https://www.R-project.org/

Rach, O., Kahmen, A., Brauer, A., & Sachse, D., 2017. A dual-biomarker approach for quantification of changes in relative humidity from sedimentary lipid D⁄H ratios. *Climate of the Past, 13*(7), 741-757. https://doi.org/10.5194/cp-13-741-2017

Rasmussen, T. L., & Thomsen, E., 2004. The role of the North Atlantic Drift in the millennial timescale glacial climate fluctuations. *Palaeogeography, Palaeoclimatology, Palaeoecology, 210*(1), 101-116. https://doi.org/10.1016/j.palaeo.2004.04.005

Rawlins, M. A., Steele, M., Holland, M. M., Adam, J. C., Cherry, J. E., Francis, J. A., Groisman, P. Y., Hinzman, L. D., Huntington, T. G., & Kane, D. L., 2010. Analysis of the Arctic system for freshwater cycle intensification: Observations and expectations. *Journal of Climate, 23*(21), 5715-5737. https://doi.org/10.1175/2010JCLI3421.1

Reimer, P. J., Austin, W. E., Bard, E., Bayliss, A., Blackwell, P. G., Ramsey, C. B., Butzin, M., Cheng, H., Edwards, R. L., & Friedrich, M., 2020. The IntCal20 Northern Hemisphere radiocarbon age calibration curve (0–55 cal kBP). *Radiocarbon, 62*(4), 725-757. https://doi.org/10.1017/RDC.2020.41

Reimer, P. J., Bard, E., Bayliss, A., Beck, J. W., Blackwell, P. G., Ramsey, C. B., Buck, C. E., Cheng, H., Edwards, R. L., & Friedrich, M., 2013. IntCal13 and Marine13 radiocarbon age calibration curves 0-50,000 years cal BP. *Radiocarbon, 55*(4), 1869-1887. https://doi.org/10.2458/azu_js_rc.55.16947

Risebrobakken, B., Jansen, E., Andersson, C., Mjelde, E., & Hevrøy, K., 2003. A high-resolution study of Holocene paleoclimatic and paleoceanographic changes in the Nordic Seas. *Paleoceanography, 18*(1). https://doi.org/10.1029/2002PA000764

Rogers, J. C., 1984. The association between the North Atlantic Oscillation and the Southern Oscillation in the northern hemisphere. *Monthly Weather Review, 112*(10), 1999-2015. https://doi.org/10.1175/1520-0493(1984)112<1999:TABTNA>2.0.CO;2

Rogers, J. C., Yang, L., & Li, L., 2005. The role of Fram Strait winter cyclones on sea ice flux and on Spitsbergen air temperatures. *Geophysical research letters, 32*(6). https://doi.org/10.1029/2004GL022262

Rosqvist, G. C., Leng, M. J., Goslar, T., Sloane, H. J., Bigler, C., Cunningham, L., Dadal, A., Bergman, J., Berntsson, A., & Jonsson, C., 2013. Shifts in precipitation during the last millennium in northern Scandinavia from lacustrine isotope records. *Quaternary Science Reviews, 66*, 22-34. https://doi.org/10.1016/j.quascirev.2012.10.030

Rozanski, K., Araguás-Araguás, L., & Gonfiantini, R., 1993. Isotopic patterns in modern global precipitation. In Swart, P.K., Lohmann, K.C., Mckenzie, J., Savin, S. (Eds.), *Climate change in continental isotopic records.* Geophysical Monograph Series 78, 1-36

Ruosteenoja, K., Jylhä, K., & Kämäräinen, M., 2016. Climate projections for Finland under the RCP forcing scenarios. *Geophysica, 51*.

Røthe, T. O., Bakke, J., Støren, E. W., & Bradley, R. S., 2018. Reconstructing Holocene glacier and climate fluctuations from lake sediments in Vårfluesjøen, northern Spitsbergen. *Frontiers in Earth Science, 6*. https://doi.org/10.3389/feart.2018.00091

Røthe, T. O., Bakke, J., Vasskog, K., Gjerde, M., D'Andrea, W. J., & Bradley, R. S., 2015. Arctic Holocene glacier fluctuations reconstructed from lake sediments at Mitrahalvøya, Spitsbergen. *Quaternary Science Reviews, 109*, 111-125. https://doi.org/10.1016/j.quascirev.2014.11.017

Sachse, D., Billault, I., Bowen, G. J., Chikaraishi, Y., Dawson, T. E., Feakins, S. J., Freeman, K. H., Magill, C. R., McInerney, F. A., van der Meer, M. T. J., Polissar, P., Robins, R. J., Sachs, J. P., Schmidt, H.-L., Sessions, A. L., White, J. W. C., West, J. B., & Kahmen, A., 2012. Molecular Paleohydrology: Interpreting the Hydrogen-Isotopic Composition of Lipid Biomarkers from Photosynthesizing Organisms. *Annual Review of Earth and Planetary Sciences, 40*(1), 221-249. https://doi.org/10.1146/annurev-earth-042711-105535

Sachse, D., Radke, J., & Gleixner, G., 2004. Hydrogen isotope ratios of recent lacustrine sedimentary n-alkanes record modern climate variability. *Geochimica et Cosmochimica Acta, 68*(23), 4877-4889. https://doi.org/10.1016/j.gca.2004.06.004

Sachse, D., Radke, J., & Gleixner, G., 2006. δD values of individual n-alkanes from terrestrial plants along a climatic gradient - Implications for the sedimentary biomarker record. *Organic Geochemistry, 37*(4), 469-483. https://doi.org/10.1016/j.orggeochem.2005.12.003

Sand, K., Winther, J.-G., Maréchal, D., Bruland, O., & Melvold, K., 2003. Regional Variations of Snow Accumulation on Spitsbergen, Svalbard, 1997-99. *Hydrology Research, 34*(1-2), 17-32. https://doi.org/10.2166/nh.2003.0026

Schomacker, A., Brynjólfsson, S., Andreassen, J. M., Gudmundsdóttir, E. R., Olsen, J., Odgaard, B. V., Håkansson, L., Ingólfsson, Ó., & Larsen, N. K., 2016. The

Drangajökull ice cap, northwest Iceland, persisted into the early-mid Holocene. *Quaternary Science Reviews, 148*, 68-84. https://doi.org/10.1016/j.quascirev.2016.07.007

Schomacker, A., Farnsworth, W. R., Ingólfsson, Ó., Allaart, L., Håkansson, L., Retelle, M., Siggaard-Andersen, M.-L., Korsgaard, N. J., Rouillard, A., & Kjellman, S. E., 2019. Postglacial relative sea level change and glacier activity in the early and late Holocene: Wahlenbergfjorden, Nordaustlandet, Svalbard. *Scientific reports, 9*(1), 1-13. https://doi.org/10.1038/s41598-019-43342-z

Screen, J. A., & Simmonds, I., 2010. The central role of diminishing sea ice in recent Arctic temperature amplification. *Nature, 464*(7293), 1334-1337. https://doi.org/10.1038/nature09051

Seppä, H., & Birks, H. J. B., 2001. July mean temperature and annual precipitation trends during the Holocene in the Fennoscandian tree-line area: pollen-based climate reconstructions. *The Holocene, 11*(5), 527-539. https://doi.org/10.1191/095968301680223486

Serreze, M., Barrett, A., Stroeve, J., Kindig, D., & Holland, M., 2009. The emergence of surface-based Arctic amplification. *The Cryosphere, 3*(1), 11-19. https://doi.org/10.5194/tc-3-11-2009

Serreze, M., Box, J., Barry, R., & Walsh, J., 1993. Characteristics of Arctic synoptic activity, 1952–1989. *Meteorology and Atmospheric Physics, 51*(3), 147-164. https://doi.org/10.1007/BF01030491

Serreze, M. C., & Barry, R. G., 2014. *The Arctic climate system*. Cambridge University Press, 404 pp.

Sessions, A. L., Burgoyne, T. W., Schimmelmann, A., & Hayes, J. M., 1999. Fractionation of hydrogen isotopes in lipid biosynthesis. *Organic Geochemistry, 30*(9), 1193-1200. https://doi.org/10.1016/S0146-6380(99)00094-7

Shanahan, T. M., Hughen, K. A., Ampel, L., Sauer, P. E., & Fornace, K., 2013. Environmental controls on the $^{2}H/^{1}H$ values of terrestrial leaf waxes in the eastern Canadian Arctic. *Geochimica et Cosmochimica Acta, 119*, 286-301. https://doi.org/10.1016/j.gca.2013.05.032

Shapiro, M., Fedor, L., & Hampel, T., 1987. Research aircraft measurements of a polar low over the Norwegian Sea. *Tellus A: Dynamic Meteorology and Oceanography, 39*(4), 272-306. https://doi.org/10.3402/tellusa.v39i4.11761

Singh, H. K., Bitz, C. M., Donohoe, A., & Rasch, P. J., 2017. A source-receptor perspective on the polar hydrologic cycle: Sources, seasonality, and Arctic-Antarctic parity in the hydrologic cycle response to CO_2 doubling. *Journal of Climate, 30*(24), 9999-10017. https://doi.org/10.1175/JCLI-D-16-0917.1

Skagseth, Ø., Furevik, T., Ingvaldsen, R., Loeng, H., Mork, K. A., Orvik, K. A., & Ozhigin, V., 2008. Volume and heat transports to the Arctic Ocean via the Norwegian and Barents Seas. In Dickson, R.R., Meincke, J., Rhines, P. (Eds.), *Arctic–Subarctic Ocean Fluxes* (pp. 45-64): Springer, Dordrecht. https://doi.org/10.1007/978-1-4020-6774-7_3

Skakun, A. A., Chikhachev, K. B., Ekaykin, A. A., Kozachek, A. V., Vladimirova, D. O., Veres, A. N., Verkulich, S. R., Sidorova, O. R., & Demidov, N. E., 2020. Stable isotopic composition of atmospheric precipitation and natural waters in the vicinity of Barentsburg (Svalbard). *Лёд и Снег, 60*(3), 379-394. https://doi.org/10.31857/S2076673420030046

Sodemann, H., Masson-Delmotte, V., Schwierz, C., Vinther, B., & Wernli, H., 2008a. Interannual variability of Greenland winter precipitation sources: 2. Effects of North

Atlantic Oscillation variability on stable isotopes in precipitation. *Journal of Geophysical Research: Atmospheres, 113*(D12). https://doi.org/10.1029/2007JD009416

Sodemann, H., Schwierz, C., & Wernli, H., 2008b. Interannual variability of Greenland winter precipitation sources: Lagrangian moisture diagnostic and North Atlantic Oscillation influence. *Journal of Geophysical Research: Atmospheres, 113*(D3). https://doi.org/10.1029/2007JD008503

Solomina, O. N., Bradley, R. S., Hodgson, D. A., Ivy-Ochs, S., Jomelli, V., Mackintosh, A. N., Nesje, A., Owen, L. A., Wanner, H., & Wiles, G. C., 2015. Holocene glacier fluctuations. *Quaternary Science Reviews, 111*, 9-34. https://doi.org/10.1016/j.quascirev.2014.11.018

Sundqvist, H. S., Kaufman, D. S., McKay, N., Balascio, N., Briner, J., Cwynar, L., Sejrup, H., Seppä, H., Subetto, D., & Andrews, J., 2014. Arctic Holocene proxy climate database - new approaches to assessing geochronological accuracy and encoding climate variables. *Climate of the Past, 10*(4), 1605-1631. https://doi.org/10.5194/cp-10-1605-2014

Svendsen, J. I., & Mangerud, J., 1997. Holocene glacial and climatic variations on Spitsbergen, Svalbard. *The Holocene, 7*(1), 45-57. https://doi.org/10.1177/095968369700700105

Swann, A. L., Fung, I. Y., Levis, S., Bonan, G. B., & Doney, S. C., 2010. Changes in Arctic vegetation amplify high-latitude warming through the greenhouse effect. *Proceedings of the National Academy of Sciences, 107*(4), 1295-1300. https://doi.org/10.1073/pnas.0913846107

Thienemann, M., Kusch, S., Vogel, H., Ritter, B., Schefuß, E., & Rethemeyer, J., 2019. Neoglacial transition of atmospheric circulation patterns over Fennoscandia recorded in Holocene Lake Torneträsk sediments. *Boreas, 48*(2), 287-298. https://doi.org/10.1111/bor.12365

Thomas, E., Castañeda, I., McKay, N., Briner, J., Salacup, J., Nguyen, K., & Schweinsberg, A., 2018. A wetter Arctic coincident with hemispheric warming 8,000 years ago. *Geophysical research letters, 45*(19), 10,637-610,647. https://doi.org/10.1029/2018GL079517

Thomas, E. K., Briner, J. P., Ryan-Henry, J. J., & Huang, Y., 2016. A major increase in winter snowfall during the middle Holocene on western Greenland caused by reduced sea ice in Baffin Bay and the Labrador Sea. *Geophysical research letters, 43*(10), 5302-5308. https://doi.org/10.1002/2016GL068513

Thomas, E. K., Hollister, K. V., Cluett, A. A., Corcoran, M. C., & Briner, J. P., 2020. Reconstructing Arctic precipitation seasonality using aquatic leaf wax δ^2H in lakes with contrasting residence times. *Paleoceanography and Paleoclimatology, 35*(7), e2020PA003886. https://doi.org/10.1029/2020PA003886

Thomas, E. K., McGrane, S., Briner, J. P., & Huang, Y., 2012. Leaf wax δ^2H and varve-thickness climate proxies from proglacial lake sediments, Baffin Island, Arctic Canada. *Journal of Paleolimnology, 48*(1), 193-207. https://doi.org/10.1007/s10933-012-9584-7

Thompson, D. W., & Wallace, J. M., 1998. The Arctic Oscillation signature in the wintertime geopotential height and temperature fields. *Geophysical research letters, 25*(9), 1297-1300. https://doi.org/10.1029/98GL00950

Throckmorton, H. M., Newman, B. D., Heikoop, J. M., Perkins, G. B., Feng, X., Graham, D. E., O'Malley, D., Vesselinov, V. V., Young, J., & Wullschleger, S. D., 2016. Active layer hydrology in an arctic tundra ecosystem: quantifying water sources and cycling

using water stable isotopes. *Hydrological processes, 30*(26), 4972-4986. https://doi.org/10.1002/hyp.10883
Tondu, J., Turner, K., Wolfe, B., Hall, R., Edwards, T., & McDonald, I., 2013. Using water isotope tracers to develop the hydrological component of a long-term aquatic ecosystem monitoring program for a northern lake-rich landscape. *Arctic, Antarctic, and Alpine Research, 45*(4), 594-614. https://doi.org/10.1657/1938-4246-45.4.594
Uvo, C. B., 2003. Analysis and regionalization of northern European winter precipitation based on its relationship with the North Atlantic Oscillation. *International Journal of Climatology: A Journal of the Royal Meteorological Society, 23*(10), 1185-1194. https://doi.org/10.1002/joc.930
van der Bilt, W. G., D'Andrea, W. J., Bakke, J., Balascio, N. L., Werner, J. P., Gjerde, M., & Bradley, R. S., 2018. Alkenone-based reconstructions reveal four-phase Holocene temperature evolution for High Arctic Svalbard. *Quaternary Science Reviews, 183*, 204-213. https://doi.org/10.1016/j.quascirev.2016.10.006
van der Bilt, W. G., DAndrea, W. J., Werner, J. P., & Bakke, J., 2019. Early Holocene temperature oscillations exceed amplitude of observed and projected warming in Svalbard lakes. *Geophysical research letters*. https://doi.org/10.1029/2019GL084384
van der Bilt, W. G. M., Lane, C. S., & Bakke, J., 2017. Ultra-distal Kamchatkan ash on Arctic Svalbard: Towards hemispheric cryptotephra correlation. *Quaternary Science Reviews, 164*, 230-235. https://doi.org/10.1016/j.quascirev.2017.04.007
van der Knaap, W., 1987. Long-distance transported pollen and spores on Spitsbergen and Jan Mayen. *Pollen et Spores, 29*(4), 449-453.
van Geldern, R., & Barth, J. A., 2012. Optimization of instrument setup and post-run corrections for oxygen and hydrogen stable isotope measurements of water by isotope ratio infrared spectroscopy (IRIS). *Limnology and Oceanography: Methods, 10*(12), 1024-1036. https://doi.org/10.4319/lom.2012.10.1024
van Pelt, W. J. J., Kohler, J., Liston, G. E., Hagen, J. O., Luks, B., Reijmer, C. H., & Pohjola, V. A., 2016. Multidecadal climate and seasonal snow conditions in Svalbard. *Journal of Geophysical Research: Earth Surface, 121*(11), 2100-2117. https://doi.org/10.1002/2016jf003999
Viau, A. E., & Gajewski, K., 2009. Reconstructing millennial-scale, regional paleoclimates of boreal Canada during the Holocene. *Journal of Climate, 22*(2), 316-330. https://doi.org/10.1175/2008JCLI2342.1
Vick, L. M., Mikkelsen, M., Corner, G. D., Kjellman, S. E., Trønnes, L., Hormes, A., Allaart, L., & Bergh, S. G., 2022. Evolution and temporal constraints of a multiphase postglacial rock slope failure. *Geomorphology, 398*, 108069. https://doi.org/10.1016/j.geomorph.2021.108069
Voldstad, L. H., Alsos, I. G., Farnsworth, W. R., Heintzman, P. D., Håkansson, L., Kjellman, S. E., Rouillard, A., Schomacker, A., & Eidesen, P. B., 2020. A complete Holocene lake sediment ancient DNA record reveals long-standing high Arctic plant diversity hotspot in northern Svalbard. *Quaternary Science Reviews, 234*, 106207. https://doi.org/10.1016/j.quascirev.2020.106207
Walczowski, W., & Piechura, J., 2011. Influence of the West Spitsbergen Current on the local climate. *International Journal of Climatology, 31*(7), 1088-1093. https://doi.org/10.1002/joc.2338
Werner, K., Müller, J., Husum, K., Spielhagen, R. F., Kandiano, E. S., & Polyak, L., 2016. Holocene sea subsurface and surface water masses in the Fram Strait–Comparisons of temperature and sea-ice reconstructions. *Quaternary Science Reviews, 147*, 194-209. https://doi.org/10.1016/j.quascirev.2015.09.007

Werner, M., Heimann, M., & Hoffmann, G., 2001. Isotopic composition and origin of polar precipitation in present and glacial climate simulations. *Tellus B: Chemical and Physical Meteorology, 53*(1), 53-71. https://doi.org/10.3402/tellusb.v53i1.16539

Wickström, S., Jonassen, M., Vihma, T., & Uotila, P., 2020. Trends in cyclones in the high-latitude North Atlantic during 1979-2016. *Quarterly Journal of the Royal Meteorological Society, 146*(727), 762-779. https://doi.org/10.1002/qj.3707

Wilkie, K., Chapligin, B., Meyer, H., Burns, S., Petsch, S., & Brigham-Grette, J., 2013. Modern isotope hydrology and controls on δD of plant leaf waxes at Lake El'gygytgyn, NE Russia. *Climate of the Past, 9*(1), 335-352. https://doi.org/10.5194/cp-9-335-2013

Wolfe, A. P., Miller, G. H., Olsen, C. A., Forman, S. L., Doran, P. T., & Holmgren, S. U., 2004. Geochronology of high latitude lake sediments. *Long-term environmental change in Arctic and Antarctic lakes*, 19-52. https://doi.org/10.1007/978-1-4020-2126-8_2

Wolfe, B. B., Edwards, T. W., Aravena, R., Forman, S. L., Warner, B. G., Velichko, A. A., & MacDonald, G. M., 2000. Holocene paleohydrology and paleoclimate at treeline, north-central Russia, inferred from oxygen isotope records in lake sediment cellulose. *Quaternary Research, 53*(3), 319-329. https://doi.org/10.1006/qres.2000.2124

Wolfe, B. B., Edwards, T. W., Aravena, R., & MacDonald, G. M., 1996. Rapid Holocene hydrologic change along boreal treeline revealed by $\delta^{13}C$ and $\delta^{18}O$ in organic lake sediments, Northwest Territories, Canada. *Journal of Paleolimnology, 15*(2), 171-181. https://doi.org/10.1007/BF00196779

Wooller, M. J., Francis, D., Fogel, M. L., Miller, G. H., Walker, I. R., & Wolfe, A. P., 2004. Quantitative paleotemperature estimates from $\delta^{18}O$ of chironomid head capsules preserved in arctic lake sediments. *Journal of Paleolimnology, 31*(3), 267-274. https://doi.org/10.1023/B:JOPL.0000021944.45561.32

Zhang, X., Walsh, J. E., Zhang, J., Bhatt, U. S., & Ikeda, M., 2004. Climatology and interannual variability of Arctic cyclone activity: 1948–2002. *Journal of Climate, 17*(12), 2300-2317. https://doi.org/10.1175/1520-0442(2004)017<2300:CAIVOA>2.0.CO;2

Østby, T. I., Schuler, T. V., Hagen, J. O., Hock, R., Kohler, J., & Reijmer, C. H., 2017. Diagnosing the decline in climatic mass balance of glaciers in Svalbard over 1957–2014. *The Cryosphere, 11*(1), 191-215. https://doi.org/10.5194/tc-11-191-2017

Årthun, M., Eldevik, T., Viste, E., Drange, H., Furevik, T., Johnson, H. L., & Keenlyside, N. S., 2017. Skillful prediction of northern climate provided by the ocean. *Nature communications, 8*(1), 1-11. https://doi.org/10.1038/ncomms15875

Paper I

Quaternary Science Reviews 240 (2020) 106388

Contents lists available at ScienceDirect

Quaternary Science Reviews

journal homepage: www.elsevier.com/locate/quascirev

Holocene precipitation seasonality in northern Svalbard: Influence of sea ice and regional ocean surface conditions

Sofia E. Kjellman [a, *], Anders Schomacker [a], Elizabeth K. Thomas [b], Lena Håkansson [c], Sandrine Duboscq [b], Allison A. Cluett [b], Wesley R. Farnsworth [c, d], Lis Allaart [a], Owen C. Cowling [b], Nicholas P. McKay [e], Skafti Brynjólfsson [f], Ólafur Ingólfsson [g]

[a] Department of Geosciences, UiT The Arctic University of Norway, Postboks 6050 Langnes, N-9037 Tromsø, Norway
[b] Department of Geology, University at Buffalo, State University of New York, 126 Cooke Hall, Buffalo, NY 14260, USA
[c] Department of Arctic Geology, The University Centre in Svalbard (UNIS), P.O. Box 156, N-9171 Longyearbyen, Norway
[d] Nordic Volcanological Center, Institute of Earth Sciences, University of Iceland, Askja, Sturlugata 7, IS-101 Reykjavík, Iceland
[e] School of Earth and Sustainability, Northern Arizona University, NAU Box 4099, Flagstaff, AZ 86011, USA
[f] Icelandic Institute of Natural History, Borgum við Norðurslóð, IS-600 Akureyri, Iceland
[g] Faculty of Earth Sciences, University of Iceland, Sturlugata 7, IS-101 Reykjavík, Iceland

ARTICLE INFO

Article history:
Received 22 February 2020
Received in revised form
21 May 2020
Accepted 22 May 2020
Available online xxx

Keywords:
Lake sediment
Biomarkers
Hydrogen isotopes
n-alkanoic acids
Precipitation seasonality
Paleoclimatology
Sea ice
Quaternary
Arctic

ABSTRACT

Arctic precipitation is predicted to increase in the coming century, due to a combination of enhanced northward atmospheric moisture transport and local surface evaporation from ice-free seas. However, large model uncertainties, limited long-term observations, and high spatiotemporal variability limit our understanding of these mechanisms, emphasizing the need for paleoclimate records of precipitation changes. Here we use lipid biomarkers in lake sediments to reconstruct precipitation seasonality in northern Spitsbergen, Svalbard. We measured the hydrogen isotopic ratios (δ^2H) of *n*-alkanoic acids (C_{20} –C_{30}) from sedimentary leaf waxes in lake Austre Nevlingen, Spitsbergen. We interpret δ^2H values of mid-chain (C_{22}) and long-chain (C_{28}) *n*-alkanoic acids to represent δ^2H of lake and soil water, respectively. Austre Nevlingen lake water δ^2H reflects amount-weighted mean annual precipitation δ^2H. In contrast, soil water is mostly recharged by summer rainfall, and therefore reflects δ^2H values of summer precipitation. Austre Nevlingen leaf wax δ^2H values are ^2H-depleted in the Early Holocene, suggesting high winter precipitation amounts. This coincides with high summer insolation, strong Atlantic water advection and reduced spring sea-ice cover in surrounding waters. Winter precipitation continued to dominate until *c.* 6 cal. kyr BP. After 6 cal. kyr BP, the trend in the biomarker record is not as clear. This could be related to colder conditions causing longer duration of seasonal lake-ice cover, thereby influencing the precipitation seasonality registered by the lake water. The Austre Nevlingen record suggests a close relationship between precipitation seasonality and regional ocean surface conditions, consistent with simulations suggesting that Arctic winter sea-ice loss will lead to increased local evaporation.

1. Introduction

By the end of the 21st century, warming in the Arctic is predicted to exceed the global average by a factor of 2.2–2.4 (Collins et al., 2013). This amplified warming will affect the amount and seasonality of precipitation, through hydrological intensification (Rawlins et al., 2010; Collins et al., 2013; Bintanja and Selten, 2014). Increased high-latitude precipitation can be caused by 1) atmospheric circulation changes and enhanced poleward moisture transport, mechanisms mainly influencing summer precipitation (Dickson et al., 2000; Zhang et al., 2013), and 2) increased local surface evaporation, due to warmer Arctic seas and reduced winter sea-ice cover, mainly influencing fall and winter precipitation (Bintanja and Selten, 2014; Kopec et al., 2016). A warmer atmosphere also causes a larger fraction of Arctic precipitation to fall as rain (Førland et al., 2020). These hydrological changes will impact Arctic ecosystems, glacier mass balance, and infrastructure (Bintanja and Andry, 2017; Adakudlu et al., 2019). In order to better assess

* Corresponding author. UiT The Arctic University of Norway, Department of Geosciences, Postbox 6050 Langnes, N-9037 Tromsø, Norway.
E-mail address: sofia.e.kjellman@uit.no (S.E. Kjellman).

https://doi.org/10.1016/j.quascirev.2020.106388

future Arctic precipitation changes, we need improved understanding of the mechanisms causing precipitation variation in the past (Sundqvist et al., 2014; Linderholm et al., 2018). In the absence of instrumental data, paleoclimate (proxy) data are necessary to fill this critical knowledge gap.

Previous reconstructions of the Holocene climate history of Svalbard have mainly focused on temperature. During the beginning of the Holocene (11.7–9 cal. kyr BP), Svalbard experienced warmer-than-present conditions, recorded by alkenones (van der Bilt et al., 2019) and thermophilous mollusks (Mangerud and Svendsen, 2018). Furthermore, glaciers were smaller (Mangerud and Svendsen, 1990; Svendsen and Mangerud, 1997; Røthe et al., 2018) and the sea-ice cover in surrounding waters reduced (Werner et al., 2016; Allaart et al., 2020). Other studies have described Early Holocene re-advances for glaciers on Svalbard (Lønne, 2005; Henriksen et al., 2014; van der Bilt et al., 2015; Farnsworth et al., 2017, 2018; Larsen et al., 2018). There are speculations if enhanced Early Holocene precipitation drove these glacier oscillations (Farnsworth, 2018). The Early Holocene warming was abrupt and could be explained by influx of warm Atlantic water (AW; Risebrobakken et al., 2011; Werner et al., 2016), peak summer insolation (Laskar et al., 2004) or a combination of both. According to Werner et al. (2016), eastern Fram Strait subsurface temperatures remained warm during the Mid Holocene until *c.* 5 cal. kyr BP, with increasing sea-ice cover from *c.* 7 cal. kyr BP. In central Spitsbergen, a stepwise cooling began already around 9 cal. kyr BP (Rasmussen et al., 2012). The Late Holocene was characterized by Neoglacial cooling from *c.* 4–3 cal. kyr BP, inferred from increased glacier activity (Svendsen and Mangerud, 1997; Røthe et al., 2015, 2018; Miller et al., 2017; Bartels et al., 2018; Lovell et al., 2018). A later cooling step, associated with the Little Ice Age, started around 0.7 cal. kyr BP (Werner, 1993; van der Bilt et al., 2015; Miller et al., 2017).

Robust records of Holocene precipitation amount and seasonality are lacking. Leaf wax hydrogen isotope ratios (δ^2H) provide means to evaluate hydrological changes over long time scales. The potential of the method for high-latitude lacustrine records has been demonstrated in Arctic Canada (Thomas et al., 2012), Greenland (Balascio et al., 2013; Thomas et al., 2016, 2018), Svalbard (Balascio et al., 2018) and northeastern Russia (Wilkie, 2012).

Leaf waxes are straight-chain hydrocarbon compounds produced by both terrestrial and aquatic plants. The *n*-alkanoic acid and *n*-alkane components of leaf waxes are well-preserved in sedimentary records due to their resistance to degradation (Eglinton and Calvin, 1967). Terrestrial plants predominantly produce long-chain wax compounds, whereas aquatic plants produce mid-chain wax compounds (Ficken et al., 2000; Meyers, 2003; Nichols et al., 2009; Gao et al., 2011). The δ^2H values of leaf waxes reflect the δ^2H values of the plant source water, with a biosynthetic fractionation that is largely constant for specific compounds (Sachse et al., 2012; McFarlin et al., 2019). The source water for terrestrial plants is soil water, which is mostly recharged by summer rainfall (Cooper et al., 1991; Throckmorton et al., 2016). The hydrogen isotope ratios of terrestrial leaf waxes (δ^2H_{terr}) therefore reflects summer precipitation isotope values, influenced by some evaporative enrichment of soil and leaf water (Kahmen et al., 2013). In contrast, the source water for aquatic plants is lake water, which may reflect summer or mean annual precipitation δ^2H values, depending on the residence time and source of lake water (Cluett and Thomas, 2020; Thomas et al., 2020). Hence, leaf wax δ^2H can be used to reconstruct source water δ^2H and ultimately δ^2H of precipitation and other aspects of climate, including evaporation (Rach et al., 2017). The δ^2H of precipitation is influenced by changes in local and source temperature, moisture source location and transport history (Frankenberg et al., 2009), as well as evaporation for terrestrial waxes (e.g., Sachse et al., 2012; Thomas et al., 2016, 2018).

The hydrogen isotope ratios of aquatic plant leaf waxes (δ^2H_{aq}) reflect the isotopic composition of the lake water during the growing season. Therefore, the precipitation isotope seasonality recorded by δ^2H_{aq} (annual mean or summer) depends on the local conditions determining the residence time of the lake water (Thomas et al., 2020). Lakes with short residence times have growing season lake water δ^2H values biased towards summer precipitation δ^2H, whereas water isotopes from lakes with long residence times reflect amount-weighted mean annual precipitation δ^2H (Jonsson et al., 2009; Cluett and Thomas, 2020). Balascio et al. (2018) inferred that δ^2H_{aq} changes in lake Hakluytvatnet (Fig. 1), which has a short residence time (i.e., the lake water during the growing season reflects summer precipitation δ^2H), reflect air temperature and the relative influence of polar and sub-polar air masses. Here, we apply the same concept for another lake in northern Svalbard. By choosing a lake with a longer residence time (i.e., lake water isotopes representing mean annual precipitation δ^2H), we can extract information about seasonal variation in Arctic precipitation. We use δ^2H of C_{22} and C_{28} *n*-alkanoic acids to infer past lake water and leaf water δ^2H values, and reconstruct Holocene precipitation seasonality in northern Spitsbergen. By better constraining precipitation seasonality during earlier Holocene warm periods, we can improve our understanding of the mechanisms causing precipitation change in the past, present and in the future.

2. Setting

2.1. Regional setting

The Svalbard archipelago is influenced by strong climate gradients, with air masses transporting heat and moisture from the Atlantic regions meeting cold polar air from the Arctic Basin (Fig. 1a; Førland et al., 2009, 2011; Vikhamar-Schuler et al., 2019). South of Svalbard, the North Atlantic Current splits into the West Spitsbergen Current (WSC) and the North Cape Current (NCaC), transporting warm saline water along the west coast of Svalbard and eastward into the Barents Sea (Fig. 1a). The Barents Sea also receives colder, fresher water masses from the Arctic Ocean transported by the East Spitsbergen Current (ESC). During extreme cold events over the Barents Sea in winter, the strong temperature gradient between cold Arctic air and relatively warm Barents Sea surface water can cause convection and development of low-pressure systems (Rasmussen, 1985). Easterly winds caused by these systems bring moisture to eastern Svalbard, resulting in high precipitation (Hagen et al., 1993).

Since the establishment of the first permanent meteorological stations in Svalbard in the 1910s, temperatures have increased during all seasons, most notably in winter and spring (Førland et al., 2011). The trend in precipitation amount for the same period is not as clear. The robustness of instrumental precipitation data on Svalbard is hindered by 1) a lack of stations - especially in the central and eastern parts of the archipelago, and 2) measurement errors - notably due to snowdrift and undercatch (Førland and Hanssen-Bauer, 2000; Hanssen-Bauer, 2002; Humlum, 2002). However, instrumental records generally display positive trends in autumn and winter precipitation, and negative trends in summer and spring (Adakudlu et al., 2019). On an annual basis, all long precipitation amount time series from Svalbard (i.e., >40 yr) show positive trends, with precipitation increases between 2–8% per decade (Førland et al., 2011). Climate model projections for Svalbard agree that precipitation amount will increase in the future as temperature rises and sea ice retreats. Førland et al. (2011) projected an annual precipitation increase from 1961–1990 to

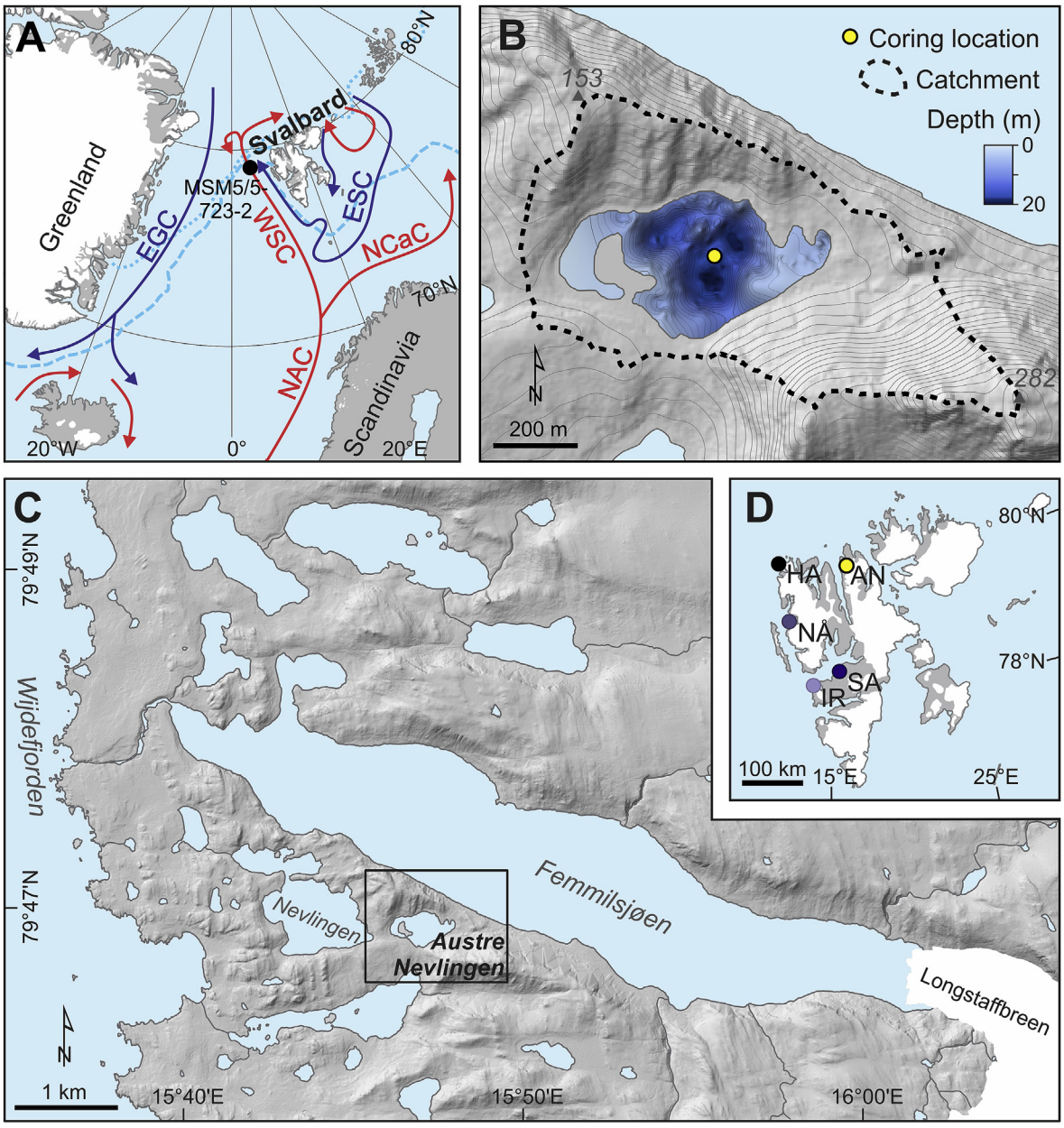

Fig. 1. (A) Map showing the location of Svalbard in the North Atlantic, with major ocean surface currents (warm currents in red, cold in dark blue; NAC = North Atlantic Current; NCaC = North Cape Current; WSC = West Spitsbergen Current; ESC = East Spitsbergen Current; EGC = East Greenland Current), median winter (light blue dashed line) and summer (light blue dotted line) sea-ice extent AD 1981–2010 (National Snow and Ice Data Center, 2019) and location of marine core MSM5/5-723-2 (Werner et al., 2016). (B) Lake Austre Nevlingen catchment, coring location and bathymetry. (C) Map of the study area in northern Spitsbergen. Black box indicates the Austre Nevlingen catchment, shown in (B). (D) Map of Svalbard, showing the locations of Austre Nevlingen (AN), Hakluytvatnet (HA) and meteorological stations (IR = Isfjord Radio; NÅ = Ny-Ålesund; SA = Svalbard Airport). (For interpretation of the references to color in this figure legend, the reader is referred to the Web version of this article.)

2071–2100 of less than 10% in southwestern Spitsbergen, but more than 40% in northeastern Svalbard. This regional climate model simulation was based on the MPIB2 scenario (Max Planck Institute global ECHAM4 model with SRES B2 emission scenario). Based on the RCP8.5 scenario ("business as usual"; Stocker et al., 2013), Adakudlu et al. (2019) projected a 65% annual precipitation increase in Spitsbergen from 1971–2000 to 2071–2100. In the same study, RCP4.5 (reductions after 2040, "medium emissions"; Stocker et al., 2013) gives a median annual precipitation increase of 45%. Both model projections indicate largest precipitation increases in northeastern Svalbard, with greatest change in winter (+54–90%) and least in summer (+27–48%; Adakudlu et al., 2019). The fact that all models agree that the greatest precipitation increases will occur in the northeast, highlights the precipitation sensitivity of our study area. Model uncertainties and high spatial and temporal variability in precipitation emphasize the need for paleoclimate records to elucidate the mechanisms causing precipitation variability on Svalbard.

2.2. Study area

Lake Austre Nevlingen is located 2 km east of the 108-km-long Wijdefjorden, close to the mouth of the fjord (Fig. 1). Wijdefjorden is associated with the Billefjorden Fault Zone, separating Devonian

sandstones and clastic sedimentary rocks in the west from Precambrian crystalline bedrock in the east (Dallmann, 2015). The landscape around Austre Nevlingen is characterized by undulating terrain with lakes in depressions (Fig. 1b and c). The timing of deglaciation of the study area remains poorly constrained. Cosmogenic exposure ages from Tyrkampen (450 m above sea level (a.s.l.), 25 km to the south), suggest that this highland area was ice free by 18.3 ± 1.2 to 17.9 ± 1.2 kyr ago (Hormes et al., 2013).

The closest meteorological stations to our study site are located in Ny-Ålesund (8 m a.s.l., 125 km SW of Austre Nevlingen), at Svalbard Airport (28 m a.s.l., 172 km S of Austre Nevlingen) and Isfjord Radio (7 m a.s.l., 198 km SSW of Austre Nevlingen; Fig. 1d). Ny-Ålesund mean annual air temperature (1990–2019, n = 30) is −4.2 °C and mean annual precipitation (1990–2019, n = 30) 477 mm, whereas corresponding values are −3.9 °C (n = 30) and 203 mm (n = 30) at Svalbard Airport, and −2.6 °C (n = 11) and 573 mm (n = 3) at Isfjord Radio (Fig. 2; MET Norway, 2020). Hagen et al. (1993) estimated annual precipitation in the Wijdefjorden area to be as low as 200 mm, based on available measurements from meteorological stations and glacier mass balance and equilibrium line altitude observations. Precipitation δ^2H in Ny-Ålesund and Isfjord Radio exhibits no significant seasonal trend (Fig. 2b; IAEA/WMO, 2019), with values close to the Global Meteoric Water Line (GMWL, $\delta^2H = 8 \times \delta^{18}O + 10$; Craig, 1961, Fig. 3). There are no measurements of precipitation isotopes in central Spitsbergen, but we would expect greater precipitation isotope seasonality at our study site. Ny-Ålesund and Isfjord Radio are close to open sea conditions all year round, whereas Wijdefjorden is less connected to the main moisture source pathway along the west coast, especially in winter (Fig. 1a).

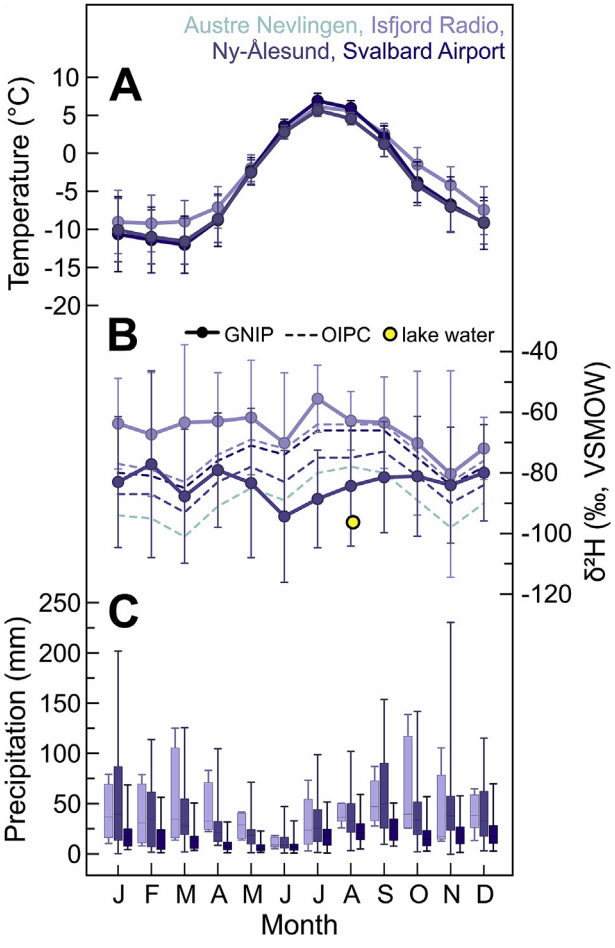

Fig. 2. Climate data from Svalbard Airport, Ny-Ålesund, Isfjord Radio and Austre Nevlingen. For locations, see Fig. 1. (A) Monthly average temperature calculated for all available data from the meteorological stations at Svalbard Airport, in Ny-Ålesund and Isfjord Radio for the period AD 1990–2019 (MET Norway, 2020), with 1σ standard deviations (vertical bars). (B) Global Network of Isotopes in Precipitation (GNIP; IAEA/WMO, 2019) δ^2H values from Isfjord Radio (AD 1960–1976) and Ny-Ålesund (AD 1990–2016), precipitation δ^2H for all sites (calculated using the Online Isotopes in Precipitation Calculator (OIPC); Bowen et al., 2005; Bowen, 2019; IAEA/WMO, 2019) and lake water δ^2H from Austre Nevlingen (2018). (C) Monthly average precipitation calculated for all available data from the meteorological stations Svalbard Airport, Ny-Ålesund and Isfjord Radio, for the period AD 1990–2019 (MET Norway, 2020). For each box plot, the middle line displays the median precipitation, the box represents the 25% to 75% quartile range and whiskers the maximum and minimum values.

The inner (southern) and middle parts of Wijdefjorden are classified as high-Arctic steppe, and have unique and high botanically diverse flora for Svalbard (Elvebakk and Nilsen, 2002; Elvebakk, 2005; Eidesen et al., 2018; Voldstad et al., 2020). The outer (northern) part is less vegetated and belongs to the Northern Arctic tundra zone (Norwegian Polar Institute, 2019). The vegetation in the north is dominated by graminoids (e.g., *Luzula confusa*, *Poa arctica*, *P. alpina*). Forbs are abundant (e.g., *Saxifraga oppositifolia*, *Cerastium arcticum*, *Oxyria digyna, Dryas octopetala*), mosses (e.g., *Tomentypnum nitens*, *Polytrichum, Racomitrium*) and lichens (e.g., *Flavocetraria*, *Stereocaulon*) are common, and dwarf shrubs (e.g., *Salix polaris*, *Cassiope tetragona*) are present (Walker et al., 2005). There are almost no aquatic vascular plants on Svalbard, but submerged bryophytes are common in lakes (Balascio et al., 2018; Voldstad et al., 2020).

2.3. Lake catchment

Austre Nevlingen (79°47′N, 15°47′E; Fig. 1) has a surface area of 0.13 km^2, a maximum depth of 18 m, and sits at an elevation of 41 m a.s.l. This is below the local marine limit, which can be estimated to *c.* 60 m a.s.l. based on reconstructed isobases of uplift (Forman, 1990). The Austre Nevlingen catchment is *c.* 0.48 km^2, sitting between 153 and 282 m a.s.l. summits (Fig. 1b). The catchment is dominated by frost-shattered bedrock and boulders with almost no soil cover, and dry non-vegetated to sparsely vegetated slopes. During the August 2015 and August 2018 field campaigns, we observed terrestrial vegetation dominated by graminoids (e.g., *Luzula confusa*) and mosses (e.g., *Polytrichum*). Submerged bryophytes, but no other aquatic plants, were observed growing in the

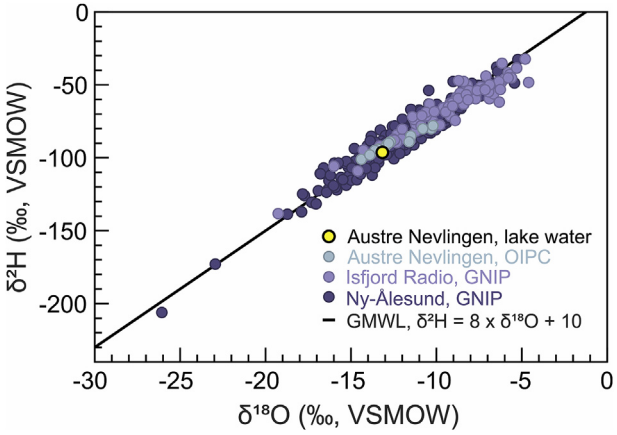

Fig. 3. Lake water isotope data from lake Austre Nevlingen (August 2018), precipitation isotope data from the GNIP stations (IAEA/WMO, 2019) at Isfjord Radio and in Ny-Ålesund, and calculated monthly precipitation δ^2H for Austre Nevlingen (OIPC; Bowen et al., 2005; Bowen, 2019; IAEA/WMO, 2019). Black line indicates the Global Meteoric Water Line (GMWL). For locations, see Fig. 1.

lake. The growing season is from mid-June to early September (ORNL DAAC, 2018) and the lake is estimated to be ice-covered from October to the beginning of July (Holm et al., 2012).

The lake is fed by surface runoff, but has no distinct inflow stream. There is also no distinct outflow stream on the surface. To estimate the proportion of lake water replaced annually and seasonally, we multiply the precipitation amount at Svalbard Airport during the different seasons (spring melt season = October to June, ice-free season = July to September) with the catchment area, and divide the product by the lake volume (Jonsson et al., 2009; Thomas et al., 2020). Svalbard Airport (Fig. 1d) has the most similar precipitation amount and seasonality to our study site. On average, approximately 11% of the lake volume is replaced each year: 7% during the spring melt season (i.e., by runoff representing precipitation from months with lake-ice cover) and 4% during the ice-free season (i.e., by runoff during the ice-free months). These values indicate a relatively long residence time, and that the lake water isotopes could be influenced by surface evaporation. Yet, isotope values of lake surface water collected in August 2018 indicate minimal evaporative enrichment. This surface water has a δ^2H value of -96.3 ± 0.2‰ and $\delta^{18}O$ of -13.2 ± 0.02‰ (Figs 2b and 3). The deuterium excess (d-excess = $\delta^2H - 8 \times \delta^{18}O$; Dansgaard, 1964) is 9.0‰. These values are well within the range of precipitation d-excess at Ny-Ålesund and Isfjord Radio (IAEA/WMO, 2019) and close to the GMWL (d-excess = 10‰). The lack of isotopic evidence for evaporative enrichment suggests that the lake water may be completely flushed each year (Cluett and Thomas, 2020), perhaps via subsurface runoff into the lake and subsurface drainage out of the lake through the frost-shattered bedrock. Lichen-free boulders up to 0.5 m above the current lake level indicate that the lake may have experienced higher water levels in the past, which could indicate subsurface drainage during periods of thawed active layer.

3. Methods

3.1. Bathymetry and sediment core collection

The bathymetry of Austre Nevlingen was surveyed in August 2018, with a Garmin ECHOMAP™ Plus 73SV with a CV52HW-TM transducer and a 5 Hz receiver, using the Quick Draw contour function. Coring in 2015 was guided in real-time with depth sounding data from a Hondex PS-7 Transducer. To minimize disturbance, sediment cores were obtained from the central, deepest part of the basin (Fig. 1b). Coring was performed through a hole in the floor of a small zodiac, which was anchored in a stable position on the lake surface. A 70-cm-long surface core (ANS1) was collected with a Universal surface corer (120 cm long and 68 mm diameter coring tubes). A 129-cm-long piston core (ANP3) was retrieved using a hand-held lightweight piston corer (200 cm long and 60 mm diameter coring tubes). To record modern conditions in the catchment, lake water and leaves from a selection of the most common plants growing in the area were collected in August 2018. Leaves were sampled from multiple plants of the same species to get representative samples, and chosen to represent different plant groups, including rushes (*Luzula confusa*), dwarf shrubs (*Salix polaris*), terrestrial mosses (*Polytrichum* sp.) and aquatic mosses (unidentified).

3.2. Lithology and stratigraphy

The lake sediment cores were split open, logged and analyzed in the sediment lab and ITRAX core facility at the University of Copenhagen. ITRAX scanning was performed to record visual and radiographic imagery and variations in the element-geochemical properties throughout the cores. A rhodium (Rh) tube with a 1 mm resolution and 30 s exposure time was used for X-ray fluorescence (XRF; e.g., Kylander et al., 2011) and 4 mm resolution for magnetic susceptibility (MS; e.g., Sandgren and Snowball, 2002). Information on the ITRAX core scanner is given by Croudace et al. (2006). We present the Ti signal and the Ca/Fe ratio to show variation in minerogenic input, as these can be used to detect glacial meltwater input (Kylander et al., 2011) and lake basin isolation (Larsen et al., 2017), respectively. The Ti peak area was normalized against the incoherent (inc) and coherent (coh) Rh scatter (Ti/(inc + coh)) to remove instrumental effects, as suggested by Kylander et al. (2011).

After scanning, the lithology and stratigraphy of the cores were visually inspected and logged. In order to determine whether the lowermost minerogenic unit was deposited in a marine or lacustrine environment, we searched for marine microfossils (e.g., foraminifera) using a stereo microscope. The total organic content was determined through loss-on-ignition (LOI; Heiri et al., 2001). For this purpose, samples (1 cm^3) were collected every 2 cm, dried at 110 °C for 24 h and ignited at 550 °C for 4 h.

3.3. Lipid biomarker extraction and analysis

Biogeochemical and isotopic analyses were performed in the Organic and Stable Isotope Biogeochemistry Laboratory at the University at Buffalo, NY, USA. Samples (3–4 cm^3) for lipid biomarker analysis were collected every 5–8 cm from ANS1 and every 4 cm from the organic part (i.e., the uppermost 97 cm) of ANP3, resulting in thirty-six samples for the composite record. The samples were freeze-dried and homogenized, and free lipids were extracted with an Accelerated Solvent Extractor (ASE) 200 (Dionex) using dichloromethane (DCM):methanol 9:1 (v:v). An internal standard ($C_{20:1}$ n-alkanoic acid, Fisher Scientific, 4.2 μg) was added to the total lipid extract (TLE) after ASE extraction, allowing biomarker quantification. Preparation for n-alkanoic acid analysis followed previously published methods (Thomas et al., 2012). Hydrocarbons were separated by flash-column chromatography using NH_2-functionalized silica gel, DCM:isopropanol 2:1 (v:v) as the neutral eluent and 4% acetic acid in DCM as the acid eluent. The acid fraction was methylated at 60 °C overnight using 5% anhydrous HCl in methanol of known isotopic composition, and purified using silica gel columns, removing hydroxyl-carboxylic acid esters with hexane and recovering the fatty acid methyl esters (FAMEs) in DCM.

The FAMEs were quantified using a Thermo Scientific Trace 1310 gas chromatograph (GC) equipped with two AI1310 autosamplers, two split/splitless injectors, and two flame ionization detectors (FIDs) operated in parallel for higher throughput. For all analyses, the inlets were held at 250 °C and operated in splitless mode for the first 45 s, after which split flow was turned on at 14 mL/min. Hydrogen carrier gas was used with a constant flow rate of 3.6 mL/min. The oven program was as follows: initial temperature of 70 °C held for 1 min, then a fast ramp of 27 °C/min to 230 °C, followed by a slower ramp of 6 °C/min to 315 °C, with a final hold at 315 °C for 10 min. Compound masses were calculated via external calibration curves determined separately for each detector using a C_{28} FAME standard (Fisher Scientific), and those masses were normalized to the mass of extracted sediment as well as the recovery of the internal standard to determine the concentration of waxes in sediment.

The δ^2H values of the FAMEs were measured using a Thermo Scientific Delta V Plus isotope ratio mass spectrometer (IRMS) coupled to a Trace 1310 GC via an Isolink II and Conflo IV. GC inlet flow settings and oven temperature program were identical to those used in GC-FID analysis except for the carrier gas, which was helium at a constant flow rate of 1.5 mL/min. The HTC reactor was held at 1420 °C for all analyses. The H_3^+ factor was monitored

regularly at the beginning of every sequence. The ANP3 samples were analyzed in November 2017, with an average H_3^+ factor of 2.8 ± 0.01‰, and the ANS1 samples in January 2019, with an H_3^+ factor of 3.6‰. FAME standards of known isotopic composition (C_{18}, C_{20}, C_{24}, Arndt Schimmelman, University of Indiana) were run along with every sequence of samples to correct for drift and the dependence of measured δ^2H on peak size, and to normalize sample results to the VSMOW (Vienna Standard Mean Ocean Water) scale. FAME δ^2H values were corrected for the isotopic composition of the hydrogens added during methylation. All isotope values are expressed in per mil (‰) relative to VSMOW, using standard δ notation:

$$\delta^2H(‰) = \left(\frac{R_{sample}}{R_{VSMOW}} - 1\right) \times 1000$$

where R is the ratio between deuterium and hydrogen, $^2H/^1H$. Total uncertainty of measured δ^2H values, calculated as the Standard Error of the Mean (SEM; which equals the root sum of squares of uncertainty for the drift and peak size corrections, replicate uncertainty of sample measurements, and uncertainty in the δ^2H value of the methylation hydrogens, divided by the root of the number of measurements), was on average better than ±2.7‰. Average chain length (ACL) was determined for C_{22} to C_{30}, using the equation:

$$ACL_{22-30} = \frac{\sum (n \times C_n)}{\sum (C_n)}$$

where C_n is μg/g sediment of each n-alkanoic acid with n carbon atoms.

3.4. Chronology and core correlation

The chronology of the sediment cores was established based on accelerator mass spectrometry (AMS) ^{14}C measurements on four terrestrial and eight aquatic plant macrofossils. The macrofossils were identified and isolated from 0.5 mm sieving residues, and measured at the Ångström Laboratory, Uppsala University and Lund University Radiocarbon Dating Laboratory, Sweden. All radiocarbon ages were calibrated using the online OxCal software (v. 4.3; Bronk Ramsey, 2009) and the IntCal13 dataset (Reimer et al., 2013). Calibrated ages are presented in calibrated year before present (cal. yr BP; BP = 1950).

For stratigraphic correlation between the cores, we used visual trends in the XRF data together with the radiocarbon age constraints. The cores were aligned in AnalySeries (v. 2.0.8; Paillard et al., 1996) using tie points in the elemental data. The Ca/Fe ratio was the main signal used (Fig. A, Appendix A), but multiple elemental ratios were compared to construct a common stratigraphic depth scale.

To establish an age-depth relationship for the composite core and incorporate age uncertainty into our biomarker records, we entered all proxy and chronology data into Linked PaleoData (LiPD) files (McKay and Emile-Geay, 2016). The data were analyzed in R (v. 3.6.3; R Core Team, 2020) using the GeoChronR package (McKay et al., 2018) and the IntCal13 dataset (Reimer et al., 2013). An age-depth model was constructed using a prior mean accumulation rate (acc. mean) of 100 years/cm and upper (d.min) and lower (d.max) depths set to the upper- and lowermost depths for the biomarker data (Fig. 4). The age ensemble was mapped to the paleo data, allowing us to display the biomarker data with age uncertainty (Figs 6 and 8) and plot the δ^2H records for both cores together (Fig. 8b). Fine lines in Figs 6 and 8 show the raw data plotted on the median of each age point, bold lines represent median values of the age model ensembles, and the light and dark shading show the 1σ and 2σ age uncertainty, respectively.

4. Results

4.1. Chronology and core correlation

Radiocarbon ages, calibrated median ages and 2σ age intervals for ANS1 and ANP3 are presented in Table 1 and Figs 4 and 5. The uppermost age in ANP3 (LuS 12222) appeared to be an outlier compared to the rest of the age-depth model, which was otherwise fairly linear, despite different terrestrial and aquatic sources of the samples. We therefore excluded this sample when running the final age-depth model (Fig. 4). Our biomarker record spans 11.5–2.2 cal. kyr BP for ANP3 and 9.2–1.9. cal. kyr BP for ANS1.

4.2. Lithology and stratigraphy

Figure 5 shows optical and X-ray imagery, sedimentological logs, LOI and selected XRF data for the two cores. The cores contain three lithological units.

Unit L1 is only present in ANP3 (129–97 cm; Fig. 5), and consists of light grey, clayey-silty diamict with interlaminated organic material. The LOI is below 2%, and Ti/(inc + coh) is higher (0.20–0.60) than in the other units, where values are generally below 0.04. Also, Ca/Fe is higher than in the overlying unit, especially in a coarser grained interval between *c.* 112–103 cm depth. L1 could be interpreted to represent minerogenic-rich sedimentation, driven by inflow of glacial meltwater, or deposited in a shallow glaciomarine setting. No foraminifera were observed in this unit. The transition from unit L1 to L2 at 97 cm depth, with decreasing minerogenic fines (silt and clay) in the lower 15 cm, indicates either an abrupt termination of glacial meltwater inflow or isolation from the fjord. Both these interpretations are supported by a sharp decrease in Ti/(inc + coh), and gradually decreasing Ca/Fe ratio.

Unit L2 (*c.* 97–34 cm in ANP3, 70–33 cm in ANS1; Fig. 5) consists of light brown to light olive grey stratified gyttja, with sporadic interbedded aquatic bryophytes and high organic content, representing accumulation of organic material with minimal minerogenic input. The organic content is higher in ANP3, increasing gradually from 13% at the lower boundary to 30% near 89 cm depth, and remaining between 30–40% for the rest of the unit. In ANS1, the same unit has LOI values between 17–27%. In both cores, Ti/(inc + coh) is generally below 0.03, and Ca/Fe ratio low and stable around 0.015–0.030.

Unit L3 (34–0 cm in ANP3, 33–0 cm in ANS1; Fig. 5) consists of dark brown gyttja, with a gradational lower boundary, and organic-rich beds interbedded with abundant aquatic bryophytes. LOI continues to gradually increase to 37% in ANS1 and just below 50% in ANP3, in the uppermost part of the cores. Ca/Fe ratios are higher and more variable (0.025–0.155), whereas Ti/(inc + coh) ratios show values similar to L2, although decreasing in ANS1.

4.3. n-alkanoic acid sources and productivity

Large isotopic differences between mid-chain (C_{20}, C_{22} and C_{24}) and long-chain (C_{26}, C_{28} and C_{30}) n-alkanoic acids, but similar values within these groups, suggests different sources of mid- and long-chain n-alkanoic acids (Fig. 6). This supports the hypothesis that Austre Nevlingen records both summer (terrestrial) and mean annual (aquatic) precipitation isotopes, and that hydrogen isotope ratios of C_{22} and C_{28} leaf waxes can be used as indicators of different plant sources (Gao et al., 2011; Thomas et al., 2016, in press) and to reflect different seasonality.

The analysis of modern plants suggests that different leaf wax

Table 1
Radiocarbon ages from sediment cores ANS1 and ANP3 from lake Austre Nevlingen, northern Spitsbergen, Svalbard. Calibrated ages are median ages within the 2σ age ranges.

Core	Depth (cm)	Lab ID[a]	^{14}C-age (yr BP)	Calibrated age (cal. yr BP)	Calibrated 2σ age ranges (cal. yr BP)	δ^{13}C (‰ VPDB)	Dated material
ANS1	4–5	Ua–60808	2200 ± 33	2232	2318–2131	−25.8	Aquatic moss
ANS1	14–15	Ua–60809	3350 ± 46	3589	3695–3469	−26.6	Aquatic moss
ANS1	24–25	Ua–60810	4818 ± 62	5532	5661–5447, 5385–5327	–	Aquatic moss
ANS1	41–42	Ua–60811	6209 ± 56	7104	7256–6973	−26.0	Aquatic moss
ANS1	55–56	Ua–60812	7410 ± 52	8250	8370–8156, 8116–8113, 8090–8056	−29.0	*Salix polaris*
ANP3	9.5–10.5	LuS 12222	4135 ± 45	4677	4824–4530	–	Aquatic moss
ANP3	25.5–26.5	LuS 12223	4215 ± 40	4740	4856–4785, 4765–4620	–	Aquatic moss
ANP3	32.5–33.5	LuS 12224	4545 ± 45	5166	5435–5423, 5320–5046	–	Wood
ANP3	50.5–51.5	LuS 12225	6085 ± 50	6953	7157–7039, 7033–6831, 6819–6798	–	*Salix polaris*
ANP3	69.5–70.5	LuS 12226	7850 ± 45	8636	8952–8919, 8862–8832, 8780–8541	–	Terrestrial plant macrofossil
ANP3	81.5–82.5	LuS 12227	8985 ± 70	10121	10256–9898	–	Aquatic moss
ANP3	95.5–96.5	LuS 12221	10070 ± 75	11622	11973–11315	–	Aquatic moss

[a] Ua = Ångström Laboratory, Uppsala University, Sweden; LuS = Lund University Radiocarbon Laboratory, Sweden.

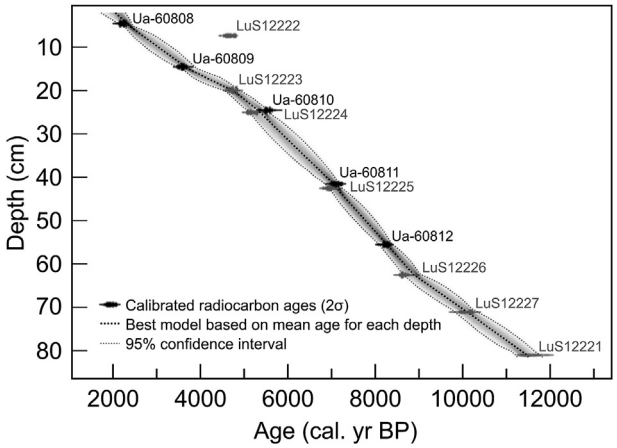

Fig. 4. Composite age depth model for surface core ANS1 (black symbols) and piston core ANP3 (grey symbols), established using GeoChronR (McKay et al., 2018), and the IntCal13 calibration curve (Reimer et al., 2013). Details of each radiocarbon age are given in Table 1.

sources (i.e., aquatic or terrestrial plants) have different chain length distribution. *Luzula confusa* contains the highest relative C_{28} concentration, followed by *Salix polaris* (Fig. 7). These two terrestrial plant species also show the lowest concentrations of mid-chain waxes. The two mosses, *Polytrichum* sp. and an aquatic bryophyte, record the highest C_{20} and C_{22} concentrations, and relatively less C_{28}.

The leaf wax concentrations were highest in the Early and Late Holocene (Fig. 6), suggesting highest productivity during these periods. Long-chain leaf wax concentrations are higher than mid-chain concentrations throughout most of the record, reflecting dominance of terrestrial vegetation or higher leaf wax productivity for terrestrial plants. Generally, the sediment record is dominated by C_{28}, C_{26} and C_{24} *n*-alkanoic acids, with relatively higher C_{20} and C_{22} concentrations in ANP3 than in ANS1 (Fig. 7).

The average chain length follows a similar trend as the leaf wax concentrations, with high values (>26) during periods of high C_{28} concentration (Fig. 6). This correlation is weaker for ANS1, where the concentration of mid-chain waxes (especially C_{24}) generally is higher than in ANP3.

4.4. δ^2H of sedimentary *n*-alkanoic acids

Based on the evidence presented above, we interpret δ^2H_{C28} to reflect terrestrial plant wax δ^2H (δ^2H_{terr}) and δ^2H_{C22} to reflect aquatic plant wax δ^2H (δ^2H_{aq}). δ^2H_{terr} is more stable throughout the Holocene than δ^2H_{aq} (Fig. 8). The difference in δ^2H_{terr} between the cores is generally less than 10‰ for most of the record, whereas δ^2H_{aq} differs as much as 80‰ at times. When interpreting the δ^2H records for the two sediment cores separately, they suggest different stories.

ANP3 covers a longer period and extends further back in time than ANS1 (Fig. 8a). δ^2H_{aq} is relatively ^{2}H-enriched prior to 9.9 cal. kyr BP (values generally above −230‰), for a short interval between 8.2–7.3 cal. kyr BP (−225‰) and after *c.* 6 cal. kyr BP (−230 to −205‰). For most of the time between 9.9–6 cal. kyr BP, δ^2H_{aq} is nearly 100‰ ^{2}H-depleted (−305 to −270‰) compared to the beginning and end of the record. In contrast, δ^2H_{terr} varies by around 40‰ throughout the Holocene and is relatively ^{2}H-depleted until *c.* 9.5 cal. kyr BP. After that, δ^2H_{terr} fluctuates between −170 and −145‰ for most of the record, with a slightly decreasing trend.

In ANS1, δ^2H_{aq} is relatively ^{2}H-enriched prior to *c.* 7.9 cal. kyr BP. On the contrary, δ^2H_{aq} in ANP3 becomes ^{2}H-depleted during this period. δ^2H_{aq} varies by around 40‰ (−300 to −260‰) for the rest of the ANS1 record, with values comparable to the ^{2}H-depleted intervals in ANP3. δ^2H_{terr} is relatively ^{2}H-enriched prior to *c.* 6.2 cal. kyr BP, with values between −160 and −150‰, compared to −180 to −165‰ for the later part of the record.

5. Discussion

The isotopic composition of *n*-alkanoic acids in the Austre Nevlingen record reveals environmental and climatic changes throughout the Holocene. Even though we are able to correlate ANS1 and ANP3 based on the XRF data (Fig. A, Appendix A), the δ^2H records of each core differ significantly, especially for the mid-chain compounds. Despite the large δ^2H_{aq} variability in the upper portion of ANP3, there are several data points with δ^2H values similar to ANS1, suggesting that this variability is real. The data do not indicate that one record should be favored over the other. Therefore, we discuss the δ^2H records for each core separately (Fig. 8a) and for the composite record (Fig. 8b). The composite record includes both the oldest sediments from ANP3 and the youngest sediments from ANS1, allowing us to discuss our results in full.

5.1. Influence of lake system dynamics on δ^2H

In Austre Nevlingen, shifts between relatively ^{2}H-enriched and ^{2}H-depleted δ^2H_{aq} values during the Mid and Late Holocene (Fig. 8a and b) suggest that the lake is close to an isotopic threshold. This means that the lake water isotopes could shift between recording summer and mean annual precipitation isotope δ^2H depending on processes acting in the catchment (Cluett and Thomas, 2020; Thomas et al., 2020).

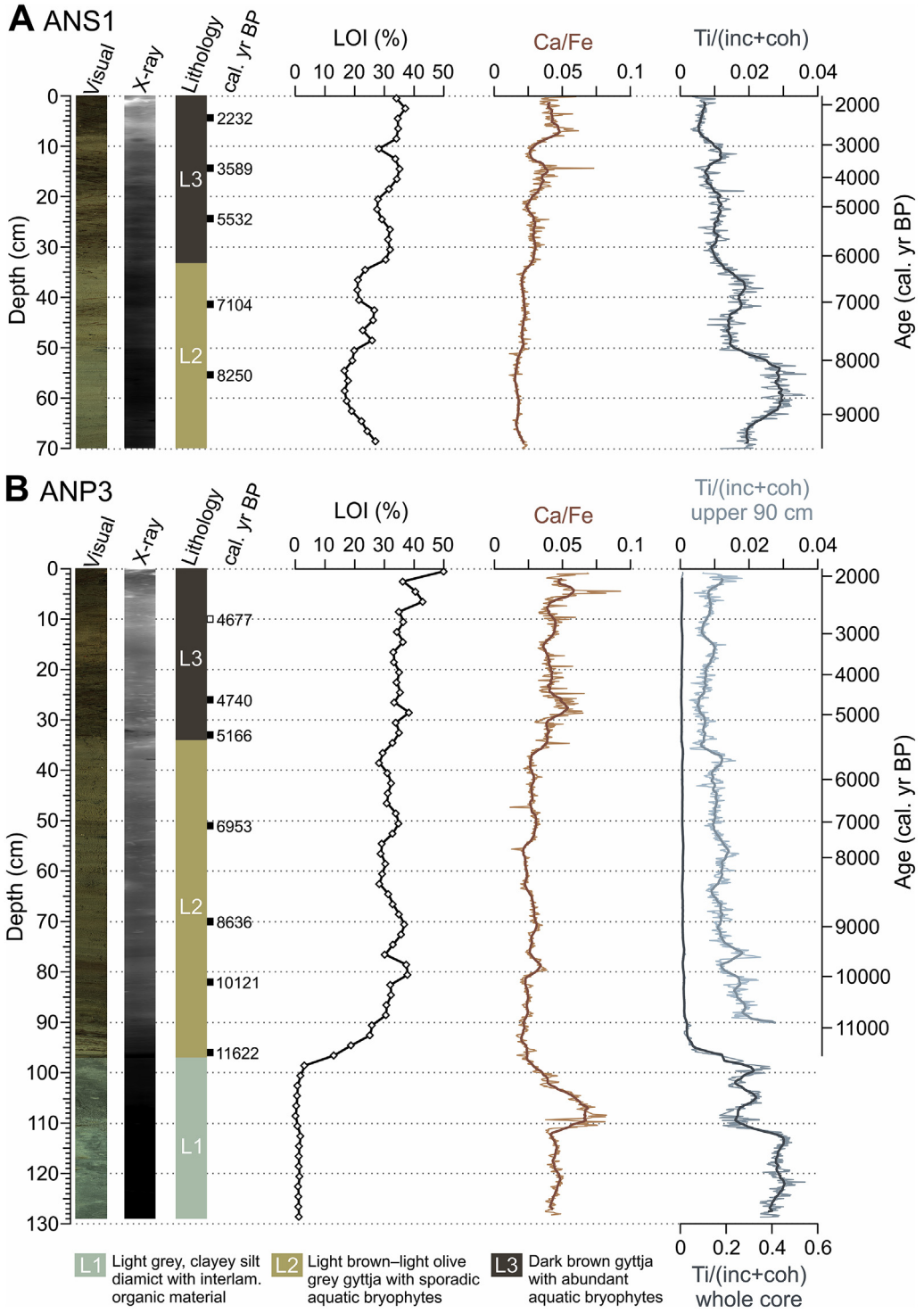

Fig. 5. Selected sediment proxies for (A) Surface core ANS1 and (B) Piston core ANP3. Core photograph, radiographic image, lithology, calibrated ^{14}C ages (median ages; see also Table 1), LOI (%), Ca/Fe and Ti normalized by the incoherent and coherent signal (Ti/(inc + coh)). The XRF data are plotted as raw data and with a 25-point running average.

We suggest that one of the main mechanisms causing the high amplitude (>80‰) variability in Austre Nevlingen δ^2H_{aq} could be the duration of ice on the lake. If lake-ice cover persists during the main spring snowmelt, most of the ^2H-depleted water could bypass the lake in these years (MacDonald et al., 2016). Furthermore, late lake-ice melt could delay the peak in primary production of the lake, and the ^2H-depleted winter precipitation isotope signal may not be incorporated into the leaf waxes. On the contrary, years without summer lake-ice cover would cause the aquatic plants to receive and incorporate more ^2H-depleted water.

Another possible factor affecting the seasonal signal preserved by the leaf waxes is fluctuating lake level, affecting the residence time of water in the lake. Previously higher lake level (and therefore larger lake volume) is suggested by the light-colored 'bathtub' rim around the lake, implying a previously longer residence time. On the other hand, a lower lake level (and therefore smaller lake

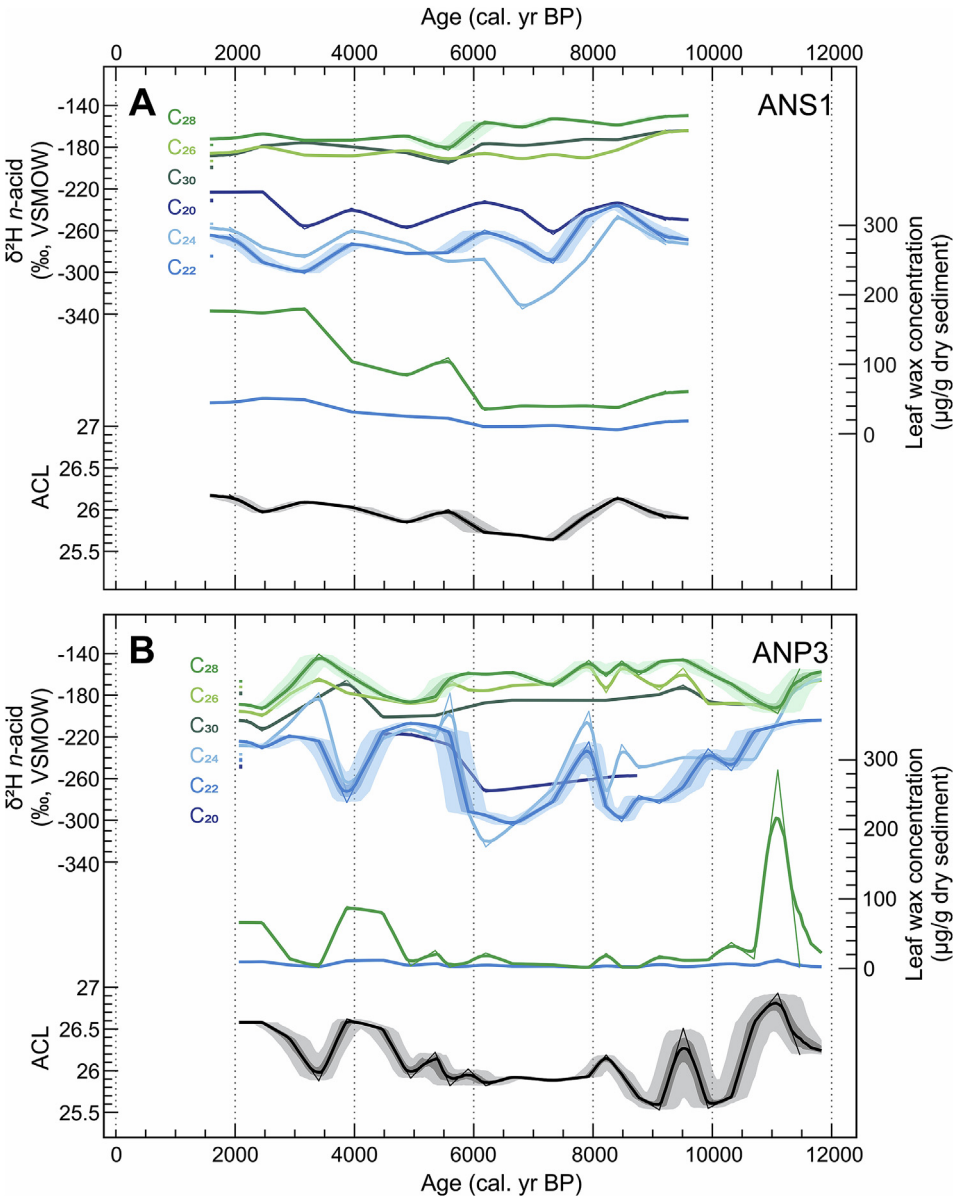

Fig. 6. Austre Nevlingen leaf wax data for (A) Surface core ANS1 and (B) Piston core ANP3. Leaf wax δ^2H for C_{20}–C_{24} (blue; aquatic) and C_{26}–C_{30} (green; terrestrial) *n*-alkanoic acids, absolute C_{22} and C_{28} leaf wax concentration and average chain length (ACL) distribution. Fine lines show the raw data plotted on the median of each age point and bold lines represent median values of the age model ensembles. The light and dark shading added to C_{22}, C_{28} and ACL show 1σ and 2σ age uncertainty, respectively (McKay et al., 2018). The vertical colored bars represent the average SEM proxy uncertainty. (For interpretation of the references to color in this figure legend, the reader is referred to the Web version of this article.)

volume) could result in a shorter residence time. If the lake was fully flushed by spring melt in some years but not in others (i.e., because of changes in lake volume), lake water, and therefore δ^2H_{aq}, could have shifted between reflecting summer and mean annual precipitation δ^2H values. Such lake level shifts, although at a much larger scale, have been described from Hakluytvatnet (Fig. 1). Balascio et al. (2018) interpret a mid-Holocene (7.5–5 cal. kyr BP) hiatus in their sedimentary record to represent desiccation of the lake as a response to warm and/or dry conditions at the time. Today, Austre Nevlingen lake water is not affected by evaporative enrichment, as the *d*-excess measured in August 2018 (9.0‰) is within the range of precipitation *d*-excess. It is possible that evaporation had a significant impact on lake water δ^2H during earlier Holocene warm periods as suggested by Balascio et al. (2018), if the ice-free periods were longer and the summers were warmer. Another possible way to switch the lake water from a mean annual to a summer signal would be by subterranean drainage during periods of deepened active layer. This process could theoretically decrease the lake volume enough to flush the lake completely in summer.

Another explanation for the up to 80‰ difference in δ^2H_{aq} between the Austre Nevlingen cores and between adjacent samples in a single core could be the relative abundance of aquatic bryophytes in the samples, since moss mats occur at different depths in the cores. If some samples mainly contain interbedded bryophytes rather than bulk sediments, δ^2H_{aq} in these samples could be dominated by one source rather than a mix of different sources. However, we could not confirm any correlation between samples dominated by aquatic mosses and significantly ^2H-enriched or ^2H-depleted δ^2H_{aq} values, when revisiting the residues after lipid extraction. Furthermore, there are no distinct shifts in the relative

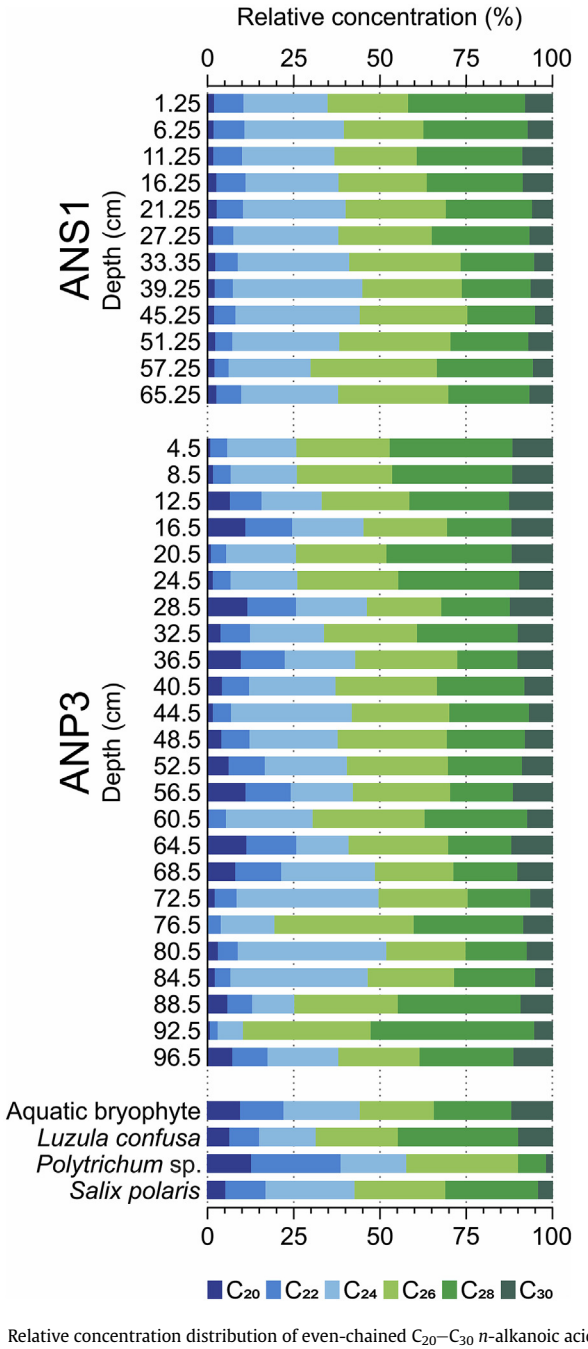

Fig. 7. Relative concentration distribution of even-chained C_{20}–C_{30} *n*-alkanoic acids in sediment cores ANS1 and ANP3, as well as selection of modern plants growing in the catchment.

chain length concentration associated with the shifts in δ^2H_{aq} values that would suggest different plant sources (Fig. 7). Therefore, the presence of aquatic plant macrofossils does not explain the observed isotopic differences.

More variable δ^2H_{aq} than δ^2H_{terr} (Fig. 8a and b) could reflect that the most prominent changes in precipitation have occurred during winter, since δ^2H_{aq} in Austre Nevlingen is interpreted to represent a mix of summer and winter precipitation, whereas δ^2H_{terr} represents summer rainfall. Additionally, δ^2H_{aq} is relatively more sensitive to local variation within the lake, whereas δ^2H_{terr} represents conditions integrated throughout the catchment.

We compare our isotope values from Austre Nevlingen (Fig. 8a and b) to those from Hakluytvatnet (Fig. 8c; Balascio et al., 2018), and find some significant differences between the two records. The precipitation isotope seasonality recorded by the two lakes differ because of the large difference in residence time between the lakes. Hakluytvatnet is much smaller than its catchment (Balascio et al., 2018), and therefore has a short residence time (i.e., it is likely fully flushed by spring melt and again by summer precipitation each year). The aquatic leaf wax δ^2H record from Hakluytvatnet should therefore be interpreted in terms of summer precipitation isotopes. This could explain the similar δ^2H patterns for C_{25} and C_{29} *n*-alkanes in that record (Fig. 8c). Austre Nevlingen has a longer residence time, and is not completely flushed by summer precipitation each year, so likely reflects the mean annual precipitation δ^2H. Because δ^2H for C_{22} and C_{28} in Austre Nevlingen represent different seasons, they show different patterns (Fig. 8a and b). Larger isotopic variation at Austre Nevlingen compared to Hakluytvatnet could also reflect greater seasonality at our site, as it is situated farther from the main moisture source pathway along the west coast of Spitsbergen. Furthermore, the difference in analyzed leaf wax compounds (i.e., *n*-alkanes for Hakluytvatnet and *n*-alkanoic acids for Austre Nevlingen) could explain the different trends (Curtin et al., 2019).

The discussed factors highlight the need to interpret lake δ^2H records carefully, depending on the local conditions. For this specific system, we interpret δ^2H_{terr} to reflect summer precipitation and evaporative enrichment and δ^2H_{aq} to reflect mean annual precipitation, sometimes modified by changing lake dynamics. Mean annual precipitation isotopes mainly change as a function of moisture transport (Frankenberg et al., 2009). Even though the main signal preserved can be assumed to reflect climatic changes, the influence of various internal lake dynamics must also be taken into account.

5.2. Early Holocene: 11.7–8.2 cal. kyr BP

Decreasing δ^2H_{aq} and increasing δ^2H_{terr} from the base of our δ^2H record at *c.* 11.5 to 9.5 cal. kyr BP (Fig. 8a and b) coincide with a June solstice insolation maximum at 80°N (Fig. 8f; Laskar et al., 2004) and rapidly increasing eastern Fram Strait surface and subsurface temperatures (Fig. 8e; Hald et al., 2007; Werner et al., 2016). Similar subsurface temperature trends are reported from the Barents Sea Margin (Risebrobakken et al., 2011). Hald et al. (2007), Werner et al. (2016), and Risebrobakken et al. (2011) interpret this warming as a response to increased influx of warm Atlantic water (AW) to the waters around Svalbard. This led to reduced spring sea-ice cover, evident by strongly decreasing PIP_{25} indices in the eastern Fram Strait (Figs 1a and 8d; P_BIP_{25} and P_DIP_{25}, based on brassicasterol and dinosterol, respectively; Werner et al., 2016). Additionally, Allaart et al. (2020) suggested an Early Holocene decline in sea-ice cover in the nearby Wijdefjorden (Fig. 1c), based on IP_{25} in marine sediments. Increased radiative forcing and greater AW heat transfer has also been suggested to cause warmer-than-present conditions in shallow waters around Svalbard between 11–9 cal. kyr BP (Mangerud and Svendsen, 2018) and peak warmth in three northern Svalbard lakes around 10 cal. kyr BP (van der Bilt et al., 2019).

Increasing Austre Nevlingen δ^2H_{terr} between 11–9.5 cal. kyr BP supports Early Holocene summer warming, suggesting enhanced evaporative enrichment during summer and/or a more proximal source for growing season precipitation. A more proximal moisture source could be explained by reduced spring sea-ice cover and increased local evaporation. Balascio et al. (2018) also interpret increasing δ^2H (for C_{25} to C_{29} *n*-alkanes) to reflect the high summer insolation and greater influence of mild air masses from the south. These processes could also explain the strong decreasing δ^2H_{aq} during the same period. Mean annual temperatures would have to

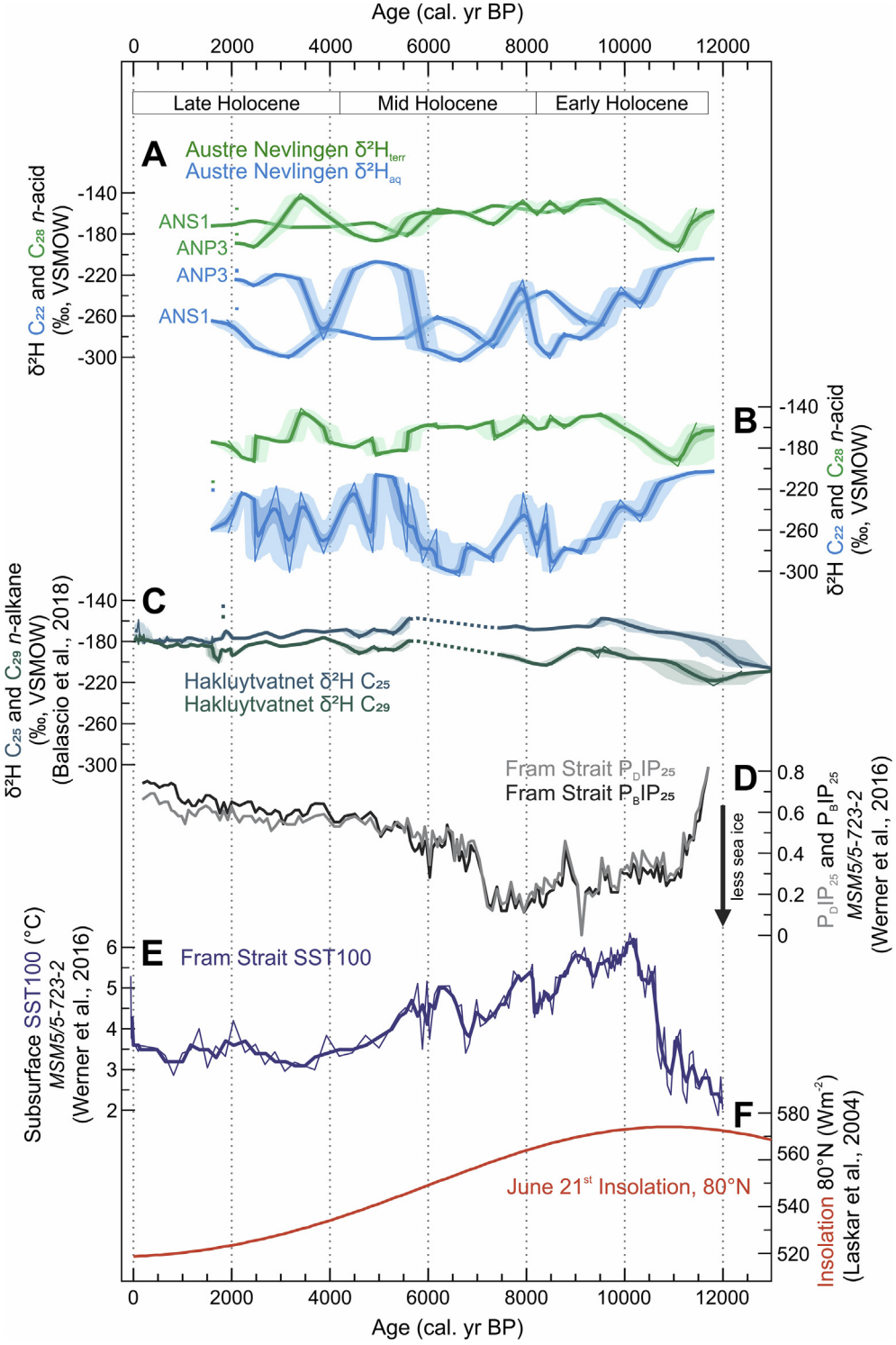

Fig. 8. Austre Nevlingen leaf wax hydrogen isotope data compared to selected regional Holocene climate records. For locations, see Fig. 1. Lines, shading and vertical colored bars shown as in Fig. 6. (A) Austre Nevlingen leaf wax δ^2H, C_{22} (blue; aquatic) and C_{28} (green; terrestrial) *n*-alkanoic acids for sediment cores ANS1 and ANP3. (B) Composite leaf wax δ^2H record for Austre Nevlingen. (C) Lake Hakluytvatnet leaf wax δ^2H, C_{25} (blue) and C_{29} (green) *n*-alkanes (Balascio et al., 2018). Dashed lines in the mid-Holocene denote a possible hiatus, suggested by Balascio et al. (2018). (D) Eastern Fram Strait sea-ice proxies P_BIP_{25} (black) and P_DIP_{25} (grey) (Werner et al., 2016). (E) Eastern Fram Strait subsurface temperature based on planktic foraminiferal fauna assemblages (fine line; Werner et al., 2016), including 3-point running means (bold line; Husum and Hald, 2012). (F) June 21st insolation at 80°N (Laskar et al., 2004). (For interpretation of the references to color in this figure legend, the reader is referred to the Web version of this article.)

be more than 30 °C cooler to explain the 100‰ depletion, considering a temperature-$\delta^{18}O$ relationship of 0.34–0.40‰/°C (Kotlyakov et al., 2004), translated to δ^2H by multiplying by 8 (Dansgaard, 1964). More likely, the ^2H-depletion reflects a strong winter signal as a response to greater winter ocean evaporation due to the reduced sea-ice cover or more distal moisture transport during this interval.

These interpretations support an early Holocene Climate Optimum, which is in agreement with other recent studies in Svalbard (Werner et al., 2016; Mangerud and Svendsen, 2018; Røthe et al., 2018; de Wet et al., 2018; van der Bilt et al., 2018, 2019; Voldstad et al., 2020), and elsewhere in the Arctic (Lecavalier et al., 2017; McFarlin et al., 2018). Our δ^2H record suggests that the regional Early Holocene warming had a strong effect on precipitation at the time, with local moisture from open seas leading to increased winter snowfall. This could also explain why some glaciers advanced in this otherwise warm period (e.g., Farnsworth et al., 2017, 2018). After *c.* 9.5 cal. kyr BP, δ^2H_{terr} stabilizes around −160‰, indicating stable summer conditions during this period. δ^2H_{aq} continues to decrease until *c.* 8.5 cal. kyr BP, reflecting continued sea-ice decrease (Werner et al., 2016; Allaart et al., 2020) and enhanced local evaporation.

5.3. Mid Holocene: 8.2–4.2 cal. kyr BP

In the Mid Holocene, δ^2H_{terr} remains stable around −160‰ until *c.* 5.6 cal. kyr BP, indicating stable summer conditions. Relatively ^2H-depleted values after 5.6 cal. kyr BP suggest gradual cooling, with less evaporative enrichment and/or more ^2H-depleted summer precipitation during this period. Mangerud and Svendsen (2018) suggest Svalbard ocean water temperatures *c.* 4 °C warmer than present between 8.2–6 cal. kyr BP, based on the presence of the marine bivalve mollusk *Mytilus edulis*, many of them along the northern coast. East Fram Strait subsurface temperatures stayed warm (up to 6 °C) until *c.* 5 cal. kyr BP, with a slightly decreasing long-term trend (Fig. 8e; Werner et al., 2016). Both Mangerud and Svendsen (2018) and Werner et al. (2016) interpret this warming to be attributed to intrusion of AW to the Svalbard shelf areas. High Mid Holocene temperatures are also inferred from lake sediment records, with minimal minerogenic accumulation, suggesting greatly reduced glacial activity or ice-free catchments (Svendsen and Mangerud, 1997; Røthe et al., 2015, 2018).

In Austre Nevlingen, ^2H-depleted δ^2H_{aq} values suggest increased winter precipitation starting *c.* 9.5 cal. kyr BP and persisting into the Mid Holocene until *c.* 6 cal. kyr BP. An increase in winter precipitation could be explained by continuously low sea-ice extent. Low P_DIP_{25} and P_BIP_{25} values until *c.* 7 cal. kyr BP support this interpretation (Fig. 8d; Werner et al., 2016). Higher winter precipitation during the Early-Mid-Holocene is also suggested by Røthe et al. (2018). They propose snowmelt dominated runoff to lake Vårfluesjøen between 10.2–7 cal. kyr BP, inferred from high frequency of 'snowmelt layers' in the sediment core. Vårfluesjøen is located on the western side of Wijdefjorden, *c.* 27 km WSW of Austre Nevlingen. After 7 cal. kyr BP, a lower frequency of snowmelt layers and the occurrence of aeolian sand in Vårfluesjøen, suggest drier Mid Holocene conditions (Røthe et al., 2018). Drier Mid Holocene climate is also proposed by Balascio et al. (2018), inferred from the hiatus (7.5–5 cal. kyr BP) in their sedimentary record. Our Austre Nevlingen record suggests that winter-dominated precipitation sustained until *c.* 6 cal. kyr BP, without any indications of desiccation of the lake.

5.4. Late Holocene: 4.2–0 cal. kyr BP

From *c.* 6 cal. kyr BP and into the Late Holocene, both δ^2H_{aq} and δ^2H_{terr} express larger amplitude variability than in the Early Holocene and first part of the Mid Holocene (Fig. 8a and b). We observe disagreement between the isotopic values in the two cores, but cannot explain exactly why. Some isotopic overlap between the cores (e.g., the ^2H-depleted δ^2H_{aq} value in ANP3 *c.* 3.9 cal. kyr BP) supports that this large-amplitude variability is real. One potential interpretation is that this variability reflects changes in the precipitation seasonality recorded by the lake. As discussed in Section 5.1, Austre Nevlingen might be close to an isotopic threshold, meaning that the lake water incorporates relatively ^2H-depleted winter precipitation isotopes in some years, but not in others. This process could be explained by changing regional conditions and/or variable conditions in the catchment, amplifying the climatic signal. These processes could affect the seasonality of the isotopes registered by the lake in the Late Holocene δ^2H_{aq} record. Hence, it is difficult to decipher the Late Holocene climate signal, except that the high-amplitude δ^2H_{aq} variability suggests greater climate variability.

The Late Holocene is generally characterized by Neoglacial cooling from *c.* 5 cal. kyr BP, with decreasing summer insolation (Fig. 8f; Laskar et al., 2004) and ocean cooling around Svalbard (Fig. 8e; Hald et al., 2004; Rasmussen et al., 2014; Werner et al., 2016). Weaker AW advection also led to increased sea-ice cover in eastern Fram Strait (Fig. 8d; Werner et al., 2016), and cooler conditions on land, registered by alkenones (van der Bilt et al., 2018) and *n*-alkanes (Fig. 8c; Balascio et al., 2018) in lakes. Glaciers started to re-advance *c.* 4–3 cal. kyr BP (Svendsen and Mangerud, 1997; Røthe et al., 2015, 2018; Miller et al., 2017; Bartels et al., 2018; Lovell et al., 2018).

In our Austre Nevlingen record, slightly ^2H-depleted δ^2H_{terr} values after 5.6 cal. kyr BP may be due to this regional cooling trend, as cooler conditions would cause less evaporative enrichment and more ^2H-depleted summer precipitation. Neoglacial cooling could also explain the more ^2H-enriched parts of the δ^2H_{aq} record after 6 cal. kyr BP. Regional cooling and concomitant increases in sea-ice cover would have caused less winter precipitation, in turn causing the lake water to be biased to ^2H-enriched summer precipitation.

6. Conclusions

- Leaf wax hydrogen isotopes from Austre Nevlingen suggest large variability in precipitation seasonality on northern Spitsbergen throughout the Holocene. One of the strengths of our reconstruction is that we can extract both the summer and mean annual precipitation signal. This is possible because terrestrial and aquatic plants use different source water (soil water and lake water, respectively). Furthermore, the lake is not completely flushed by spring melt, with the long residence time allowing winter precipitation isotopes to be incorporated into the aquatic leaf waxes. Contrasting isotopic composition of mid-chain and long-chain *n*-alkanoic acids suggests different leaf wax sources for these two sets of compounds.
- Most prominent Holocene precipitation changes occurred in winter, reflected in greater variability of the aquatic (mean annual) than terrestrial (summer) leaf wax hydrogen isotope ratios.
- Early Holocene regional warming had a strong effect on moisture availability and precipitation seasonality in northern Svalbard. High summer insolation and strong Atlantic water influx contributed to reduced sea ice, which we suggest favored greater local winter evaporation leading to increasing winter precipitation.
- Between 9.5–6 cal. kyr BP, the record is characterized by ^2H-enriched terrestrial and ^2H-depleted aquatic hydrogen

isotope ratios, which we interpret to reflect enhanced summer evaporation and/or ^{2}H-enriched summer precipitation, reduced sea-ice cover and local moisture contributing to high winter precipitation.

- After *c.* 6 cal. kyr BP, the δ^{2}H records show greater amplitude variability. We interpret these shifts to be influenced by lake system dynamics, such as the duration of ice cover on the lake, that amplify the climate signal. Hence, we cannot clearly distinguish the amplitude of climate variability in this portion of the record, although the lake variability is most likely in phase with climate variability.
- Our results suggest that the precipitation seasonality in northern Spitsbergen is strongly linked to regional ocean surface conditions. As a result, the positive trend in winter precipitation observed in Svalbard today, may amplify because of warming ocean surface waters and reduction in sea ice.

Data availability

All chronological and geochemical data presented in this paper are freely available at the NOAA/World Data Service for Paleoclimatology website: https://www.ncdc.noaa.gov/paleo/study/29852.

Author contributions

AS, EKT, LH and SEK developed the idea; SEK, AS, WRF, LA, SB and ÓI conducted fieldwork; SEK, WRF, AS and LH described and interpreted the lithology; AS and LH identified plant macrofossils for radiocarbon dating; LA processed the bathymetry data; SEK, OCC and SD conducted organic and stable isotope biogeochemical work; SEK, EKT and NPM did the age modelling and leaf wax data analysis and visualization; all authors contributed with interpretation and discussion of results; SEK wrote the paper with contributions from all co-authors.

AS = Anders Schomacker, EKT = Elizabeth K. Thomas, LA = Lis Allaart, LH = Lena Håkansson, NPM = Nicholas P. McKay, OCC = Owen C. Cowling, ÓI = Ólafur Ingólfsson, SB = Skafti Brynjólfsson, SD = Sandrine Duboscq, SEK = Sofia E. Kjellman, WRF = Wesley R. Farnsworth.

Declaration of competing interest

The authors declare that they have no known competing financial interests or personal relationships that could have appeared to influence the work reported in this paper.

Acknowledgements

Fieldwork, radiocarbon dates, and laboratory analyses were funded by the Carlsberg Foundation (grant number CF14-0756 to AS), the Nansen Foundation (to AS), and the Svalbard Environmental Protection Fund (grant number 17/101 to AS and 17/114 to LA). The 2015 fieldwork was partly funded by the University Centre in Svalbard (UNIS) Research Fund (grant to ÓI). Laboratory analyses and technician support were also funded by National Science Foundation Grant (grant number 1652274 to EKT) and a UB Center for Undergraduate Research and Creative Activities Grant (to SD). We thank Sveinn Brynjólfsson and Sara Mollie Cohen for field assistance, Mike Retelle for providing field equipment, Marie-Louise Siggaard-Andersen for assistance with the ITRAX-scanning, and Alexandra Rouillard for macrofossil identification and data discussion. Finally, we thank Willem van der Bilt and one anonymous reviewer for constructive comments that improved this manuscript.

Appendix. A

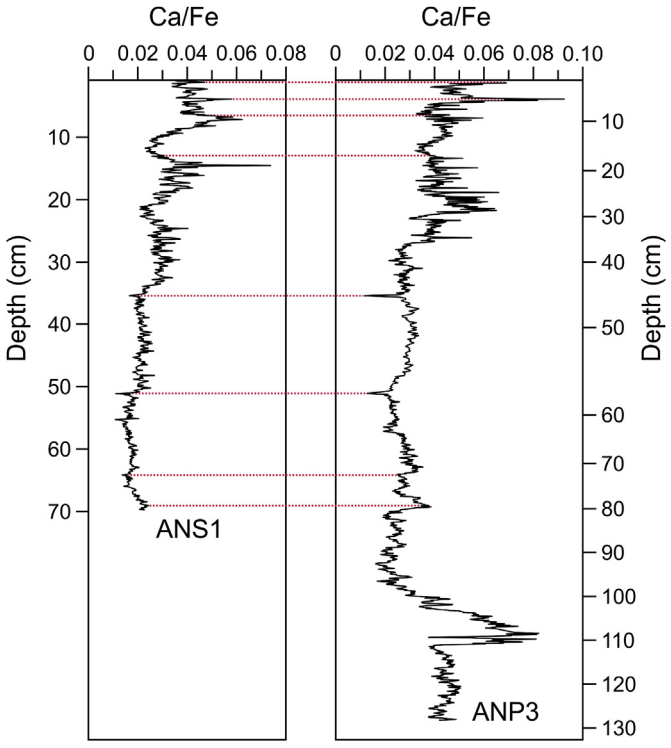

Fig. A. Correlation between surface core ANS1 and piston core ANP3 from lake Austre Nevlingen, Svalbard. The records were aligned in AnalySeries (v. 2.0.8; Paillard et al., 1996), based on tie points in the Ca/Fe data.

References

Adakudlu, M., Andresen, J., Bakke, J., Beldring, S., Benestad, R., Bilt, W.v. d., Bogen, J., Borstad, C.P., Breili, K., Breivik, Ø., Børsheim, K.Y., Christiansen, H.H., Dobler, A., Engeset, R., Frauenfelder, R., Gerland, S., Gjelten, H.M., Gundersen, J., Isaksen, K., Jaedicke, C., Kierulf, H., Kohler, J., Li, H., Lutz, J., Melvold, K., Mezghani, A., Nilsen, F., Nilsen, I.B., Nilsen, J.E.Ø., Pavlova, O., Ravndal, O., Risebrobakken, B., Saloranta, T., Sandven, S., Schuler, T.V., Simpson, M.J.R., Skogen, M., Smedsrud, L.H., Sund, M., Vikhamar-Schuler, D., Westermann, S., Wong, W.K., 2019. *Climate in Svalbard 2100 - A Knowledge Base for Climate Adaptation* (2387-3027). Norwegian Centre for Climate Services (NCCS). NCCS report no. 1/2019.

Allaart, L., Müller, J., Schomacker, A., Rydningen, T.A., Håkansson, L., Kjellman, S.E., Mollenhauer, G., Forwick, M., 2020. Late Quaternary glacier and sea-ice history of northern Wijdefjorden, Svalbard. Boreas. https://doi.org/10.1111/bor.12435.

Balascio, N.L., D'Andrea, W.J., Bradley, R.S., Perren, B.B., 2013. Biogeochemical evidence for hydrologic changes during the Holocene in a lake sediment record from southeast Greenland. Holocene 23 (10), 1428–1439. https://doi.org/10.1177/0959683613493938.

Balascio, N.L., D'Andrea, W.J., Gjerde, M., Bakke, J., 2018. Hydroclimate variability of High Arctic Svalbard during the Holocene inferred from hydrogen isotopes of leaf waxes. Quat. Sci. Rev. 183, 177–187. https://doi.org/10.1016/j.quascirev.2016.11.036.

Bartels, M., Titschack, J., Fahl, K., Stein, R., Hebbeln, D., 2018. Wahlenbergfjord, eastern Svalbard: a glacier-surrounded fjord reflecting regional hydrographic variability during the Holocene? Boreas 47 (4), 1003–1021. https://doi.org/10.1111/bor.12325.

Bintanja, R., Andry, O., 2017. Towards a rain-dominated Arctic. Nat. Clim. Change 7 (4), 263. https://doi.org/10.1038/nclimate3240.

Bintanja, R., Selten, F.M., 2014. Future increases in Arctic precipitation linked to local evaporation and sea-ice retreat. Nature 509 (7501), 479–482. https://doi.org/10.1038/nature13259.

Bowen, G.J., 2019. OIPC: the Online Isotopes in Precipitation Calculator. Version 3.1. Retrieved from: http://www.waterisotopes.org.

Bowen, G.J., Wassenaar, L.I., Hobson, K.A., 2005. Global application of stable hydrogen and oxygen isotopes to wildlife forensics. Oecologia 143 (3), 337–348. https://doi.org/10.1007/s00442-004-1813-y.

Bronk Ramsey, C., 2009. Bayesian analysis of radiocarbon dates. Radiocarbon 511 (1), 337–360. https://doi.org/10.1017/S0033822200033865.
Cluett, A.A., Thomas, E.K., 2020. Resolving combined influences of inflow and evaporation on western Greenland lake water isotopes to inform paleoclimate inferences. J. Paleolimnol. 63, 251–268. https://doi.org/10.1007/s10933-020-00114-4.
Collins, M., Knutti, R., Arblaster, J., Dufresne, J.-L., Fichefet, T., Friedlingstein, P., Gao, X., Gutowski, W.J., Johns, T., Krinner, G., Shongwe, M., Tebaldi, C., Weaver, A.J., Wehner, M., 2013. Long-term climate change: projections, commitments and irreversibility. In: Stocker, T.F., Qin, D., Plattner, G.-K., Tignor, M., Allen, S.K., Boschung, J., Nauels, A., Xia, Y., Bex, V., Midgley, P.M. (Eds.), Climate Change 2013: the Physical Science Basis. Contribution of Working Group I to the Fifth Assessment Report of the Intergovernmental Panel on Climate Change. Cambridge University Press, Cambridge, United Kingdom and New York, NY, USA.
Cooper, L.W., Olsen, C.R., Solomon, D.K., Larsen, I.L., Cook, R.B., Grebmeier, J.M., 1991. Stable isotopes of oxygen and natural and fallout radionuclides used for tracing runoff during snowmelt in an Arctic watershed. Water Resour. Res. 27 (9), 2171–2179. https://doi.org/10.1029/91WR01243.
Craig, H., 1961. Isotopic variations in meteoric waters. Science 133 (3465), 1702–1703. https://doi.org/10.1126/science.133.3465.1702.
Croudace, I.W., Rindby, A., Rothwell, R.G., 2006. ITRAX: description and evaluation of a new multi-function X-ray core scanner. Geol. Soc. Lond. Special Publ. 267 (1), 51–63. https://doi.org/10.1144/GSL.SP.2006.267.01.04.
Curtin, L., D'Andrea, W.J., Balascio, N., Pugsley, G., de Wet, G., Bradley, R., 2019. Holocene and Last Interglacial climate of the Faroe Islands from sedimentary plant wax hydrogen and carbon isotopes. Quat. Sci. Rev. 223, 105930. https://doi.org/10.1016/j.quascirev.2019.105930.
Dallmann, W.K.E., 2015. Geoscience Atlas of Svalbard. Norwegian Polar Institute, Report Series 148, 292 pp.
Dansgaard, W., 1964. Stable isotopes in precipitation. Tellus 16 (4), 436–468. https://doi.org/10.3402/tellusa.v16i4.8993.
de Wet, G.A., Balascio, N.L., D'Andrea, W.J., Bakke, J., Bradley, R.S., Perren, B., 2018. Holocene glacier activity reconstructed from proglacial lake Gjøavatnet on Amsterdamøya, NW Svalbard. Quat. Sci. Rev. 183, 188–203. https://doi.org/10.1016/j.quascirev.2017.03.018.
Dickson, R., Osborn, T., Hurrell, J., Meincke, J., Blindheim, J., Adlandsvik, B., Vinje, T., Alekseev, G., Maslowski, W., 2000. The Arctic ocean response to the North Atlantic oscillation. J. Clim. 13 (15), 2671–2696. https://doi.org/10.1175/1520-0442(2000)013%3C2671:TAORTT%3E2.0.CO;2.
Eglinton, G., Calvin, M., 1967. Chemical fossils. Sci. Am. 216 (1), 32–43.
Eidesen, P.B., Arnesen, G., Elven, R., Søli, G., 2018. Kartlegging av Ringhorndalen, Wijdefjorden: en uutforsket arktisk oase. The University Centre in Svalbard, The University of Oslo, Ecofact Nord AS, 43 pp.
Elvebakk, A., 2005. 'Arctic hotspot complexes'—proposed priority sites for studying and monitoring effects of climatic change on arctic biodiversity. Phytocoenologia 35 (4), 1067–1079. https://doi.org/10.1127/0340-269X/2005/0035-1067.
Elvebakk, A., Nilsen, L., 2002. Indre Wijdefjorden Med Sidefjordar: Eit Botanisk Unikt Steppeområde På Svalbard. Rapport Til Sysselmannen På Svalbard. Universitety of Tromsø, Tromsø.
Farnsworth, W.R., 2018. Holocene Glacier History of Svalbard: Retracing the Style of (De-) Glaciation.. PhD thesis Department of Geosciences, UiT The Arctic University of Norway, pp. 1–227.
Farnsworth, W.R., Ingólfsson, Ó., Noormets, R., Allaart, L., Alexanderson, H., Henriksen, M., Schomacker, A., 2017. Dynamic Holocene glacial history of st. Jonsfjorden, svalbard. Boreas 46 (3), 585–603. https://doi.org/10.1111/bor.12269.
Farnsworth, W.R., Ingólfsson, Ó., Retelle, M., Allaart, L., Håkansson, L.M., Schomacker, A., 2018. Svalbard glaciers re-advanced during the Pleistocene–Holocene transition. Boreas 47 (4), 1022–1032. https://doi.org/10.1111/bor.12326.
Ficken, K.J., Li, B., Swain, D.L., Eglinton, G., 2000. An *n*-alkane proxy for the sedimentary input of submerged/floating freshwater aquatic macrophytes. Org. Geochem. 31 (7–8), 745–749. https://doi.org/10.1016/S0146-6380(00)00081-4.
Førland, E.J., Hanssen-Bauer, I., 2000. Increase precipitation in the Norwegian Arctic: true or false? Clim. Change 46, 485–509. https://doi.org/10.1023/A:1005613304674.
Førland, E.J., Flatøy, F., Hanssen-Bauer, I., Haugen, J.E., Isaksen, K., Sorteberg, A., Ådlandsvik, B., Benestad, R.E., 2009. Climate Development in North Norway and the Svalbard Region during 1900–2100. Norwegian Polar Institute. Report 128/2009.
Førland, E.J., Benestad, R., Hanssen-Bauer, I., Haugen, J.E., Skaugen, T.E., 2011. Temperature and precipitation development at svalbard 1900–2100. Adv. Meteorol. 2011, 1–14. https://doi.org/10.1155/2011/893790.
Førland, E.J., Isaksen, K., Lutz, J., Hanssen-Bauer, I., Schuler, T.V., Dobler, A., Gjelten, H.M., Vikhamar-Schuler, D., 2020. Measured and modelled historical precipitation trends for Svalbard. J. Hydrometeorol. 21, 1279–1296. https://doi.org/10.1175/JHM-D-19-0252.1.
Forman, S.L., 1990. Post-glacial relative sea-level history of northwestern Spitsbergen, Svalbard. Geol. Soc. Am. Bull. 102 (11), 1580–1590. https://doi.org/10.1130/0016-7606(1990)102%3C1580:PGRSLH%3E2.3.CO;2.
Frankenberg, C., Yoshimura, K., Warneke, T., Aben, I., Butz, A., Deutscher, N., Griffith, D., Hase, F., Notholt, J., Schneider, M., Schrijver, H., Röckmann, T., 2009. Dynamic processes governing lower-tropospheric HDO/H2O ratios as observed from space and ground. Science 325 (5946), 1374–1377. https://doi.org/10.1126/science.1173791.
Gao, L., Hou, J., Toney, J., MacDonald, D., Huang, Y., 2011. Mathematical modeling of the aquatic macrophyte inputs of mid-chain n-alkyl lipids to lake sediments: implications for interpreting compound specific hydrogen isotopic records. Geochem. Cosmochim. Acta 75 (13), 3781–3791. https://doi.org/10.1016/j.gca.2011.04.008.
Hagen, J.O., Liestøl, O., Roland, E., Jørgensen, T., 1993. Glacier Atlas of Svalbard and Jan Mayen, Vol. 129. Norwegian Polar Institute, Oslo.
Hald, M., Ebbesen, H., Forwick, M., Godtliebsen, F., Khomenko, L., Korsun, S., Olsen, L.R., Vorren, T.O., 2004. Holocene paleoceanography and glacial history of the West Spitsbergen area, Euro-Arctic margin. Quat. Sci. Rev. 23, 2075–2088. https://doi.org/10.1016/j.quascirev.2004.08.006.
Hald, M., Andersson, C., Ebbesen, H., Jansen, E., Klitgaard-Kristensen, D., Risebrobakken, B., Salomonsen, G.R., Sarnthein, M., Sejrup, H.P., Telford, R.J., 2007. Variations in temperature and extent of atlantic water in the northern North Atlantic during the Holocene. Quat. Sci. Rev. 26 (25–28), 3423–3440. https://doi.org/10.1016/j.quascirev.2007.10.005.
Hanssen-Bauer, I., 2002. Temperature and precipitation in Svalbard 1912–2050: measurements and scenarios. Polar Rec. 38 (206), 225–232. https://doi.org/10.1017/S0032247400017757.
Heiri, O., Lotter, A.F., Lemcke, G., 2001. Loss on ignition as a method for estimating organic and carbonate content in sediments: reproducibility and comparability of results. J. Paleolimnol. 25 (1), 101–110. https://doi.org/10.1023/A:1008119611481.
Henriksen, M., Alexanderson, H., Landvik, J.Y., Linge, H., Peterson, G., 2014. Dynamics and retreat of the late weichselian kongsfjorden ice stream, NW svalbard. Quat. Sci. Rev. 92, 235–245. https://doi.org/10.1016/j.quascirev.2013.10.035.
Holm, T.M., Koinig, K.A., Andersen, T., Donali, E., Hormes, A., Klaveness, D., Psenner, R., 2012. Rapid physicochemical changes in the high Arctic Lake Kongressvatn caused by recent climate change. Aquat. Sci. 74 (3), 385–395. https://doi.org/10.1007/s00027-011-0229-0.
Hormes, A., Gjermundsen, E.F., Rasmussen, T.L., 2013. From mountain top to the deep sea – deglaciation in 4D of the northwestern Barents Sea ice sheet. Quat. Sci. Rev. 75, 78–99. https://doi.org/10.1016/j.quascirev.2013.04.009.
Humlum, O., 2002. Modelling late 20th-century precipitation in Nordenskiold Land, Svalbard, by geomorphic means. Norsk Geografisk Tidsskrift-Norwegian J. Geography 56 (2), 96–103. https://doi.org/10.1080/002919502760056413.
Husum, K., Hald, M., 2012. Arctic planktic foraminiferal assemblages: implications for subsurface temperature reconstructions. Mar. Micropaleontol. 96, 38–47. https://doi.org/10.1016/j.marmicro.2012.07.001.
IAEA/WMO, 2019. Global Network of Isotopes in Precipitation. The GNIP Database. Retrieved from. https://nucleus.iaea.org/wiser.
Jonsson, C.E., Leng, M.J., Rosqvist, G.C., Seibert, J., Arrowsmith, C., 2009. Stable oxygen and hydrogen isotopes in sub-Arctic lake waters from northern Sweden. J. Hydrol. 376 (1–2), 143–151. https://doi.org/10.1016/j.jhydrol.2009.07.021.
Kahmen, A., Schefuß, E., Sachse, D., 2013. Leaf water deuterium enrichment shapes leaf wax n-alkane δD values of angiosperm plants I: experimental evidence and mechanistic insights. Geochem. Cosmochim. Acta 111, 39–49. https://doi.org/10.1016/j.gca.2012.09.003.
Kopec, B.G., Feng, X., Michel, F.A., Posmentier, E.S., 2016. Influence of sea ice on Arctic precipitation. Proc. Natl. Acad. Sci. U. S. A. 113 (1), 46–51. https://doi.org/10.1073/pnas.1504633113.
Kotlyakov, V., Arkhipov, S., Henderson, K., Nagornov, O., 2004. Deep drilling of glaciers in Eurasian Arctic as a source of paleoclimatic records. Quat. Sci. Rev. 23 (11–13), 1371–1390. https://doi.org/10.1016/j.quascirev.2003.12.013.
Kylander, M.E., Ampel, L., Wohlfarth, B., Veres, D., 2011. High-resolution X-ray fluorescence core scanning analysis of Les Echets (France) sedimentary sequence: new insights from chemical proxies. J. Quat. Sci. 26 (1), 109–117. https://doi.org/10.1002/jqs.1438.
Larsen, N.K., Strunk, A., Levy, L.B., Olsen, J., Bjørk, A., Lauridsen, T.L., Jeppesen, E., Davidson, T.A., 2017. Strong altitudinal control on the response of local glaciers to Holocene climate change in southwest Greenland. Quat. Sci. Rev. 168, 69–78. https://doi.org/10.1016/j.quascirev.2017.05.008.
Larsen, E., Lysså, A., Rubensdotter, L., Farnsworth, W.R., Jensen, M., Nadeau, M.J., Ottesen, D., 2018. Lateglacial and Holocene glacier activity in the van mijenfjorden area, western svalbard. arktos 4 (1), 9. https://doi.org/10.1007/s41063-018-0042-2.
Laskar, J., Robutel, P., Joutel, F., Gastineau, M., Correia, A., Levrard, B., 2004. A long-term numerical solution for the insolation quantities of the Earth. Astron. Astrophys. 428 (1), 261–285. https://doi.org/10.1051/0004-6361:20041335.
Lecavalier, B.S., Fisher, D.A., Milne, G.A., Vinther, B.M., Tarasov, L., Huybrechts, P., Lacelle, D., Main, B., Zheng, J., Bourgeois, J., 2017. High Arctic Holocene temperature record from the Agassiz ice cap and Greenland ice sheet evolution. Proc. Natl. Acad. Sci. Unit. States Am. 114 (23), 5952–5957. https://doi.org/10.1073/pnas.1616287114.
Linderholm, H.W., Nicolle, M., Francus, P., Gajewski, K., Helama, S., Korhola, A., Solomina, O., Yu, Z., Zhang, P., D'Andrea, W.J., 2018. Arctic Hydroclimate Variability during the Last 2000 Years. Climate of the Past. https://doi.org/10.5194/cp-14-473-2018.
Lønne, I.D.A., 2005. Faint traces of high Arctic glaciations: an early Holocene ice-front fluctuation in Bolterdalen, Svalbard. Boreas 34 (3), 308–323. https://doi.org/10.1111/j.1502-3885.2005.tb01103.x.
Lovell, H., Benn, D.I., Lukas, S., Ottesen, D., Luckman, A., Hardiman, M., Barr, I.D., Boston, C.M., Sevestre, H., 2018. Multiple late Holocene surges of a high-arctic

tidewater glacier system in svalbard. Quat. Sci. Rev. 201, 162–185. https://doi.org/10.1016/j.quascirev.2018.10.024.
MacDonald, L.A., Wolfe, B.B., Turner, K.W., Anderson, L., Arp, C.D., Birks, S.J., Bouchard, F., Edwards, T.W.D., Farquharson, N., Hall, R.I., McDonald, I., Narancic, B., Ouimet, C., Pienitz, R., Tondu, J., White, H., 2016. A synthesis of thermokarst lake water balance in high-latitude regions of North America from isotope tracers. Arct. Sci. 3 (2), 118–149. https://doi.org/10.1139/as-2016-0019.
Mangerud, J., Svendsen, J.I., 1990. Deglaciation chronology inferred from marine sediments in a proglacial lake basin, western Spitsbergen, Svalbard. Boreas 19 (3), 249–272. https://doi.org/10.1111/j.1502-3885.1990.tb00450.x.
Mangerud, J., Svendsen, J.I., 2018. The Holocene thermal maximum around svalbard, arctic North Atlantic; molluscs show early and exceptional warmth. Holocene 28 (1), 65–83. https://doi.org/10.1177/0959683617715701.
McFarlin, J.M., Axford, Y., Osburn, M.R., Kelly, M.A., Osterberg, E.C., Farnsworth, L.B., 2018. Pronounced summer warming in northwest Greenland during the Holocene and last interglacial. Proc. Natl. Acad. Sci. Unit. States Am. 115 (25), 6357–6362. https://doi.org/10.1073/pnas.1720420115.
McFarlin, J.M., Axford, Y., Masterson, A.L., Osburn, M.R., 2019. Calibration of modern sedimentary δ^2H plant wax-water relationships in Greenland lakes. Quat. Sci. Rev. 225, 105978. https://doi.org/10.1016/j.quascirev.2019.105978.
McKay, N., Emile-Geay, J., 2016. Technical note: the Linked Paleo Data framework–a common tongue for paleoclimatology. Clim. Past 12 (4), 1093–1100. https://doi.org/10.5194/cp-12-1093-2016.
McKay, N., Julien, E.-G., Heiser, C., Khider, D., 2018. GeoChronR Development Repository. https://doi.org/10.5281/zenodo.60812.
MET Norway, 2020. eKlima. Norwegian Meteorological Institute.. Retrieved from. http://sharki.oslo.dnmi.no
Meyers, P.A., 2003. Applications of organic geochemistry to paleolimnological reconstructions: a summary of examples from the Laurentian Great Lakes. Org. Geochem. 34 (2), 261–289. https://doi.org/10.1016/S0146-6380(02)00168-7.
Miller, G.H., Landvik, J.Y., Lehman, S.J., Southon, J.R., 2017. Episodic Neoglacial snowline descent and glacier expansion on Svalbard reconstructed from the ^{14}C ages of ice-entombed plants. Quat. Sci. Rev. 155, 67–78. https://doi.org/10.1016/j.quascirev.2016.10.023.
National Snow and Ice Data Center, 2019. SOTC: Sea Ice. Retrieved from. http://nsidc.org/cryosphere/sotc/sea_ice.html.
Nichols, J.E., Walcott, M., Bradley, R., Pilcher, J., Huang, Y., 2009. Quantitative assessment of precipitation seasonality and summer surface wetness using ombrotrophic sediments from an Arctic Norwegian peatland. Quat. Res. 72 (3), 443–451. https://doi.org/10.1016/j.yqres.2009.07.007.
Norwegian Polar Institute, 2019. SvalbardKartet. Fauna & Flora - Biogeographical Zones. Retrieved from. https://svalbardkartet.npolar.no/.
ORNL DAAC, 2018. MODIS and VIIRS Land Products Global Subsetting and Visualization Tool. Oak Ridge, Tennessee, USA.
Paillard, D., Labeyrie, L., Yiou, P., 1996. Macintosh program performs time-series analysis. Eos, Trans. Am Geophys Union 77, 379. https://doi.org/10.1029/96EO00259.
R Core Team, 2020. R: A Language and Environment for Statistical Computing. R Foundation for Statistical Computing, Vienna, Austria. Retrieved from. https://www.R-project.org/.
Rach, O., Kahmen, A., Brauer, A., Sachse, D., 2017. A dual-biomarker approach for quantification of changes in relative humidity from sedimentary lipid D/H ratios. Clim. Past 13 (7), 741–757. https://doi.org/10.5194/cp-13-741-2017.
Rasmussen, E., 1985. A case study of a polar low development over the Barents Sea. Tellus A 37 (5), 407–418. https://doi.org/10.1111/j.1600-0870.1985.tb00440.x.
Rasmussen, T.L., Forwick, M., Mackensen, A., 2012. Reconstruction of inflow of atlantic water to isfjorden, svalbard during the Holocene: correlation to climate and seasonality. Mar. Micropaleontol. 94, 80–90. https://doi.org/10.1016/j.marmicro.2012.06.008.
Rasmussen, T.L., Thomsen, E., Skirbekk, K., Ślubowska-Woldengen, M., Kristensen, D.K., Koç, N., 2014. Spatial and temporal distribution of Holocene temperature maxima in the northern Nordic seas: interplay of Atlantic-, Arctic- and polar water masses. Quat. Sci. Rev. 92, 280–291. https://doi.org/10.1016/j.quascirev.2013.10.034.
Rawlins, M.A., Steele, M., Holland, M.M., Adam, J.C., Cherry, J.E., Francis, J.A., Groisman, P.Y., Hinzman, L.D., Huntington, T.G., Kane, D.L., 2010. Analysis of the Arctic system for freshwater cycle intensification: observations and expectations. J. Clim. 23 (21), 5715–5737. https://doi.org/10.1175/2010JCLI3421.1.
Reimer, P.J., Bard, E., Bayliss, A., Beck, J.W., Blackwell, P.G., Ramsey, C.B., Buck, C.E., Cheng, H., Edwards, R.L., Friedrich, M., 2013. IntCal13 and Marine13 radiocarbon age calibration curves 0–50,000 years cal BP. Radiocarbon 55 (4), 1869–1887. https://doi.org/10.2458/azu_js_rc.55.16947.
Risebrobakken, B., Dokken, T., Smedsrud, L.H., Andersson, C., Jansen, E., Moros, M., Ivanova, E.V., 2011. Early Holocene temperature variability in the Nordic Seas: the role of oceanic heat advection versus changes in orbital forcing. Paleoceanography 26 (4). https://doi.org/10.1029/2011PA002117.
Røthe, T.O., Bakke, J., Vasskog, K., Gjerde, M., D'Andrea, W.J., Bradley, R.S., 2015. Arctic Holocene glacier fluctuations reconstructed from lake sediments at Mitrahalvøya, Spitsbergen. Quat. Sci. Rev. 109, 111–125. https://doi.org/10.1016/j.quascirev.2014.11.017.
Røthe, T.O., Bakke, J., Støren, E.W., Bradley, R.S., 2018. Reconstructing Holocene glacier and climate fluctuations from lake sediments in Vårfluesjøen, northern Spitsbergen. Front. Earth Sci. 6, 91. https://doi.org/10.3389/feart.2018.00091.
Sachse, D., Billault, I., Bowen, G.J., Chikaraishi, Y., Dawson, T.E., Feakins, S.J., Freeman, K.H., Magill, C.R., McInerney, F.A., van der Meer, M.T.J., Polissar, P., Robins, R.J., Sachs, J.P., Schmidt, H.-L., Sessions, A.L., White, J.W.C., West, J.B., Kahmen, A., 2012. Molecular paleohydrology: interpreting the hydrogen-isotopic composition of lipid biomarkers from photosynthesizing organisms. Annu. Rev. Earth Planet Sci. 40 (1), 221–249. https://doi.org/10.1146/annurev-earth-042711-105535.
Sandgren, P., Snowball, I., 2002. Application of mineral magnetic techniques to paleolimnology. In: Last, W.M., Smol, J.P. (Eds.), Tracking Environmental Change Using Lake Sediments, Developments in Paleoenvironmental Research, vol. 2. Springer, Dordrecht.
IPCC, 2013. In: Stocker, T.F., Qin, D., Plattner, G.-K., Tignor, M., Allen, S.K., Boschung, J., Nauels, A., Xia, Y., Bex, V., Midgley, P.M. (Eds.), Climate Change 2013: The Physical Science Basis. Contribution of Working Group I to the Fifth Assessment Report of the Intergovernmental Panel on Climate Change. Cambridge University Press, Cambridge, United Kingdom and New York, NY, USA, 1535 pp.
Sundqvist, H.S., Kaufman, D.S., McKay, N., Balascio, N., Briner, J., Cwynar, L., Sejrup, H., Seppä, H., Subetto, D., Andrews, J., 2014. Arctic Holocene proxy climate database–new approaches to assessing geochronological accuracy and encoding climate variables. Clim. Past 10 (4), 1605–1631. https://doi.org/10.5194/cp-10-1605-2014.
Svendsen, J.I., Mangerud, J., 1997. Holocene glacial and climatic variations on Spitsbergen, Svalbard. Holocene 7 (1), 45–57. https://doi.org/10.1177/095968369700700105.
Thomas, E.K., Hollister, K.V., Cluett, A.A., Corcoran, M.C., Briner, J.P., 2020. Reconstructing Arctic precipitation seasonality using aquatic leaf wax δ2H in lakes with contrasting residence times. Paleoceanogr. Paleoclimatol. https://doi.org/10.1029/2020PA003886.
Thomas, E.K., McGrane, S., Briner, J.P., Huang, Y., 2012. Leaf wax δ^2H and varve-thickness climate proxies from proglacial lake sediments, Baffin Island, Arctic Canada. J. Paleolimnol. 48 (1), 193–207. https://doi.org/10.1007/s10933-012-9584-7.
Thomas, E.K., Briner, J.P., Ryan-Henry, J.J., Huang, Y., 2016. A major increase in winter snowfall during the middle Holocene on western Greenland caused by reduced sea ice in Baffin Bay and the Labrador Sea. Geophys. Res. Lett. 43 (10), 5302–5308. https://doi.org/10.1002/2016gl068513.
Thomas, E., Castañeda, I., McKay, N., Briner, J., Salacup, J., Nguyen, K., Schweinsberg, A., 2018. A wetter Arctic coincident with hemispheric warming 8,000 years ago. Geophys. Res. Lett. 45 (19) https://doi.org/10.1029/2018GL079517, 10,637-610,647.
Throckmorton, H.M., Newman, B.D., Heikoop, J.M., Perkins, G.B., Feng, X., Graham, D.E., O'Malley, D., Vesselinov, V.V., Young, J., Wullschleger, S.D., Wilson, C.J., 2016. Active layer hydrology in an arctic tundra ecosystem: quantifying water sources and cycling using water stable isotopes. Hydrol. Process. 30 (26), 4972–4986. https://doi.org/10.1002/hyp.10883.
van der Bilt, W.G., Bakke, J., Vasskog, K., D'Andrea, W.J., Bradley, R.S., Ólafsdóttir, S., 2015. Reconstruction of glacier variability from lake sediments reveals dynamic Holocene climate in Svalbard. Quat. Sci. Rev. 126, 201–218. https://doi.org/10.1016/j.quascirev.2015.09.003.
van der Bilt, W.G., D'Andrea, W.J., Bakke, J., Balascio, N.L., Werner, J.P., Gjerde, M., Bradley, R.S., 2018. Alkenone-based reconstructions reveal four-phase Holocene temperature evolution for High Arctic Svalbard. Quat. Sci. Rev. 183, 204–213. https://doi.org/10.1016/j.quascirev.2016.10.006.
van der Bilt, W.G., D'Andrea, W.J., Werner, J.P., Bakke, J., 2019. Early Holocene temperature oscillations exceed amplitude of observed and projected warming in Svalbard lakes. Geophys. Res. Lett. 46 https://doi.org/10.1029/2019GL084384, 14,732-14,741.
Vikhamar-Schuler, D., Førland, E.J., Lutz, J., Gjelten, H.M., 2019. Evaluation of Downscaled Reanalysis and Observations for Svalbard - Background Report for Climate in Svalbard 2100. Norwegian Centre for Climate Services (NCCS). NCCS report no. 4/2019.
Voldstad, L.H., Alsos, I.G., Farnsworth, W.R., Heintzman, P.D., Håkansson, L., Kjellman, S.E., Rouillard, A., Schomacker, A., Eidesen, P.B., 2020. A complete Holocene lake sediment ancient DNA record reveals long-standing high Arctic plant diversity hotspot in northern Svalbard. Quat. Sci. Rev. 234, 106207. https://doi.org/10.1016/j.quascirev.2020.106207.
Walker, D.A., Raynolds, M.K., Daniëls, F.J., Einarsson, E., Elvebakk, A., Gould, W.A., Katenin, A.E., Kholod, S.S., Markon, C.J., Melnikov, E.S., 2005. The circumpolar Arctic vegetation map. J. Veg. Sci. 16 (3), 267–282. https://doi.org/10.1111/j.1654-1103.2005.tb02365.x.
Werner, A., 1993. Holocene moraine chronology, Spitsbergen, Svalbard: lichenometric evidence for multiple Neoglacial advances in the Arctic. Holocene 3 (2), 128–137. https://doi.org/10.1177/095968369300300204.
Werner, K., Müller, J., Husum, K., Spielhagen, R.F., Kandiano, E.S., Polyak, L., 2016. Holocene sea subsurface and surface water masses in the Fram Strait–Comparisons of temperature and sea-ice reconstructions. Quat. Sci. Rev. 147, 194–209. https://doi.org/10.1016/j.quascirev.2015.09.007.
Wilkie, K.M., 2012. Compound-Specific Hydrogen Isotopes of Lipid Biomarkers in Lake El'gygytgyn, Ne Russia.. Open Access Dissertations. 561. https://scholarworks.umass.edu/open_access_dissertations/561.
Zhang, X., He, J., Zhang, J., Polyakov, I., Gerdes, R., Inoue, J., Wu, P., 2013. Enhanced poleward moisture transport and amplified northern high-latitude wetting trend. Nat. Clim. Change 3 (1), 47. https://doi.org/10.1038/nclimate1631.

Paper II

Journal of Hydrology 607 (2022) 127556

Contents lists available at ScienceDirect

Journal of Hydrology

journal homepage: www.elsevier.com/locate/jhydrol

Research papers

Arctic and sub-Arctic lake water δ^2H and $\delta^{18}O$ along a coastal-inland transect: Implications for interpreting water isotope proxy records

Sofia E. Kjellman [a,*], Elizabeth K. Thomas [b], Anders Schomacker [a]

[a] Department of Geosciences, UiT The Arctic University of Norway, P.O. Box 6050 Langnes, NO-9037 Tromsø, Norway
[b] Department of Geology, University at Buffalo, State University of New York, 126 Cooke Hall, Buffalo, NY 14260, USA

ARTICLE INFO

This manuscript was handled by Sally Elizabeth Thompson, Editor-in-Chief, with the assistance of Carlos Oroza, Associate Editor

Keywords:
Lake water isotopes
Precipitation isotopes
Moisture source
Evaporation
Seasonality
Proxy interpretation

ABSTRACT

High-latitude lakes are sensitive to climate change and store information about large-scale circulation changes and catchment-integrated processes. Lakes are mainly recharged by meteoric water, meaning that some lake sediment proxies may indirectly archive the stable isotopic composition of hydrogen (δ^2H) and oxygen ($\delta^{18}O$) of past precipitation. Yet, despite similar precipitation input, lakes within a region may exhibit a wide range of isotopic values due to the varying influence of inflow seasonality and evaporation. Moreover, the relative sensitivity of each lake to these controls may vary through time, something that is difficult to account for. Here, we evaluate the impact of variable inflow δ^2H and evaporation on the lake water isotopic composition across northern Fennoscandia (Norway, Finland, and Sweden). We measured lake water δ^2H and $\delta^{18}O$ of 135 lakes spanning from the north Norwegian coast along a 460 km transect to the Bothnian Bay, sampled from 2018 to 2020. Our data show that both coastal and inland lakes are sensitive to distillation during moisture transport, and that lakes farther from the Atlantic Ocean are additionally impacted by evaporation. We estimated the isotopic composition of lake water inflow values for evapo-concentrated transect lakes (δ^2H_I) using a Bayesian method. Resampled transect lakes had more depleted δ^2H_I in 2020 than in 2019, indicating either that precipitation was ^2H-depleted or that more winter precipitation contributed inflow to the lakes in 2020 compared to in 2019. We suggest that the more ^2H-depleted values in 2020 were a response to a snow-rich winter, associated with extremely positive Arctic Oscillation (AO+) conditions and increased moisture supply from the North Atlantic. We find evidence that lake water isotopic variability in this region reflects a combination of seasonal precipitation changes associated with atmospheric circulation changes, and catchment-integrated evaporation. Careful consideration of the variable sensitivity to these processes is essential when making inferences about past climate based on lake water isotope proxies.

1. Introduction

Amplified warming in the northern high latitudes is predicted to cause an intensification of the hydrological cycle (Rawlins et al., 2010; Collins et al., 2013; Bintanja & Selten, 2014; Bintanja et al., 2020). These changes affect both terrestrial and ocean freshwater budgets and have great cryospheric and ecological impact (Bring et al., 2016; Vihma et al., 2016; Wrona et al., 2016). Arctic precipitation change is caused by two main mechanisms with different seasonal imprints. Increased local evaporation mainly occurs in fall and winter, due to accelerated sea-ice loss (Bintanja & Selten, 2014; Bailey et al., 2021). In contrast, poleward moisture transport is greatest in summer, when the meridional temperature and moisture gradients increase the most and continental moisture sources play a significant role (Vázquez et al., 2016; Singh et al., 2017). Furthermore, greater interannual variability in the summer moisture influx from extrapolar regions is projected to contribute to increasing interannual variability in Arctic precipitation (Bintanja et al., 2020). The projected trends remain uncertain, relying on sparse observational data to describe complex spatiotemporal patterns. To improve the constraints on long-term variability in precipitation and atmospheric circulation, we can use lake-water-derived proxy records (Sundqvist et al., 2014; Linderholm et al., 2018).

Stable isotope ratios of oxygen ($\delta^{18}O$) and hydrogen (δ^2H) in precipitation are frequently used to infer processes in the hydrological cycle due to their sensitivity to changes in atmospheric temperature, moisture, and circulation (Dansgaard, 1964; Rozanski et al., 1993; Gat, 1996).

* Corresponding author.
E-mail addresses: sofia.e.kjellman@uit.no (S.E. Kjellman), ekthomas@buffalo.edu (E.K. Thomas), anders.schomacker@uit.no (A. Schomacker).

https://doi.org/10.1016/j.jhydrol.2022.127556
Received 12 July 2021; Received in revised form 21 January 2022; Accepted 27 January 2022
Available online 4 February 2022

Much of the variation in precipitation isotopic composition results from equilibrium fractionation during phase changes (e.g., evaporation, condensation, and freezing) during transport from the moisture source to the precipitation site (Gat, 1996). Equilibrium fractionation is highly temperature dependent, and therefore varies both spatially and temporally. The global average relationship between δ^2H and $\delta^{18}O$ in meteoric waters is described by the global meteoric water line (GMWL), defined as $\delta^2H = 8 \times \delta^{18}O + 10$ (Craig, 1961). Local meteoric water lines (LMWLs) account for site-specific variation in the isotopic composition due to factors including moisture sources, transport conditions and seasonality. For example, in seasonally snowy regions, slopes of the LMWLs tend to be similar to the GMWL, but the intercepts lower than in other regions due to snow formation processes (Putman et al., 2019).

The isotopic signal of precipitation can be preserved in climate proxies, allowing us to extend our records back beyond the instrumental period. In northern Fennoscandia, the oldest temperature and precipitation amount observations date back to the 1860′s (Alexandersson, 2002), whereas precipitation isotope records are limited to a handful of sites, most of them only measuring $\delta^{18}O$, covering timespans of less than ten years each, and only after 1975 (IAEA/WMO, 2019).

Lakes are excellent archives of past climate change, as their isotopic composition often at least partially reflects precipitation isotopes, and they contain a wide range of proxies that preserve the lake water isotopic composition. In northern Fennoscandia, reconstructions of Holocene precipitation, humidity and atmospheric circulation have mainly been based on $\delta^{18}O$ from lacustrine carbonates (Hammarlund et al., 2002; Rosqvist et al., 2007), diatom biogenic silica (Shemesh et al., 2001; Rosqvist et al., 2004, 2013; Jonsson et al., 2010), and lake sediment cellulose (St. Amour et al., 2010). Other studies use δ^2H of lipid biomarkers to reconstruct different aspects of the water cycle (Nichols et al., 2009; Thienemann et al., 2019; Balascio et al., 2020).

Recent dual biomarker approaches have focused on comparing leaf waxes produced by aquatic and terrestrial plants to reconstruct Holocene and Last Interglacial atmospheric circulation changes, precipitation seasonality and summer moisture balance (Rach et al., 2017; Thomas et al., 2018, 2020; Curtin et al., 2019; Kjellman et al., 2020; Katrantsiotis et al., 2021). These approaches rely on the assumption that the aquatic plant biomarkers are minimally impacted by evaporative enrichment. This might be true for lakes in regions with positive moisture balance (precipitation > evaporation), but not for lakes in more arid areas (Cluett & Thomas, 2020).

When lakes undergo evapo-concentration, they will deviate from their starting isotopic compositions along the MWL due to kinetic fractionation, and evolve along a local evaporation line (LEL; Gat, 1996). The slope of the LEL is controlled by atmospheric conditions (e.g., temperature, relative humidity, and the isotopic composition of atmospheric moisture) and is usually between 5 and 6 at the mid-latitudes and sometimes steeper at high-latitudes (Gibson et al., 2008). If the slope of the LEL is known, it can be used, along with the lake water δ^2H and $\delta^{18}O$ values, to calculate the intersection between the LEL and the MWL, which represents lake water inflow values. One common approach to estimate regional LEL slopes is to adopt a linear regression fit to a group of lakes within the region (Clark & Fritz, 1997). This approach assumes that all the isotopic variation is a result of evaporation, and that all lakes in a region start with the same source isotopic composition (i.e., the lake inflow value; Bowen et al., 2018). This is seldom true, especially for systems with a strong seasonality. At high latitudes, the relative proportion of isotopically depleted snowfall and isotopically enriched rainfall can change between years, resulting in different inflow values from year to year (Tondu et al., 2013). Another approach is to apply theoretical modeling, based on the Craig-Gordon model, which requires knowledge of the isotopic composition of both precipitation and atmospheric moisture (Craig & Gordon, 1965), to infer inflow values for each lake individually. Regardless the technique used to calculate inflow values from evapo-concentrated lakes, most lake water δ^2H and $\delta^{18}O$ values contain information about both the degree of evaporative enrichment and the inflow isotopic composition. Thus, lake water δ^2H and $\delta^{18}O$ values can be used to infer past change in precipitation δ^2H and $\delta^{18}O$ values and evaporation, but the influence of both inflow and evaporation also confounds isotopic interpretation. Examining spatial and temporal variations in lake water δ^2H and $\delta^{18}O$ values along modern climate gradients can guide interpretations of lake water isotope proxy records.

In northern Fennoscandia, Holocene changes in lake-water-derived $\delta^{18}O$ and δ^2H are often assumed to reflect changes in North Atlantic atmospheric and oceanic circulation (e.g., Hammarlund et al., 2002; Rosqvist et al., 2007; Thienemann et al., 2019). The North Atlantic is the predominant moisture source, but during periods with a more southerly position of the polar front, precipitation can originate from Arctic air masses (Rosqvist et al., 2007). This is further complicated by the fact that Arctic and sub-Arctic lakes can display a wide range of water isotopic compositions, despite similar precipitation input (Gibson & Edwards, 2002; Jonsson et al., 2009; Cluett & Thomas, 2020). This is because meteoric water inputs are modulated by catchment characteristics and additionally modified by lake water evaporation (Leng & Marshall, 2004; Cluett & Thomas, 2020). Lake and catchment morphometry and precipitation amount control the throughflow regime of the lake, since these factors govern the lake water residence time (Jonsson et al., 2009). Furthermore, the travel time of water through surface and groundwater systems and into lakes varies in time and space depending on factors such as catchment size, slope, soil type and seasonality (Botter et al., 2010; Heidbüchel et al., 2012; Jutebring Sterte et al., 2021). Lakes with wetland-dominated catchments generally have shorter residence times and lower evaporation-to-inflow (E/I) ratios (Gibson et al., 2002). To make inferences about past climate based on changes in lake-water-derived $\delta^{18}O$ and δ^2H, we therefore need to understand both the regional climate and local hydrology (Jonsson et al., 2009; Jones et al., 2016; Cluett & Thomas, 2020).

Jonsson et al. (2009) measured the water isotopic composition of 11 lakes close to Abisko in northwestern Sweden and found that lakes in this region are mainly recharged by precipitation and shallow groundwater, with little influence of evaporation. They also demonstrated that the lake water isotopic composition varies on a seasonal basis, and that lakes with short residence time (<6 months) are more sensitive to seasonal changes, whereas lakes with longer residence times (>6 months) have lake water isotopic compositions closer to mean annual precipitation. Balascio et al. (2018) measured modern lake water isotopic composition of 15 lakes along a transect from near Tromsø in Norway to the Finnish-Swedish border. The lakes displayed decreasing isotopic values moving inland from the coast, and most of them showed little influence of evaporation. On western Greenland, a recent study of 140 lakes along an aridity gradient between the Labrador Sea and the Greenland Ice Sheet margin demonstrated that lake water $\delta^{18}O$ and δ^2H are impacted by inflow isotopic composition and catchment-integrated evaporation in all lakes, but that the relative importance of those two variables in a given lake depends on climate and lake and catchment morphometry (Cluett & Thomas, 2020).

Here, we investigate the water isotopic composition of lakes across Arctic and sub-Arctic Fennoscandia (Norway, Finland, and Sweden) to better constrain the influence of inflow isotopic composition and seasonality on the lake water isotopic composition throughout this region. We target lakes across a 460-km-long climatic gradient to explore the relative importance of inflow values and evaporative enrichment, and consider the interannual variability by comparing the isotopic composition from lakes sampled in several years. By identifying modern controls on the lake water isotopic composition, we aim to evaluate the sensitivity of lake water to changes in these hydrological and climate processes. This information is crucial to identify lakes that have the potential to accurately record the aspect of the water cycle we are interested in, and to make solid proxy interpretations.

2. Regional setting

The study area spans from the North Atlantic Ocean in the northwest to the Bothnian Bay in the southeast, between 65.74°N to 71.11°N and 18.39°E to 30.06°E (Fig. 1). The Late Weichselian Scandinavian Ice Sheet retreated from the outer coast *c.* 18–16 cal. kyr BP, whereas the interior parts were not ice-free until 11–10 cal. kyr BP (Hughes et al., 2016; Stroeven et al., 2016). The coast is characterized by alpine topography, with steep mountains intersected by subglacially eroded fjords and U-shaped valleys. The highest mountains are the Lyngen Alps, reaching up to *c.* 1800 m a.s.l. (Fig. 1b-c). The bedrock is often exposed, especially at high elevation, whereas areas closer to sea level are partly covered by Quaternary deposits (mainly till; NGU, 2021). To the southeast, the Scandinavian Mountains gradually become lower, transitioning into more gently undulating hilly terrain, reaching sea level by the Bothnian Bay (Fig. 1c). East of the Scandinavian Mountains, the till cover becomes thicker (Hirvas et al., 1988) and glaciofluvial deposits (e.g., eskers) are common (GTK, 2021).

Many of the lakes in the region owe their existence to the advances and retreats of the ice sheet and glaciers during the last glacial/interglacial cycle (Brosius et al., 2021). Lakes formed in depressions carved by the ice itself, some were dammed by glacial deposits, and still others are kettles formed due to melting of dead-ice. These processes combined resulted in a landscape with numerous lakes with diverse morphometrics. Many lakes and ponds are also associated with the minerotrophic aapa mires, characteristic for the area (Ruuhijärvi, 1983). These types of mire complexes form in flat areas with high precipitation and low evaporation (Seppä, 2002).

The water in the lakes can reflect different precipitation seasonality depending on duration of lake-ice cover, governing the amount of snowmelt bypass (i.e., how much of the snow that melts off the landscape before the lake becomes ice free; MacDonald et al., 2017). Along the Sweden-Finland border, the average duration of ice cover on the lakes (1961–2000) varies between 200 and 225 days (Laasanen, 1982; Eklund, 1999; Korhonen, 2006). Average lake freeze-up is around October 15 in northwestern Finland and November 5 in the southernmost part of the study area, whereas ice break-up occurs earlier in the south (May 18) than in the north (June 15) (Laasanen, 1982; Korhonen, 2006). In Norway, north of the Arctic Circle, the duration of ice cover on 18 lakes was monitored for periods of 7–61 years (with an average observation period of 27 years) between 1912 and 1987. Ice-cover duration varies between 175 and 220 days with a mean of 198 days. The average freeze-up date for these lakes is November 10, and the average ice break-up date is May 29 (L'Abée-Lund et al., 2021). Air temperature is the most important factor for the timing of freeze-up and break-up (Palecki & Barry, 1986; Weyhenmeyer et al., 2004), modulated by regional atmospheric circulation (Blenckner et al., 2004). Small and shallow lakes generally freeze over earlier than large and deep lakes, but lake size has less influence on the break-up dates (Korhonen, 2006).

Most of the study area lies in the middle and northern boreal zones, with areas above the tree line classified as alpine (Moen, 1998). The middle boreal zone is characterized by coniferous forest and mires, dominating the southern part of the study area and found in the lowlands along parts of the Norwegian coast. Deciduous trees are also common. The central part of the study area belongs to the northern boreal zone, characterized by birch forests, low-growing coniferous forest, and mires. In mountainous areas, the northern boreal zone transitions into tundra. The low-alpine areas are characterized by continuous cover of dwarf-shrubs and mires, whereas grasses, sedges, mosses, lichens, and forbs dominate the mid-alpine zone. At higher elevations (the high-alpine zone), the vegetation cover is sparse. Plant cover can affect runoff into lakes, and therefore the seasonal lake water inflow values (Gibson & Edwards, 2002).

The topography contributes to a strong hydroclimate gradient, with the Scandinavian Mountains acting as a barrier for air masses from the North Atlantic. The study region is located in the polar front zone, where dynamic low-pressure systems bringing warm moist air masses from the Atlantic meet dry cool air from the Arctic. The prevailing westerly winds bring the humid Atlantic air onshore, and precipitation amounts are highest along the southwestern coast due to orographic lift where the westerlies first meet the mountains (Hanssen-Bauer and Førland, 2000). Most of the moisture falls on the windward side of the mountains, sheltering the leeward side of the mountains from precipitation (Uvo, 2003). The west coast experiences mild winters and cool summers,

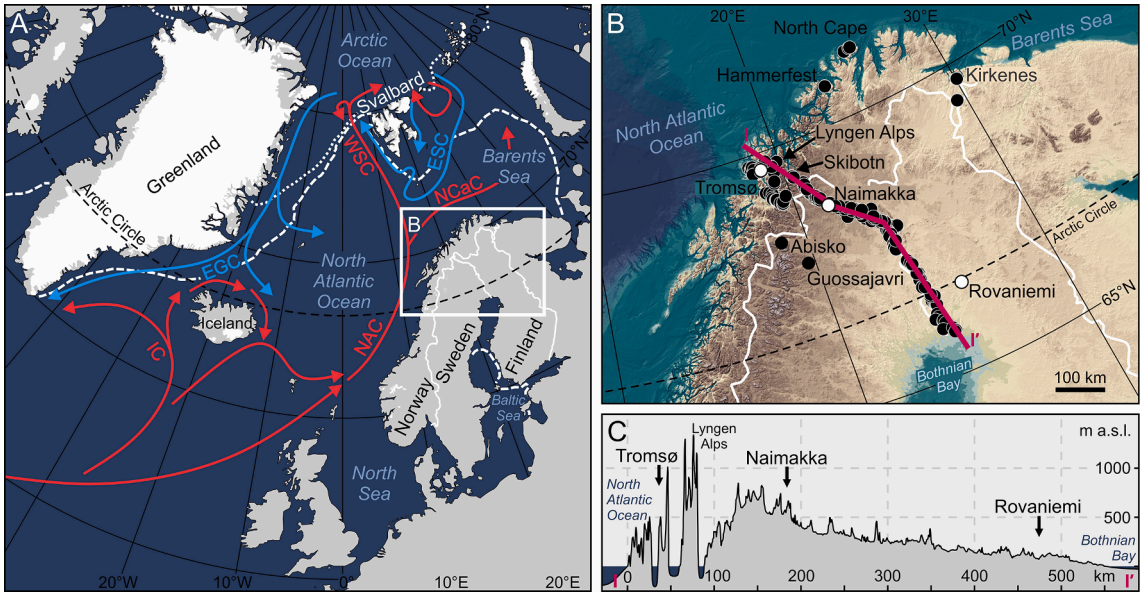

Fig. 1. (a) Overview map of the North Atlantic region, with major ocean surface currents (warm currents in red, cold in blue; NAC = North Atlantic Current; NCaC = North Cape Current; WSC = West Spitsbergen Current; IC = Irminger Current, ESC = East Spitsbergen Current; EGC = East Greenland Current), and median winter (white dashed line) and summer (white dotted line) sea-ice extent 1981–2010 (National Snow and Ice Data Center, 2019). (b) Map of the study area, showing locations of meteorological stations (white circles), sampled lakes and place names mentioned in the text (black circles) and extent of elevation profile in C (red line). Background map from IBCAO (Jakobsson et al., 2012). (c) Elevation profile from the North Atlantic Ocean in the northwest to the Bothnian Bay in the southeast. (For interpretation of the references to color in this figure legend, the reader is referred to the web version of this article.)

whereas the climate in the interior is more continental, with colder winters and warmer summers (Fig. 2a).

Seasonal variation in moisture source and moisture availability can be affected by changes in sea-ice cover. During winter (January-March), the Arctic sea ice reaches its maximum southward extent, covering the northern and eastern parts of the Barents Sea (National Snow and Ice Data Center, 2019; Fig. 1a). In winters with low sea-ice extent in the Barents Sea, more Arctic moisture can reach northern Fennoscandia (Bailey et al., 2021). Sea ice has not formed along the Norwegian coast during the Holocene (Belt et al., 2015) except in inner fjords, where it still forms today (O'Sadnick et al., 2020). Seasonal ice cover in the Bothnian Bay lasts 130–200 days, with sea ice forming in the shallow coastal areas in October–November and reaching a maximum ice extent in March (Haapala et al., 2015).

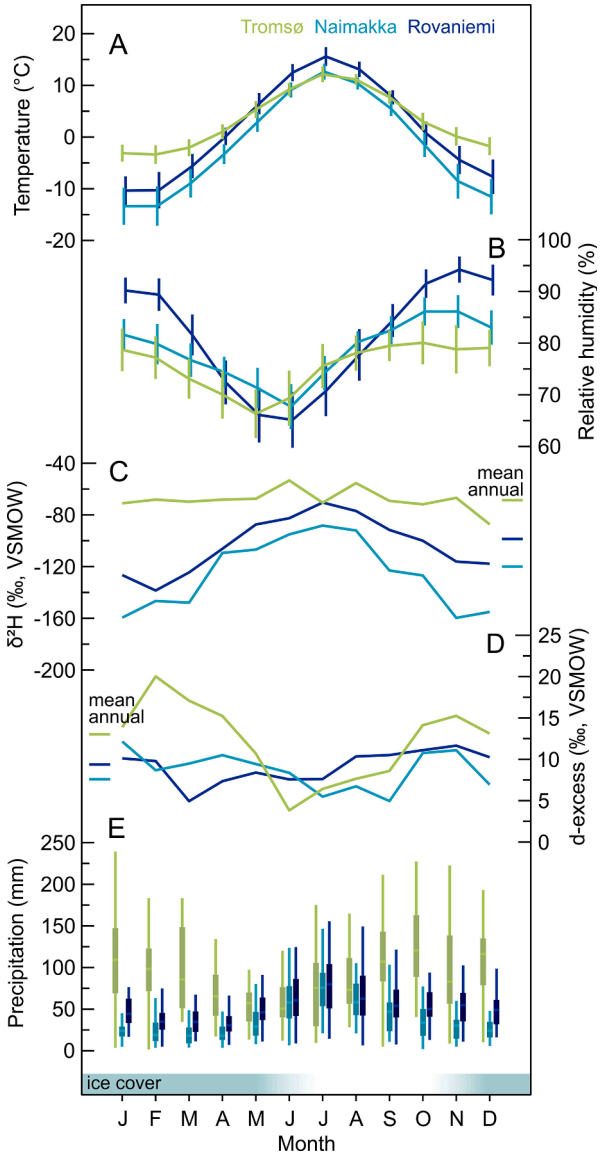

Fig. 2. Climate data from Tromsø, Naimakka and Rovaniemi (for locations, see Fig. 1). Mean monthly air temperatures (a) and relative humidity (b) between 1991-2020 (for Naimakka calculated using all months with>80% data coverage, 1995–2020). Vertical bars represent one standard deviation. (c-d) Amount-weighted monthly δ^2H and d-excess in precipitation from Tromsø (2019–2021; this study), and Naimakka (1990–1995) and Rovaniemi (2003–2014), both from IAEA/WMO (2019). (e) Monthly accumulated precipitation, 1991–2020. For each box plot, the middle line displays the median precipitation, the box represents the 25% to 75% quartile range and whiskers the maximum and minimum values. Temperature and precipitation data are retrieved from FMI (2021), MET Norway (2021) and SMHI (2021).

Winter precipitation is also strongly influenced by the North Atlantic Oscillation (NAO), controlling the strength of the westerlies (Hurrell, 1995; Uvo, 2003; Irannezhad et al., 2014). During times of positive NAO index (large atmospheric pressure difference between the Iceland Low and the Azores High), the North Atlantic storm track shifts northwards, increasing the moisture flux to Scandinavia (Hurrell, 1995; Marshall et al., 2001; Uvo, 2003). The NAO is closely related to the Arctic Oscillation (AO), which is linked to the polar low-pressure system, also known as the polar vortex (Thompson & Wallace, 1998). In the winter of 2019/2020 (January-March), which preceded one of our sampling campaigns, an exceptionally strong stratospheric polar vortex related to extreme AO+ conditions (lower than average air pressure over the Arctic and higher than average pressure over the northern Atlantic and Pacific Oceans) caused strong positive temperature (warmer) and precipitation (wetter) anomalies. The highest precipitation anomalies were observed between 60 and 70°N, greatly affecting the Norwegian coast (Lawrence et al., 2020). In contrast, some extreme snowfall events can be attributed to cold air outbreaks during strongly negative NAO and AO, when dry polar air from sea-ice covered areas moves in over a relatively warm ocean, creating large sea-air heat and moisture exchange (Shapiro et al., 1987; Papritz & Sodemann, 2018). One example of an event like this occurred in February 2018, when anomalously high temperatures and low sea-ice extent in the Barents Sea caused a high net moisture flux to the atmosphere and extreme snowfall over northern Europe (Bailey et al., 2021).

In summer, the atmospheric circulation patterns are generally not as strong, and more precipitation forms due to local convection (Jaagus, 2009). Notably, a recent Pan-Arctic study of the isotopic composition of summer 2018 rainfall identified precipitation air masses in Finland originating from two different transport regimes (Mellat et al., 2021). During NAO+ conditions, prevailing westerlies supplied Atlantic moisture, whereas summer cyclone activity related to a deepening low-pressure system over the Kara Sea caused northerly airflow and moisture transport from the Barents Sea (Mellat et al., 2021). These seasonal and synoptic changes in source impact the precipitation isotopic composition in this region (see section 2.1).

At the meteorological station in Tromsø (69.65°N, 18.94°E; 100 m a.s.l.; Fig. 1), the mean annual air temperature (MAAT, 1991–2020) is 3.3 °C and mean annual precipitation (MAP, 1991–2020) is 1091 mm (MET Norway, 2021). At the two more inland sites Naimakka (68.68°N, 21.53°E; 403 m a.s.l.) and Rovaniemi (66.50°N, 25.75°E; 107 m a.s.l.), MAAT is –1.6 °C and 1.5 °C, and MAP 466 mm and 633 mm, respectively (FMI, 2021; SMHI, 2021). Naimakka is the most continental (coldest and driest) of these sites, located on the eastern side of the Scandinavian Mountains (Fig. 1). Rovaniemi is farther from the North Atlantic Ocean, but experiences a warmer and wetter climate than Naimakka, perhaps due to its proximity to the Bothnian Bay. Significant differences in precipitation amount between the coastal and inland sites occur in fall and winter (Fig. 2e). This is the season when the relative temperature difference between (warm) ocean and (cold) land is greatest, causing high precipitation amounts at coastal locations such as Tromsø. In Rovaniemi and Naimakka, the relative humidity is high during the fall and winter months (Fig. 2b), and most precipitation falls during the warm months (Fig. 2e).

2.1. Isotopic setting

Northern Fennoscandia receives moisture from sources with different isotopic composition, where Arctic and Baltic sea surface waters are relatively depleted compared to the predominant North Atlantic source region, and the western Barents Sea (LeGrande & Schmidt, 2006; Bonne et al., 2019). In our study area, precipitation δ^2H and $\delta^{18}O$ have been monitored in Naimakka (1990–1995) and Rovaniemi (2003–2014) as part of the Global Network of Isotopes in Precipitation (GNIP; IAEA/

WMO, 2019; Fig. 1b). These data yield LMWLs with the equations $\delta^2H = 7.61\times\delta^{18}O + 2.59$ (Naimakka) and $\delta^2H = 7.70\times\delta^{18}O + 5.01$ (Rovaniemi; Fig. 3), having slightly lower slopes than the GMWL and lower intercepts. Precipitation is most depleted at Naimakka, where amount-weighted mean annual precipitation δ^2H and $\delta^{18}O$ are –119.94‰ and –16.04‰, respectively (Figs. 2 and 3). The mean isotopic composition of precipitation δ^2H and $\delta^{18}O$ during the ice-free season (June-October) are –102.38‰ and –13.70‰, and during the ice-cover season (November-May) –144.14‰ and –19.40‰. In Rovaniemi, amount-weighted mean annual precipitation δ^2H and $\delta^{18}O$ are –98.56‰ and –13.52‰, whereas ice-free season mean values are –83.31‰ and –11.59‰ and ice-cover season mean values –113.43‰ and –15.35‰, respectively. The amount-weighted mean annual values in Rovaniemi are close to Naimakka mean summer (ice-free season) values, and 21.38‰ (δ^2H) and 2.52‰ ($\delta^{18}O$) enriched compared to Naimakka amount-weighted annual values.

For regions with no GNIP stations nearby, interpolated precipitation isotope values can be generated using the Online Isotopes in Precipitation Calculator (OIPC; Bowen, 2021). However, these values can be biased towards the closest GNIP station values, not capturing local variability. Balascio et al. (2018) noted that water from lakes close to Tromsø was significantly enriched compared to both annual and summer OIPC estimations, indicating that the OIPC generates too depleted values for Tromsø, located at lower elevation and more coastal than the nearest GNIP stations. To evaluate the modern isotopic range of precipitation by the coast, we analyzed precipitation samples collected in Tromsø (69.68°N, 18.96°E; 73 m a.s.l.) between September 6, 2019, and September 5, 2021 (n = 407). These data yield a LMWL with the equation $\delta^2H = 6.68\times\delta^{18}O - 0.85$, having a lower slope and intercept than Rovaniemi and Naimakka (Fig. 3). The amount-weighted mean annual precipitation δ^2H and $\delta^{18}O$ values in Tromsø are –68.61‰ and –10.20‰, respectively (Figs. 2 and 3). This is 42.39‰ and 4.70‰ enriched compared to the OIPC estimated mean annual values (–111‰ and –14.9‰) for δ^2H and $\delta^{18}O$ at this site, respectively (Bowen, 2021). The mean annual precipitation values in Tromsø are 29.95‰ and 51.33‰ (^2H) and 3.32‰ and 5.84‰ (^{18}O) enriched compared to Rovaniemi and Naimakka, respectively. Mean ice-free season precipitation δ^2H and $\delta^{18}O$ values in Tromsø are –65.23‰ and –9.19‰, and ice-cover season mean values are –70.63‰ and –10.81‰ (Fig. 3).

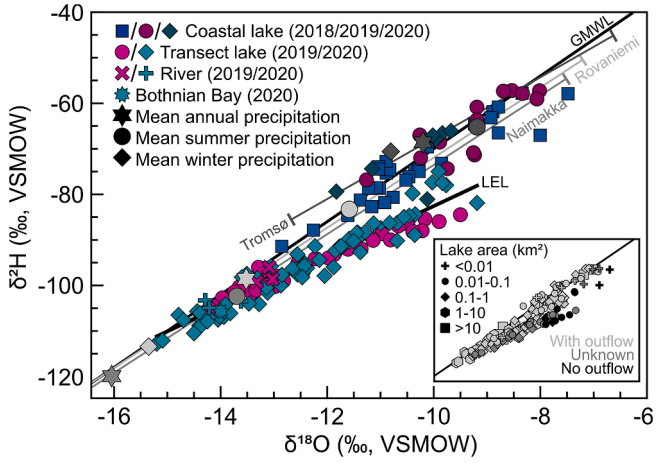

Fig. 3. $\delta^{18}O$ versus δ^2H values for all lakes and rivers sampled from 2018 to 2020, plotted against the global meteoric water line (GMWL, $\delta^2H = 8\times\delta^{18}O + 10$) and local meteoric water lines (LMWLs) from Tromsø ($\delta^2H = 6.68\times\delta^{18}O - 0.85$), Naimakka ($\delta^2H = 7.61\times\delta^{18}O + 2.59$) and Rovaniemi ($\delta^2H = 7.70\times\delta^{18}O + 5.01$). Amount-weighted mean annual, mean ice-cover (November-May = winter) and mean ice-free season (June-October = summer) precipitation are displayed for the three stations in grey. Mean ice-cover season precipitation $\delta^{18}O$ and δ^2H for Naimakka are too depleted (–19.40‰ and –144.14‰, respectively) to be displayed in the plot. Local evaporation line (LEL) is included for the transect lakes ($\delta^2H = 5.50\times\delta^{18}O - 27.55$). Inset panel has the same axes as the main figure and shows values by lake size (symbol) and throughflow regime (color).

3. Materials and methods

3.1. Water sample collection and isotope analysis

We collected lake water samples from a total of 135 lakes in northern Norway, Finland, and Sweden (Fig. 1, Supplementary Information) between 2018 and 2020. Most of the samples were collected during the first week of July, in 2018, 2019 and 2020. This is after the snowmelt season, although some high elevation lakes are fed by snowmelt throughout summer. In July 2018, we sampled lakes in the coastal Tromsø area (n = 30), and at the end of June 2019 along the north Norwegian coast (n = 9). The July 2019 and 2020 field campaigns targeted lakes (n = 35 and n = 68, respectively) along a NW-SE transect from southeast of the Lyngen Alps to the Bothnian Bay (hereafter referred to as the 'transect lakes'), between 69.4°N, 20.3°E and 65.7°N, 24.6°E (Fig. 1b–c). This transect spans *c.* 460 km, with lakes spanning elevations from close to sea level in NW and SE, up to *c.* 560 m a.s.l. close to the tripoint between Norway, Finland, and Sweden (Fig. 1c). We also collected samples from the Muonio and Torne Rivers (two rivers forming the border between Sweden and Finland) and the Bothnian Bay. To evaluate the interannual variability, we sampled 12 of the lakes along the transect and two locations on the Muonio River for two consecutive years. Furthermore, 11 of the transect lakes were sampled in July 2013 by Balascio et al. (2018), and five have been sampled all three years (2013, 2019 and 2020). Additionally, a couple of the coastal lakes were resampled in July 2019 and 2020 (n = 2 and n = 4, respectively) and/or during other times of the year (n = 5; Supplementary Information). Two coastal lakes were sampled for the first time in 2020. We collected the samples from the shoreline, approximately 10 cm below the lake surface to avoid evaporatively enriched water and stored them in 4 mL glass vials with no headspace. The vials were sealed with Parafilm to prevent evaporation during transportation and storage.

Precipitation samples were collected in Tromsø (69.68°N, 18.96°E; 73 m a.s.l.) from September 6, 2019, to September 5, 2021 (n = 407). Samples were collected each morning, using a 4-inch diameter RG202 Stratus All-Weather Rain Gauge. Liquid precipitation was collected using a funnel and an inner 1-inch cylinder, and solid precipitation from the 4-inch cylinder. The samples were transferred to 4 mL glass vials, sealed with Parafilm, and kept at 4 °C until analysis. Frozen samples were brought inside and melted in a sealed container at room temperature before transfer. Prior to analysis, all samples (lake water and precipitation) were filtered through a 0.2-μm PTFE filter.

The lake water samples collected in 2018 and 2019 were measured on a Picarro L2130-i WS-CRDS analyzer with vaporization module V1102-i coupled to a CTC PAL autosampler, at the Organic and Stable Isotope Biogeochemistry Laboratory at the University at Buffalo, USA. Each sample was measured four times, and the first injection discarded. Reported values are the average of the last three measurements. Calibration to the VSMOW scale was done using three in-house standards, spanning a range of –265.86 to + 21.43‰ for δ^2H and –33.62 to + 12.41‰ for $\delta^{18}O$, calibrated against primary standards (GISP, VSMOW2, and SLAP2) from the International Atomic Energy Agency (IAEA). A memory correction was applied, following van Geldern & Barth (2012). Average standard deviations of replicate measurements were 0.08‰ and 0.02‰ for δ^2H and $\delta^{18}O$, respectively. For lake water samples collected in 2020, and for all precipitation samples, δ^2H and $\delta^{18}O$ were measured on a Picarro L2140-i WS-CRDS with a A0211 vaporizer and an A0325 autosampler at the Facility for advanced isotopic research and monitoring of weather, climate, and biogeochemical cycling (FARLAB), University of Bergen, Norway. Each sample was measured 12 times, and the reported values are averaged over the last four to six injections. Calibration was done using a drift standard and two laboratory

standards, spanning a range of –308.14 to + 9.2‰ for δ^2H and –40.06 to + 1.77‰ for $\delta^{18}O$, calibrated against VSMOW2 and SLAP2. To reduce memory effects, a 2-component memory correction was applied, following Gröning (2011). Average standard uncertainties for calibrated measurement values (provided according to Gröning, 2018) were 0.43‰ and 0.06‰ for δ^2H and $\delta^{18}O$, respectively.

Isotope ratios are reported in per mil (‰) relative to Vienna Standard Mean Ocean Water (VSMOW), where $\delta = 1000\times((R_{sample}/R_{VSMOW}) - 1)$ and R is the ratio between $^2H/^1H$ or $^{18}O/^{16}O$. Deuterium excess (d-excess) was calculated as d-excess $= \delta^2H - 8\times\delta^{18}O$ (Dansgaard, 1964). The daily precipitation data were converted into monthly amount-weighted mean values using the equation $\delta_{aw} = \frac{1}{P}\times\sum_{i=1}^{n}(p_i\times\delta_i)$, where P and p_i are the monthly and daily precipitation amounts (in mm), δ_i is δ^2H or $\delta^{18}O$ and n is the number of sampling days.

3.2. Inferring inflow δ^2H values

To estimate lake inflow δ^2H and $\delta^{18}O$ values for the evapo-concentrated transect lakes, we applied the Bayesian 'MWL source implementation' method by Bowen et al. (2018). This method allows the user to supply a MWL equation and a hypothesized LEL slope, each with confidence intervals. Since the LMWLs in Naimakka and Rovaniemi are parallel to and have similar intercepts as the GMWL (Fig. 3), we used the default MWL equation provided with the model, which is a re-calibrated GMWL ($\delta^2H = 8.01\times\delta^{18}O + 9.57$; $n = 80{,}672$; Bowen et al., 2018). The GMWL has much less uncertainty than the LMWLs, which are constrained by only hundreds of data points. To allow for interannual comparison, we based the LEL estimations on linear regression using the isotopic composition of lakes sampled in both 2019 and 2020 ($n = 12$). To run the model, we supplied the estimated LEL slope for each subset (4.82 and 5.18 for 2019 and 2020, respectively) with a standard deviation of 0.5 (as suggested by Bowen et al., 2018), lake water δ^2H and $\delta^{18}O$ with uncertainties and covariance (0.95), and the number of iterations (10,000). We acknowledge the assumptions involved in a regression-based approach for LEL slope estimation, but consider the supplied LEL slopes to be a good starting estimate, because they agree with theoretical LEL slope values (~5) modeled by Gibson et al. (2008). Given uncertainties in the LEL regression approach, we do not interpret interannual or spatial differences in LELs, and instead use them as a guide to infer whether lakes have experienced evaporative enrichment. We present modeled mean source water values, hereafter referred to as inferred inflow δ^2H (δ^2H_I). For the discussion where we compare the seasonality of inflow between coastal and transect lakes, we include only the coastal lakes that are through-flowing, as lake water δ^2H (δ^2H_L) in these lakes is not significantly affected by evaporative enrichment, and therefore equal to δ^2H_I. We exclude small isolated coastal basins, since we do not have a well-constrained estimate of the LEL by the coast.

4. Results

4.1. Lake water isotopic composition

The lake water surface samples from 2018 to 2020 span a broad range of isotopic compositions (Fig. 3). Generally, lakes close to the

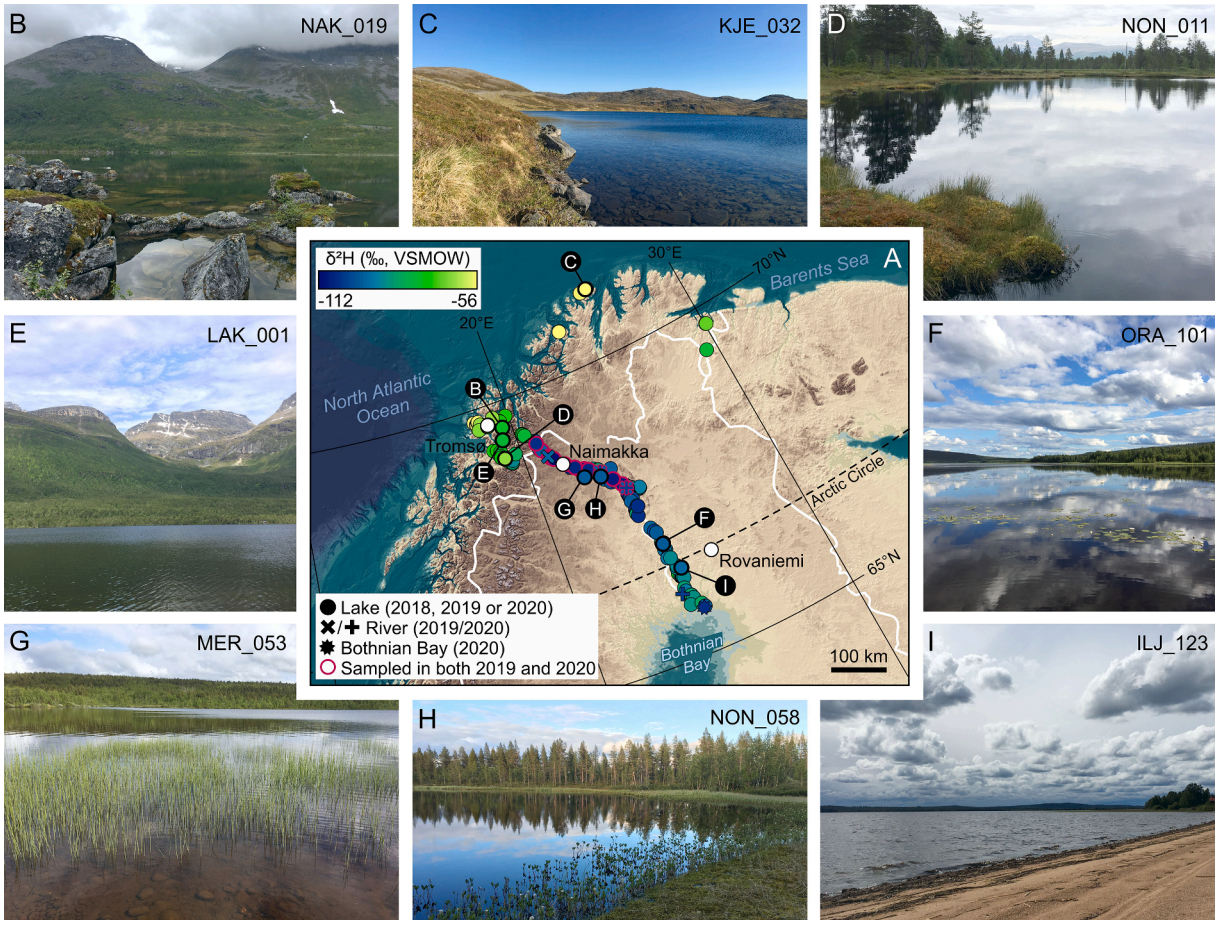

Fig. 4. (a) Geographical distribution of surface water δ^2H for 135 lakes, two rivers and the Bothnian Bay, in Arctic and sub-Arctic Norway, Finland, and Sweden. Twelve lakes and two locations along the Muonio River sampled in both 2019 and 2020 are outlined in red. Background map from IBCAO (Jakobsson et al., 2012). (b-i) Photographs of a selection of the sampled lakes. Codes refer to lake IDs (Supplementary Information). (For interpretation of the references to color in this figure legend, the reader is referred to the web version of this article.)

Norwegian (Atlantic) coast lie on or close to the GMWL, with a trend toward more ^{2}H-depleted values moving inland (Figs. 4–7). This trend is likely controlled by the increasing distance from the coast, which is likely a proxy for the degree of distillation resulting from air masses advecting over the mountain peaks (Fig. 5a and 7). The lake elevation, which is often below the highest mountain peaks in the region (Fig. 5b), is less important than the elevation of the mountains over which the moisture has to pass along its transport path (Fig. 7). In the following paragraphs we present the measured lake water δ^{2}H and δ^{18}O values, starting with the coastal lakes, followed by the transect lakes.

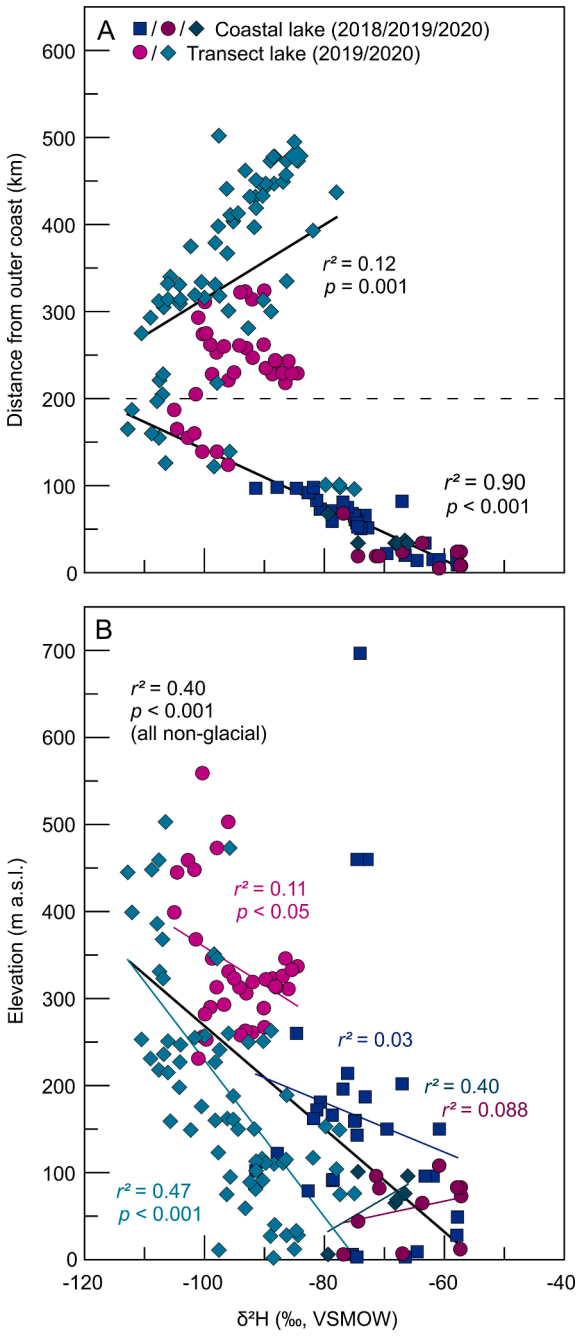

Fig. 5. Spatial trends in lake water δ^{2}H. (a) δ^{2}H versus distance from the outer coast (North Atlantic Ocean or Barents Sea). Linear regression fits are included for all lakes (2018, 2019 and 2020 combined) located less and >200 km from the outer coast (distance = –3.18×δ^{2}H – 176.19 and distance = 4.25×δ^{2}H + 739.39, respectively), separated by dashed line. (b) δ^{2}H versus elevation, with linear regressions for each subset of coastal and transect lakes (2018, 2019 and 2020), as well as for all non-glacial lakes (excluding three high-elevation lakes (>460 m a.s.l.) and one lake close to sea level receiving glacial meltwater).

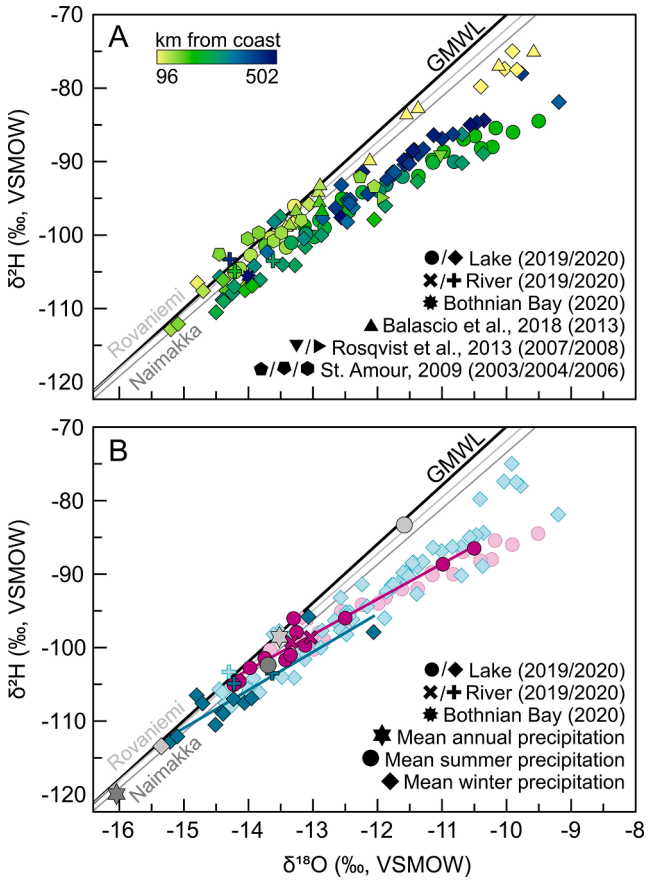

Fig. 6. δ^{18}O versus δ^{2}H values for transect lakes and rivers sampled in 2019 and 2020, colored by distance to the North Atlantic coast (a), and by sampling year (b). (a) includes lakes sampled in the study area by St. Amour (2009) and Balascio et al. (2018), and lake surface water (depth ≤ 1 m) from Guossajavri (Rosqvist et al., 2013; Fig. 1). Dark symbols in (b) show lakes (n = 12) and locations along the Muonio River (n = 2) sampled both year, and light symbols are all samples. Local evaporation lines (LELs) for 2019 (δ^{2}H = 4.82×δ^{18}O – 35.58) and 2020 (δ^{2}H = 5.18×δ^{18}O – 33.27) are included for the 12 resampled lakes. Local meteoric water lines and amount-weighted mean annual and seasonal precipitation values (winter = November-May; summer = June-October) for Naimakka and Rovaniemi are displayed in grey.

All lakes along the outermost coast plot in the upper right corner of the co-isotope plot (Fig. 3). In 2018, δ^{2}H and δ^{18}O of 30 coastal lakes ranged from –91.43 to –57.82‰ (median = –74.72 ± 8.36‰ (±1σ)) and –12.85 to –7.48‰ (median = –10.64 ± 1.23‰), respectively. Deuterium excess ranged from –3.00 to + 14.37‰ (median = 9.10 ± 3.59‰). In 2019, δ^{2}H and δ^{18}O of 11 coastal lakes ranged from –76.84 to –57.22‰ (median = –63.69 ± 7.11‰) and –11.27 to –8.02‰ (median = –9.19 ± 0.88‰), respectively. For these lakes, d-excess ranged from 2.52 to 15.12‰ (median = 9.85 ± 4.20‰). δ^{2}H and δ^{18}O of six coastal lakes sampled in 2020 ranged from –79.40 to –66.10‰ (median = –68.05 ± 4.85‰) and –11.83 to –9.68‰ (median = –10.07 ± 0.78‰), respectively. Deuterium excess ranged from 11.30 to 15.20‰ (median = 12.65 ± 1.49‰). For lakes sampled along the NW-SE transect in 2019 (n = 35), δ^{2}H and δ^{18}O ranged from –105.04 to –84.49‰ (median = –95.05 ± 5.82‰) and –14.22 to –9.50‰ (median = –12.44 ± 1.32‰), respectively (Figs. 3–7). Deuterium excess of these lakes ranged from –8.47 to + 10.28‰ (median = 3.55 ± 4.97‰). For transect lakes sampled in 2020 (n = 68), δ^{2}H and δ^{18}O ranged from –112.80 to –75.00‰ (median = –95.75 ± 9.35‰) and –15.20 to –9.19‰ (median = –12.43 ± 1.51‰), respectively. Deuterium excess ranged from –8.40 to 11.80‰ (median = 3.25 ± 3.84‰). All transect lakes plot along a LEL (δ^{2}H = 5.50×δ^{18}O –

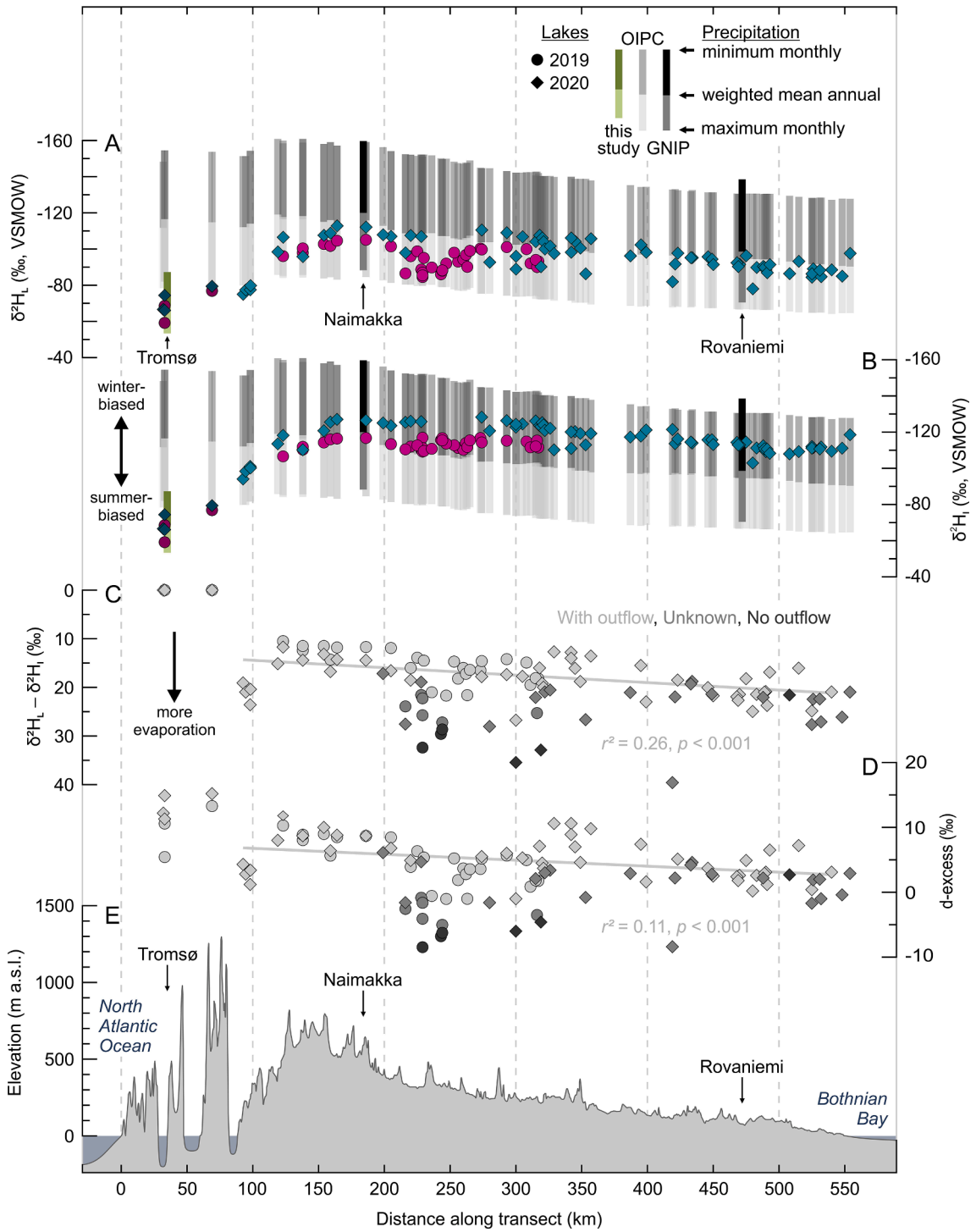

Fig. 7. Lake water δ^2H_L (a), inferred inflow δ^2H_I (b), offset between δ^2H_L and δ^2H_I (c), d-excess (d), and elevation (e) for all lakes along transect (colors and shapes as in Fig. 3). Four coastal lakes along an extension of the transect (NW of Skibotn; Fig. 1) are plotted for comparison. Vertical bars in (a-b) represent the ranges between weighted mean annual and maximum and minimum monthly precipitation δ^2H in Tromsø (this study), Naimakka and Rovaniemi (GNIP; IAEA/WMO, 2019), and for the location of each lake, modeled using the Online Isotopes in Precipitation Calculator (OIPC; Bowen, 2021). Symbols in (c-d) are colored according to throughflow regime (with outflow, without outflow, or unknown), and linear regression fits are included for all through-flowing lakes ($\delta^2H_L - \delta^2H_I = 0.015 \times \text{distance} + 12.89$; d-excess = $-0.0092 \times \text{distance} + 7.69$). Note that the y-axes in (a-c) are inverted.

27.55; Fig. 3), a further indication that some of the lakes undergo evaporation.

Transect lakes sampled in both 2019 and 2020 ($n = 12$) generally showed similar interannual variability (Fig. 6b and 8). Samples collected in 2020 were ^2H-depleted relative to samples collected from the same lakes in 2019 (Fig. 6b and 8) but had similar d-excess both years. The average offset (2020 minus 2019) was –8.43‰ for δ^2H and + 0.90‰ for d-excess. One large lake (Kilpisjärvi; 69.05°N, 20.79°E, 37 km^2) was slightly ^2H-enriched in 2020 compared to 2019, with an offset of + 2.12‰ for δ^2H and + 0.66‰ for d-excess (Fig. 8a). Applying linear regression fits to these 12 lakes resulted in LELs with the equations $\delta^2H = 4.82 \times \delta^{18}O - 35.58$ and $\delta^2H = 5.18 \times \delta^{18}O - 33.27$, for 2019 and 2020

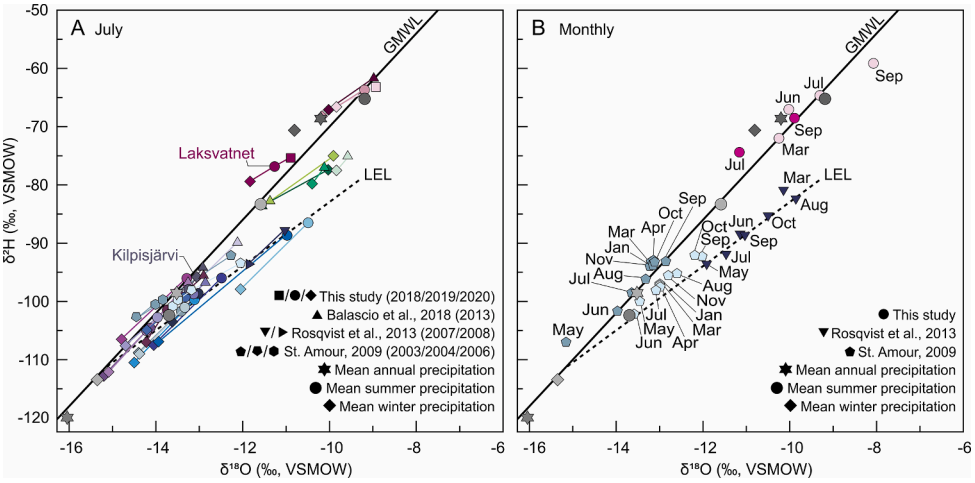

Fig. 8. (a) Interannual variability in summer (July) lake water δ^2H and $\delta^{18}O$ from this study (2018–2020), lakes sampled in the same area (St. Amour, 2009; Balascio et al., 2018) and lake Guossajavri (Rosqvist et al., 2013; 125 km SW of our transect). Lakes water samples collected from the same lakes in July different years (from 2013 to 2020) are illustrated in the same color and connected with lines. Coastal lakes are colored pink, lakes in the Skibotn valley are green, and transect lakes are purple and blue. (b) Monthly average isotopic composition of lakes sampled 1–4 years from 2002 to 2020. All samples were taken at the surface (this study: *c.* 10 cm below the lake surface) from the shoreline, or from in the middle of the lake (depth ≤ 1 m). Samples from inlets were excluded. Amount-weighted mean annual and seasonal precipitation values (winter = November-May; summer = June-October) are displayed in grey (dark grey = Tromsø; middle grey = Naimakka; light grey = Rovaniemi), and black dashed line represents the local evaporation line (LEL; $\delta^2H = 5.50 \times \delta^{18}O - 27.55$) for transect lakes in this study. For locations, see Fig. 1. (For interpretation of the references to color in this figure legend, the reader is referred to the web version of this article.)

respectively (Fig. 6b). Two locations along the Muonio River exhibited similar interannual variation as the lakes (Fig. 6b), indicating different inflow values in 2019 and 2020. In 2019, the river water had δ^2H of –98.62 and –99.24‰, respectively. In 2020, the same two sites along the river had δ^2H of –103.50 and –104.90‰, resulting in an average offset of –5.27‰. The average offset for d-excess was + 0.69‰. One sample collected from the Bothnian Bay in 2020 had δ^2H and $\delta^{18}O$ of –105.60 and –14.00‰, respectively, reflecting the high river-runoff to this northernmost part of the Baltic Sea (Figs. 3, 4 and 6).

The four northernmost lakes in the transect (located in Skibotn; Fig. 1b) had relatively enriched δ^2H and $\delta^{18}O$ values compared to the rest of the transect lakes (Figs. 4, 8 and S1). δ^2H and $\delta^{18}O$ ranged from –79.80 to –75.00‰ (median = –77.45 ± 1.70‰) and from –10.40 to –9.84‰ (median = –9.97 ± 0.22‰), respectively. Deuterium excess ranged from 1.20 to 4.30‰ (median = 3.10 ± 1.13‰). These four lakes are located within 9 km from the Lyngen fjord, and could therefore be considered coastal (Figs. 1 and 4). However, there is a strong rain-shadow effect in Skibotn, where the mean annual precipitation is 465 mm (MET Norway, 2021), compared to 1091 mm in Tromsø, located on the other side of the Lyngen Alps (Fig. 1c), *c.* 60 km northwest of Skibotn.

For lakes by the coast and along the beginning of the transect (<*c.* 200 km from the North Atlantic) there is a significant ($p < 0.001$) trend toward more ^2H-depleted lakes moving away from the coast, whereas farther inland, this trend is still significant ($p = 0.001$), though reversed (Fig. 5a). δ^2H also decreases with elevation (Fig. 5b). This trend is significant for the transect lakes ($p < 0.05$ and $p < 0.001$ in 2019 and 2020, respectively), but not for the coastal lakes. Considering the strong correlation between δ^2H and $\delta^{18}O$ for both coastal ($r^2 = 0.84$) and transect ($r^2 = 0.92$) lake samples, we assume that trends in $\delta^{18}O$ follow δ^2H and hereafter primarily focus on δ^2H and d-excess.

4.2. Inferred inflow δ^2H values

The conventional LEL-MWL intersection approach yielded δ^2H_I values for the transect lakes of –104.78 and –112.90‰ in 2019 and 2020, respectively. Bayesian inflow modeling, which we did for all 91 transect lakes, yielded δ^2H_I ranging from –116.87 to –106.57‰ (median = –112.72 ± 2.57‰) in 2019, and –128.27 to –94.08‰ (median = –115.75 ± 7.53‰) in 2020. This is on average 18.27‰ (2019) and 20.55‰ (2020) more ^2H-depleted than measured lake water δ^2H (Fig. 7). The 90% confidence intervals for δ^2H_I ranged from –148.44 to –111.52‰ for the lower bound and from –118.11 to –83.00‰ for the upper bound, with an average of –132.30 and –104.26‰, respectively. For comparison, δ^2H_L for the coastal lakes ranged from –91.43 to –57.82‰ (median = –74.72 ± 8.36‰) in 2018, –76.84 to –57.22‰ (median = –63.69 ± 7.11‰) in 2019, and from –79.40 to –66.10‰ (median = –68.05 ± 4.85‰) in 2020.

In the area with lakes sampled in both 2019 and 2020 (<320 km from the North Atlantic), δ^2H_I values were ^2H-depleted in 2020 compared to in 2019. For the 12 resampled lakes, δ^2H_I ranged from –116.72 to –106.57‰ (median = –113.79 ± 2.97‰) in 2019, and –128.27 to –110.21‰ (median = –125.67 ± 4.87‰) in 2020, resulting in an average offset of –10.68‰ (Fig. 7). Kilpisjärvi had a similar, but slightly more negative inferred δ^2H_I value in 2019 (–110.30‰) compared to 2020 (–110.21‰), with an offset of + 0.09‰. In 2020, the four lakes in Skibotn had δ^2H_I values from –101.06 to –94.08‰ (median = –99.27 ± 2.69‰), comparable to coastal δ^2H_L, whereas the rest of the transect lakes had δ^2H_I ranging from –128.27 to –102.94‰ (median = –116.72 ± 6.23‰).

Moving inland, δ^2H_I decreased rapidly in the first *c.* 160 km along the transect, after which δ^2H_I stayed relatively stable, with a slightly increasing trend towards the Bothnian Bay. Generally, lakes closer to the North Atlantic had δ^2H_L closer to inferred δ^2H_I, for through-flowing lakes δ^2H_L-δ^2H_I increased moving southeast along the transect (+1.53‰ per 100 km), and closed basins had the largest offsets between δ^2H_L and δ^2H_I (Fig. 7c).

5. Discussion

Lake water isotopes in our study area display mainly two kinds of variability, caused by differences in 1) inflow value (moving along the MWL) and 2) evaporation (moving below the MWL; Fig. 3). In most cases, lake water inflow values reflect a mixture of sources with different isotopic composition (e.g., summer and winter runoff, groundwater). The seasonality of lake water is primarily governed by the lake water residence time, since this determines the proportion of summer and winter precipitation in the lake (Jonsson et al., 2009). The position of a lake along the MWL and its relation to local precipitation isotopic composition can thus give information about lake water biases toward summer or winter season precipitation. In δ^2H-$\delta^{18}O$ space, lakes experiencing evaporative enrichment (decreasing d-excess) plot below the MWL, and along LELs. In the following sections, we discuss the sensitivity of modern lake water δ^2H along the climate gradient to differences

in inflow isotopic composition and evaporation, how these two controls vary in time and space, and why this variability needs to be considered when inferring lake-water-isotope proxy records.

5.1. Regional variability in lake water δ^2H and inferred inflow δ^2H

5.1.1. Coastal lakes

The strong correlation between increasing distance from the coast and decreasing δ^2H_L ($r^2 = 0.90$, $p < 0.001$; Fig. 5a) for the lakes closest to the coast (<*c.* 200 km; both coastal and the northernmost part of the transect), suggests that distillation during atmospheric moisture transport, prior to precipitation, is the most important control on δ^2H_L for coastal lakes in this area. δ^2H and $\delta^{18}O$ decrease by *c.* 57‰ and 6.8‰ over 200 km, or 28‰ and 3.4‰ per 100 km, respectively (Fig. 5a). In the Pacific Northwest, USA (mountainous but drier than coastal Norway), the $\delta^{18}O$ isotopic gradient is 1.2‰ per 100 km (Welker, 2000) and in the Sierra Nevada, USA (wet year-round, most precipitation in winter, some mountains) 5‰ per 100 km (Ingraham & Taylor, 1991). Across the European Plain (from mild and wet coastal Ireland to the continental foothills of the Ural Mountains), the gradient is 0.2‰ per 100 km (Rozanski et al., 1993). This means that our gradient is within ranges found elsewhere and most similar to gradients in similar environments (wet, mountainous, coastal). The least ^2H-depleted lakes are the ones at the northern coast and the outermost coast to the west of Tromsø (Fig. 4), since the transport from the source is shorter and there is not much rain-out prior to precipitation. Three lakes in Kirkenes are slightly ^2H-depleted compared to the other lakes at the outermost coast (Fig. 1b and 4). None of these lakes have distinct outflows, and relatively low d-excess (Supplementary Fig. S1) suggests they are likely experiencing evaporative enrichment. They may also receive source water with a slightly different isotopic signal, being located near the Barents Sea. Lakes near Tromsø are relatively ^2H-enriched compared to lakes slightly farther from the coast (Fig. 4).

In the coastal region, most of the large through-flowing lakes plot close to the MWL, whereas some smaller lakes with low or unknown throughflow and long residence times fall below the MWL, being more affected by evaporation (Fig. 3). A couple of large through-flowing lakes with large mountainous catchments plot above the MWL and close to Tromsø amount-weighted winter precipitation (e.g., Laksvatnet; Fig. 4a and e, 8), suggesting a longer response time, and that the depleted meltwater from snow has not yet been flushed through in early July.

Some of the local variability in coastal lake water δ^2H can also be explained by differences in elevation (Fig. 5b), likely reflecting heterogeneous airflow patterns, with fjords funneling onshore winds and mountains causing orographic precipitation. The mountains cause the air masses to rise as they move inland from Tromsø, causing rainout and more negative δ^2H values (Figs. 4, 5 and 7). Lakes at a given distance from the coast have similar isotope values, despite differences in elevation (Fig. 5a-b). This is likely because precipitation at a given location forms at the same elevation in the atmosphere, and that elevation rises over the mountains moving inland. Three high elevation coastal lakes (>460 m a.s.l.) have δ^2H_L values comparable to other coastal lakes, despite their high elevation (Fig. 5b). They have high d-excess (average = 14.2 ± 0.3‰) and plot above the MWL, suggesting that their isotopic signals are biased toward winter precipitation. In Tromsø, precipitation δ^2H is relatively enriched compared to the more inland stations and does not show a strong seasonality. In contrast, d-excess is significantly higher in fall and winter than in summer (Figs. 2 and 3), due to kinetic fractionation effects when snow forms in mixed-phase clouds (vapor supersaturated over ice; Jouzel & Merlivat, 1984). It is common for mountain lakes to receive most precipitation as snowfall and for their catchments to experience late snowmelt, explaining the high d-excess lake water values. Furthermore, two of the lakes have small niche glaciers in their catchments, contributing glacial meltwater. Thus, our dataset suggests that coastal lakes are primarily influenced by varying degrees of distillation during atmospheric moisture transport, precipitation amount and lake and catchment morphometry, the latter two determining the lake water residence time.

5.1.2. Transect lakes

In contrast to the coastal lakes, most of the transect lakes experience more evaporative enrichment, plotting below the MWL and along a LEL (Figs. 3 and 6). Lake surface water from Oikojärvi (located close to Naimakka; St. Amour, 2009) and Guossajavri (125 km SW of our transect; Rosqvist et al., 2013; Fig. 1b) sampled between 2002 and 2008 fall along similar LELs, suggesting similar evaporation patterns on a regional scale and between years (Figs. 6 and 8). The North Atlantic is still the main moisture source, so precipitation δ^2H, and as a result lake water δ^2H, becomes more and more depleted the first *c.* 160 km along the transect, reflecting Rayleigh distillation during moisture transport (Figs. 4–7).

On the southeastern side of the mountains, where the relief changes from highlands with incised valleys to a gently sloping plain with few hills, there is a larger spread in δ^2H_L (Fig. 7a) and larger and more variable offsets between δ^2H_L and δ^2H_I (Fig. 7c). This coincides with the northern boundary of the northern aapa mire zone, where large, branched mire systems are common (Ruuhijärvi, 1983). Although lakes in wetland-dominated catchments tend to have low E/I (Gibson et al., 2002), many of the lakes in this area are evaporatively enriched, plotting on a LEL and having low d-excess (Figs. 3, 6 and 7d). Hydrologically closed basins, lack of clear surface flow, and/or only seasonal connection by small streams or wetland areas may make these lakes susceptible to evaporation. Furthermore, in continental regions at high latitudes, seasonally arid conditions can increase the evaporative enrichment during the thaw season (Gibson et al., 2005). Smaller inter-lake variation in δ^2H_I than in δ^2H_L (Fig. 7a-c), suggests that most lakes have similar inflow seasonality and sources, whereas evaporation, indicated by decreasing d-excess (–0.92‰ per 100 km; Fig. 7d), increases moving southeast. Moreover, some lakes possibly have δ^2H_L values influenced by factors in addition to evaporative enrichment.

Some of the lakes might be groundwater fed, since till and glaciofluvial aquifers are common in this region (Kortelainen & Karhu, 2004). However, there are no significant differences between the isotopic composition of precipitation and shallow groundwater (till aquifers) in northern Finland and Sweden (Kortelainen & Karhu, 2004). Both follow the same seasonal cycle with most enriched values in late fall, and most depleted values after snowmelt. We do therefore not expect shallow groundwater recharge to the lakes to significantly alter δ^2H_L.

Lakes on the southeastern side of the Scandinavian mountains most likely also receive precipitation from other moisture sources, such as the Baltic region and Eurasia. These sources are more depleted (Schmidt et al., 1999; Bailey et al., 2021), but the travel distance may be shorter, potentially resulting in less distillation and precipitation that is relatively enriched compared to Atlantic moisture, a phenomenon also observed in precipitation events in Arctic Alaska (Putman et al., 2017). In summer, precipitation can be induced by local convection, and less influenced by atmospheric circulation (Jaagus, 2009). Local moisture could in this way at least partly explain the slightly enriched δ^2H_L of lakes closest to the Bothnian Bay (Fig. 7a). Furthermore, transpiration, another process most important in summer, can partly compensate for isotopic depletion caused by distillation during moisture transport, by recycling soil moisture without fractionation (Rozanski et al., 1982). The relative contribution of moisture from different source regions and the resulting isotopic compositions of precipitation can be assessed on an event basis at a given station (Bailey et al., 2021; Mellat et al., 2021), but we do not have any data on this over longer time scales (i.e., covering our study period), or know how it varies within our study region. Most likely, the isotopic composition of precipitation along our transect, and therefore lake water inflow, is controlled by a combination of different moisture source regions, local convection, and evapotranspiration.

5.1.3. Lake location and inflow seasonality

Comparing δ^2H_I to precipitation δ^2H data from Tromsø, Naimakka and Rovaniemi, as well as OIPC-modeled precipitation δ^2H (Bowen, 2021), suggests that winter precipitation is more important for inland lakes, whereas coastal lakes tend to be summer-biased or have an isotopic composition close to mean annual precipitation δ^2H (Fig. 7b). A similar trend is seen on western Greenland, likely reflecting lake water inflow seasonality along an aridity gradient (Cluett & Thomas, 2020). In our study area, the inland region normally receives a greater fraction of the annual precipitation during the summer months (Fig. 2). This lake water bias towards winter precipitation for inland lakes is likely due to lower relative humidity and higher evapotranspiration at inland sites in

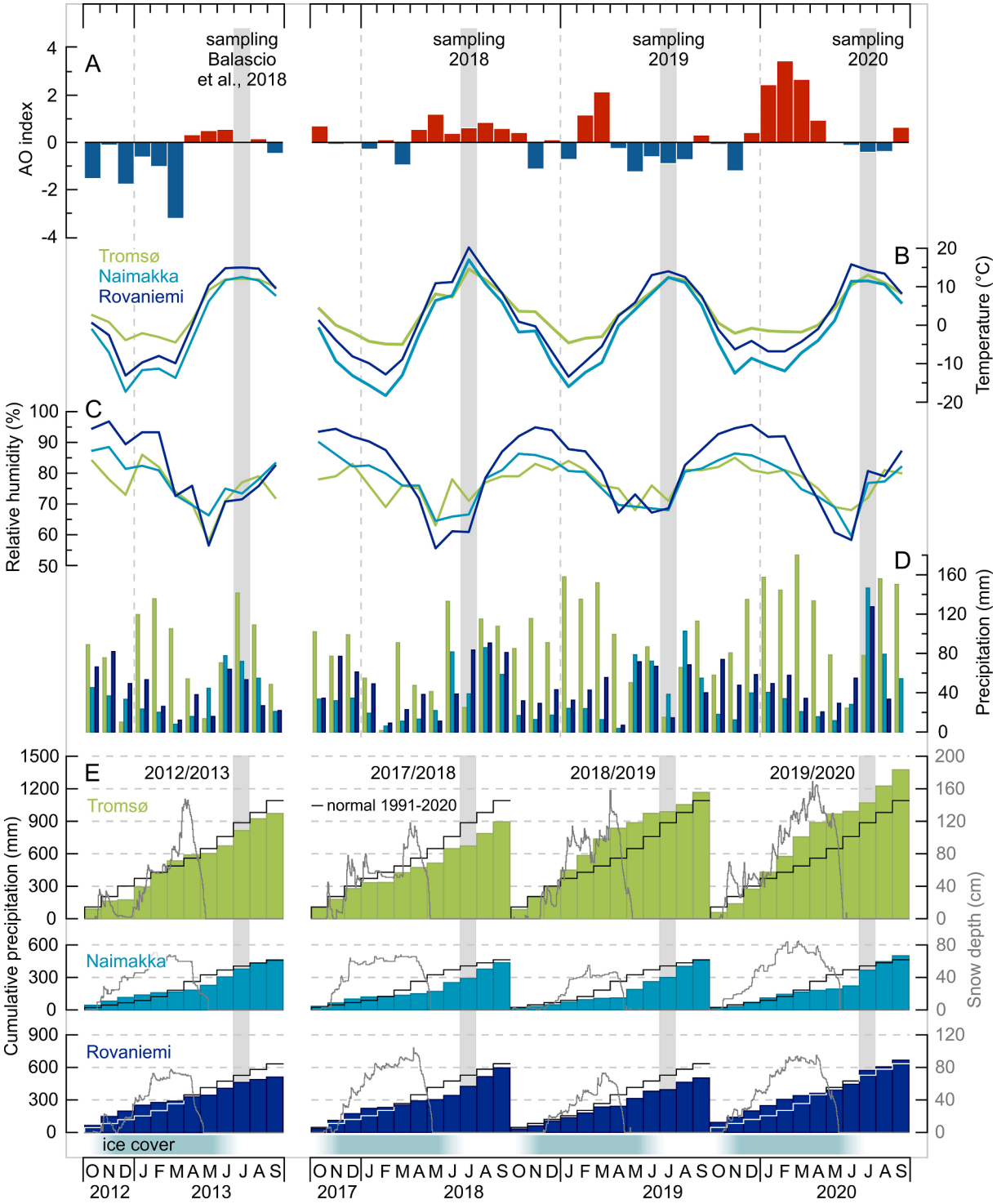

Fig. 9. (a) Monthly Arctic Oscillation (AO) index (National Weather Service Climate Prediction Center, 2021). (b) Mean monthly air temperature, (c) relative humidity, (d) accumulated precipitation and (e) cumulative precipitation and snow depths for the hydrological years (October-September) 2012/2013, 2017/2018, 2018/2019 and 2019/2020 for Tromsø, Naimakka and Rovaniemi (FMI, 2021; MET Norway, 2021; SMHI, 2021). Black stepped lines in (e) illustrate mean cumulative precipitation values for 1991–2020. Snow depths for Naimakka were obtained from Saarikoski (68.81°N, 21.25°E, 450 m a.s.l.), 18 km NW of Naimakka (SMHI, 2021).

summer (Fig. 2), even if a greater fraction of total precipitation falls in summer (Bowen et al., 2018).

That coastal lakes appear to be summer-biased is somewhat unexpected, considering that Tromsø receives more winter precipitation than Naimakka and Rovaniemi (Figs. 2 and 9d-e). OIPC-modeled precipitation δ^2H values are based on interpolation using GNIP values. They are therefore biased towards the nearest GNIP stations (i.e., Naimakka and Rovaniemi), which are more continental and experience a larger seasonality than Tromsø (Figs. 2 and 3). We compare the OIPC values with precipitation samples collected in Tromsø in 2019–2021 and can confirm that the modeled coastal values are, indeed, too depleted compared to our new precipitation isotope dataset (Fig. 7a-b). However, it cannot be excluded that the ^2H-depleted winter isotopes might have been efficiently flushed from some coastal lakes with short residence times, especially considering the high precipitation amounts in June 2018 and 2019 (Fig. 9). This suggests that lakes in this region likely reflect a range of summer to mean annual to winter-biased precipitation δ^2H (Figs. 3 and 7).

5.2. Lake water δ^2H and inferred inflow δ^2H changes over time

5.2.1. Interannual variability

Sampling campaigns concentrated in the first week of July in 2018, 2019 and 2020 allowed us to get an insight into the interannual variability in δ^2H_L and δ^2H_I. We focus this comparison on the transect lakes, since we sampled coastal lakes in different locations each year (i.e., in the Tromsø area vs. along the northern coast). Only three coastal lakes were sampled two or three of these years, and they follow similar interannual patterns as the transect lakes (Fig. 8a). We sampled the transect lakes in 2019 and 2020, and extended the transect farther southeast in 2020 (Fig. 7). Twelve transect lakes sampled in both years had more ^2H-depleted δ^2H_L in 2020, and a LEL intersecting the MWL at a more depleted value compared to 2019 (Fig. 6b and 7a), suggesting more depleted inflow water in 2020 than in 2019. This is supported by more depleted modeled δ^2H_I in 2020 compared to in 2019 (Fig. 7b). We suggest that the more ^2H-depleted values in 2020 were a response to 1) more precipitation in winter 2019/2020 than in 2018/2019 (Fig. 9d–e), 2) later spring melt in 2020 than 2019 (Fig. 9e) resulting in less time prior to our July sampling for ^2H-enriched summer precipitation to flush the ^2H-depleted winter melt out of the lakes, and/or 3) more May-June rainfall in 2019 than in 2020 (Fig. 9d) contributing to higher snowmelt bypass in 2019 (i.e., more snow melting off the high-elevation portions landscape before the lakes become ice free in the first half of June), which would remove ^2H-depleted winter precipitation from the catchment without entering the lake. The high precipitation amounts in January-March 2020 were associated with extreme AO+ conditions and an exceptionally strong stratospheric polar vortex, causing strong winter westerlies that carried greater-than-average amounts of moisture from the North Atlantic over Fennoscandia (Lawrence et al., 2020; Fig. 9a, d-e).

An additional explanation for ^2H-depleted lake inflow values in 2020 could be a change in moisture source. Surface waters in the Baltic Sea are relatively ^{18}O-depleted compared to the North Atlantic (Schmidt et al., 1999), and a greater influence of Baltic moisture to our study area could therefore contribute to more depleted precipitation. In winter 2018/2019 most of the Bothnian Bay was sea-ice covered, whereas winter 2019/2020 Baltic Sea sea-ice cover set a record for minimum winter extent in the 120-year-long measuring period (Sjöfartsverket & SMHI, 2020a, 2020b). However, predominantly southwesterly winds and pressure systems moving eastward over the Baltic Sea in both years imply a low impact of Baltic Sea moisture to our study area during this period.

Some lakes in the area have been sampled in previous studies, allowing us to extend our interannual comparison further back in time. In 2013, nine of the transect lakes were relatively enriched compared to the same lakes sampled in 2019 and/or 2020 (Balascio et al., 2018; Fig. 6a and 8). The interannual changes in lake water isotopic composition were parallel to the MWL, suggesting that the lakes had more ^2H-enriched inflow water in 2013 than in 2019 and 2020, but that all years had a similar influence of evaporation. The hydrological year 2012/2013 was relatively dry compared to 2018/2019 and 2019/2020 (especially in Tromsø; Fig. 9d-e). However, June and July 2013 were wet (Fig. 9d), and the lakes were sampled several weeks later than in 2019 and 2020 (July 26, 2013; N. Balascio, personal communication), suggesting that the relatively enriched lake water values reflect greater summer precipitation inflow to the lakes in 2013. Two lakes close to Naimakka (Oikojärvi and Keitjoru) that were sampled by St. Amour (2009) in July 2003, 2004 and 2006 displayed a similar magnitude of interannual variability to the lakes in our dataset (Fig. 8a). The Oikojärvi samples from July 2004 and 2006 were close to the MWL, whereas the 2003 sample was evaporatively enriched along a LEL, perhaps due to exceptional dryness that year, as suggested by St. Amour (2009).

5.2.2. Seasonal variability

The lake water isotopic composition also follows a seasonal cycle. St. Amour (2009) collected monthly samples (excluding February and December) from the two lakes in Naimakka from 2002 to 2005, generally recording lowest values in the beginning of the ice-free season due to isotopically depleted snowmelt, increasing values over summer due to more enriched inflow isotopic composition and/or evaporative enrichment, and high and relatively stable composition during the ice-cover season (Fig. 8b). Guossajavri, northern Sweden, showed a similar trend in 2007 and 2008, with the lake moving up along the LEL during the summer months, and being recharged in winter (Rosqvist et al., 2013; Fig. 8b). This is in agreement with other lakes in northern Sweden (Jonsson et al., 2009) and elsewhere in the Arctic (Leng & Anderson, 2003; Tondu et al., 2013).

We sampled two lakes in Tromsø in March, June, July and/or September in 2018–2020. Except for a low March value, the seasonal isotope patterns in these lakes are similar to interannual patterns in all the lakes: isotope values tend to move parallel to the MWL, implying changes in inflow isotopic composition, rather than changes in evaporation. Although we do not have samples to examine seasonal variability in the transect lakes, given the similarities in interannual variability between the coast and transect, we hypothesize the transect lakes experience similar seasonal changes in inflow isotopic composition, with constant influence of evaporative enrichment.

5.3. Implications for precipitation proxy reconstructions

Interpreting isotope proxy records often assumes that, for a given record, the control on the lake water isotopic variability is constant through time. We have demonstrated that lakes in this region display variable sensitivity to changes in inflow (precipitation) isotopic composition and to evaporative enrichment, and that these controls vary in both time and space. Resolving these controls on modern lake water isotopes is important for making quantitative paleoclimate inferences. Depending on what aspect of the hydrological cycle we aim to reconstruct (e.g., atmospheric circulation, precipitation amount or seasonality, moisture balance), we can target different lakes.

In parts of our study area, modern precipitation isotopes have strong seasonal variability (Figs. 2 and 7), and if this signal is preserved in lake sediment proxy records, we can use it to reconstruct changes in precipitation seasonality (Cluett & Thomas, 2020; Thomas et al., 2020). The seasonality preserved in a proxy record depends on the δ^2H or $\delta^{18}O$ of source (lake or soil) water at the time of proxy synthesis, which can vary between proxies (Corcoran et al., 2021). Lake water isotopic composition and seasonal variability depends on the lake water residence time (Jonsson et al., 2010; Tondu et al., 2013; Ala-Aho et al., 2018), which may also change through time.

Previous paleoclimate work in northern Fennoscandia suggests that changes in Holocene precipitation isotopes are strongly linked to

changes in air temperature and air mass sources. Lacustrine carbonates, biogenic silica, and cellulose from non-evaporated lakes in northern Sweden have been used to reconstruct past changes in lake water $\delta^{18}O$ and precipitation (Shemesh et al., 2001; Hammarlund et al., 2002; Rosqvist et al., 2004, 2007, 2013; St. Amour, 2009; Jonsson et al., 2010). In most of these studies, depleted summer lake water $\delta^{18}O$ was inferred to reflect increased influence of Arctic air masses. Furthermore, Rosqvist et al. (2013) suggested that periods of relatively high $\delta^{18}O_{diatom}$ reflect a dominance of summer precipitation, related to a positive AO index, whereas low $\delta^{18}O_{diatom}$ reflects dominant winter precipitation due to positive NAO.

Studying modern conditions can aid proxy interpretations since it allows us to directly link isotopic changes to observations of atmospheric circulation change. Arctic Ocean and Baltic Sea surface waters are relatively depleted compared to North Atlantic moisture (LeGrande & Schmidt, 2006; Bonne et al., 2019), suggesting that depleted precipitation isotopes, and thereby lake water isotopes, may reflect a change to dominance of Arctic or Baltic air masses. However, this will depend on the location of the lake and the moisture travel distance. Atlantic moisture (which is originally less depleted) that has been transported a long distance may have experienced more distillation than more locally derived moisture with a more depleted starting isotopic composition, and therefore also be relatively depleted (Putman et al., 2017; Cluett et al., 2021). Our ^{2}H-depleted lake water values in 2020 were likely not caused by a shift in moisture source region, but by high winter precipitation amounts associated with AO+ conditions and an increase in North Atlantic moisture (Lawrence et al. 2020). Greater-than-average winter precipitation amounts over Fennoscandia can result from both extremely positive and negative winter AO conditions, although from different moisture sources (North Atlantic vs. Barents Sea; Lawrence et al., 2020; Bailey et al., 2021). Complicating things further, modern moisture from the Barents Sea has an isotopic composition comparable to North Atlantic moisture, due to increased strength of the North Atlantic Current (Bailey et al., 2021). If conditions were similar in the past, the Atlantic and Barents Sea moisture sources would be difficult to distinguish from one another in proxy records. Our lake water isotope observations imply that seasonal changes in precipitation amounts need to be taken into account when inferring atmospheric circulation from a proxy record in this region, and that changes in precipitation isotope values can be a result of a change in precipitation seasonality, moisture source, or a combination of both.

For reconstructions of atmospheric circulation and precipitation, we should target lakes that are minimally impacted by evaporative enrichment, since evaporation overprints the precipitation signal. In our dataset, most lakes >100 km from the coast have low d-excess values, suggesting that evaporative enrichment affects them to some degree, regardless of their throughflow regime (Figs. 3, 6a and 7). All transect lakes appear to fall on similar LELs, but with slope and intercept varying from year to year, depending on seasonality (Fig. 6). On interannual and seasonal timescales, changes in inflow appear to have a larger impact than evaporation, with isotope values moving along the MWL (Fig. 8). On longer timescales, evaporation may be more important, making it difficult to disentangle how much of the variability derives from each process (i.e., inflow vs. evaporation). Hence, we suggest that through-flowing coastal lakes are better targets for precipitation reconstructions, since changes in their lake water isotopic composition are more likely to primarily reflect changes in the inflow.

For evapo-concentrated lakes there are a few possible approaches to separate the precipitation from the evaporation signal, including 1) comparing two lakes with contrasting residence times (Anderson et al., 2001), 2) comparing terrestrial and aquatic leaf waxes in the same lake (Rach et al., 2017), or 3) measuring both $\delta^{2}H$ and $\delta^{18}O$ in the same records (Gibson et al., 2005). For the first approach, one needs to identify a non-evaporated lake with short residence time (low $\delta^{2}H_L$-$\delta^{2}H_I$) and one evaporated lake with longer residence time (high $\delta^{2}H_L$-$\delta^{2}H_I$; Anderson et al., 2001). Moreover, the lakes must receive source water reflecting the same precipitation seasonality, and evaporation should be the only factor that differs between the two. The offset between $\delta^{2}H_L$ and $\delta^{2}H_I$ for our transect lakes is >10‰ independent of throughflow, suggesting that it will be difficult to identify an unevaporated lake in this region, which would be needed for this approach. Using the second approach, one compares terrestrial and aquatic leaf wax $\delta^{2}H$ in the same record, which have source water representing the same seasonality. In areas where terrestrial plant source water is evaporatively enriched, but the aquatic plant source water is not, the isotopic difference between the two reflects leaf water evaporative enrichment (Rach et al., 2017; Thomas et al., 2018; Curtin et al., 2019). In contrast, lake water in arid areas has been suggested to be more evaporatively enriched than terrestrial leaf water, meaning that the difference primarily reflects the evaporative enrichment of lake water (Mügler et al., 2008; Balascio et al., 2013). Along our transect, both aquatic and terrestrial leaf waxes likely incorporate a signal of evaporative ^{2}H-enrichment due to low relative humidity and warm conditions in summer (Figs. 2 and 9b-c). Thus, a dual leaf wax approach to separate precipitation and evaporation signals might not be applicable along the transect but may be possible at coastal lakes. For the third approach, one measures $\delta^{2}H$ and $\delta^{18}O$ in the same lakes, which may allow estimation of past changes in the slope of the LEL (Gibson et al., 2005) that could subsequently be used to infer past inflow values. Theoretically, this is possible, however, it involves many uncertainties. First, one needs to analyze the same proxies at the same time slice in several lakes. Second, those two proxies (one with $\delta^{2}H$ and one with $\delta^{18}O$) need to reflect the same pool of water for the same window of time in a season. Moreover, one needs to have good constraints on biosynthetic and other fractionation factors (Brandriss et al., 1998; Sachse et al., 2012; Lombino et al., 2021) to be able to estimate lake water $\delta^{2}H$ and $\delta^{18}O$ and directly compare $\delta^{2}H$ and $\delta^{18}O$ from different proxies (Corcoran et al., 2021).

A more recent approach to guide paleoclimate interpretations is to use proxy system modeling, which uses modern climate variables as inputs to mathematical descriptions of lake water isotope and energy balance (e.g., PRYSM2.0; Dee et al., 2018). By conducting sensitivity tests in which we iteratively change values of one or more climate parameters (e.g., lower relative humidity, more winter precipitation), we can quantify the parameter, or combination of parameters, that could explain changes recorded in lake water isotope proxies. For lakes in our transect, we could for example focus on variables that affect the lake water inflow isotopic signal and amount of evaporative enrichment, to assess the sensitivity of the lake water isotopic composition to these variables. If we have an estimate of how a change in moisture source would affect the precipitation isotopes, we can modify the inflow isotope value in the model to see how this would impact the lake water isotope value. One way to simulate how a shift in moisture source would influence the lake water inflow value is to use a one-dimensional Rayleigh-type distillation model along a theoretical trajectory (Sodemann et al., 2008; Steen-Larsen et al., 2011; Cluett et al., 2021). These approaches can provide us with quantitative constraints on past climate changes.

When interpreting lake-water-derived isotope proxy data from northern Fennoscandia, we need to consider the magnitude of variability in both inflow isotopic composition and evaporation. On the coast, inflow causes more variability than evaporation. Considering the variability among the transect lakes, the ranges for $\delta^{2}H_I$ and $\delta^{2}H_L$ are similar, suggesting that inflow and evaporation might be equally important. Interannual variability is largely due to changes in inflow isotopic composition, however, suggesting the importance of inflow isotopic composition even in lakes that are strongly influenced by evaporation. Therefore, we recommend targeting through-flowing lakes by the coast for precipitation reconstructions. If working with more continental records, we need to address the significance of both inflow and evaporation processes. Importantly, our data show that we cannot interpret all isotopic variability in evapo-concentrated basins in terms of evaporation, as there might also be a substantial variability in inflow isotopic composition through time.

Data availability

Water isotope data are freely available in the Water Isotopes Database at www.waterisotopes.org (Project IDs 00292 (surface waters) and 00293 (precipitation)), and in the Supplementary Information.

CRediT authorship contribution statement

Sofia E. Kjellman: Conceptualization, Investigation, Visualization, Writing – original draft, Project administration, Funding acquisition. **Elizabeth K. Thomas:** Conceptualization, Investigation, Writing – review & editing, Supervision, Funding acquisition. **Anders Schomacker:** Conceptualization, Investigation, Writing – review & editing, Supervision, Funding acquisition.

Declaration of Competing Interest

The authors declare that they have no known competing financial interests or personal relationships that could have appeared to influence the work reported in this paper.

Acknowledgements

This research was supported by grants from the Nansen Foundation and Olle Engkvists Stiftelse (204-0129) to SEK and AS, and NSF grant EAR-IF 1652274 to EKT. We thank Lis Allaart, Jack Percival, and Paul Eric Aspholm for assistance with lake water sampling, and John Arne Opheim, Emma Bender, Marie Bulínová, Carmen Braun, Amicia Lee, and Maxine King for assistance with precipitation collection. We would also like to thank Owen Cowling and Kayla Hollister for instrumental analysis of lake water samples at the Organic and Stable Isotope Biogeochemistry Laboratory at the University at Buffalo, USA. Handling and processing of liquid stable isotope samples was also done at the Norwegian National Infrastructure project FARLAB (Facility for advanced isotopic research and monitoring of weather, climate, and biogeochemical cycling, Project Nr. 245907) at the University of Bergen, Norway. We thank four anonymous reviewers for constructive comments that improved the manuscript.

Appendix A. Supplementary data

Supplementary data to this article can be found online at https://doi.org/10.1016/j.jhydrol.2022.127556.

References

Ala-Aho, P., Soulsby, C., Pokrovsky, O., Kirpotin, S., Karlsson, J., Serikova, S., Vorobyev, S., Manasypov, R., Loiko, S., Tetzlaff, D., 2018. Using stable isotopes to assess surface water source dynamics and hydrological connectivity in a high-latitude wetland and permafrost influenced landscape. J. Hydrol. 556, 279–293. https://doi.org/10.1016/j.jhydrol.2017.11.024.

Alexandersson, H., 2002. *Temperature and precipitation in Sweden 1860–2001*. Swedish Meteorological and Hydrological Institute (SMHI) Meteorological Report No. 104. 28 pp.

Anderson, L., Abbott, M.B., Finney, B.P., 2001. Holocene climate inferred from oxygen isotope ratios in lake sediments, central Brooks Range, Alaska. Q. Res. 55 (3), 313–321. https://doi.org/10.1006/qres.2001.2219.

Bailey, H., Hubbard, A., Klein, E.S., Mustonen, K.-R., Akers, P.D., Marttila, H., Welker, J. M., 2021. Arctic sea-ice loss fuels extreme European snowfall. Nat. Geosci. 14 (5), 283–288. https://doi.org/10.1038/s41561-021-00719-y.

Balascio, N.L., Anderson, R.S., D'Andrea, W.J., Wickler, S., D'Andrea, R.M., Bakke, J., 2020. Vegetation changes and plant wax biomarkers from an ombrotrophic bog define hydroclimate trends and human-environment interactions during the Holocene in northern Norway. Holocene 30 (12), 1849–1865. https://doi.org/10.1177/0959683620950456.

Balascio, N.L., D'Andrea, W.J., Anderson, R.S., Wickler, S., 2018. Influence of vegetation type on *n*-alkane composition and hydrogen isotope values from a high latitude ombrotrophic bog. Org. Geochem. 121, 48–57. https://doi.org/10.1016/j.orggeochem.2018.03.008.

Balascio, N.L., D'Andrea, W.J., Bradley, R.S., Perren, B.B., 2013. Biogeochemical evidence for hydrologic changes during the Holocene in a lake sediment record from southeast Greenland. Holocene 23 (10), 1428–1439. https://doi.org/10.1177/0959683613493938.

Belt, S.T., Cabedo-Sanz, P., Smik, L., Navarro-Rodriguez, A., Berben, S.M., Knies, J., Husum, K., 2015. Identification of paleo Arctic winter sea ice limits and the marginal ice zone: optimised biomarker-based reconstructions of late Quaternary Arctic sea ice. Earth Planet. Sci. Lett. 431, 127–139. https://doi.org/10.1016/j.epsl.2015.09.020.

Bintanja, R., Selten, F.M., 2014. Future increases in Arctic precipitation linked to local evaporation and sea-ice retreat. Nature 509 (7501), 479–482. https://doi.org/10.1038/nature13259.

Bintanja, R., van der Wiel, K., van der Linden, E., Reusen, J., Bogerd, L., Krikken, F., Selten, F., 2020. Strong future increases in Arctic precipitation variability linked to poleward moisture transport. Sci. Adv. 6 (7), eaax6869. https://doi.org/10.1126/sciadv.aax6869.

Blenckner, T., Järvinen, M., Weyhenmeyer, G., 2004. Atmospheric circulation and its impact on ice phenology in Scandinavia. Boreal Environ. Res. 9, 371–380. http://www.borenv.net/BER/pdfs/ber9/ber9-371.pdf.

Bonne, J.-L., Behrens, M., Meyer, H., Kipfstuhl, S., Rabe, B., Schönicke, L., Steen-Larsen, H.C., Werner, M., 2019. Resolving the controls of water vapour isotopes in the Atlantic sector. Nat. Commun. 10 (1), 1–10. https://doi.org/10.1038/s41467-019-09242-6.

Botter, G., Bertuzzo, E., Rinaldo, A., 2010. Transport in the hydrologic response: Travel time distributions, soil moisture dynamics, and the old water paradox. Water Resour. Res. 46 (3) https://doi.org/10.1029/2009WR008371.

Bowen, G. J., 2021. OIPC: The online isotopes in precipitation calculator, version 3.1. Available at: http://www.waterisotopes.org.

Bowen, G.J., Putman, A., Brooks, J.R., Bowling, D.R., Oerter, E.J., Good, S.P., 2018. Inferring the source of evaporated waters using stable H and O isotopes. Oecologia 187 (4), 1025–1039. https://doi.org/10.1007/s00442-018-4192-5.

Brandriss, M.E., O'Neil, J.R., Edlund, M.B., Stoermer, E.F., 1998. Oxygen isotope fractionation between diatomaceous silica and water. Geochim. Cosmochim. Acta 62 (7), 1119–1125. https://doi.org/10.1016/S0016-7037(98)00054-4.

Bring, A., Fedorova, I., Dibike, Y., Hinzman, L., Mård, J., Mernild, S.H., Prowse, T., Semenova, O., Stuefer, S.L., Woo, M.-K., 2016. Arctic terrestrial hydrology: A synthesis of processes, regional effects, and research challenges. J. Geophys. Res. Biogeosci. 121 (3), 621–649. https://doi.org/10.1002/jgrg.v121.310.1002/2015JG003131.

Brosius, L.S., Anthony, K.M.W., Treat, C.C., Lenz, J., Jones, M.C., Bret-Harte, M.S., Grosse, G., 2021. Spatiotemporal patterns of northern lake formation since the Last Glacial Maximum. Quat. Sci. Rev. 253, 106773. https://doi.org/10.1016/j.quascirev.2020.106773.

Clark, I.D., Fritz, P., 1997. Environmental isotopes in hydrogeology. CRC Press, Cambridge, p. 342.

Cluett, A.A., Thomas, E.K., 2020. Resolving combined influences of inflow and evaporation on western Greenland lake water isotopes to inform paleoclimate inferences. J. Paleolimnol. 63 (4), 251–268. https://doi.org/10.1007/s10933-020-00114-4.

Cluett, A.A., Thomas, E.K., Evans, S.M., Keys, P.W., 2021. Seasonal Variations in Moisture Origin Explain Spatial Contrast in Precipitation Isotope Seasonality on Coastal Western Greenland. J. Geophys. Res.: Atmos. 126, e2020JD033543 https://doi.org/10.1029/2020JD033543.

Collins, M., Knutti, R., Arblaster, J., Dufresne, J.-L., Fichefet, T., Friedlingstein, P., Gao, X., Gutowski, W.J., Johns, T., Krinner, G., Shongwe, M., Tebaldi, C., Weaver, A.J., Wehner, M., 2013. Long-term climate change: projections, commitments and irreversibility. In: Stocker, T.F., Qin, D., Plattner, G.-K., Tignor, M., Allen, S.K., Boschung, J., Nauels, A., Xia, Y., Bex, V., Midgley, P.M. (Eds.), *Climate Change 2013: the Physical Science Basis. Contribution of Working Group I to the Fifth Assessment Report of the Intergovernmental Panel on Climate Change*. Cambridge University Press, Cambridge, United Kingdom and New York, NY, USA.

Corcoran, M.C., Thomas, E.K., Morrill, C., 2021. Using a paired chironomid $\delta^{18}O$ and aquatic leaf wax $\delta^{2}H$ approach to reconstruct seasonality on western Greenland during the Holocene. Paleoceanogr. Paleoclimatol. 36 (4), e2020PA004169 https://doi.org/10.1029/2020PA004169.

Craig, H., 1961. Isotopic variations in meteoric waters. Science 133 (3465), 1702–1703. https://doi.org/10.1126/science.133.3465.1702.

Craig, H., & Gordon, L. I. (1965). Deuterium and oxygen 18 variations in the ocean and the marine atmosphere. In: Tongiorgi, E. (Ed.), *Stable Isotopes in Oceanographic Studies and Paleo-Temperatures*. Consiglio nazionale delle ricerche, Pisa, Italy, Spoleto: Conferences in Nuclear Geology. pp. 9-130.

Curtin, L., D'Andrea, W.J., Balascio, N., Pugsley, G., de Wet, G., Bradley, R., 2019. Holocene and Last Interglacial climate of the Faroe Islands from sedimentary plant wax hydrogen and carbon isotopes. Quat. Sci. Rev. 223, 105930. https://doi.org/10.1016/j.quascirev.2019.105930.

Dansgaard, W., 1964. Stable isotopes in precipitation. Tellus 16 (4), 436–468. https://doi.org/10.3402/tellusa.v16i4.8993.

Dee, S.G., Russell, J.M., Morrill, C., Chen, Z., Neary, A., 2018. PRYSM v2. 0: A proxy system model for lacustrine archives. Paleoceanogr. Paleoclimatol. 33 (11), 1250–1269. https://doi.org/10.1029/2018PA003413.

Eklund, A., 1999. *Islägging och islossning på sjöar*. Swedish Meteorological and Hydrological Institute (SMHI) Hydrological Report No. 81. 24 pp.

FMI, 2021. Download observations. Finnish Meteorological Institute, Available at: https://en.ilmatieteenlaitos.fi/download-observations.

Gat, J.R., 1996. Oxygen and hydrogen isotopes in the hydrologic cycle. Annu. Rev. Earth Planet. Sci. 24 (1), 225–262. https://doi.org/10.1146/earth.1996.24.issue-110.1146/annurev.earth.24.1.225.

Gibson, J.J., Birks, S.J., Edwards, T.W.D., 2008. Global prediction of δA and δ^2H-$\delta^{18}O$ evaporation slopes for lakes and soil water accounting for seasonality. Global Biogeochem. Cycles 22, GB2031. https://doi.org/10.1029/2007GB002997.

Gibson, J.J., Edwards, T.W.D., 2002. Regional water balance trends and evaporation-transpiration partitioning from a stable isotope survey of lakes in northern Canada. Global Biogeochem. Cycles 16 (2), 10-1–10-14. https://doi.org/10.1029/2001GB001839.

Gibson, J.J., Edwards, T.W.D., Birks, S.J., St Amour, N.A., Buhay, W.M., McEachern, P., Wolfe, B.B., Peters, D.L., 2005. Progress in isotope tracer hydrology in Canada. Hydrol. Processes: Int. J. 19 (1), 303–327. https://doi.org/10.1002/(ISSN)1099-108510.1002/hyp.v19:110.1002/hyp.5766.

Gibson, J., Prepas, E., McEachern, P., 2002. Quantitative comparison of lake throughflow, residency, and catchment runoff using stable isotopes: modelling and results from a regional survey of Boreal lakes. J. Hydrol. 262 (1–4), 128–144. https://doi.org/10.1016/S0022-1694(02)00022-7.

Gröning, M., 2018. SICalib User Manual (Stable Isotope Calibration for routine δ-scale measurements) Ver 2.16 j. Terrestrial Environment Laboratory (TEL) Technical Note No. 01. International Atomic Energy Agency, Vienna, Austria. 37 pp.

Gröning, M., 2011. Improved water δ^2H and $\delta^{18}O$ calibration and calculation of measurement uncertainty using a simple software tool. Rapid Commun. Mass Spectrom. 25 (19), 2711–2720. https://doi.org/10.1002/rcm.5074.

GTK, 2021. Surficial Deposits of Finland 1:1 000 000. Geological Survey of Finland. Available at: https://gtkdata.gtk.fi/Maankamara/index.html.

Hammarlund, D., Barnekow, L., Birks, H.J.B., Buchardt, B., Edwards, T.W., 2002. Holocene changes in atmospheric circulation recorded in the oxygen-isotope stratigraphy of lacustrine carbonates from northern Sweden. The Holocene 12 (3), 339–351. https://doi.org/10.1191/0959683602hl548rp.

Heidbüchel, I., Troch, P.A., Lyon, S.W., Weiler, M., 2012. The master transit time distribution of variable flow systems. Water Resour. Res. 48 (6), 1–19. https://doi.org/10.1029/2011WR011293.

Hirvas, H., Lagerbäck, R., Mäkinen, K., Nenonen, K., Olsen, L., Rodhe, L., Thoresen, M., 1988. The Nordkalott Project: studies of Quaternary geology in northern Fennoscandia. Boreas 17 (4), 431–437. https://doi.org/10.1111/j.1502-3885.1988.tb00560.x.

Hughes, A.L.C., Gyllencreutz, R., Lohne, Ø.S., Mangerud, J., Svendsen, J.I., 2016. The last Eurasian ice sheets–a chronological database and time-slice reconstruction, DATED-1. Boreas 45 (1), 1–45. https://doi.org/10.1111/bor.2016.45.issue-110.1111/bor.12142.

Hurrell, J.W., 1995. Decadal trends in the North Atlantic Oscillation: regional temperatures and precipitation. Science 269 (5224), 676–679. https://doi.org/10.1126/science.269.5224.676.

Haapala, J.J., Ronkainen, I., Schmelzer, N., Sztobryn, M., 2015. Recent Change - Sea Ice. In: Team, T.B.I.A. (Ed.), Second Assessment of Climate Change for the Baltic Sea Basin. Regional Climate Studies. Springer International Publishing, Cham, pp. 145–153. https://doi.org/10.1007/978-3-319-16006-1_8.

Hanssen-Bauer, I., Førland, E., 2000. Temperature and precipitation variations in Norway 1900–1994 and their links to atmospheric circulation. Int. J. Climatol.: A J. Royal Meteorolog. Soc. 20 (14), 1693–1708. https://doi.org/10.1002/1097-0088(20001130)20:14<1693::AID-JOC567>3.0.CO;2-7.

IAEA/WMO., 2019. Global Network of Isotopes in Precipitation. The GNIP Database. Available at: https://nucleus.iaea.org/wiser.

Ingraham, N.L., Taylor, B.E., 1991. Light stable isotope systematics of large-scale hydrologic regimes in California and Nevada. Water Resour. Res. 27 (1), 77–90. https://doi.org/10.1029/90WR01708.

Irannezhad, M., Marttila, H., Kløve, B., 2014. Long-term variations and trends in precipitation in Finland. Int. J. Climatol. 34 (10), 3139–3153. https://doi.org/10.1002/joc.2014.34.issue-1010.1002/joc.3902.

Jakobsson, M., Mayer, L., Coakley, B., Dowdeswell, J.A., Forbes, S., Fridman, B., Hodnesdal, H., Noormets, R., Pedersen, R., Rebesco, M., Schenke, H.W., Zarayskaya, Y., Accettella, D., Armstrong, A., Anderson, R.M., Bienhoff, P., Camerlenghi, A., Church, I., Edwards, M., Gardner, J.V., Hall, J.K., Hell, B., Hestvik, O., Kristoffersen, Y., Marcussen, C., Mohammad, R., Mosher, D., Nghiem, S. V., Pedrosa, M.T., Travaglini, P.G., Weatherall, P., 2012. The International Bathymetric Chart of the Arctic Ocean (IBCAO) version 3.0. Geophys. Res. Lett. 39 (12), L12609. https://doi.org/10.1029/2012GL052219.

Jones, M.D., Dee, S., Anderson, L., Baker, A., Bowen, G., Noone, D., 2016. Water isotope systematics: improving our palaeoclimate interpretations. Quat. Sci. Rev. 131 (B), 243–249. https://doi.org/10.1016/j.quascirev.2015.11.014.

Jonsson, C.E., Leng, M.J., Rosqvist, G.C., Seibert, J., Arrowsmith, C., 2009. Stable oxygen and hydrogen isotopes in sub-Arctic lake waters from northern Sweden. J. Hydrol. 376 (1–2), 143–151. https://doi.org/10.1016/j.jhydrol.2009.07.021.

Jonsson, C.E., Rosqvist, G.C., Leng, M.J., Bigler, C., Bergman, J., Tillman, P.K., Sloane, H. J., 2010. High-resolution diatom $\delta^{18}O$ records, from the last 150 years, reflecting changes in amount of winter precipitation in two sub-Arctic high-altitude lakes in the Swedish Scandes. J. Quat. Sci. 25 (6), 918–930. https://doi.org/10.1002/jqs.1372.

Jouzel, J., Merlivat, L., 1984. Deuterium and oxygen 18 in precipitation: Modeling of the isotopic effects during snow formation. J. Geophys. Res.: Atmos. 89 (D7), 11749–11757. https://doi.org/10.1029/JD089iD07p11749.

Jutebring Sterte, E., Lidman, F., Lindborg, E., Sjöberg, Y., Laudon, H., 2021. How catchment characteristics influence hydrological pathways and travel times in a boreal landscape. Hydrol. Earth Syst. Sci. 25 (4), 2133–2158. https://doi.org/10.5194/hess-25-2133-2021.

Jaagus, J., 2009. Regionalisation of the precipitation pattern in the Baltic Sea drainage basin and its dependence on large-scale atmospheric circulation. Boreal Environ. Res. 14, 31–44.

Katrantsiotis, C., Norström, E., Smittenberg, R.H., Salonen, J.S., Plikk, A., Helmens, K., 2021. Seasonal variability in temperature trends and atmospheric circulation systems during the Eemian (Last Interglacial) based on *n*-alkanes hydrogen isotopes from Northern Finland. Quat. Sci. Rev. 273, 107250. https://doi.org/10.1016/j.quascirev.2021.107250.

Kjellman, S.E., Schomacker, A., Thomas, E.K., Håkansson, L., Duboscq, S., Cluett, A.A., Farnsworth, W.R., Allaart, L., Cowling, O.C., McKay, N.P., Brynjólfsson, S., Ingólfsson, Ó., 2020. Holocene precipitation seasonality in northern Svalbard: Influence of sea ice and regional ocean surface conditions. Quat. Sci. Rev. 240, 106388. https://doi.org/10.1016/j.quascirev.2020.106388.

Korhonen, J., 2006. Long-term changes in lake ice cover in Finland. Hydrol. Res. 37 (4–5), 347–363. https://doi.org/10.2166/nh.2006.019.

Kortelainen, N.M., Karhu, J.A., 2004. Regional and seasonal trends in the oxygen and hydrogen isotope ratios of Finnish groundwaters: a key for mean annual precipitation. J. Hydrol. 285 (1–4), 143–157. https://doi.org/10.1016/j.jhydrol.2003.08.014.

L'Abée-Lund, J.H., Vøllestad, L.A., Brittain, J.E., Kvambekk, Å.S., Solvang, T., 2021. Geographic variation and temporal trends in ice phenology in Norwegian lakes during the period 1890–2020. Cryosphere 15 (5), 2333–2356. https://doi.org/10.5194/tc-15-2333-2021.

Lawrence, Z.D., Perlwitz, J., Butler, A.H., Manney, G.L., Newman, P.A., Lee, S.H., Nash, E.R., 2020. The remarkably strong Arctic stratospheric polar vortex of winter 2020: Links to record-breaking Arctic oscillation and ozone loss. J. Geophys. Res.: Atmos. 125 (22), e2020JD033271 https://doi.org/10.1029/2020JD033271.

LeGrande, A.N., Schmidt, G.A., 2006. Global gridded data set of the oxygen isotopic composition in seawater. Geophys. Res. Lett. 33 (12) https://doi.org/10.1029/2006GL026011.

Leng, M.J., Anderson, N.J., 2003. Isotopic variation in modern lake waters from western Greenland. Holocene 13 (4), 605–611. https://doi.org/10.1191/0959683603hl620rr.

Leng, M.J., Marshall, J.D., 2004. Palaeoclimate interpretation of stable isotope data from lake sediment archives. Quat. Sci. Rev. 23 (7–8), 811–831. https://doi.org/10.1016/j.quascirev.2003.06.012.

Linderholm, H.W., Nicolle, M., Francus, P., Gajewski, K., Helama, S., Korhola, A., Solomina, O., Yu, Z., Zhang, P., D'Andrea, W.J., 2018. Arctic hydroclimate variability during the last 2000 years. Clim. Past 14 (4), 473–514. https://doi.org/10.5194/cp-14-473-2018.

Lombino, A., Atkinson, T., Brooks, S.J., Gröcke, D.R., Holmes, J., Jones, V.J., Marshall, J. D., 2021. Experimental determination of the temperature dependence of oxygen-isotope fractionation between water and chitinous head capsules of chironomid larvae. J. Paleolimnol. 66 (2), 117–124. https://doi.org/10.1007/s10933-021-00191-z.

Laasanen, O., 1982. *Vesistöjen jäätymis-, jäänlähtö-, jäänpaksuus-ja pintaveden lämpötilatilastoja. Freeze-up, break-up, ice thickness and surface water temperature statistics in lakes and rivers in Finland*: Vesihallitus. National Board of Waters, Finland. Publ. Water Res. Inst. 77, 68 pp.

MacDonald, L.A., Wolfe, B.B., Turner, K.W., Anderson, L., Arp, C.D., Birks, S.J., Bouchard, F., Edwards, T.W.D., Farquharson, N., Hall, R.I., McDonald, I., Narancic, B., Ouimet, C., Pienitz, R., Tondu, J., White, H., 2017. A synthesis of thermokarst lake water balance in high-latitude regions of North America from isotope tracers. Arct. Sci. 3 (2), 118–149. https://doi.org/10.1139/as-2016-0019.

Marshall, J., Kushnir, Y., Battisti, D., Chang, P., Czaja, A., Dickson, R., Hurrell, J., McCartney, M., Saravanan, R., Visbeck, M., 2001. North Atlantic climate variability: phenomena, impacts and mechanisms. Int. J. Climatol.: J. R. Meteorol. Society 21 (15), 1863–1898. https://doi.org/10.1002/(ISSN)1097-008810.1002/joc.v21:1510.1002/joc.693.

Mellat, M., Bailey, H., Mustonen, K.-R., Marttila, H., Klein, E.S., Gribanov, K., Bret-Harte, M.S., Chupakov, A.V., Divine, D.V., Else, B., Filippov, I., Hyöky, V., Jones, S., Kirpotin, S.N., Kroon, A., Markussen, H.T., Nielsen, M., Olsen, M., Paavola, R., Pokrovsky, O.S., Prokushkin, A., Rasch, M., Raundrup, K., Suominen, O., Syvänperä, I., Vignisson, S.R., Zarov, E., Welker, J.M., 2021. Hydroclimatic controls on the isotopic ($\delta^{18}O$, δ^2H, *d-excess*) traits of pan-Arctic summer rainfall events. Front. Earth Sci. 9, 651731 https://doi.org/10.3389/feart.2021.651731.

MET Norway, 2021. seKlima. Norwegian Meteorological Institute. Available at: https://klimaservicesenter.no/observations/.

Moen, A., 1998. Vegetasjonsatlas for Norge: Vegetasjon. Norwegian Mapping Authority, Hønefoss, p. 199.

Mügler, I., Sachse, D., Werner, M., Xu, B., Wu, G., Yao, T., Gleixner, G., 2008. Effect of lake evaporation on δD values of lacustrine *n*-alkanes: A comparison of Nam Co (Tibetan Plateau) and Holzmaar (Germany). Org Geochem. 39 (6), 711–729. https://doi.org/10.1016/j.orggeochem.2008.02.008.

National Snow and Ice Data Center, 2019. SOTC: Sea ice. Available at: http://nsidc.org/cryosphere/sotc/sea_ice.html.

National Weather Service Climate Prediction Center, 2021. Arctic Oscillation. Available at: https://www.cpc.ncep.noaa.gov/data.

NGU, 2021. Superficial deposits - National Database. Geological Survey of Norway, Available at: http://geo.ngu.no/kart/losmasse_mobil/.

Nichols, J.E., Walcott, M., Bradley, R., Pilcher, J., Huang, Y., 2009. Quantitative assessment of precipitation seasonality and summer surface wetness using ombrotrophic sediments from an Arctic Norwegian peatland. Quat. Res. 72 (3), 443–451. https://doi.org/10.1016/j.yqres.2009.07.007.

O'Sadnick, M., Petrich, C., Brekke, C., Skarðhamar, J., 2020. Ice extent in sub-arctic fjords and coastal areas from 2001 to 2019 analyzed from MODIS imagery. Ann. Glaciol. 61 (82), 210–226. https://doi.org/10.1017/aog.2020.34.

Palecki, M., Barry, R., 1986. Freeze-up and break-up of lakes as an index of temperature changes during the transition seasons: a case study for Finland. J. Appl. Meteorol.

Climatol. 25 (7), 893–902. https://doi.org/10.1175/1520-0450(1986)025<0893:FUABUO>2.0.CO;2.
Papritz, L., Sodemann, H., 2018. Characterizing the local and intense water cycle during a cold air outbreak in the Nordic seas. Mon. Weather Rev. 146 (11), 3567–3588. https://doi.org/10.1175/MWR-D-18-0172.1.
Putman, A.L., Feng, X., Sonder, L.J., Posmentier, E.S., 2017. Annual variation in event-scale precipitation δ^2H at Barrow, AK, reflects vapor source region. Atmos. Chem. Phys. 17 (7), 4627–4639. https://doi.org/10.5194/acp-17-4627-2017.
Putman, A.L., Fiorella, R.P., Bowen, G.J., Cai, Z., 2019. A global perspective on local meteoric water lines: Meta-analytic insight into fundamental controls and practical constraints. Water Resour. Res. 55 (8), 6896–6910. https://doi.org/10.1029/2019WR025181.
Rach, O., Kahmen, A., Brauer, A., Sachse, D., 2017. A dual-biomarker approach for quantification of changes in relative humidity from sedimentary lipid D/ H ratios. Clim. Past 13 (7), 741–757. https://doi.org/10.5194/cp-13-741-2017.
Rawlins, M.A., Steele, M., Holland, M.M., Adam, J.C., Cherry, J.E., Francis, J.A., Groisman, P.Y., Hinzman, L.D., Huntington, T.G., Kane, D.L., 2010. Analysis of the Arctic system for freshwater cycle intensification: Observations and expectations. J. Clim. 23 (21), 5715–5737. https://doi.org/10.1175/2010JCLI3421.1.
Rosqvist, G., Jonsson, C., Yam, R., Karlén, W., Shemesh, A., 2004. Diatom oxygen isotopes in pro-glacial lake sediments from northern Sweden: a 5000 year record of atmospheric circulation. Quat. Sci. Rev. 23 (7–8), 851–859. https://doi.org/10.1016/j.quascirev.2003.06.009.
Rosqvist, G.C., Leng, M.J., Goslar, T., Sloane, H.J., Bigler, C., Cunningham, L., Dadal, A., Bergman, J., Berntsson, A., Jonsson, C., Wastegård, S., 2013. Shifts in precipitation during the last millennium in northern Scandinavia from lacustrine isotope records. Quat. Sci. Rev. 66, 22–34. https://doi.org/10.1016/j.quascirev.2012.10.030.
Rosqvist, G.C., Leng, M.J., Jonsson, C., 2007. North Atlantic region atmospheric circulation dynamics inferred from a late-Holocene lacustrine carbonate isotope record, northern Swedish Lapland. Holocene 17 (7), 867–873. https://doi.org/10.1177/0959683607080508.
Rozanski, K., Araguás-Araguás, L., Gonfiantini, R., 1993. Isotopic patterns in modern global precipitation. In: Swart, P.K., Lohmann, K.C., Mckenzie, J., Savin, S. (Eds.), Climate Change in Continental Isotopic Records. Geophysical Monograph Series 78, 1-36.
Rozanski, K., Sonntag, C., Münnich, K., 1982. Factors controlling stable isotope composition of European precipitation. Tellus 34 (2), 142–150. https://doi.org/10.1111/j.2153-3490.1982.tb01801.x.
Ruuhijärvi, R., 1983. The Finnish mire types and their regional distribution. In: Gore, A. (Ed.), Mires: swamp, bog, fen and moor, regional studies. Elsevier, Amsterdam, pp. 47–67.
Sachse, D., Billault, I., Bowen, G.J., Chikaraishi, Y., Dawson, T.E., Feakins, S.J., Freeman, K.H., Magill, C.R., McInerney, F.A., van der Meer, M.T.J., Polissar, P., Robins, R.J., Sachs, J.P., Schmidt, H.-L., Sessions, A.L., White, J.W.C., West, J.B., Kahmen, A., 2012. Molecular Paleohydrology: Interpreting the Hydrogen-Isotopic Composition of Lipid Biomarkers from Photosynthesizing Organisms. Annu. Rev. Earth Planet. Sci. 40 (1), 221–249. https://doi.org/10.1146/earth.2012.40.issue-110.1146/annurev-earth-042711-105535.
Schmidt, G.A., Bigg, G.R., Rohling, E.J., 1999. Global Seawater Oxygen-18 Database - v1.22. Available at: https://data.giss.nasa.gov/o18data/.
Seppä, H., 2002. Mires of Finland: Regional and local controls of vegetation, landforms, and long-term dynamics. Fennia-Int. J. Geogr. 180 (1–2), 43–60. https://fennia.journal.fi/article/view/3763.
Shapiro, M., Fedor, L., Hampel, T., 1987. Research aircraft measurements of a polar low over the Norwegian Sea. Tellus A: Dynamic Meteorol. Oceanogr. 39 (4), 272–306. https://doi.org/10.3402/tellusa.v39i4.11761.
Shemesh, A., Rosqvist, G., Rietti-Shati, M., Rubensdotter, L., Bigler, C., Yam, R., Karlén, W., 2001. Holocene climatic change in Swedish Lapland inferred from an oxygen-isotope record of lacustrine biogenic silica. Holocene 11 (4), 447–454. https://doi.org/10.1191/095968301678302887.
Singh, H.K., Bitz, C.M., Donohoe, A., Rasch, P.J., 2017. A source–receptor perspective on the polar hydrologic cycle: Sources, seasonality, and Arctic-Antarctic parity in the hydrologic cycle response to CO_2 doubling. J. Clim. 30 (24), 9999–10017. https://doi.org/10.1175/JCLI-D-16-0917.1.
Sjöfartsverket & SMHI, 2020a. *A Summary of the Ice Season and Icebreaking Activities 2018/2019*. Swedish Maritime Administration and Swedish Meteorological and Hydrological Institute. 55 pp. Available at: https://www.smhi.se/oceanografi/istjanst/havsis_en.php.
Sjöfartsverket & SMHI, 2020b. *A Summary of the Ice Season and Icebreaking Activities 2019/2020*. Swedish Maritime Administration and Swedish Meteorological and Hydrological Institute. 52 pp. Available at: https://www.smhi.se/oceanografi/istjanst/havsis_en.php.
SMHI, 2021. Download meteorological observations. Swedish Meteorological and Hydrological Institute. Available at: https://www.smhi.se/data/meteorologi/ladda-ner-meteorologiska-observationer.
Sodemann, H., Masson-Delmotte, V., Schwierz, C., Vinther, B.M., Wernli, H., 2008. Interannual variability of Greenland winter precipitation sources: 2. Effects of North Atlantic Oscillation variability on stable isotopes in precipitation. J. Geophys. Res. *Atmospheres* 113 (D12). https://doi.org/10.1029/2007JD009416.
St. Amour, N.A., 2009. A multi-proxy study of Holocene atmospheric circulation dynamics recorded in lake sediments in Fennoscandia. PhD Thesis, University of Waterloo, Ontario, Canada. 253 pp. http://hdl.handle.net/10012/4225.
St. Amour, N.A., Hammarlund, D., Edwards, T.W., Wolfe, B.B., 2010. New insights into Holocene atmospheric circulation dynamics in central Scandinavia inferred from oxygen-isotope records of lake-sediment cellulose. Boreas 39 (4), 770–782. https://doi.org/10.1111/j.1502-3885.2010.00169.x.
Steen-Larsen, H.C., Masson-Delmotte, V., Sjolte, J., Johnsen, S.J., Vinther, B.M., Bréon, F.-M., Clausen, H.B., Dahl-Jensen, D., Falourd, S., Fettweis, X., Gallée, H., Jouzel, J., Kageyama, M., Lerche, H., Minster, B., Picard, G., Punge, H.J., Risi, C., Salas, D., Schwander, J., Steffen, K., Sveinbjörnsdottír, A.E., Svensson, A., White, J., 2011. Understanding the climatic signal in the water stable isotope records from the NEEM shallow firn/ice cores in northwest Greenland. J. Geophys. Res.: Atmos. 116 (D6) https://doi.org/10.1029/2010JD014311.
Stroeven, A.P., Hättestrand, C., Kleman, J., Heyman, J., Fabel, D., Fredin, O., Goodfellow, B.W., Harbor, J.M., Jansen, J.D., Olsen, L., Caffee, M.W., Fink, D., Lundqvist, J., Rosqvist, G.C., Strömberg, B., Jansson, K.N., 2016. Deglaciation of Fennoscandia. Quat. Sci. Rev. 147, 91–121. https://doi.org/10.1016/j.quascirev.2015.09.016.
Sundqvist, H.S., Kaufman, D.S., McKay, N., Balascio, N., Briner, J., Cwynar, L., Sejrup, H., Seppä, H., Subetto, D., Andrews, J., 2014. Arctic Holocene proxy climate database–new approaches to assessing geochronological accuracy and encoding climate variables. Clim. Past 10 (4), 1605–1631. https://doi.org/10.5194/cp-10-1605-2014.
Thienemann, M., Kusch, S., Vogel, H., Ritter, B., Schefub, E., Rethemeyer, J., 2019. Neoglacial transition of atmospheric circulation patterns over Fennoscandia recorded in Holocene Lake Torneträsk sediments. Boreas 48 (2), 287–298. https://doi.org/10.1111/bor.2019.48.issue-210.1111/bor.12365.
Thomas, E., Castañeda, I., McKay, N., Briner, J., Salacup, J., Nguyen, K., Schweinsberg, A., 2018. A wetter Arctic coincident with hemispheric warming 8,000 years ago. Geophys. Res. Lett. 45 (19), 10,637–610,647. https://doi.org/10.1029/2018GL079517.
Thomas, E.K., Hollister, K.V., Cluett, A.A., Corcoran, M.C., Briner, J.P., 2020. Reconstructing Arctic precipitation seasonality using aquatic leaf wax δ^2H in lakes with contrasting residence times. Paleoceanogr. Paleoclimatol. 35 (7), e2020PA003886 https://doi.org/10.1029/2020PA003886.
Thompson, D.W., Wallace, J.M., 1998. The Arctic Oscillation signature in the wintertime geopotential height and temperature fields. Geophys. Res. Lett. 25 (9), 1297–1300. https://doi.org/10.1029/98GL00950.
Tondu, J., Turner, K., Wolfe, B., Hall, R., Edwards, T., McDonald, I., 2013. Using water isotope tracers to develop the hydrological component of a long-term aquatic ecosystem monitoring program for a northern lake-rich landscape. Arct. Antarct. Alp. Res. 45 (4), 594–614. https://doi.org/10.1657/1938-4246-45.4.594.
Uvo, C.B., 2003. Analysis and regionalization of northern European winter precipitation based on its relationship with the North Atlantic Oscillation. Int. J. Climatol.: J. R. Meteorol. Soc. 23 (10), 1185–1194. https://doi.org/10.1002/(ISSN)1097-008810.1002/joc.v23:1010.1002/joc.930.
van Geldern, R., Barth, J.A., 2012. Optimization of instrument setup and post-run corrections for oxygen and hydrogen stable isotope measurements of water by isotope ratio infrared spectroscopy (IRIS). Limnol. Oceanogr. Methods 10 (12), 1024–1036. https://doi.org/10.4319/lom.2012.10.1024.
Vázquez, M., Nieto, R., Drumond, A., Gimeno, L., 2016. Moisture transport into the Arctic: Source-receptor relationships and the roles of atmospheric circulation and evaporation. Journal of Geophysical Research: Atmospheres 121 (22), 13,493–13,509. https://doi.org/10.1002/2016JD025400.
Vihma, T., Screen, J., Tjernström, M., Newton, B., Zhang, X., Popova, V., Deser, C., Holland, M., Prowse, T., 2016. The atmospheric role in the Arctic water cycle: A review on processes, past and future changes, and their impacts. J. Geophys. Res. Biogeosci. 121 (3), 586–620. https://doi.org/10.1002/jgrg.v121.310.1002/2015JG003132.
Welker, J.M., 2000. Isotopic (δ^{18}O) characteristics of weekly precipitation collected across the USA: an initial analysis with application to water source studies. Hydrol. Process. 14 (8), 1449–1464. https://doi.org/10.1002/1099-1085(20000615)14:8<1449::AID-HYP993>3.0.CO;2-7.
Weyhenmeyer, G.A., Meili, M., Livingstone, D.M., 2004. Nonlinear temperature response of lake ice breakup. Geophys. Res. Lett. 31, L07203. https://doi.org/10.1029/2004GL019530.
Wrona, F.J., Johansson, M., Culp, J.M., Jenkins, A., Mård, J., Myers-Smith, I.H., Prowse, T.D., Vincent, W.F., Wookey, P.A., 2016. Transitions in Arctic ecosystems: Ecological implications of a changing hydrological regime. J. Geophys. Res. Biogeosci. 121 (3), 650–674. https://doi.org/10.1002/2015JG003133.

Paper III

Holocene precipitation seasonality along a climatic gradient from western Spitsbergen to Nordaustlandet, Svalbard

Sofia E. Kjellman[a,*], Elizabeth K. Thomas[b], Anders Schomacker[a], Wesley R. Farnsworth[c,d], Owen C. Cowling[b], Lis Allaart[a,**], Skafti Brynjólfsson[e]

[a]Department of Geosciences, UiT The Arctic University of Norway, P.O. Box 6050 Langnes, NO-9037 Tromsø, Norway.

[b]Department of Geology, University at Buffalo, State University of New York, 126 Cooke Hall, Buffalo, NY 14260, USA.

[c]Globe Institute, University of Copenhagen, Øster Voldgade 5-7, DK-1350 Copenhagen K., Denmark.

[d]Institute of Earth Sciences, University of Iceland, Askja, Sturlugata 7, IS-102, Reykjavík, Iceland.

[e]Icelandic Institute of Natural History, Borgum við Norðurslóð, IS-600, Akureyri, Iceland.

*Corresponding author: Sofia E. Kjellman: sofia.e.kjellman@uit.no

**Present address: Geological Survey of Denmark and Greenland (GEUS), Department of Marine Geology, Universitetsbyen 81, DK-8000 Aarhus C., Denmark.

Highlights

- Four sedimentary leaf wax records from Svalbard to reconstruct water cycle changes.
- δ^2H_{wax} as proxy for seasonal distribution of precipitation or summer precipitation δ^2H.
- Warm, dry Early and Middle Holocene summers followed by cooler Late Holocene trend.
- Increased Early and Middle Holocene winter precipitation on northern Svalbard.
- Constraints on modern conditions help strengthen paleo-precipitation proxy studies.

Abstract

The Svalbard archipelago spans large climate gradients, associated with large-scale atmospheric circulation patterns, variations in ocean heat content, and sea-ice cover. Future increases in precipitation are projected to be greatest in the northeast and mainly occur in winter, but large uncertainties underscore the need for reconstructions of long-term spatial and temporal variations in precipitation amounts and seasonality. We use lipid biomarkers from four sedimentary lake records along a climatic gradient from western Spitsbergen to Nordaustlandet to reconstruct Holocene water cycle changes. We measured the leaf wax hydrogen isotopic composition of long-chain (terrestrial; δ^2H_{terr}) and mid-chain (aquatic; δ^2H_{aq}) *n*-alkanoic acids. δ^2H_{terr} mainly reflects summer precipitation δ^2H and evapotranspiration, whereas δ^2H_{aq} can reflect varying seasonality due to varying lake hydrology. For one lake, we used the difference between δ^2H_{terr} and δ^2H_{aq} ($\varepsilon_{28–22}$) to infer summer evapotranspiration changes. Relatively ^2H-enriched δ^2H_{terr} and higher $\varepsilon_{28–22}$ in the Early and Middle Holocene suggests warm summers with higher evapotranspiration, and/or more proximal moisture in summer. After 6–5.5 cal. kyr BP, ^2H-depleted δ^2H_{terr} and lower $\varepsilon_{28–22}$ indicate summer cooling, less evapotranspiration, or more distally derived moisture. We propose that an Early Holocene decrease in δ^2H_{aq} in two lakes on northern Spitsbergen reflects an increase in the proportion of winter relative to summer precipitation associated with regional warming and increased moisture supply as the sea ice diminished. The proportion of winter precipitation likely decreased after *c*. 6 cal. kyr BP, when the ocean surface cooled and sea-ice cover increased. On northern Svalbard, intermittent ^2H-depleted δ^2H_{aq} in the Late Holocene suggests periodic increases in winter precipitation or decreases in summer precipitation inflow to the lakes. Our records provide support for predictions that Svalbard precipitation is sensitive to sea-ice cover and ocean surface heat flux.

Keywords: Lake sediment, Biomarker, Leaf wax δ^2H, Paleoclimate, Quaternary, Arctic precipitation

1. Introduction

The Arctic region is of key interest in climate change research due to its sensitivity to changes in global climate and amplified response (e.g., IPCC, 2021). Climate models project precipitation increases of more than 50% in the Arctic regions in the 21st century (Bintanja & Selten, 2014; Bintanja & Andry, 2017). A wetter Arctic results from enhanced evaporation from ice-free seas (Bintanja & Selten, 2014; Kopec et al., 2016), increased poleward moisture transport (Dufour et al., 2016; Singh et al., 2017; Bintanja et al., 2020), and increases in water vapor (Screen & Simmonds, 2010; Swann et al., 2010). These factors are also contributing to increased interannual precipitation variability (Bintanja et al., 2020), and a transition towards a rain-dominated Arctic (Bintanja & Andry, 2017; Førland et al., 2020; McCrystall et al., 2021).

The Svalbard archipelago is located on the primary pathway for atmospheric energy transport into the Arctic (Serreze et al., 2007) and has since 1991 experienced a warming rate of 1.7 °C per decade, which is more than twice the Arctic average and seven times the global average (Nordli et al., 2020). From 1936 to 2010, glaciers on Svalbard thinned on average 0.35 m yr^{-1}, and a space-for-time-model suggests an average Svalbard-wide glacier thinning rate of 0.67–0.92 m yr^{-1} from 2010 to 2100 (Geyman et al., 2022). Over the last 50 years, annual precipitation amounts on Svalbard have increased by 20–35% (Førland et al., 2020), and heavy precipitation events have become more intense and frequent (Hanssen-Bauer et al., 2019). Müller et al. (2022) explained extreme precipitation events on Svalbard in the last four decades by a declining sea-ice cover in the Greenland Sea, providing a source of moisture. Ensemble median projections for regional models and emission scenario RCP8.5 (“business

as usual") indicate a precipitation increase of around 65% by 2071–2100 relative to 1971–2000 annual precipitation amount (Hanssen-Bauer et al., 2019). Emission reductions after 2040 (RCP4.5, "medium emissions") lower this estimated precipitation increase to 45% (Hanssen-Bauer et al., 2019). The increase is heterogenous in both time and space, being most pronounced in the winter months and with the largest increase in the northeast. These future projections are associated with large uncertainties due to limitations in the climate models and inadequate knowledge about the sensitivity of the climate system (Hanssen-Bauer et al., 2019).

When, how much, and in what phase (rain or snow) precipitation falls have substantial environmental and societal impact, affecting e.g., the surface energy budget, slope processes, glacier mass balance, permafrost, ecosystems, and infrastructure (e.g., Larsson, 1982; Hansen et al., 2014; Vihma et al., 2016; Hanssen-Bauer et al., 2019; Łupikasza et al., 2019; McCrystall et al., 2021). Most of our understanding of past and present-day Arctic hydrological change is based on in situ and remote sensing observations, atmospheric reanalyses, and climate model hindcasts (e.g., Dufour et al., 2016; Førland et al., 2020; Wickström et al., 2020). One way to improve our understanding of the mechanisms behind precipitation changes is looking beyond the short and sparse instrumental records, using paleoclimate proxies (e.g., Linderholm et al., 2018; Konecky et al., 2020).

Water isotope proxies are commonly used in paleoclimate research, as they reflect multiple aspects of the water cycle, including temperature and moisture source changes (Masson-Delmotte et al., 2005; Cowling et al., 2021; Katrantsiotis et al., 2021), moisture balance (Anderson et al., 2007; Balascio et al., 2013) and precipitation seasonality (Thomas et al., 2020; Corcoran et al., 2021). An increasing number of Arctic studies uses the hydrogen isotopic composition (δ^2H) of sedimentary leaf waxes to reconstruct the isotopic composition of precipitation in the past (e.g., Thomas et al., 2012; Wilkie, 2012; Balascio et al., 2013;

Thomas et al., 2016; Thomas et al., 2018; Thomas et al., 2020; Cowling et al., 2021; Gorbey et al., in press), including Svalbard (Balascio et al., 2018; Kjellman et al., 2020). Studies of the modern relationship between leaf wax δ^2H and precipitation δ^2H have demonstrated that there is a strong correlation between the two, with the leaf wax values being more ^2H-depleted than precipitation (Sachse et al., 2004; Sachse et al., 2012; McFarlin et al., 2019). Leaf wax δ^2H reflects the δ^2H of the plant source water with an offset (apparent fractionation, ε_{app}) due to several processes, including biosynthetic fractionation (Sachse et al., 2012). The biosynthetic fractionation can differ between plant types (Daniels et al., 2017; Berke et al., 2019; Dion-Kirschner et al., 2020), but is relatively constant for specific compounds (Sachse et al., 2012; McFarlin et al., 2019). The leaf waxes can be traced back to aquatic or terrestrial sources, with mid-chain waxes primarily being produced by aquatic plants (Ficken et al., 2000; Aichner et al., 2010) and long-chain waxes by terrestrial plants (Wilkie et al., 2013; Thomas et al., 2016; Daniels et al., 2017). Terrestrial plants use soil water as their source water, and the hydrogen isotopic composition of terrestrial leaf waxes (δ^2H_{terr}) therefore reflects growing season soil water δ^2H, which might be influenced by evaporation (Kahmen et al., 2013). Aquatic plants use lake water as their moisture source, so that the hydrogen isotopic composition of aquatic leaf waxes (δ^2H_{aq}) reflects ice-free growing season lake water δ^2H. The lake water δ^2H can reflect different precipitation seasonality depending on the residence time of the lake (Cluett & Thomas, 2020; Thomas et al., 2020).

Here, we present Holocene records of sedimentary leaf wax δ^2H from four lakes in the high-Arctic archipelago Svalbard. The aim of this study is to document how different parts of Svalbard have responded to past climate change, and more specifically to reconstruct Holocene variations in precipitation seasonality in time and space. We targeted lakes along a climatic gradient from the relatively warm, humid western Spitsbergen to the relatively cold, arid Nordaustlandet (Fig. 1). The majority of the investigated sedimentary records consist of

clayey or silty gyttja, from organic lacustrine sedimentation without inflow of glacial meltwater. The lakes reflect different precipitation seasonality due to their different water residence times, and we regard the biomarkers from the lake sediment sequences as archives of regional paleoclimate. Further, we discuss our findings in relation to established terrestrial and marine paleoenvironmental records as well as glaciation history of Svalbard.

2. Regional setting and study sites

High-Arctic Svalbard (74–81°N and 10–35°E) is one of the world's northernmost landmasses, but the archipelago experiences warmer, wetter, and cloudier conditions than other areas at the same latitude (Eckerstorfer & Christiansen, 2011). This is mainly due to the strong influence of the warm West Spitsbergen Current and associated northward atmospheric heat and moisture transport along the west coast of Spitsbergen (Skagseth et al., 2008; Walczowski & Piechura, 2011; Fig. 1). The archipelago is located near the north end of the North Atlantic cyclone track and experiences highest cyclonic intensity in the winter months (December to February; Serreze et al., 1993; Zhang et al., 2004). This cyclonic activity is associated with heat and moisture transport, high precipitation amounts, and strong winds. The interplay between warm Atlantic and cold Arctic ocean currents and atmospheric air masses, as well as pronounced topography, cause substantial regional differences in climate, with milder conditions on the west coast and colder and drier climate in the central parts and in the northeast. In addition, the West and East Spitsbergen Currents have a large impact on the distribution of sea ice, affecting the surface temperature.

Available climate data from Svalbard are limited, especially in terms of spatial distribution. The meteorological stations are concentrated on low-elevation coastal western Spitsbergen, where the first weather station (Green Harbour) was established in 1911 (Nordli et al., 1996). The alpine topography of Spitsbergen has a strong orographic influence on

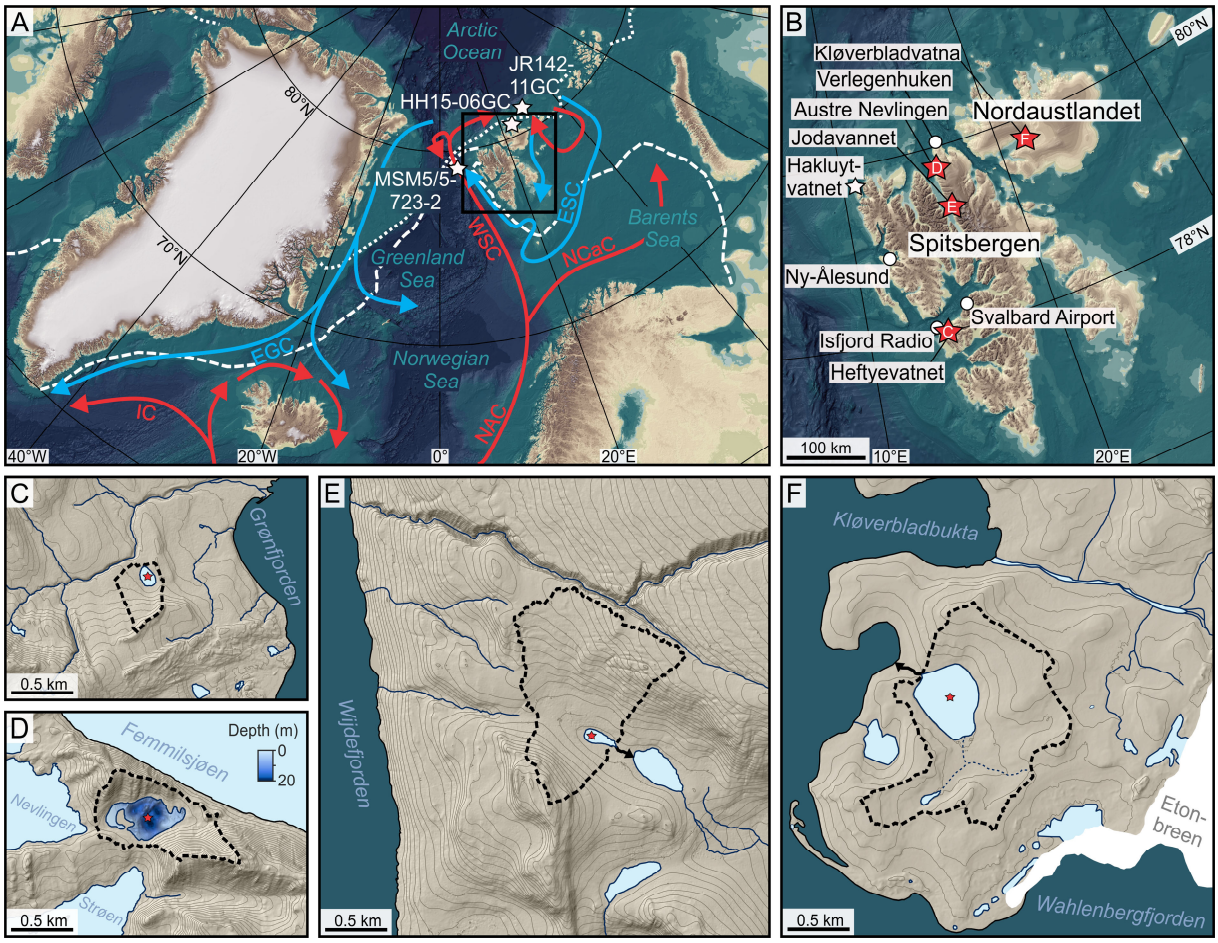

Fig. 1. (a) Overview map of the North Atlantic region, with major ocean surface currents (warm currents in red, cold in blue; NAC = North Atlantic Current; NCaC = North Cape Current; WSC = West Spitsbergen Current; IC = Irminger Current, ESC = East Spitsbergen Current; EGC = East Greenland Current), median winter (white dashed line) and summer (white dotted line) sea-ice extent AD 1981–2010 (National Snow and Ice Data Center, 2019), and locations of marine cores (white stars) MSM5/5-723-2 (Werner et al., 2016), HH15-06GC and JR142-11GC (Pieńkowski et al., 2021). (b) Map of Svalbard, showing locations of lakes in this (red stars) and previous (white star; Balascio et al., 2018) studies and meteorological stations (white circles). Coring locations (red stars) and lake catchments (black dashed lines) for (c) Heftyevatnet, (d) Austre Nevlingen, (e) Jodavannet, and (f) Kløverbladvatna. Black arrows mark outflow streams. Background maps in (a)-(b) from IBCAO (Jakobsson et al., 2012) and in (c)-(f) based on 5x5 m digital elevation models from Norwegian Polar Institute (2014) with 10-m contour lines.

precipitation. Snow accumulation (in water equivalent) is 40% higher on the east coast compared to the west coast of Spitsbergen, with the steepest east-west gradient in the south (Sand et al., 2003). There is also a south-north gradient, with the south receiving approximately twice as much precipitation as the north. This gradient is steepest in the central and eastern parts. Large local gradients also occur (Humlum, 2002). For instance, precipitation amounts in Longyearbyen are approximately three times lower than along the west coast of Spitsbergen, less than 50 km away (Førland & Hanssen-Bauer, 2003).

The large spatial variability in precipitation influences the glaciers' equilibrium line altitude (ELA), which is a good climate change indicator due to its sensitivity to changes in summer temperature and winter precipitation (Hagen et al., 1993). On Svalbard, the spatial variability in precipitation is larger than in temperature, causing ELA differences to mainly reflect precipitation variability, with lower ELAs in wet coastal regions and higher ELAs in arid inlands settings (Hagen et al., 1993; van Pelt et al., 2016).

Svalbard receives both Atlantic and Arctic moisture resulting in precipitation that falls over different parts of the archipelago may consist of water from a mix of different sources, and with varying transport history. Modern precipitation isotopes have been measured at two sites at the west coast of Spitsbergen as part of the Global Network of Isotopes in Precipitation (GNIP; IAEA/WMO, 2019). Monthly precipitation δ^2H and $\delta^{18}O$ at Isfjord Radio (78.07°N, 13.63°E; 1961–1965, 1972–1975) and in Ny-Ålesund (78.92°N, 11.93°E; 1990–2016) do not exhibit a significant seasonal trend, whereas deuterium excess is over 6‰ higher during the winter months at both sites (IAEA/WMO, 2019; Fig. 2). The values fall close to the Global Meteoric Water Line (GMWL, $\delta^2H = 8\times\delta^{18}O + 10$; Craig, 1961; Fig. S4). There are no precipitation isotope measurements from central and northeastern Svalbard, but stronger isotopic seasonality is expected due to the larger contrast between summer and winter climate farther from the open water along the west coast.

To explore regional differences in paleo-precipitation trends, we targeted four lakes across Svalbard: one on the west coast of central Spitsbergen, two on north-central Spitsbergen, and one on Nordaustlandet (Fig. 1). The four selected lakes are fed by catchment runoff, and do not currently receive glacial meltwater. The precipitation seasonality reflected in the lake and soil water is influenced by a range of factors, including the relative amount of winter and summer precipitation falling in the catchment, the lake water residence time, and duration of ice cover on the lake (Thomas et al., 2020). No long time series of lake ice

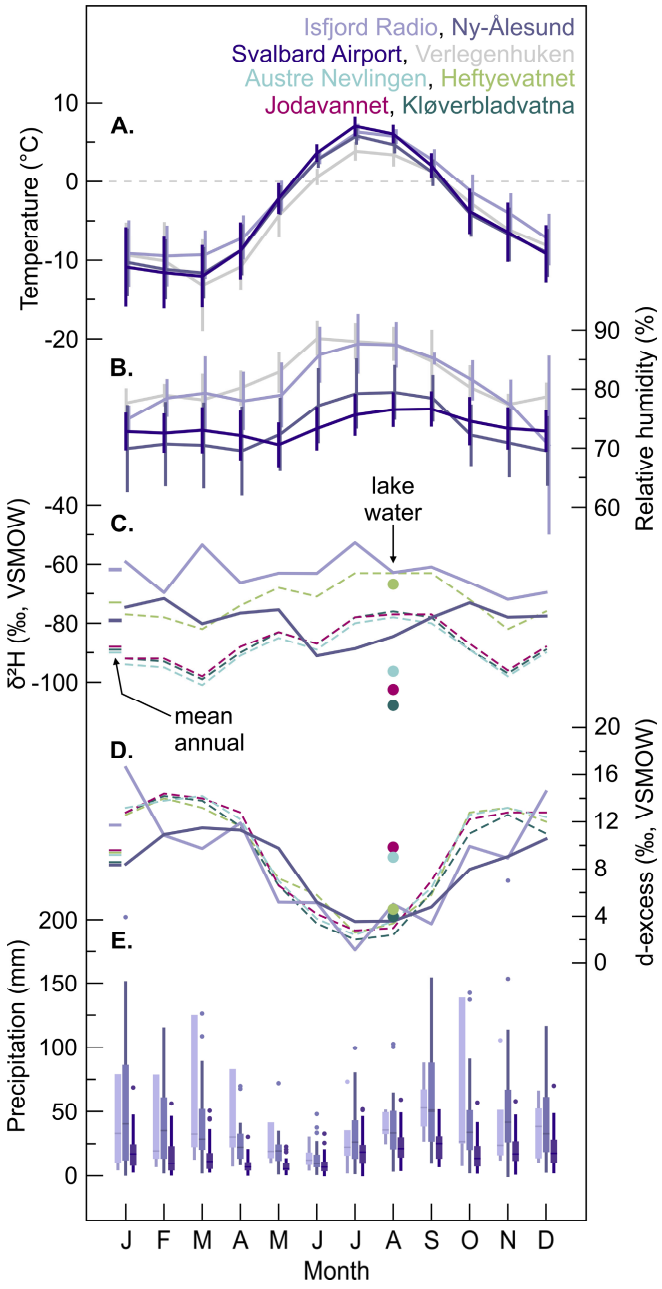

Fig. 2. Climate data from Svalbard Airport, Ny-Ålesund, Isfjord Radio and Verlegenhuken (for locations, see Fig. 1). Mean monthly air temperatures (a) and relative humidity (b) between 1991–2020 (2011–2020 for Verlegenhuken). Vertical bars represent 1σ standard deviation. Amount-weighted monthly Global Network of Isotopes in Precipitation (GNIP; IAEA/WMO, 2019) δ^2H (c) and d-excess (d) in precipitation (solid lines) from Isfjord Radio (1961–1965, 1972–1975) and Ny-Ålesund (1990–2016). Estimated precipitation δ^2H for all sites (dashed lines), calculated using the Online Isotopes in Precipitation Calculator (OIPC; Bowen et al., 2005; IAEA/WMO, 2019; Bowen, 2021). (e) Monthly accumulated precipitation, 1991–2020. For each box plot, the middle line displays the median precipitation, the box represents the 25% to 75% quartile range, whiskers are maximum and minimum values, and dots are outliers. Temperature and precipitation data were retrieved from MET Norway (2021). There were no precipitation data available for Verlegenhuken.

phenology exist from Svalbard. On western Spitsbergen, the ice-free season at smaller lakes is from early July to early October (Kongressvatnet; Holm et al., 2012), and ice freeze-up at larger lakes starts later in October (Linnévatnet; Tuttle et al., 2022). In the cooler northeastern part of Svalbard, the ice-free period is likely shorter, from July to September. Aquatic plants produce most of their waxes during the ice-free season, since primary production is controlled by light availability and temperature (Guo et al., 2013; Riis et al., 2014). Terrestrial leaf waxes are likely produced throughout the short Arctic growing season (Shanahan et al., 2013), which in most parts of Svalbard start in mid-June to early July and ends in early September (Karlsen et al., 2014; ORNL DAAC, 2018).

Heftyevatnet (78.00°N, 14.15°E, 43 m a.s.l.) is located on the western flank of Grønfjorden, close to the west coast of central Spitsbergen (Fig. 1b-c). Grønfjorden (Barentsburg; 1979–2018) has a mean annual precipitation of 568 mm, with highest precipitation amounts falling in autumn and winter, and lowest amounts in the summer months (Førland et al., 2020). The 0.02 km^2 lake has a maximum depth of 6.5 meter and a 0.15 km^2 catchment. The bedrock in the area is composed of Early-Middle Triassic dark shale, siltstone, and sandstone (Dallmann, 2015). The lake sits in a topographic depression, flanked by a moraine ridge to the south, and a 52-meter terrace to the east. The lake is located below the postglacial marine limit and was glacio-isostatically uplifted and isolated from the fjord *c*. 12.2 cal. kyr BP (Farnsworth et al., 2022). At present, the lake has no active inlet or outlet. Heftyevatnet is located in the Middle Arctic tundra zone, and the lake shore and surrounding slopes are covered by moist to wet moss tundra. The dominant vascular plants in almost all plant communities and habitats in Grønfjorden are *Bistorta vivipara*, *Salix polaris*, and *Luzula confusa* (Koroleva et al., 2008).

Jodavannet (79.34°N, 16.02°E, 140 m a.s.l.) is a small, 0.02 km^2 lake in Ringhorndalen, on the eastern flank of the 108-km-long Wijdefjorden, northern Spitsbergen

(Fig. 1b and e). Inner Wijdefjorden receives the lowest precipitation amounts on Svalbard (Hagen et al., 1993; Østby et al., 2017), as a result of strong rain-shadow effects by the high mountains surrounding the fjord. Furthermore, the straight and narrow fjord acts as a wind tunnel, removing air and soil moisture, especially during summer (Elvebakk & Nilsen, 2002). Jodavannet sits on a plateau close to the mouth of Ringhorndalen, has a maximum depth of 6.4 m, and a relatively large, 1.31-km^2 catchment. The bedrock consists of Mesoproterozoic mica schist, metapsammite, and amphibolite (Dallmann, 2015). In the inner part of the valley, the valley floor is mostly covered by outwash plains originating from two outlet glaciers from the Åsgardfonna Ice Cap. Silt and sand from the outwash plains are partly redistributed by wind, covering portions of the landscape. Surface runoff is brought to the lake from the southern, western, and northern slopes, and an outlet stream drains into a larger lake to the southeast. Ringhorndalen has a unique and highly diverse flora (Elvebakk & Nilsen, 2002; Eidesen et al., 2018; Voldstad et al., 2020). The valley mouth is characterized by high-Arctic steppe communities, and typical plants are *Potentilla pulchella* and *Puccinellia augustata*, adapted to wind-exposed, dry, and alkaline sites (Eidesen et al., 2018). Similar to Heftyevatnet, Jodavannet is bordered by a moss belt, stretching *c*. 5 m from the lake shore. The vascular plants closest to the lake include *Saxifraga oppositifolia*, *Carex subspathaceae*, *Dupontia fisheri*, *Bistorta vivipara*, *Salix polaris*, and *Equisetum arvense*, whereas more thermophilous plants such as *Dryas octopetala* and *Cassiope tetragona* occur farther away from the lake (Voldstad et al., 2020). Submerged bryophytes are abundant in the lake.

Austre Nevlingen (79.78°N, 15.79°E, 41 m a.s.l.) is *c*. 50 km north of Jodavannet, close to the mouth of Wijdefjorden (Fig. 1b and d). This outer part of the fjord is not as affected by the rain-shadow and wind tunnel effects as inner Wijdefjorden, and is less arid (Østby et al., 2017). The surface area of the lake is 0.13 km^2, the maximum depth 18 m, and the lake sits within a small, 0.48-km^2 catchment. Bedrock in the area consists of

Paleoproterozoic gneiss, migmatite and amphibolite (Dallmann, 2015), and the catchment is characterized by frost-shattered bedrock and boulders. Austre Nevlingen sits between *c*. 150–280 m a.s.l. mountain peaks and has no active inflow or outflow. The lake is located in the Northern Arctic tundra zone, and the catchment is sparsely vegetated. Vascular plants include *Luzula confusa* and *Salix polaris*, and mosses *Tomentypnum nitens* and *Polytrichum* sp. Lichens are common, and aquatic bryophytes are growing in the lake.

Kløverbladvatna (79.77°N, 21.71°E, 8 m a.s.l.) is a threshold lake, located on Oxfordhalvøya in the innermost part of Wahlenbergfjorden, Nordaustlandet (Fig. 1b and f). The peninsula is surrounded by ice caps on three sides and the climate is relatively dry (Østby et al., 2017). The lake was glacio-isostatically uplifted and isolated from the fjord *c*. 5.4 cal. kyr BP (Schomacker et al., 2019). Kløverbladvatna has a surface area of 0.23 km^2 and a maximum water depth of 17.5 m. Its catchment is 1.64 km^2, consisting of Neoproterozoic clastic sedimentary rocks (Dallmann, 2015). The lake has no active inflow today, but a dry channel on the southeastern side indicates that the lake previously received glacial meltwater from Etonbreen, which likely reached the lake during a glacier surge in 1938 (Schomacker et al., 2019). The modern vegetation cover is very sparse, and the landscape is dominated by mosses and lichen. Vascular plants include *Salix polaris* and *Saxifraga* spp. We did not observe aquatic plants in the lake.

3. Materials and methods

3.1. Seasonal lake water residence time calculations

To infer the seasonality of the lake water, we estimated seasonal (ice-cover and ice-free season) residence times for the four lakes (Table S1). These calculations were based on lake and catchment size and monthly precipitation amounts at what we estimated to be the most representative meteorological station. Lake volumes were calculated from bathymetric

measurements in the field (Austre Nevlingen) or by multiplying the lake surface area by the maximum depth divided by two (Heftyevatnet, Jodavannet, and Kløverbladvatna) (Jonsson et al., 2009). Catchment areas were measured using a digital elevation model (Norwegian Polar Institute, 2014) and ArcMap 10.5. Runoff was estimated by multiplying the monthly precipitation amount (in Ny-Ålesund for Heftyevatnet and at Svalbard Airport for Austre Nevlingen, Jodavannet and Kløverbladvatna; MET Norway, 2021) by the lake catchment area, assuming that 50% of the precipitation reaches the lake (i.e., a runoff/precipitation ratio of 0.5; Gibson et al., 2002). The calculated residence times are rough estimates, considering the poor constraints on precipitation amounts falling on northern and northeastern Svalbard. Svalbard Airport is located more than 100 km south of Austre Nevlingen and Jodavannet, and more than 200 km southwest of Kløverbladvatna, with mountains, ice caps, fjords, and sounds in between (Fig. 1).

3.2. Modern lake water δ^2H analysis

To better constrain the precipitation seasonality reflected in lake water δ^2H and to quantify the influence of evaporative enrichment, we collected surface water samples from the four lakes during field campaigns in August 2018, 2019, and 2021. The samples were collected from the shoreline in 4 mL glass vials with no headspace, sealed with Parafilm, and stored cold until analysis. The Austre Nevlingen and Jodavannet samples were measured on a Picarro L2130-i wavelength scanned cavity ring down spectrometer (WS-CRDS) with vaporization module V1102-i coupled to a CTC PAL autosampler, at the Organic and Stable Isotope Biogeochemistry Laboratory at the University at Buffalo, USA, and the Kløverbladvatna and Heftyevatnet samples on a Picarro L2140-i WS-CRDS with a A0211 vaporizer and an A0325 autosampler at the Facility for advanced isotopic research and monitoring of weather, climate, and biogeochemical cycling (FARLAB), University of Bergen, Norway. For details on the

analytical procedures, see Kjellman et al. (2022). By comparing lake water δ^2H to regional precipitation δ^2H we can assess the seasonality reflected in the lake water δ^2H. Heftyevatnet is 14 km southeast of Isfjord Radio, whereas the other lakes are far away from the closest GNIP station. Precipitation δ^2H values at the lake sites were estimated using the Online Isotopes of Precipitation Calculation (OIPC; Bowen, 2021). The uncertainty in these interpolated values is considerable due to the lack of Arctic precipitation isotope data (Bowen & Revenaugh, 2003), and they might not capture local variability due to the coarse grid resolution, but they do provide the best available estimate.

3.3. Sediment cores

We present data from nine sediment cores collected from the four lakes between 2015 and 2019. The bathymetry of the lakes was surveyed with a hand-held depth sounder (Hondex PS-7 Transducer) for point measurements. The Austre Nevlingen bathymetry was additionally surveyed with a Garmin ECHOMAP™ Plus 73SV with a CV52HW-™ transducer and a 5 Hz receiver, using the Quick Draw contour function (Fig. 1d). All cores were obtained from the central, deepest parts of the basins. Overlapping cores were collected with a Universal surface corer (120 cm long and 68 mm diameter coring tubes) and a hand-held lightweight piston corer (200 cm long and 60 mm diameter coring tubes). In this study, we focus on the organic parts of each record, i.e., the time after lake basin isolation for lakes below the marine limit (Austre Nevlingen, Heftyevatnet and Kløverbladvatna) and periods with no/low inflow of glacial meltwater or aeolian sand. All cores were split open, logged, and analyzed with an ITRAX core scanner (Croudace et al., 2006), providing high-resolution X-ray fluorescence (XRF), magnetic susceptibility (MS), and optical and radiographic images. The organic content was measured through loss on ignition (LOI) at 550 °C for 4 hours (Heiri et al., 2001). Detailed methodology and full core descriptions and lithostratigraphy are presented by

Schomacker et al. (2019) (Kløverbladvatna), Kjellman et al. (2020) (Austre Nevlingen), Voldstad et al. (2020) (Jodavannet), and Farnsworth et al. (2022) (Heftyevatnet), and in Fig. S1. The uppermost two meters of the Heftyevatnet record were not described previously but constitute a continuation of unit 2 of Farnsworth et al. (2022) with finely laminated brown gyttja with intermittent beds of clayey silt.

3.4. Composite core construction and age-depth modeling

All sediment cores have been dated using accelerator mass spectrometry (AMS) radiocarbon dating of handpicked plant macrofossils, measured at the Ångström Laboratory, Uppsala University, Sweden, and Lund University Radiocarbon Dating Laboratory, Sweden (Table S2). Age-depth models based on these radiocarbon ages are presented by Schomacker et al. (2019), Kjellman et al. (2020), Voldstad et al. (2020), and Farnsworth et al. (2022). To improve the resolution for Heftyevatnet, we picked out and dated seven additional bryophyte samples. We also present three new radiocarbon ages from a surface core from Jodavannet. For Kløverbladvatna, we combined ages from both cores into a composite age-depth model. With these additional constraints, we generated new age-depth models for Jodavannet, Kløverbladvatna and Heftyevatnet.

To generate one composite sedimentary record for each lake, we aligned the overlapping surface and piston cores in AnalySeries (v. 2.0.8; Paillard et al., 1996), using tie-points in the elemental data (Fig. S2). All proxy and chronological data were entered into Linked PaleoData (LiPD) files (McKay & Emile-Geay, 2016), and age-depth models (Fig. S3) were generated in R (v. 4.1.3; R Core Team, 2021) using Bacon (v. 2.5.7; Blaauw & Christen, 2011) within the geoChronR package (v. 1.1.5; McKay et al., 2021). For each record, we set the upper depth (d.min) to the uppermost leaf wax sample depth and the lower depth (d.max) to the lowermost leaf wax or radiocarbon sample depth. For records where

changes in lithology suggested changes in sedimentation rate, we added boundaries and adjusted the prior mean accumulation rates (bacon.acc.mean; Fig. S3). The rest of the settings were kept at the default values. One sample from Kløverbladvatna and one sample from Jodavannet that were used as age-constraints in the previously published models (Schomacker et al., 2019; Voldstad et al., 2020) appeared to be outliers (Fig. S3). All radiocarbon ages were (re)calibrated using the IntCal20 dataset (Reimer et al., 2020), and are presented in calibrated years before present (cal. yr BP; BP = 1950). The age ensembles were mapped to the leaf wax data, allowing us to present proxy data with age model uncertainty.

3.5. Lipid biomarker extraction and analysis

Biomarker analyses were performed in the University at Buffalo Organic and Stable Isotope Biogeochemistry Laboratory. Sediment samples (3–4 cm^3 for Austre Nevlingen, Heftyevatnet and Kløverbladvatna, 6–8 cm^3 for Jodavannet) were collected based on estimated age (Heftyevatnet, Jodavannet, Kløverbladvatna) or depth (Austre Nevlingen), depending on the status of available chronological data at the time of sampling. Methods for leaf wax extraction, purification and *n*-alkanoic acid analysis followed previously published procedures (Thomas et al., 2012; Kjellman et al., 2020). The total lipid extract (TLE) was extracted from freeze-dried sediments using a Dionex 200 Accelerated Solvent Extractor with dichloromethane (DCM):methanol 9:1 (v/v). After adding $C_{20:1}$ *n*-alkanoic acid (Fisher Scientific, 4.2 µg) as an internal standard, the compounds in the TLE were separated into neutral and acid fractions using flash-column chromatography with aminopropyl silica gel solid phase, eluting neutral compounds with DCM:isopropanol 2:1 (v/v) and acids using 4% acetic acid in DCM. We methylated the acid fraction at 60 °C overnight using 5% anhydrous HCl in methanol with a known isotopic composition and cleaned the samples on silica gel columns, eluting the fatty acid methyl esters (FAMEs) in DCM.

FAME peak areas were quantified on a Thermo Scientific Trace 1310 gas chromatograph (GC) equipped with two flame ionization detectors (FIDs) operated in parallel, with AI1310 autosamplers and two split/splitless injectors. The inlets were held at 250 °C and operated in splitless mode for 45 s, after which split flow was turned on at 14 mL min^{-1}. After that we held a constant column flow of 3.6 mL min^{-1} using helium carrier gas. The oven was held at an initial temperature of 70 °C for 1 min, then ramped to 230 °C at 27 °C min^{-1}, followed by a final ramp to 315 °C at 6 °C min^{-1}, where we held for 10 min. Compounds were identified by retention time, using an added internal standard as a reference. We calculated FAME concentrations using external calibration curves determined for a C_{28} FAME standard, and normalized the FAME masses to the dry mass of extracted sediment and the recovery of the internal standard.

Hydrogen isotope analyses of the FAMEs were made on a Thermo Scientific Delta V Plus isotope ratio mass spectrometer (IRMS) coupled via an Isolink II and Conflo IV to a Trace 1310 GC. We used the FAME concentrations to dilute and inject target amounts of compounds. The GC conditions and programs were the same as those used during FAME quantification, except that we used helium as the carrier gas at a flow rate of 1.5 mL min^{-1}. The H_3^+ factor was determined at the beginning of every sequence, ranging from 2.19 ± 0.02 to 5.00 ± 0.04 ppm/nA (Table S3). We ran samples in triplicate (or in duplicates or singles for small samples) along with FAME standards of known isotopic composition (A. Schimmelman, University of Indiana) to constrain drift (C_{18} and C_{24}) and linearity (C_{20} and C_{28}) and to normalize all δ^2H values to the Vienna Standard Mean Ocean Water (VSMOW) scale. We also corrected FAME δ^2H values for hydrogens added during methylation. To constrain the peak-size effects on the measured isotopic composition we injected the C_{20} and C_{28} FAME standards at a range of masses. We excluded peaks that were below a threshold (*c.* 2-4 V·s for each sequence) where the uncertainty of the linearity correction was too high. For

samples that were between the standard constraints (i.e., with peak areas below the threshold but within the range of standard peak areas), we compared the triplicate (or duplicate) injections and kept sample peaks with similar δ^2H values. For sequences without clear linearity and small C_{20} and/or C_{30} peaks (*c*. one third of the Jodavannet and all of the Heftyevatnet samples), all C_{20} (Jodavannet and Heftyevatnet) and C_{30} (Heftyevatnet) injections were discarded. We calculated the total uncertainty of measured δ^2H values as the Standard Error of the Mean (SEM), which equals the square root of the sum of the squares of total measurement uncertainty for each sample (drift and peak size corrections, replicate uncertainty of sample measurements, uncertainty in the δ^2H value of the methanol-derived hydrogens), divided by the square root of the number of measurements. The average SEM was 2.7‰ for Austre Nevlingen, 3.4‰ for Heftyevatnet, 2.7‰ for Jodavannet and 2.4‰ for Kløverbladvatna. C_{20}, C_{22} and C_{30} had higher average SEM (3.0–3.1‰) than C_{24}, C_{26} and C_{28} (2.5–2.6‰).

We calculated the difference between the δ^2H of C_{28} and C_{22} *n*-alkanoic acids ($\varepsilon_{28–22}$) using the equation $\varepsilon_{28–22} = (((1000 + \delta^2H_{C28}) / (1000 + \delta^2H_{C22})) – 1) \times 1000$, assuming that the compounds have similar ε_{app} (Thomas et al., 2020). $\varepsilon_{28–22}$ can be interpreted as the isotopic difference between terrestrial- and aquatic-plant-derived *n*-alkanoic acids, and thus the isotopic difference between soil and lake water. Depending on the lake hydrology, time series of this value can reflect changes in relative humidity (Rach et al., 2017) or precipitation seasonality (Thomas et al., 2020). We also calculated the average chain length (ACL) for C_{22} to C_{30} even chain lengths using the equation $ACL_{22\text{-}30} = \Sigma(n \times C_n) / \Sigma (C_n)$, where *n* is the µg/g dry sediment of each *n*-alkanoic acid with *n* carbon atoms.

4. Results

4.1. Lake water residence times and δ^2H seasonality

Heftyevatnet (large catchment-to-lake ratio, Fig. 1c) has a spring melt residence time of *c*. 2 months, meaning that approximately half of the lake water is flushed during spring melt and that the lake water continues to be replaced by summer precipitation during the ice-free season (Table S1). Modern lake water δ^2H is between mean annual summer and ice-free season Isfjord Radio precipitation δ^2H, and d-excess is close to summer precipitation d-excess (Figs 2 and S4). This suggests that most of the water in the lake is exchanged during the growing season and that the aquatic δ^2H signal from Heftyevatnet is likely to be summer-biased. The short residence time and lake water δ^2H in line with modeled precipitation δ^2H suggest that the lake water experiences minimal evaporative enrichment.

The residence time calculations suggest that the lake water in Jodavannet (large catchment-to-lake ratio; Fig. 1e) is replaced by spring melt in less than a month (Table S1). Yet, modern lake water δ^2H from Jodavannet is more depleted than modeled winter precipitation δ^2H and has a d-excess close to modeled mean annual precipitation d-excess (Figs 2 and S4). Modern lake water plotting on the GMWL indicated that Jodavannet is not significantly influenced by evaporation (Fig. S4).

Austre Nevlingen (small catchment-to-lake ratio; Fig. 1d) has no distinct outflow and a spring melt residence time over 2 years, suggesting that only 4% of the lake volume is flushed by ^2H-depleted snowmelt each year (Table S1). The ice-free season residence time is 13 years, suggesting that only 2% of the lake water is replaced during the growing season. This is supported by depleted modern lake water δ^2H and $\delta^{18}O$, and d-excess close to mean annual precipitation d-excess (Figs 2 and S4; Kjellman et al., 2020).

Kløverbladvatna (small catchment-to-lake ratio; Fig. 1f) has a median spring melt residence time of 19 months (Table S1), indicating that the exchange of water in the lake is

slow. Only 5% of the lake water is estimated to be replaced during the spring melt, and 3% during the ice-free season. Lake water $\delta^{18}O$ is close to Jodavannet lake water $\delta^{18}O$ but $\delta^{2}H$ is relatively depleted, suggesting that Kløverbladvatna is more evaporated (Fig. S4). d-excess is close to summer precipitation d-excess (Fig. 2).

Seasonal lake water residence time calculations and modern summer lake water isotopic composition of the lakes suggest that the water in the different lakes reflects different seasonal signals: Heftyevatnet is summer-biased, Austre Nevlingen and Kløverbladvatna are reflecting mean annual to winter-biased precipitation, whereas Jodavannet could be either summer-biased, mean annual, or winter-biased. It is possible that the precipitation seasonality reflected in the lake water changes through time, e.g., by an increase in precipitation amount decreasing the residence time of a lake. Another process that is likely important on Svalbard is "snowmelt bypass", i.e., snow melting off the landscape before the lake becomes ice free (MacDonald et al., 2017). Satellite imagery suggests that large portions of the landscape become snow free before the lake ice melts. During years with a shorter lake-ice season, more of the ^{2}H-depleted winter precipitation is likely to enter the lake. Furthermore, snow can be redistributed by the wind. Variable influence of these factors has implications for our leaf wax $\delta^{2}H$ interpretations (see section 5.2).

4.2. Chronology and core descriptions

The lacustrine sequences from Heftyevatnet and Jodavannet represent full Holocene records (Heftyevatnet extending back into the end of the Late Weichselian), Austre Nevlingen lacks the recentmost *c*. 1.9 cal. kyr, and Kløverbladvatna spans from 5.4 cal. kyr BP to the present (Fig. S3 and Table S2). The average temporal resolution for leaf wax analyses in the four lakes records ranged from *c*. 220 to 450 years between samples. For Jodavannet, we used the age-depth model from Voldstad et al. (2020) to guide us during subsampling, whereas the

data are presented using the current age-depth model (Fig. S3). This affects the sample resolution at the end of the Early Holocene (higher resolution) and most of the Middle Holocene (lower resolution).

The Austre Nevlingen sediment sequence consists of a basal clayey-silty diamict overlain by stratified gyttja. Beds of aquatic bryophytes occur throughout the sequence and are most abundant after *c*. 6 cal. kyr BP (Fig. S1a; Kjellman et al., 2020). In Heftyevatnet, the base of the sediment sequence consists of a fine-grained diamict with marine foraminifera. A finely laminated gyttja with clay-silt beds characterizes the rest of the sequence (Fig. S1b; Farnsworth et al., 2022). The Jodavannet sequence consists of a laminated sand facies at the base, overlain by laminated silty gyttja, and a clayey silt facies at the very top (Fig. S1c; Voldstad et al., 2020). Bryophytes occur throughout the sequence, often in interlaminated beds, and *Nostoc* (colonial cyanobacteria) are abundant between 8.2–5.4 cal. kyr BP. Kløverbladvatna has clay-silt with clasts at the base, overlain by a laminated clayey gyttja. The top sediments consist of clay-silt (Fig. S1d; Schomacker et al., 2019).

4.3. Leaf wax concentrations and chain-length distributions

The *n*-alkanoic acid concentrations varied between lakes and between different parts of the records. Due to inconsistent recovery of the internal standard for some of the runs, all Heftyevatnet samples and 13 of the Jodavannet samples were normalized to just the sediment mass, and not the internal standard. To avoid presenting concentration data from the same lake normalized in different ways, the concentrations of samples normalized to just the sediment mass are not presented for Jodavannet. Heftyevatnet leaf wax concentrations are presented normalized to sediment mass (Fig. S6). All concentrations were kept in the fractional abundance plots for both lakes, since the relative distributions within each sample are still reliable (Figs S6 to S7).

In all lakes, C_{24}, C_{26}, or C_{28} is the most abundant homologue. Long-chain waxes (C_{26} and C_{28}) dominated for most of the records, reflecting either that terrestrial plants dominated the catchments, or that the terrestrial plants produced more waxes. In addition, Austre Nevlingen and Jodavannet had relatively high C_{24} for part of the record, and Jodavannet a couple of C_{30} peaks in the Early and Middle Holocene (Figs S5b and S7b). Austre Nevlingen displayed the highest leaf wax concentrations in the Early and Late Holocene, and variable values throughout (Fig. S5b). Jodavannet had higher concentrations in the Middle Holocene, and more consistent concentrations throughout the record compared to Austre Nevlingen (Fig. S7b). Kløverbladvatna and Heftyevatnet had lower leaf wax concentrations for most of the Holocene. Except for four samples in Jodavannet with C_{30} concentrations above 50 µg/g dry sediment, the C_{20} and C_{30} concentrations stayed consistently low in all lakes.

Jodavannet displayed the largest shifts in average chain length (ACL), going from high (26–28) in most of the Early Holocene to below 25.5 in the Late Holocene, following a similar trend as the C_{28} concentration (Fig. S7b-c). Austre Nevlingen and Kløverbladvatna ACL remained relatively stable with most samples between 25.5 and 26.5, with a decreasing trend for Kløverbladvatna in the Late Holocene (Figs S5c and S8c). Heftyevatnet ACL stayed within the same interval (25.5–26.5) for most of the record, with slightly lower values (down to 24.1) in the Early and Late Holocene (Fig. S6c).

4.4. δ^2H of leaf wax n-alkanoic acids

For most parts of the four leaf wax records, the leaf wax homologues can be separated into two groups, with the mid-chain waxes (C_{20}, C_{22} and C_{24}) and long-chain waxes (C_{26}, C_{28} and C_{30}) displaying similar isotope values within each group, but different values when comparing the two (Figs S5 to S8). We therefore infer them to originate from two different plant sources; aquatic and terrestrial plants (for further discussion, see section 5.2). For simplicity, we

hereafter focus on the δ^2H of C_{22} and C_{28} *n*-alkanoic acids, reflecting aquatic leaf wax δ^2H (δ^2H_{aq}) and terrestrial leaf wax δ^2H (δ^2H_{terr}), respectively.

Generally, δ^2H_{aq} shows more ^2H-depleted values than δ^2H_{terr} (Figs 3 and 4), especially in Austre Nevlingen, where ε_{28-22} is over 100‰ for most of the Holocene (Fig. S5a and d). Jodavannet had ε_{28-22} values around 100‰ for most of the record, and more than 200‰ for parts of the Late Holocene (Fig. S7d). In contrast, Kløverbladvatna has relatively ^2H-depleted δ^2H_{terr} compared to δ^2H_{aq} until *c*. 3.1 cal. kyr BP, and thereafter δ^2H values that vary with less than 20‰ between all homologues (Fig. S8a). Heftyevatnet displays more similar δ^2H_{aq} and δ^2H_{terr} values, with ε_{28-22} always lower than 40‰ (Figs 4, S6a and d). Austre Nevlingen and Jodavannet also show larger amplitude δ^2H_{aq} variability than Kløverbladvatna and Heftyevatnet (Fig. 3b).

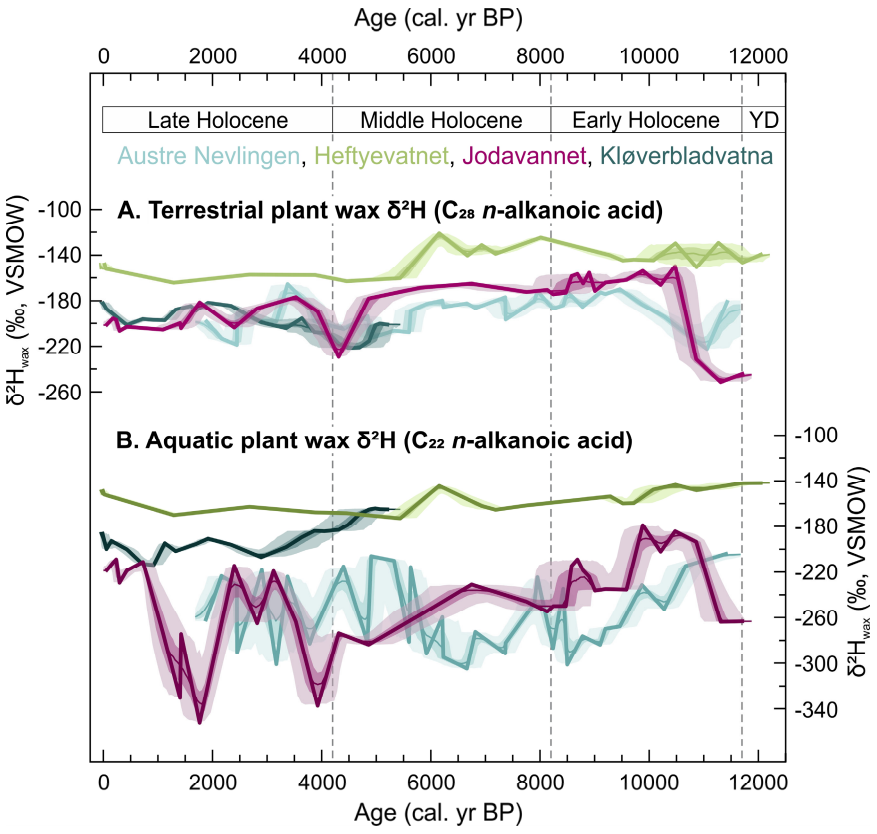

Fig. 3. Leaf wax δ^2H for (a) terrestrial (C_{28}) and (b) aquatic (C_{22}) plant *n*-alkanoic acids from Austre Nevlingen, Heftyevatnet, Jodavannet and Kløverbladvatna, Svalbard. Bold line: measured values plotted on the median age of each sample; fine line: median value of all age model iterations; light and dark shading: 1 and 2 σ age model uncertainty, respectively.

Austre Nevlingen displays relatively ^{2}H-depleted δ^2H_{terr} in the Early Holocene, with an increasing trend until 9.5 cal. kyr BP, after which δ^2H_{terr} generally fluctuates between –185 and –145‰, with a slightly decreasing trend (Figs 3a and S5a). In the Early Holocene, δ^2H_{aq} shows an opposite trend to δ^2H_{terr}, decreasing from –203 to –301 ‰ between 11.2 and 8.5 cal. kyr BP. From 8.5 to 6 cal. kyr BP, δ^2H_{aq} remains mostly ^{2}H-depleted between –305 and –272‰ (Figs 3b and S5a). After 6 cal. kyr BP δ^2H_{aq} displays larger amplitude variability, fluctuating between –301 and 206‰.

Jodavannet δ^2H_{terr} and δ^2H_{aq} display a similar trend for most of the Holocene, but like Austre Nevlingen, δ^2H_{aq} has larger amplitude changes (Figs 3, 4 and S7a). In the Early Holocene both chain lengths experience a rapid increase (from –251 to –150‰ for δ^2H_{terr}, and from –264 to –184‰ for δ^2H_{aq}) until *c*. 10.5 cal. kyr BP. From 10.5 to 4.7 cal. kyr BP, $^2H_{terr}$ decreased to –178‰, and δ^2H_{aq} to –284‰. After 4.7 cal. kyr BP, δ^2H_{terr} continues decreasing with a similar trend, except for one more ^{2}H-depleted value (–229‰) at 4.4 cal. kyr BP. δ^2H_{aq} experiences larger amplitude variability, with values fluctuating between –352 and –209‰. For the recentmost 0.8 cal. kyr, δ^2H_{terr} and δ^2H_{aq} display similar values (between –239 and –196‰).

In Heftyevatnet, δ^2H_{terr} and δ^2H_{aq} co-vary for most of the record, especially in the Middle and Late Holocene (Figs 3, 4 and S6a). From 12.1 to 11.0 cal. kyr BP, δ^2H_{terr} fluctuates between –151 and –129‰, whereas δ^2H_{aq} decreases from –142 to –148‰, and continues to decrease until 7.2 cal. kyr BP (–165‰). From 11.0 to 8.0 cal. kyr BP, δ^2H_{terr} increases to –125‰, after which it fluctuates between –140 and –121‰ until 6.2 cal. kyr BP. After 6.2 cal. kyr BP, δ^2H_{terr} and δ^2H_{aq} follow the same trend. After one ^{2}H-enriched value at 6.2 cal. kyr BP (–121‰ for δ^2H_{terr}, and –144‰ for δ^2H_{aq}), both δ^2H_{terr} and δ^2H_{aq} show a distinct drop (from –39‰ and –28‰, to –160‰ and –172‰, respectively). After 5.4 cal. kyr

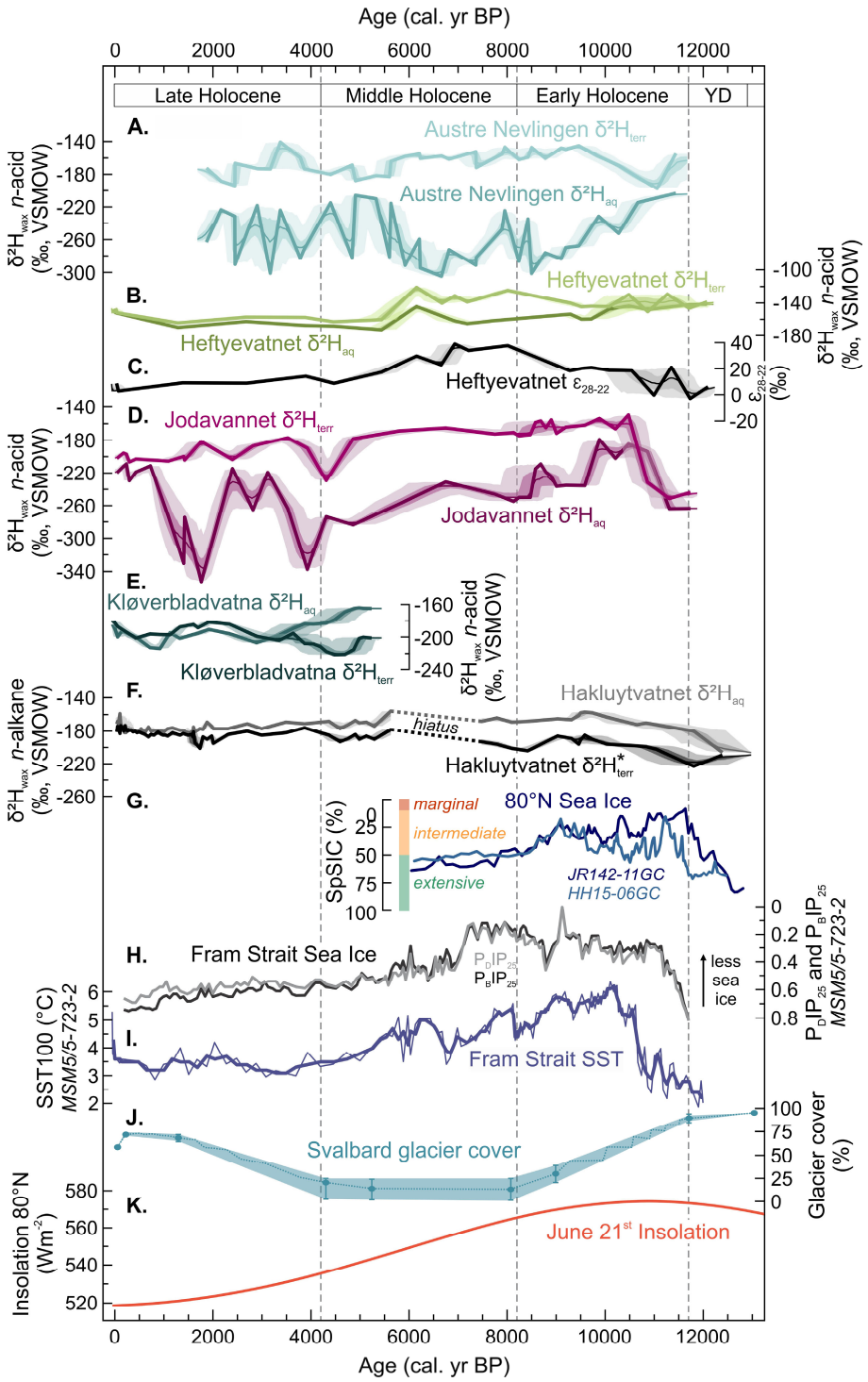

Fig. 4. Svalbard leaf wax hydrogen isotope data compared to regional Holocene climate records. For locations, see Fig. 1. (a-b and d-e) Austre Nevlingen, Heftyevatnet, Jodavannet and Kløverbladvatna leaf wax δ^2H for C_{22} (aquatic) and C_{28} (terrestrial) *n*-alkanoic acids. (c) Calculated isotopic difference between C_{28} and C_{22} (ε_{28-22}) for Heftyevatnet. Higher values are inferred to reflect higher summer evapotranspiration. (f) Lake Hakluytvatnet leaf wax δ^2H for C_{25} and C_{29} *n*-alkanes (Balascio et al., 2018). Lines and shading in (a-f) are shown as in Fig. 3. (g) Biomarker-based spring sea-ice concentrations (SpSIC) from north of Nordaustlandet (Pieńkowski et al., 2021) with sea-ice categories sensu Köseoğlu et al. (2018). (h) Eastern Fram Strait sea-ice proxies P_BIP_{25} and P_DIP_{25} (based on brassicasterol and dinosterol respectively; Werner et al., 2016) (i) Eastern Fram Strait subsurface temperature based on planktic foraminiferal fauna assemblages (fine line; Werner et al., 2016), including 3-point running means (bold line; Husum & Hald, 2012). (j) Estimated percentage of glacier cover across Svalbard (Farnsworth et al., 2020; modified from Fjeldskaar et al., 2018). (k) June 21st insolation at 80°N (Laskar et al., 2004).

BP, both δ^2H_{terr} and δ^2H_{aq} increase slightly towards the present, reaching –145‰ and –147‰ in the youngest sample.

The Kløverbladvatna δ^2H record starts 5.2 cal. kyr BP, with relatively ^2H-depleted δ^2H_{terr} in the Middle Holocene (Figs 3a and S8a). δ^2H_{terr} decreases from –201‰ at 5.2 cal. kyr BP to –221‰ at 4.5 cal. kyr BP, before increasing to –195‰ at 3.6 cal. kyr BP. During the same period (5.2–3.6 cal. kyr BP) δ^2H_{aq} decreases from –165 to –190‰ (Figs 3b and S8a). After 3.6 cal. kyr BP, δ^2H_{terr} and δ^2H_{aq} follow a similar trend (Fig. 4), with values increasing until 1.9 cal. kyr BP (to –182 and –190‰, respectively), decreasing from 1.9 to 0.9 cal. kyr BP (to –197 and –214‰, respectively), and increasing again for the last 0.9 kyr (to –181 and –185‰, respectively).

5. Discussion

In this study we compile leaf wax δ^2H data from four lakes in different locations, with different settings, diverse lake and catchment morphometrics, ultimately reflecting different precipitation δ^2H seasonality. We find similarities between the lake records suggesting similar mechanisms modulating precipitation and leaf wax δ^2H across Svalbard, as well as differences that we interpret as differences in seasonality, climate and/or moisture sources. We start by discussing the sources and seasonality of the δ^2H values of modern precipitation as well as the different *n*-alkanoic acid chain lengths presented here. We then discuss the climatic implications based on the Holocene sedimentary δ^2H records and in relation to terrestrial and marine paleoenvironmental records from Svalbard and surrounding waters.

5.1. Modern precipitation seasonality on Svalbard

We lack robust constraints on modern precipitation isotope variability across Svalbard. The only available data are from western Spitsbergen (Figs 1 and 2; Arppe et al., 2017;

IAEA/WMO, 2019; Skakun et al., 2020). The Online Isotopes in Precipitation Calculator (OIPC) can estimate precipitation values, but since there are no observational constraints in the central and eastern part of the archipelago, the modeled OIPC values have large uncertainties; on the order of *c*. 30‰ for δ^2H (Bowen & Revenaugh, 2003). Comparing our lake water data to the observed and modeled values, Heftyevatnet δ^2H is close to summer precipitation δ^2H from Isfjord Radio (14 km northwest of the lake). Austre Nevlingen δ^2H is close to the modeled winter values, whereas Jodavannet and Kløverbladvatna are too ^2H-depleted to be explained by any of the modeled values (winter, summer, or a mix of seasons). If the modeled values are biased towards the two GNIP stations on the west coast, they might not capture the presumably larger seasonality and more ^2H-depleted values in the northeast. In the Arctic, there is usually a strong relationship between the isotopic composition of precipitation and local temperature (Dansgaard, 1964). At both Isfjord Radio and Ny-Ålesund, there is a poor correlation between mean monthly precipitation δ^2H and air temperature, possibly due to seasonally variable moisture sources, a process that explains a similar lack of seasonal precipitation δ^2H variability on western Greenland (Cluett et al., 2021). On northern Spitsbergen and Nordaustlandet, we expect more frequent influence by Arctic air masses, poorer connection to North Atlantic moisture in winter, and more pronounced precipitation δ^2H seasonality.

5.2. Leaf wax sources and precipitation isotope seasonality in Svalbard lake sediment records

5.2.1. Sources of mid- and long-chain n-alkanoic acids

To interpret leaf wax δ^2H records in terms of seasonal precipitation changes, we need to 1) identify the plant source of each leaf wax homologue, and 2) determine the dominating seasonality of water used by the plants when they synthesize their waxes. As presented in section 4.4, our Svalbard leaf wax homologues can be separated into two groups based on

their δ^2H values, which most likely reflect that they come from two different plant sources. We interpret these sources to be terrestrial leaf waxes for the long-chain *n*-alkanoic acids and aquatic leaf waxes for mid-chain *n*-alkanoic acids, in accordance with previous studies (e.g., Ficken et al., 2000; Sachse et al., 2012; Wilkie et al., 2013; Daniels et al., 2017; Kjellman et al., 2020; Thomas et al., 2020). There are almost no vascular aquatic plants on Svalbard, but aquatic bryophytes are abundant in Austre Nevlingen and Jodavannet, and a likely source of mid-chain waxes. In addition, *Nostoc* probably accounts for some of the aquatic waxes in Jodavannet. *Nostoc* produces predominantly C_{22} *n*-alkanoic acids (Dion-Kirschner et al., 2020), and can therefore be interpreted together with the aquatic bryophytes. Modern terrestrial plants from Svalbard (*Luzula confusa* and *Salix polaris*) have higher C_{28} relative to C_{22} concentration than aquatic bryophytes (Kjellman et al., 2020).

One possible exception from the two-sources interpretation (mid-chain waxes predominantly being produced by aquatic plants and long-chain waxes by terrestrial plants) is the Kløverbladvatna record, where there is no clear separation between long- and mid-chain waxes after 3.6 cal. kyr BP (Fig. S8). We provide two possible explanations for this: 1) the waxes come from two different sources before 3.6 cal. kyr BP and the same source after 3.6 cal. kyr BP, or 2) the waxes are derived from two sources, with similar δ^2H after 3.6 cal. kyr BP reflecting minimal evaporation. Balascio et al. (2018) interpreted similar δ^2H values and wax distributions similar to modern aquatic mosses to indicate that all waxes after *c*. 5 cal. kyr in Hakluytvatnet, Amsterdamøya, northwestern Svalbard (Figs 1 and 4f) were derived from aquatic plants, and therefore interpreted all chain lengths in that part of the record to reflect lake water δ^2H. Similarly, in Kløverbladvatna, chain-length distributions change at 3.6 cal. kyr BP (Fig. S8c). Before 3.6 cal. kyr BP, C_{28} was the most abundant chain length, followed by C_{26} and C_{24}. After 3.6 cal. kyr BP, C_{24} to C_{28} were still the dominating chain lengths, but with C_{24} being most abundant. We do not see a change in lithology at 3.6 cal. kyr BP (Fig.

S1), and bryophytes or other aquatic plants are not abundant in this lake or the sedimentary record. It is possible that terrestrial plants were more dominant before 3.6 cal. kyr BP, as suggested by the relatively higher C_{28} concentration, but based on our limited knowledge about *n*-alkanoic acid chain-length distribution of plants on Svalbard, and specifically in the Kløverbladvatna catchment, we cannot confirm a shift to higher aquatic production in the Late Holocene. Another possibility is that the dominant species producing C_{22} and C_{28} *n*-alkanoic acids are different in Kløverbladvatna compared to the other lakes, since the Kløverbladvatna catchment is dominated by mosses and lichen. The dominant wax producers could have changed at 3.6 cal. kyr BP, thus causing the observed change in distributions and isotope values. Without more detailed information on the leaf wax sources it is difficult to know which interpretation is correct, so we discuss both as possibilities when we interpret these records in terms of climate history.

5.2.2. Seasonality of terrestrial leaf wax δ^2H

Terrestrial leaf wax δ^2H is often interpreted to reflect summer precipitation δ^2H, based on the assumption that terrestrial plants mostly use soil water during the growing season when producing their waxes, and that the soil water during the growing season is mainly recharged by summer precipitation (Cooper et al., 1991; Throckmorton et al., 2016). This might be true in most cases, especially in areas where the active layer became saturated toward the end of the preceding ice-free season and/or the winter precipitation stored as snow melts rapidly in early summer when the active layer is still frozen (Woo et al., 2008). However, this is complicated by the fact that snow patches and puddles of melted snow in some locations remain in the landscape for much of the growing season. Throughout summer, when the active layer of the permafrost thaws, some of this winter precipitation can percolate into the soil. Furthermore, some parts of Svalbard, in particular the Wijdefjorden region (Jodavannet

and Austre Nevlingen), receive very little precipitation in the summer months (Fig. 2; MET Norway, 2021). If the active layer is not saturated at the end of summer, it might be recharged by winter precipitation during the snowmelt season. Soil moisture measurements in Ringhorndalen (*c*. 2 km from Jodavannet) between May and July 2017 showed that the main moisture source for terrestrial plants that summer was snowmelt early in the season rather than summer precipitation (Eidesen et al., 2018). Based on this evidence, we interpret δ^2H_{terr} from all lakes to be summer-biased, but propose that Jodavannet, Austre Nevlingen and Kløverbladvatna δ^2H_{terr} might incorporate some winter precipitation as well, due to more winter-biased soil water. This, and/or more Rayleigh distillation during moisture transport to these northeastern lakes, can explain why those three lakes show ^{2}H-depleted δ^2H_{terr} compared to Heftyevatnet (Fig. 3). More arid summer conditions in inner Wijdefjorden and more evapotranspiration in the Jodavannet catchment than at Austre Nevlingen can explain the relatively ^{2}H-enriched δ^2H_{terr} in Jodavannet compared to Austre Nevlingen, despite the proximity between the lakes. In addition to precipitation δ^2H, terrestrial plant waxes can also be ^{2}H-enriched by evapotranspiration of soil and leaf water (e.g., Kahmen et al., 2013). In cases where terrestrial and aquatic waxes reflect the same precipitation seasonality, the influence of evapotranspiration on δ^2H_{terr} can be determined by calculating the isotopic offset between δ^2H_{terr} and δ^2H_{aq} ($\varepsilon_{28–22;}$ see section 5.2.4).

5.2.3. Seasonality of aquatic leaf wax δ^2H

Aquatic plants use lake water when producing their waxes, and therefore reflect the seasonality of the lake water δ^2H during the growing season (e.g., Thomas et al., 2020). If the lake is flushed by spring melt (i.e., winter precipitation) and flushed again by summer precipitation, the lake water δ^2H during the growing season is likely to be biased towards summer precipitation δ^2H. This is the case for Heftyevatnet, which we interpret to have a

summer-biased δ^2H_{aq}. On the other hand, if the lake has a long residence time and/or does not receive enough runoff from summer precipitation, the lake water δ^2H during the growing season can be closer to mean annual precipitation δ^2H. A third option is to interpret δ^2H_{aq} to be biased towards winter precipitation δ^2H (e.g., Katrantsiotis et al., 2021). Winter-biased lake water during the growing season can be the result of a higher proportion of the annual precipitation falling as snow, and late snowmelt (Jonsson et al., 2009; Kjellman et al., 2022). Groundwater, in the form of water flowing through the thawed active layer, can also be an important source of lake water in the Arctic (Gorbey et al., 2022). As groundwater δ^2H values reflect the seasonality of the precipitation that recharges the active layer, this water can be either summer- or winter-biased (see section 5.2.2).

Although Jodavannet has a large catchment-to-lake ratio and a short residence time, which would suggest the lake should be recharged by summer precipitation, it has lake water δ^2H similar to Austre Nevlingen and Kløverbladvatna (i.e., mean annual to winter precipitation). We interpret Austre Nevlingen and Jodavannet δ^2H_{aq} to reflect mean annual or winter precipitation δ^2H changes. There are several possible mechanisms that could explain why Jodavannet does not reflect summer precipitation despite its short residence time: 1) Due to its small volume and large catchment, Jodavannet is sensitive to short-term changes in seasonality, with the relative amount of winter and summer precipitation modulating lake water δ^2H. 2) Regional aridity and a relatively low proportion of summer precipitation may cause summer precipitation to evaporate before it reaches the lake. 3) Groundwater, likely at least partially recharged by winter precipitation in this region, might be an important source of water to the lake as the active layer thaws.

Both Jodavannet and Austre Nevlingen also appear to be close to an isotopic threshold, with large δ^2H_{aq} shifts suggesting changing sensitivity of the lake basin to the seasonal distribution of precipitation (Kjellman et al., 2020). Some possible mechanisms

explaining this change in sensitivity could be variable duration of lake-ice cover, changes in the degree of snowmelt bypass, lake level changes, and varying degrees of summer evapotranspiration, affecting both the proportion of winter and summer precipitation that enters the lake and the lake water residence time. Another explanation for distinct δ^2H_{aq} changes could be a change in the source of the C_{22} *n*-alkanoic acid, which, if the plant source has different ε_{app}, would result in a different δ^2H_{aq} value without any change in the lake water δ^2H value. Both the Austre Nevlingen and Jodavannet sequences contain interbedded bryophytes, which may indicate some samples were more dominated by bryophyte-derived waxes than others, but the ^2H-depleted or ^2H-enriched values do not correspond with moss-dominated samples, nor do the bryophyte-rich samples contain major changes in the relative chain-length concentrations. The Late Holocene part of the Jodavannet record shows lower ACL, but both for relatively ^2H-enriched and ^2H-depleted samples. Therefore, we interpret large δ^2H_{aq} shifts to reflect lake or catchment processes that control the proportion of winter and summer precipitation entering the lake and/or the lake water residence time, rather than *n*-alkanoic acid source changes.

Kløverbladvatna is located farthest east, where we lack good constraints on precipitation sources and isotopic composition, as well as on leaf wax sources. In autumn, an ice-free Arctic Ocean might provide a more local moisture source to Nordaustlandet, which has a ^2H-depleted starting value, but shorter travel distance. At present, Kløverbladvatna has a small catchment-to-lake ratio, which together with ^2H-depleted lake water suggest that the lake has a long residence time. Thus, Kløverbladvatna δ^2H_{aq} likely reflects mean-annual precipitation δ^2H, possibly receiving more summer precipitation than Austre Nevlingen and Jodavannet, or experiencing more snowmelt bypass due to a longer lake-ice cover season.

5.2.4. Interpreting ε_{28-22}

The isotopic difference between the δ^2H of terrestrial and aquatic *n*-alkanoic acids (ε_{28-22}) can be used to infer changes in summer evapotranspiration from lakes meeting the following criteria: 1) the isotopic composition of the source water for terrestrial and aquatic plants reflects the same precipitation seasonality, 2) aquatic source water does not experience evaporative enrichment, whereas terrestrial source water does, and 3) the terrestrial and aquatic waxes can be assumed to have similar ε_{app} (Kahmen et al., 2013; Rach et al., 2017; Thomas et al., 2020). We hypothesize that Heftyevatnet fulfill these criteria, and we therefore use ε_{28-22} to reconstruct summer evaporative ^2H enrichment of leaf water. Austre Nevlingen, Jodavannet, and Kløverbladvatna have different terrestrial and aquatic plant source water seasonality, as well as more complex lake hydrology. Thus, we do not explicitly interpret ε_{28-22} from these three lakes.

5.3. Regional variability in Holocene precipitation isotope seasonality across Svalbard

5.3.1. Early Holocene: 11.7–8.2 cal. kyr BP

A distinct increase in δ^2H_{terr} and δ^2H_{aq} in Jodavannet at the start of the Early Holocene likely reflects a shift from ^2H-depleted glacially derived source water to source water reflecting precipitation δ^2H, marked by the transition from glacial fine sand to silty gyttja (Figs 4c and S1; Voldstad et al., 2020). After 10.5 cal. kyr BP, δ^2H_{terr} stayed ^2H-enriched and relatively stable for the remainder of the Early Holocene. In Austre Nevlingen, increasing δ^2H_{terr} from 11.0 to 9.6 cal. kyr BP (Fig. 4a) suggests warming summer conditions with enhanced evaporative enrichment and/or a more proximal moisture source for growing season precipitation on northeastern Spitsbergen. Decreasing trends for both Jodavannet and Austre Nevlingen δ^2H_{aq} until 8.5–8.1 cal. kyr BP (Fig. 4a and d) suggests an increasing proportion of ^2H-depleted winter precipitation contributing to the δ^2H_{aq}, since the mean annual temperature

would have to decrease by more than 30 °C to explain the 100‰ ^{2}H-depletion in Austre Nevlingen (Kjellman et al., 2020). A stronger winter signal recorded in both lakes is likely due to a climatic shift, perhaps greater ocean surface evaporation resulting in increased winter precipitation amount, rather than a change in individual lake dynamics. We cannot say whether this winter trend was consistent across Svalbard, as our $\delta^{2}H_{aq}$ record from the west coast (Heftyevatnet) reflects summer precipitation changes. Heftyevatnet $\delta^{2}H_{terr}$ and $\delta^{2}H_{aq}$ remained relatively stable throughout the Early Holocene (Fig. 4b), indicating stable summer conditions. Slightly increasing $\delta^{2}H_{terr}$ trend and higher ε_{28-22} after 9.3 cal. kyr BP (Fig. 4c) suggests drier summer climate and higher evapotranspiration.

Warmer summer conditions and more evaporation from ice-free seas agree with both terrestrial and marine environmental reconstructions. The onset of the Early Holocene was characterized by warm regional conditions and significant changes in ocean circulation, sea-ice extent and glacier activity. The June solstice isolation at 80°N peaked around 11 cal. kyr BP (Fig. 4k; Laskar et al., 2004), and warmer-than-present temperatures were recorded by alkenones in lakes on northwestern Spitsbergen *c*. 10 cal. kyr BP (van der Bilt et al., 2019). Considerably warmer Early Holocene conditions have also been suggested by the presence of strongly thermophilous vascular plants in a *sed*aDNA record from Jodavannet (Voldstad et al., 2020). Balascio et al. (2018) interpreted increasing $\delta^{2}H$ for C_{25} to C_{29} *n*-alkanes in Hakluytvatnet from 12.8 to 9.5 cal. kyr BP to reflect insolation-driven warming and greater influence of mild sub-polar air masses.

In the eastern Fram Strait, subsurface temperatures increased by 4 °C between 12–10.2 cal. kyr BP (Fig. 4i; Werner et al., 2016), and shallow waters around Svalbard experienced temperatures 2–6 °C warmer than present between 11–9.2 cal. kyr BP (Mangerud & Svendsen, 2018). These changes have been interpreted to be a response to the high summer insolation and increased meridional Atlantic heat flux (Hald et al., 2007; Werner et al., 2016;

Mangerud & Svendsen, 2018). The pronounced inflow of warm Atlantic Water (AW) caused a reduction in sea-ice cover in the eastern Fram Strait (Fig. 4h; Werner et al., 2016), as well as in many Svalbard fjord systems (Hald et al., 2004; Forwick & Vorren, 2009; Bartels et al., 2017; Bartels et al., 2018; Allaart et al., 2020). Although seasonal sea ice persisted in the northern Barents Sea throughout the warm Early Holocene, there were only intermediate concentrations (10–50%) until *c*. 9.1 cal. kyr BP, followed by an increase towards predominantly extensive (>50%) sea ice by *c*. 8.3 cal. kyr BP (Fig. 4g; Pieńkowski et al., 2021). The low Early Holocene sea-ice concentrations coincided with the δ^2H_{aq} depletion in Austre Nevlingen and Jodavannet, suggesting that sea ice might be the main driving force behind increased winter precipitation amounts on northern Spitsbergen. Røthe et al. (2018) suggested higher winter precipitation amounts on northern Spitsbergen between 10.2–7 cal. kyr BP, inferred from high frequency of "snowmelt layers" (i.e., silty inorganic and graded sediment layers indicating rapid input of minerogenic material) in Vårfluesjøen. Thus, multiple lines of evidence, including our new leaf wax δ^2H records, suggest that there was a greater winter precipitation amount on Svalbard due to decreased sea-ice cover during the Early Holocene.

There was also a substantial reduction in glacier cover on Svalbard during the Early Holocene (Fig. 4j; Fjeldskaar et al., 2018; Farnsworth et al., 2020). The fjord systems experienced rapid time-transgressive glacier retreat from 12 to 10.5 cal. kyr BP (Farnsworth et al., 2020), and it has been suggested that most marine-terminating glaciers retreated onto land during this time (e.g., Svendsen & Mangerud, 1997; Hald et al., 2004). Cirque glaciers were greatly reduced in size, or disappeared completely (e.g., Svendsen & Mangerud, 1997; Snyder et al., 2000; de Wet et al., 2018). However, despite the warm unfavorable conditions for glacier growth, widespread evidence suggests that glacier re-advances still occurred (e.g., Lønne, 2005; Farnsworth et al., 2017; Farnsworth et al., 2018; Larsen et al., 2018), with the

highest frequency between 11–10 cal. kyr BP (Farnsworth et al., 2020). The key driver behind these advances is still unknown. One possibility is that high winter precipitation during this time counterbalanced the summer temperature-induced glacier mass loss, resulting in positive glacier mass balance. Our δ^2H records from Austre Nevlingen and Jodavannet suggest that there was an Early Holocene increase in winter precipitation on northern Spitsbergen and in inner Wijdefjorden, but it remains unclear whether this was enough to outpace mass loss caused by the high summer temperatures. Early Holocene mass-balance driven glacier advances are contradicted by the asynchronous pattern of the glacier re-advances, suggesting that they might be caused by changing internal glacier dynamics or surges (Jiskoot et al., 2000; Farnsworth et al., 2018). However, as precipitation is more spatially variable than temperature, perhaps different parts of Svalbard experienced winter precipitation increases at different times, as the sea-ice configuration changed.

5.3.2. Middle Holocene: 8.2–4.2 cal. kyr BP

Austre Nevlingen δ^2H_{aq} continued to be ^2H-depleted until *c*. 6 cal. kyr BP (Fig. 4a), suggesting continued high winter precipitation amount, associated with continuously low sea-ice extent in the Fram Strait (Fig. 4h; Werner et al., 2016). As the temporal resolution for Jodavannet in the Middle Holocene is low (up to 1000 years between samples), we do not discuss this part of the record in detail. Relatively stable δ^2H_{terr} in Austre Nevlingen and Jodavannet and stable δ^2H_{terr} and δ^2H_{aq} in Heftyevatnet until *c*. 6 cal. kyr BP indicates stable summer conditions (Fig. 4a, b, and d). ^2H-enriched δ^2H_{aq} in the Middle Holocene in Kløverbladvatna (Fig. 4e) may be due to more evaporative enrichment of lake water during longer ice-free seasons. Continuously high $\varepsilon_{28–22}$ (Fig. 4c) indicates relatively higher summer evapotranspiration, likely due to dry summers on western Spitsbergen. More ^2H-depleted δ^2H_{terr} and δ^2H_{aq}, and lower $\varepsilon_{28–22}$ in Heftyevatnet after 6 cal. kyr BP indicates a trend towards

colder summers or more distal or Arctic moisture sources, and less evapotranspiration. This corroborates well with widespread occurrence of the thermophilous mollusc *Mytilus edulis* indicating that Svalbard sea surface temperatures were *c*. 4 °C warmer than present between 8.2–6 cal. kyr BP. After *c*. 6.2 cal. kyr BP, the frequency of *Mytilus* declined, and it disappeared in northern and eastern Svalbard by 5.7 cal. kyr BP. This is interpreted as a declining sea surface temperature following the Holocene thermal maximum (Mangerud & Svendsen, 2018). A similar trend is seen in the eastern Fram Strait, where sea subsurface temperatures remained higher than at present (up to 5 °C) until *c*. 5 cal. kyr BP (Werner et al., 2016). At Hakluytvatnet, a hiatus in the sedimentary record from *c*. 7.5 to 5 cal. kyr BP is interpreted to reflect non-deposition due to dry conditions and complete desiccation of the lake (Fig. 4f; Balascio et al., 2018; Gjerde et al., 2018). Warm and dry Middle Holocene conditions on northern Spitsbergen have also been suggested by Voldstad et al. (2020), based on the appearance of *Dryas* in the Jodavannet *sed*aDNA record. Relatively ^{2}H-enriched $\delta^{2}H_{aq}$ in Kløverbladvatna from 5.2 to 3.6 cal. kyr BP (Fig. 4e) could indicate dry conditions on Nordaustlandet, with a larger effect on evaporation of the lake water than evapotranspiration on land, due to the long residence time of the lake.

Proglacial lake sediment records are characterized by reduced or absent minerogenic sedimentation in the Middle Holocene, indicating that glaciers were absent or much smaller than at present both on northern Spitsbergen (e.g., Røthe et al., 2015; Røthe et al., 2018; Allaart et al., 2021) and western Spitsbergen (e.g., Svendsen & Mangerud, 1997). The Holocene glacier minimum on Svalbard occurred between 8–6 cal. kyr BP, with glaciers presumably covering *c*. 25% of the land area in the north and east (Farnsworth et al., 2020). Surviving glaciers in the northeast could partly be explained by higher winter precipitation amounts, as suggested by the Austre Nevlingen $\delta^{2}H_{aq}$ record.

More ^{2}H-depleted $\delta^{2}H_{terr}$ in all four lakes after *c*. 5.5 cal. kyr BP suggests that summer precipitation became ^{2}H-depleted due to cooler local temperatures or more distal moisture sources, with less evaporative enrichment. More variable $\delta^{2}H_{aq}$ in Austre Nevlingen from 6 cal. kyr BP into the Late Holocene suggests greater climate variability and that the lake experienced changes in the precipitation seasonality recorded by the lake, e.g., that the lake some years incorporated the relatively ^{2}H-depleted winter precipitation and some years not (Kjellman et al., 2020).

5.3.3. Late Holocene: 4.2–0 cal. kyr BP

The relatively stable or slight ^{2}H-depletion of summer precipitation continued on northern Spitsbergen in the Late Holocene, with relatively stable or slightly decreasing $\delta^{2}H_{terr}$ trends in Austre Nevlingen, Jodavannet and Kløverbladvatna (Fig. 4). Stable $\delta^{2}H_{terr}$ and $\delta^{2}H_{aq}$ and low ε_{28-22} in Heftyevatnet (Fig. 4b-c) suggest stable summer conditions and minimal evaporative enrichment of terrestrial plant source water. The Jodavannet lithology (Fig. S1c) and a distinct shift in the *sed*aDNA *c*. 4.3 cal. kyr BP (Voldstad et al., 2020) are interpreted to reflect the onset of Neoglacial cooling. The neoglacial cooling is well-documented on Svalbard, with lower temperatures inferred from plant macrofossils (Birks, 1991) and alkenones (van der Bilt et al., 2018), permafrost aggradation (Humlum, 2005), and glacier re-advances (e.g., Werner, 1993; Svendsen & Mangerud, 1997; Røthe et al., 2015; van der Bilt et al., 2015; Allaart et al., 2021). Most Late Holocene glacier re-advances are dated to between 4–0.5 cal. kyr BP, with the highest frequency from 1.0 to 0.5 cal. kyr BP (Farnsworth et al., 2020). The Neoglacial was generally characterized by decreasing insolation (Laskar et al., 2004; Fig. 4k), weakened AW advection, lower sea surface temperatures and extended sea-ice cover in the Fram Strait (e.g., Müller et al., 2012; Werner et al., 2013; Werner et al., 2016) and the Svalbard fjords (e.g., Forwick & Vorren, 2009; Bartels et al., 2018). However, Müller et al. (2012) propose

that a temporarily strengthened West Spitsbergen Current and/or atmospheric circulation changes caused northward retreat of the sea-ice edge in the Fram Strait on several occasions during the Late Holocene, and that this triggered glacier advances on Spitsbergen (Svendsen & Mangerud, 1997). This is supported by abrupt increases in sea surface temperature south of Svalbard *c.* 2.2 and 1.7 cal. kyr BP (Sarnthein et al., 2003). Furthermore, Røthe et al. (2015) suggested that the (close to) maximum extent of Karlbreen on northwestern Spitsbergen from 1.7 to 1.5 cal. kyr BP could be explained by open water conditions west of Spitsbergen (Müller et al., 2012), and that maritime glaciers might be sensitive to changes in winter precipitation.

Increasing winter precipitation amounts have also been suggested to drive Little Ice Age (LIA, 1250–1920 AD) glacier re-advances. Alkenones from Kongressvatnet, western Spitsbergen, suggested relatively mild LIA conditions, and that the LIA glacier expansion in the 18th and 19th century was driven by increased winter precipitation rather than low summer temperatures (D'Andrea et al., 2012). Ice core $\delta^{18}O$ records from Spitsbergen show progressive cooling (*c.* 0.9 °C century^{-1}) from 800–1800 AD, with lowest winter temperatures in the 1800s (4 °C colder than the 1900s), followed by rapid warming (Divine et al., 2011). Similarly, lake water $\delta^{18}O$ reconstructed from chironomid head capsules in lacustrine sediments from Svartvatnet, southern Spitsbergen shows a distinct decrease from *c*. –12 to –19‰ from *c*. 1600–1900 AD (Arppe et al., 2017). This is by far the largest drop in $\delta^{18}O$ in the 5500-year-long record of Arppe et al. (2017), which they attribute to lower winter temperatures and increased seasonal contrasts during the LIA. As temperature alone cannot explain the drop in $\delta^{18}O$ in Svartvatnet during the LIA, Arppe et al. (2017) proposed that some of the change was caused by moisture source changes, variable sea-ice extent and/or increased snowfall.

Whilst the Neoglacial and LIA cooling is well documented in numerous proxy records, much less is known about the Late Holocene precipitation seasonality. Since Heftyevatnet is a summer-biased record, it does not reveal anything about winter precipitation on western Spitsbergen. However, our three lake records from northern Spitsbergen and Nordaustlandet provide information about variable seasonal distribution of precipitation. Large fluctuations in the Austre Nevlingen and Jodavannet δ^2H_{aq} records indicate that the lakes reach a climate threshold and/or changes in the lake hydrology, altering the seasonality of precipitation that is reflected in the lake water. Jodavannet, which is a small lake with a relatively large catchment, is likely more sensitive to perturbations than Austre Nevlingen. For most of the Jodavannet record, δ^2H_{aq} follows δ^2H_{terr}, suggesting that both chain lengths are influenced by summer precipitation, although δ^2H_{aq} likely reflects a mix of summer and winter precipitation, as indicated by the more ^{2}H-depleted δ^2H_{aq}. In the Late Holocene, δ^2H_{aq} is decoupled from δ^2H_{terr}, indicating a stronger influence of winter precipitation. Concurrent changes in Jodavannet and Austre Nevlingen (e.g., decreasing δ^2H_{aq} at the Middle to Late Holocene transition) could suggest the same climate forcing, whereas asynchronous changes (after *c.* 3.3 cal. kyr BP) might be a result of changes in lake hydrology. Due to the relatively low resolution (>300 years between most samples in the Late Holocene) and uncertainties in the age-depth models, it is difficult to determine whether the changes occur simultaneously in the two lakes. The Jodavannet δ^2H_{aq} record, which contains the most ^{2}H-depleted values and may be the most sensitive to winter precipitation, suggests winter precipitation was relatively high around 3.9, 1.8 and 1.4 cal. kyr BP. The lack of similar trends in Kløverbladvatna could be explained by a slightly different seasonality or less winter precipitation on Nordaustlandet or reflect that the much larger Kløverbladvatna is not as sensitive to seasonal precipitation changes.

6. Conclusions

We present δ^2H of Holocene sedimentary leaf waxes from four lakes on Svalbard. The aim of this study was to investigate seasonal precipitation variability in time and space, targeting lakes across a climatic gradient from relatively warm and humid western Spitsbergen to relatively cold and dry Nordaustlandet. In our records, soil water δ^2H (used by terrestrial plants) mainly reflects summer precipitation δ^2H and evapotranspiration, whereas lake water δ^2H (used by aquatic plants) reflects different seasonality depending on the residence time of the lake. The main findings are:

- Similar Holocene summer precipitation isotope trends for all study sites suggest similar summer climate forcing across Svalbard. The Early and Middle Holocene summers were characterized by warmer, drier conditions and/or a more proximal moisture source, followed by a trend towards cooler conditions or more distally derived moisture. Less ^2H-depleted δ^2H_{terr} in Heftyevatnet reflects the closeness to the North Atlantic, whereas the more ^2H-depleted δ^2H_{terr} in Jodavannet, Austre Nevlingen and Kløverbladvatna reflects more Rayleigh distillation during moisture transport over the mountains and/or incorporation of some winter precipitation due to more winter-biased soil water.
- In the Early Holocene, regional warming and increased moisture availability due to enhanced evaporation from ice-free seas resulted in higher winter precipitation amounts on northern Spitsbergen. The winter precipitation likely stayed high until *c*. 6 cal. kyr BP, after which surface waters around Svalbard cooled and the sea-ice cover increased, limiting the available moisture. During the Late Holocene, our northern Spitsbergen δ^2H_{aq} records suggest that periods of increased winter precipitation occurred. Additionally, asynchronous δ^2H_{aq} changes between the lakes indicate that changes in lake hydrology affected the seasonality reflected in the lake water δ^2H.

- The precipitation seasonality reflected in the lake water (and therefore aquatic leaf wax δ^2H) may vary through time and space due to catchment processes that might be controlled by climate change. Soil water (and therefore terrestrial leaf wax δ^2H) seasonality might vary spatially depending on the seasonality of the precipitation recharging the active layer. To strengthen future paleo-precipitation proxy studies, we need better constraints on modern precipitation sources and isotopic composition, soil and lake water recharge and evaporation, and site-specific leaf wax sources.

CRediT authorship contribution statement

Sofia E. Kjellman: Conceptualization, Investigation, Visualization, Writing - Original Draft, Project administration, Funding acquisition. **Elizabeth K. Thomas:** Conceptualization, Investigation, Writing - Review & Editing, Supervision, Funding acquisition. **Anders Schomacker:** Conceptualization, Investigation, Writing - Review & Editing, Supervision, Funding acquisition. **Wesley R. Farnsworth:** Investigation, Writing - Review & Editing, Funding acquisition. **Owen C. Cowling:** Investigation, Writing - Review & Editing. **Lis Allaart:** Investigation, Writing - Review & Editing. **Skafti Brynjólfsson**: Investigation, Writing - Review & Editing.

Declaration of Competing Interest

The authors declare that they have no known competing financial interests or personal relationships that could have appeared to influence the work reported in this paper.

Data availability

Chronology and proxy data presented in this paper will be publicly available in both LiPD (McKay & Emile-Geay, 2016) and text format at the National Centers for Environmental

Information for Paleoclimatology: https://www.ncei.noaa.gov/products/paleoclimatology. Water isotope data will be made available in the Water Isotopes Database: www.waterisotopes.org.

Acknowledgements

This research was supported by grants from the Nansen Foundation to AS, The Arctic Research and Studies program of the Ministries for Foreign Affairs of Norway and Iceland (2017-ARS-79772) to AS, The Research Council of Norway (269984/E10) to AS, The Carlsberg Foundation (CF14-0756) to AS, Svalbard Environmental Protection Fund (16/35, 17/101, and 20/36) to AS, SEK, and WRF, Olle Engkvists Stiftelse (204-0129) to AS and SEK, Helge A:xson Johnsons Stiftelse to SEK, and National Science Foundation (EAR-IF 1652274) to EKT. We thank Sveinn Brynjólfsson, Sara Mollie Cohen, Lena Håkansson, Ólafur Ingólfsson, Marc Macias-Fauria, and Michael Retelle for participating in fieldwork during lake sediment coring. Furthermore, Michael Retelle and Tina Dahl are thanked for lake water sampling. We thank Katie Lovell for sample processing and are grateful to Nick McKay for LiPD troubleshooting and debugging.

References

Aichner, B., Herzschuh, U., Wilkes, H., Vieth, A., & Böhner, J., 2010. δD values of n-alkanes in Tibetan lake sediments and aquatic macrophytes–A surface sediment study and application to a 16 ka record from Lake Koucha. *Organic Geochemistry, 41*(8), 779-790. https://doi.org/10.1016/j.orggeochem.2010.05.010

Allaart, L., Müller, J., Schomacker, A., Rydningen, T. A., Håkansson, L., Kjellman, S. E., Mollenhauer, G., & Forwick, M., 2020. Late Quaternary glacier and sea-ice history of northern Wijdefjorden, Svalbard. *Boreas, 49*(3), 417-437. https://doi.org/10.1111/bor.12435

Allaart, L., Schomacker, A., Larsen, N. K., Nørmark, E., Rydningen, T. A., Farnsworth, W. R., Retelle, M., Brynjólfsson, S., Forwick, M., & Kjellman, S. E., 2021. Glacial history of the Åsgardfonna Ice Cap, NE Spitsbergen, since the last glaciation. *Quaternary Science Reviews, 251*, 106717. https://doi.org/10.1016/j.quascirev.2020.106717

Anderson, L., Abbott, M. B., Finney, B. P., & Burns, S. J., 2007. Late Holocene moisture balance variability in the southwest Yukon Territory, Canada. *Quaternary Science Reviews, 26*(1-2), 130-141. https://doi.org/10.1016/j.quascirev.2006.04.011

Arppe, L., Kurki, E., Wooller, M. J., Luoto, T. P., Zajączkowski, M., & Ojala, A. E., 2017. A 5500-year oxygen isotope record of high arctic environmental change from southern Spitsbergen. *The Holocene, 27*(12), 1948-1962. https://doi.org/10.1177/0959683617715698

Balascio, N. L., D'Andrea, W. J., Bradley, R. S., & Perren, B. B., 2013. Biogeochemical evidence for hydrologic changes during the Holocene in a lake sediment record from southeast Greenland. *The Holocene, 23*(10), 1428-1439. https://doi.org/10.1177/0959683613493938

Balascio, N. L., D'Andrea, W. J., Gjerde, M., & Bakke, J., 2018. Hydroclimate variability of High Arctic Svalbard during the Holocene inferred from hydrogen isotopes of leaf waxes. *Quaternary Science Reviews, 183*, 177-187. https://doi.org/10.1016/j.quascirev.2016.11.036

Bartels, M., Titschack, J., Fahl, K., Stein, R., Seidenkrantz, M.-S., Hillaire-Marcel, C., & Hebbeln, D., 2017. Atlantic Water advection vs. glacier dynamics in northern Spitsbergen since early deglaciation. *Climate of the Past, 13*(12), 1717-1749. https://doi.org/10.5194/cp-13-1717-2017

Bartels, M., Titschack, J., Fahl, K., Stein, R., & Hebbeln, D., 2018. Wahlenbergfjord, eastern Svalbard: a glacier-surrounded fjord reflecting regional hydrographic variability during the Holocene? *Boreas, 47*(4), 1003-1021. https://doi.org/10.1111/bor.12325

Berke, M. A., Sierra, A. C., Bush, R., Cheah, D., & O'Connor, K., 2019. Controls on leaf wax fractionation and δ2H values in tundra vascular plants from western Greenland. *Geochimica et Cosmochimica Acta, 244*, 565-583. https://doi.org/10.1016/j.gca.2018.10.020

Bintanja, R., & Andry, O., 2017. Towards a rain-dominated Arctic. *Nature Climate Change, 7*(4), 263. https://doi.org/10.1038/nclimate3240

Bintanja, R., & Selten, F. M., 2014. Future increases in Arctic precipitation linked to local evaporation and sea-ice retreat. *Nature, 509*(7501), 479-482. https://doi.org/10.1038/nature13259

Bintanja, R., van der Wiel, K., van der Linden, E., Reusen, J., Bogerd, L., Krikken, F., & Selten, F., 2020. Strong future increases in Arctic precipitation variability linked to poleward moisture transport. *Science advances, 6*(7), eaax6869. https://doi.org/10.1126/sciadv.aax6869

Birks, H. H., 1991. Holocene vegetational history and climatic change in west Spitsbergen-plant macrofossils from Skardtjørna, an Arctic lake. *The Holocene, 1*(3), 209-218. https://doi.org/10.1177/095968369100100303

Blaauw, M., & Christen, J. A., 2011. Flexible paleoclimate age-depth models using an autoregressive gamma process. *Bayesian analysis, 6*(3), 457-474. https://doi.org/10.1214/11-BA618

Bowen, G. J., 2021. OIPC: The online isotopes in precipitation calculator, version 3.1. Retrieved from http://www.waterisotopes.org

Bowen, G. J., & Revenaugh, J., 2003. Interpolating the isotopic composition of modern meteoric precipitation. *Water Resources Research, 39*(10). https://doi.org/10.1029/2003WR002086

Bowen, G. J., Wassenaar, L. I., & Hobson, K. A., 2005. Global application of stable hydrogen and oxygen isotopes to wildlife forensics. *Oecologia, 143*(3), 337-348. https://doi.org/10.1007/s00442-004-1813-y

Cluett, A. A., & Thomas, E. K., 2020. Resolving combined influences of inflow and evaporation on western Greenland lake water isotopes to inform paleoclimate inferences. *Journal of Paleolimnology, 63*, 251-268. https://doi.org/10.1007/s10933-020-00114-4

Cluett, A., Thomas, E., Evans, S., & Keys, P., 2021. Seasonal variations in moisture origin explain spatial contrast in precipitation isotope seasonality on coastal western Greenland. *Journal of Geophysical Research: Atmospheres, 126*(11), e2020JD033543. https://doi.org/10.1029/2020JD033543

Cooper, L., Olsen, C., Solomon, D., Larsen, I., Cook, R., & Grebmeier, J., 1991. Stable isotopes of oxygen and natural and fallout radionuclides used for tracing runoff during snowmelt in an Arctic watershed. *Water Resources Research, 27*(9), 2171-2179. https://doi.org/10.1029/91WR01243

Corcoran, M. C., Thomas, E. K., & Morrill, C., 2021. Using a paired chironomid δ18O and aquatic leaf wax δ2H approach to reconstruct seasonality on western Greenland during the Holocene. *Paleoceanography and Paleoclimatology, 36*(4), e2020PA004169. https://doi.org/10.1029/2020PA004169

Cowling, O. C., Thomas, E. K., Svendsen, J. I., Mangerud, J., Haflidason, H., Regnéll, C., & Brendryen, J., 2021. Western Siberia experienced rapid shifts in moisture source and summer water balance during the last deglaciation and early Holocene. *Journal of Quaternary Science*. https://doi.org/10.1002/jqs.3386

Craig, H., 1961. Isotopic variations in meteoric waters. *Science, 133*(3465), 1702-1703. https://doi.org/10.1126/science.133.3465.1702

Croudace, I. W., Rindby, A., & Rothwell, R. G., 2006. ITRAX: description and evaluation of a new multi-function X-ray core scanner. *Geological Society, London, Special Publications, 267*(1), 51-63. https://doi.org/10.1144/GSL.SP.2006.267.01.04

D'Andrea, W. J., Vaillencourt, D. A., Balascio, N. L., Werner, A., Roof, S. R., Retelle, M., & Bradley, R. S., 2012. Mild Little Ice Age and unprecedented recent warmth in an 1800 year lake sediment record from Svalbard. *Geology, 40*(11), 1007-1010. https://doi.org/10.1130/G33365.1

Dallmann, W. K. E., 2015. *Geoscience Atlas of Svalbard*. Norwegian Polar Institute, Report Series 148, 292 pp.

Daniels, W. C., Russell, J. M., Giblin, A. E., Welker, J. M., Klein, E. S., & Huang, Y., 2017. Hydrogen isotope fractionation in leaf waxes in the Alaskan Arctic tundra. *Geochimica et Cosmochimica Acta, 213*, 216-236. https://doi.org/10.1016/j.gca.2017.06.028

Dansgaard, W., 1964. Stable isotopes in precipitation. *Tellus, 16*(4), 436-468. https://doi.org/10.3402/tellusa.v16i4.8993
de Wet, G. A., Balascio, N. L., D'Andrea, W. J., Bakke, J., Bradley, R. S., & Perren, B., 2018. Holocene glacier activity reconstructed from proglacial lake Gjøavatnet on Amsterdamøya, NW Svalbard. *Quaternary Science Reviews, 183*, 188-203. https://doi.org/10.1016/j.quascirev.2017.03.018
Dion-Kirschner, H., McFarlin, J. M., Masterson, A. L., Axford, Y., & Osburn, M. R., 2020. Modern constraints on the sources and climate signals recorded by sedimentary plant waxes in west Greenland. *Geochimica et Cosmochimica Acta, 286*, 336-354. https://doi.org/10.1016/j.gca.2020.07.027
Divine, D., Isaksson, E., Martma, T., Meijer, H. A., Moore, J., Pohjola, V., van de Wal, R. S., & Godtliebsen, F., 2011. Thousand years of winter surface air temperature variations in Svalbard and northern Norway reconstructed from ice-core data. *Polar Research, 30*(1), 7379. https://doi.org/10.3402/polar.v30i0.7379
Dufour, A., Zolina, O., & Gulev, S. K., 2016. Atmospheric moisture transport to the Arctic: Assessment of reanalyses and analysis of transport components. *Journal of Climate, 29*(14), 5061-5081. https://doi.org/10.1175/JCLI-D-15-0559.1
Eckerstorfer, M. & Christiansen, H. H., 2011. The "High Arctic Maritime Snow Climate" in Central Svalbard. *Arctic, Antarctic, and Alpine Research, 43*(1), 11-21. https://doi.org/10.1657/1938-4246-43.1.11
Eidesen, P. B., Arnesen, G., Elven, R., & Søli, G., 2018. *Kartlegging av Ringhorndalen, Wijdefjorden: en uutforsket arktisk oase*. The University Centre in Svalbard, The University of Oslo, Ecofact Nord AS, 43 pp.
Elvebakk, A., & Nilsen, L., 2002. Indre Wijdefjorden med sidefjordar: eit botanisk unikt steppeområde på Svalbard. *Rapport til Sysselmannen på Svalbard Universitetet i Tromsø, Tromsø*.
Farnsworth, W. R., Ingólfsson, Ó., Noormets, R., Allaart, L., Alexanderson, H., Henriksen, M., & Schomacker, A., 2017. Dynamic Holocene glacial history of St. Jonsfjorden, Svalbard. *Boreas, 46*(3), 585-603. https://doi.org/10.1111/bor.12269
Farnsworth, W. R., Ingólfsson, Ó., Retelle, M., Allaart, L., Håkansson, L. M., & Schomacker, A., 2018. Svalbard glaciers re-advanced during the Pleistocene–Holocene transition. *Boreas, 47*(4), 1022-1032. https://doi.org/10.1111/bor.12326
Farnsworth, W. R., Allaart, L., Ingólfsson, Ó., Alexanderson, H., Forwick, M., Noormets, R., Retelle, M., & Schomacker, A., 2020. Holocene glacial history of Svalbard: Status, perspectives and challenges. *Earth-Science Reviews, 208*, 103249. https://doi.org/10.1016/j.earscirev.2020.103249
Farnsworth, W. R., Ingólfsson, Ó., Mannerfelt, E. S., Kalliokoski, M. H., Guðmundsdóttir, E. R., Retelle, M., Allaart, L., Brynjólfsson, S., Furze, M. F., & Hancock, H. J., 2022. Vedde Ash constrains Younger Dryas glacier re-advance and rapid glacio-isostatic rebound on Svalbard. *Quaternary Science Advances, 5*, 100041. https://doi.org/10.1016/j.qsa.2021.100041
Ficken, K. J., Li, B., Swain, D., & Eglinton, G., 2000. An n-alkane proxy for the sedimentary input of submerged/floating freshwater aquatic macrophytes. *Organic Geochemistry, 31*(7-8), 745-749. https://doi.org/10.1016/S0146-6380(00)00081-4
Fjeldskaar, W., Bondevik, S., & Amantov, A., 2018. Glaciers on Svalbard survived the Holocene thermal optimum. *Quaternary Science Reviews, 199*, 18-29. https://doi.org/10.1016/j.quascirev.2018.09.003
Forwick, M., & Vorren, T. O., 2009. Late Weichselian and Holocene sedimentary environments and ice rafting in Isfjorden, Spitsbergen. *Palaeogeography,*

Palaeoclimatology, Palaeoecology, 280(1-2), 258-274. https://doi.org/10.1016/j.palaeo.2009.06.026

Førland, E. J., & Hanssen-Bauer, I., 2003. Past and future climate variations in the Norwegian Arctic: overview and novel analyses. *Polar Research, 22*(2), 113-124. https://doi.org/10.3402/polar.v22i2.6450

Førland, E. J., Isaksen, K., Lutz, J., Hanssen-Bauer, I., Schuler, T. V., Dobler, A., Gjelten, H. M., & Vikhamar-Schuler, D., 2020. Measured and Modeled Historical Precipitation Trends for Svalbard. *Journal of Hydrometeorology, 21*(6), 1279-1296. https://doi.org/10.1175/JHM-D-19-0252.1

Geyman, E. C., JJ van Pelt, W., Maloof, A. C., Aas, H. F., & Kohler, J., 2022. Historical glacier change on Svalbard predicts doubling of mass loss by 2100. *Nature, 601*(7893), 374-379. https://doi.org/10.1038/s41586-021-04314-4

Gibson, J., Prepas, E., & McEachern, P., 2002. Quantitative comparison of lake throughflow, residency, and catchment runoff using stable isotopes: modelling and results from a regional survey of Boreal lakes. *Journal of Hydrology, 262*(1-4), 128-144. https://doi.org/10.1016/S0022-1694(02)00022-7

Gjerde, M., Bakke, J., D'Andrea, W. J., Balascio, N. L., Bradley, R. S., Vasskog, K., Ólafsdóttir, S., Røthe, T. O., Perren, B. B., & Hormes, A., 2018. Holocene multi-proxy environmental reconstruction from lake Hakluytvatnet, Amsterdamøya Island, Svalbard (79.5 N). *Quaternary Science Reviews, 183*, 164-176. https://doi.org/10.1016/j.quascirev.2017.02.017

Gorbey, D. B., Thomas, E. K., Sauer, P. E., Raynolds, M. K., Miller, G. H., Corcoran, M. C., Cowling, O. C., Crump, S. E., Lovell, K., & Raberg, J. H., 2022. Modern Eastern Canadian Arctic Lake Water Isotopes Exhibit Latitudinal Patterns in Inflow Seasonality and Minimal Evaporative Enrichment. *Paleoceanography and Paleoclimatology, 37*(5), e2021PA004384. https://doi.org/10.1029/2021PA004384

Gorbey, D. B., Thomas, E. K., Crump, S. E., Hollister, K. V., Raynolds, M. K., Raberg, J. H., de Wet, G., Sepúlveda, J., & Miller, G. H. Southern Baffin Island mean annual precipitation isotopes modulated by summer and autumn moisture source changes during the past 5800 years. *Journal of Quaternary Science*. In press. https://doi.org/10.1002/jqs.3390

Guo, C.-Q., Ochyra, R., Wu, P.-C., Seppelt, R. D., Yao, Y.-F., Bian, L.-G., Li, S.-P., & Li, C.-S., 2013. Warnstorfia exannulata, an aquatic moss in the Arctic: seasonal growth responses. *Climatic Change, 119*(2), 407-419. https://doi.org/10.1007/s10584-013-0724-5

Hagen, J. O., Liestøl, O., Roland, E., & Jørgensen, T., 1993. Glacier atlas of Svalbard and Jan Mayen. Norwegian Polar Institute Meddelelser 129.

Hald, M., Ebbesen, H., Forwick, M., Godtliebsen, F., Khomenko, L., Korsun, S., Olsen, L. R., & Vorren, T. O., 2004. Holocene paleoceanography and glacial history of the West Spitsbergen area, Euro-Arctic margin. *Quaternary Science Reviews, 23*(20-22), 2075-2088. https://doi.org/10.1016/j.quascirev.2004.08.006

Hald, M., Andersson, C., Ebbesen, H., Jansen, E., Klitgaard-Kristensen, D., Risebrobakken, B., Salomonsen, G. R., Sarnthein, M., Sejrup, H. P., & Telford, R. J., 2007. Variations in temperature and extent of Atlantic Water in the northern North Atlantic during the Holocene. *Quaternary Science Reviews, 26*(25-28), 3423-3440. https://doi.org/10.1016/j.quascirev.2007.10.005

Hansen, B. B., Isaksen, K., Benestad, R. E., Kohler, J., Pedersen, Å. Ø., Loe, L. E., Coulson, S. J., Larsen, J. O., & Varpe, Ø., 2014. Warmer and wetter winters: characteristics and implications of an extreme weather event in the High Arctic. *Environmental Research Letters, 9*(11), 114021. https://doi.org/10.1088/1748-9326/9/11/114021

Hanssen-Bauer, I., Førland, E. J., Hisdal, H., Mayer, S., Sandø, A. B., & Sorteberg, A., 2019. *Climate in Svalbard 2100 - A knowledge base for climate adaptation* 2387-3027. Norwegian Centre for Climate Services (NCCS), NCCS report no. 1/2019, 207 pp.

Heiri, O., Lotter, A. F., & Lemcke, G., 2001. Loss on ignition as a method for estimating organic and carbonate content in sediments: reproducibility and comparability of results. *Journal of Paleolimnology, 25*(1), 101-110. https://doi.org/10.1023/A:1008119611481

Holm, T. M., Koinig, K. A., Andersen, T., Donali, E., Hormes, A., Klaveness, D., & Psenner, R., 2012. Rapid physicochemical changes in the high Arctic Lake Kongressvatn caused by recent climate change. *Aquatic sciences, 74*(3), 385-395. https://doi.org/10.1007/s00027-011-0229-0

Humlum, O., 2002. Modelling late 20th-century precipitation in Nordenskiold Land, Svalbard, by geomorphic means. *Norsk Geografisk Tidsskrift-Norwegian Journal of Geography, 56*(2), 96-103. https://doi.org/10.1080/002919502760056413

Humlum, O., 2005. Holocene permafrost aggradation in Svalbard. *Geological Society, London, Special Publications, 242*(1), 119-129. https://doi.org/10.1144/GSL.SP.2005.242.01.11

Husum, K., & Hald, M., 2012. Arctic planktic foraminiferal assemblages: Implications for subsurface temperature reconstructions. *Marine micropaleontology, 96*, 38-47. https://doi.org/10.1016/j.marmicro.2012.07.001

IAEA/WMO, 2019. Global Network of Isotopes in Precipitation. The GNIP Database. Retrieved from https://nucleus.iaea.org/wiser

IPCC, 2021. Climate Change 2021: The Physical Science Basis. Contribution of Working Group I to the Sixth Assessment Report of the Intergovernmental Panel on Climate Change [Masson-Delmotte, V., P. Zhai, A. Pirani, S.L. Connors, C. Péan, S. Berger, N. Caud, Y. Chen, L. Goldfarb, M.I. Gomis, M. Huang, K. Leitzell, E. Lonnoy, J.B.R. Matthews, T.K. Maycock, T. Waterfield, O. Yelekçi, R. Yu, and B. Zhou (eds.)]. Cambridge University Press, Cambridge, United Kingdom and New York, NY, USA, In press, https://doi:10.1017/9781009157896.

Jakobsson, M., Mayer, L., Coakley, B., Dowdeswell, J. A., Forbes, S., Fridman, B., Hodnesdal, H., Noormets, R., Pedersen, R., & Rebesco, M., 2012. The international bathymetric chart of the Arctic Ocean (IBCAO) version 3.0. *Geophysical research letters, 39*(12). https://doi.org/10.1029/2012GL052219

Jiskoot, H., Murray, T., & Boyle, P., 2000. Controls on the distribution of surge-type glaciers in Svalbard. *Journal of Glaciology, 46*(154), 412-422. https://doi.org/10.3189/172756500781833115

Jonsson, C. E., Leng, M. J., Rosqvist, G. C., Seibert, J., & Arrowsmith, C., 2009. Stable oxygen and hydrogen isotopes in sub-Arctic lake waters from northern Sweden. *Journal of Hydrology, 376*(1-2), 143-151. https://doi.org/10.1016/j.jhydrol.2009.07.021

Kahmen, A., Schefuß, E., & Sachse, D., 2013. Leaf water deuterium enrichment shapes leaf wax n-alkane δD values of angiosperm plants I: Experimental evidence and mechanistic insights. *Geochimica et Cosmochimica Acta, 111*, 39-49. https://doi.org/10.1016/j.gca.2012.09.003

Karlsen, S. R., Elvebakk, A., Høgda, K. A., & Grydeland, T., 2014. Spatial and temporal variability in the onset of the growing season on Svalbard, Arctic Norway—measured by MODIS-NDVI satellite data. *Remote Sensing, 6*(9), 8088-8106. https://doi.org/10.3390/rs6098088

Katrantsiotis, C., Norström, E., Smittenberg, R. H., Salonen, J. S., Plikk, A., & Helmens, K., 2021. Seasonal variability in temperature trends and atmospheric circulation systems

during the Eemian (Last Interglacial) based on n-alkanes hydrogen isotopes from Northern Finland. *Quaternary Science Reviews, 273*, 107250. https://doi.org/10.1016/j.quascirev.2021.107250

Kjellman, S. E., Schomacker, A., Thomas, E. K., Håkansson, L., Duboscq, S., Cluett, A. A., Farnsworth, W. R., Allaart, L., Cowling, O. C., & McKay, N. P., 2020. Holocene precipitation seasonality in northern Svalbard: Influence of sea ice and regional ocean surface conditions. *Quaternary Science Reviews, 240*, 106388. https://doi.org/10.1016/j.quascirev.2020.106388

Kjellman, S. E., Thomas, E. K., & Schomacker, A., 2022. Arctic and sub-Arctic lake water δ2H and δ18O along a coastal-inland transect: implications for interpreting water isotope proxy records. *Journal of Hydrology*, 127556. https://doi.org/10.1016/j.jhydrol.2022.127556

Konecky, B. L., McKay, N. P., Comas-Bru, L., Dassié, E. P., DeLong, K. L., Falster, G. M., Fischer, M. J., Jones, M. D., Jonkers, L., & Kaufman, D. S., 2020. The Iso2k database: a global compilation of paleo-δ 18 O and δ 2 H records to aid understanding of Common Era climate. *Earth System Science Data, 12*(3), 2261-2288. https://doi.org/10.5194/essd-12-2261-2020

Kopec, B. G., Feng, X., Michel, F. A., & Posmentier, E. S., 2016. Influence of sea ice on Arctic precipitation. *Proc Natl Acad Sci U S A, 113*(1), 46-51. https://doi.org/10.1073/pnas.1504633113

Koroleva, N., Konstantinova, N., Belkina, O., Davydov, D., Likhachev, A. Y., Savchenko, A., & Urbanavichene, I., 2008. Flora and vegetation of Grønfjord area (Spitsbergen archipelago). *Apatity, K & M*.

Köseoğlu, D., Belt, S. T., Smik, L., Yao, H., Panieri, G., & Knies, J., 2018. Complementary biomarker-based methods for characterising Arctic sea ice conditions: A case study comparison between multivariate analysis and the PIP25 index. *Geochimica et Cosmochimica Acta, 222*, 406-420. https://doi.org/10.1016/j.gca.2017.11.001

Larsen, E., Lyså, A., Rubensdotter, L., Farnsworth, W. R., Jensen, M., Nadeau, M. J., & Ottesen, D., 2018. Lateglacial and Holocene glacier activity in the Van Mijenfjorden area, western Svalbard. *arktos, 4*(1), 1-21. https://doi.org/10.1007/s41063-018-0042-2

Larsson, S., 1982. Geomorphological effects on the slopes of Longyear Valley, Spitsbergen, after a heavy rainstorm in July 1972. *Geografiska Annaler: Series A, Physical Geography, 64*(3-4), 105-125. https://doi.org/10.1080/04353676.1982.11880059

Laskar, J., Robutel, P., Joutel, F., Gastineau, M., Correia, A., & Levrard, B., 2004. A long-term numerical solution for the insolation quantities of the Earth. *Astronomy & Astrophysics, 428*(1), 261-285. https://doi.org/10.1051/0004-6361:20041335

Linderholm, H. W., Nicolle, M., Francus, P., Gajewski, K., Helama, S., Korhola, A., Solomina, O., Yu, Z., Zhang, P., & D'Andrea, W. J., 2018. Arctic hydroclimate variability during the last 2000 years. *Climate of the Past*. https://doi.org/10.5194/cp-14-473-2018

Łupikasza, E. B., Ignatiuk, D., Grabiec, M., Cielecka-Nowak, K., Laska, M., Jania, J., Luks, B., Uszczyk, A., & Budzik, T., 2019. The role of winter rain in the glacial system on Svalbard. *Water, 11*(2), 334. https://doi.org/10.3390/w11020334

Lønne, I., 2005. Faint traces of high Arctic glaciations: an early Holocene ice-front fluctuation in Bolterdalen, Svalbard. *Boreas, 34*(3), 308-323. https://doi.org/10.1111/j.1502-3885.2005.tb01103.x

MacDonald, L. A., Wolfe, B. B., Turner, K. W., Anderson, L., Arp, C. D., Birks, S. J., Bouchard, F., Edwards, T. W., Farquharson, N., & Hall, R. I., 2017. A synthesis of thermokarst lake water balance in high-latitude regions of North America from isotope tracers. *Arctic Science, 3*(2), 118-149. https://doi.org/10.1139/as-2016-0019

Mangerud, J., & Svendsen, J. I., 2018. The Holocene Thermal Maximum around Svalbard, Arctic North Atlantic; molluscs show early and exceptional warmth. *The Holocene, 28*(1), 65-83. https://doi.org/10.1177/0959683617715701

Masson-Delmotte, V., Landais, A., Stievenard, M., Cattani, O., Falourd, S., Jouzel, J., Johnsen, S. J., Dahl-Jensen, D., Sveinsbjornsdottir, A., & White, J., 2005. Holocene climatic changes in Greenland: Different deuterium excess signals at Greenland Ice Core Project (GRIP) and NorthGRIP. *Journal of Geophysical Research: Atmospheres, 110*(D14). https://doi.org/10.1029/2004JD005575

McCrystall, M. R., Stroeve, J., Serreze, M., Forbes, B. C., & Screen, J. A., 2021. New climate models reveal faster and larger increases in Arctic precipitation than previously projected. *Nature communications, 12*(1), 1-12. https://doi.org/10.1038/s41467-021-27031-y

McFarlin, J. M., Axford, Y., Masterson, A. L., & Osburn, M. R., 2019. Calibration of modern sedimentary δ^2H plant wax-water relationships in Greenland lakes. *Quaternary Science Reviews, 225*, 105978. https://doi.org/10.1016/j.quascirev.2019.105978

McKay, N., & Emile-Geay, J., 2016. Technical note: The Linked Paleo Data framework–a common tongue for paleoclimatology, *Climate of the Past, 12*, 1093-1100. https://doi.org/10.5194/cp-12-1093-2016

McKay, N. P., Emile-Geay, J., & Khider, D., 2021. geoChronR–an R package to model, analyze, and visualize age-uncertain data. *Geochronology, 3*(1), 149-169. https://doi.org/10.5194/gchron-3-149-2021

MET Norway, 2021. seKlima. Retrieved from https://klimaservicesenter.no/observations/

Müller, J., Werner, K., Stein, R., Fahl, K., Moros, M., & Jansen, E., 2012. Holocene cooling culminates in sea ice oscillations in Fram Strait. *Quaternary Science Reviews, 47*, 1-14. https://doi.org/10.1016/j.quascirev.2012.04.024

Müller, M., Kelder, T., & Palerme, C., 2022. Decline of sea-ice in the Greenland Sea intensifies extreme precipitation over Svalbard. *Weather and Climate Extremes, 36*, 100437. https://doi.org/10.1016/j.wace.2022.100437

National Snow and Ice Data Center, 2019. SOTC: Sea ice. Retrieved from http://nsidc.org/cryosphere/sotc/sea_ice.html

Nordli, P. Ø., Hanssen-Bauer, I., & Førland, E., 1996. *Homogeneity analyses of temperature and precipitation series from Svalbard and Jan Mayen*: Norges Meteorologiske Institutt. DNMI report no. 16/96 KLIMA, 41 pp.

Nordli, Ø., Wyszyński, P., Gjelten, H., Isaksen, K., Łupikasza, E., Niedźwiedź, T., & Przybylak, R., 2020. Revisiting the extended Svalbard Airport monthly temperature series, and the compiled corresponding daily series 1898–2018. https://doi.org/10.33265/polar.v39.3614

Norwegian Polar Institute, 2014. *Terrengmodell Svalbard (S0 Terrengmodell)*. https://doi.org/10.21334/npolar.2014.dce53a47

ORNL DAAC. 2018. MODIS and VIIRS Land Products Global Subsetting and Visualization Tool. ORNL DAAC, Oak Ridge, Tennessee, USA. https://doi.org/10.3334/ORNLDAAC/1379

Paillard, D., Labeyrie, L., & Yiou, P., 1996. AnalySeries 1.0: a Macintosh software for the analysis of geophysical time-series. *Eos, 77*, 379. https://doi.org/10.1029/96EO00259

Pieńkowski, A. J., Husum, K., Belt, S. T., Ninnemann, U., Köseoğlu, D., Divine, D. V., Smik, L., Knies, J., Hogan, K., & Noormets, R., 2021. Seasonal sea ice persisted through the Holocene Thermal Maximum at 80°N. *Communications Earth & Environment, 2*(1), 1-10. https://doi.org/10.1038/s43247-021-00191-x

R Core Team, 2021. R: A language and environment for statistical computing. R Foundation for Statistical Computing, Vienna, Austria. 2016. Retrieved from https://www.R-project.org/

Rach, O., Kahmen, A., Brauer, A., & Sachse, D., 2017. A dual-biomarker approach for quantification of changes in relative humidity from sedimentary lipid D/H ratios. *Climate of the Past, 13*(7), 741-757. https://doi.org/10.5194/cp-13-741-2017

Reimer, P. J., Austin, W. E., Bard, E., Bayliss, A., Blackwell, P. G., Ramsey, C. B., Butzin, M., Cheng, H., Edwards, R. L., & Friedrich, M., 2020. The IntCal20 Northern Hemisphere radiocarbon age calibration curve (0–55 cal kBP). *Radiocarbon, 62*(4), 725-757. https://doi.org/10.1017/RDC.2020.41

Riis, T., Christoffersen, K. S., & Baattrup-Pedersen, A., 2014. Effects of warming on annual production and nutrient-use efficiency of aquatic mosses in a high Arctic lake. *Freshwater biology, 59*(8), 1622-1632. https://doi.org/10.1111/fwb.12368

Røthe, T. O., Bakke, J., Vasskog, K., Gjerde, M., D'Andrea, W. J., & Bradley, R. S., 2015. Arctic Holocene glacier fluctuations reconstructed from lake sediments at Mitrahalvøya, Spitsbergen. *Quaternary Science Reviews, 109*, 111-125. https://doi.org/10.1016/j.quascirev.2014.11.017

Røthe, T. O., Bakke, J., Støren, E. W., & Bradley, R. S., 2018. Reconstructing Holocene glacier and climate fluctuations from lake sediments in Vårfluesjøen, northern Spitsbergen. *Frontiers in Earth Science, 6*. https://doi.org/10.3389/feart.2018.00091

Sachse, D., Radke, J., & Gleixner, G., 2004. Hydrogen isotope ratios of recent lacustrine sedimentary n-alkanes record modern climate variability. *Geochimica et Cosmochimica Acta, 68*(23), 4877-4889. https://doi.org/10.1016/j.gca.2004.06.004

Sachse, D., Billault, I., Bowen, G. J., Chikaraishi, Y., Dawson, T. E., Feakins, S. J., Freeman, K. H., Magill, C. R., McInerney, F. A., van der Meer, M. T. J., Polissar, P., Robins, R. J., Sachs, J. P., Schmidt, H.-L., Sessions, A. L., White, J. W. C., West, J. B., & Kahmen, A., 2012. Molecular Paleohydrology: Interpreting the Hydrogen-Isotopic Composition of Lipid Biomarkers from Photosynthesizing Organisms. *Annual Review of Earth and Planetary Sciences, 40*(1), 221-249. https://doi.org/10.1146/annurev-earth-042711-105535

Sand, K., Winther, J.-G., Maréchal, D., Bruland, O., & Melvold, K., 2003. Regional Variations of Snow Accumulation on Spitsbergen, Svalbard, 1997-99. *Hydrology Research, 34*(1-2), 17-32. https://doi.org/10.2166/nh.2003.0026

Sarnthein, M., Van Kreveld, S., Erlenkeuser, H., Grootes, P. M., Kucera, M., Pflaumann, U., & Schulz, M., 2003. Centennial-to-millennial-scale periodicities of Holocene climate and sediment injections off the western Barents shelf, 75 N. *Boreas, 32*(3), 447-461. https://doi.org/10.1111/j.1502-3885.2003.tb01227.x

Schomacker, A., Farnsworth, W. R., Ingólfsson, Ó., Allaart, L., Håkansson, L., Retelle, M., Siggaard-Andersen, M.-L., Korsgaard, N. J., Rouillard, A., & Kjellman, S. E., 2019. Postglacial relative sea level change and glacier activity in the early and late Holocene: Wahlenbergfjorden, Nordaustlandet, Svalbard. *Scientific reports, 9*(1), 1-13. https://doi.org/10.1038/s41598-019-43342-z

Screen, J. A., & Simmonds, I., 2010. The central role of diminishing sea ice in recent Arctic temperature amplification. *Nature, 464*(7293), 1334-1337. https://doi.org/10.1038/nature09051

Serreze, M., Box, J., Barry, R., & Walsh, J., 1993. Characteristics of Arctic synoptic activity, 1952–1989. *Meteorology and Atmospheric Physics, 51*(3), 147-164. https://doi.org/10.1007/BF01030491

Serreze, M. C., Barrett, A. P., Slater, A. G., Steele, M., Zhang, J., & Trenberth, K. E., 2007. The large-scale energy budget of the Arctic. *Journal of Geophysical Research: Atmospheres, 112*(D11). https://doi.org/10.1029/2006JD008230

Shanahan, T. M., Hughen, K. A., Ampel, L., Sauer, P. E., & Fornace, K., 2013. Environmental controls on the 2H/1H values of terrestrial leaf waxes in the eastern Canadian Arctic. *Geochimica et Cosmochimica Acta, 119*, 286-301. https://doi.org/10.1016/j.gca.2013.05.032

Singh, H. K., Bitz, C. M., Donohoe, A., & Rasch, P. J., 2017. A source–receptor perspective on the polar hydrologic cycle: Sources, seasonality, and Arctic–Antarctic parity in the hydrologic cycle response to CO2 doubling. *Journal of Climate, 30*(24), 9999-10017. https://doi.org/10.1175/JCLI-D-16-0917.1

Skagseth, Ø., Furevik, T., Ingvaldsen, R., Loeng, H., Mork, K. A., Orvik, K. A., & Ozhigin, V., 2008. Volume and heat transports to the Arctic Ocean via the Norwegian and Barents Seas. In *Arctic–Subarctic Ocean Fluxes* (pp. 45-64): Springer. https://doi.org/10.1007/978-1-4020-6774-7_3

Skakun, A. A., Chikhachev, K. B., Ekaykin, A. A., Kozachek, A. V., Vladimirova, D. O., Veres, A. N., Verkulich, S. R., Sidorova, O. R., & Demidov, N. E., 2020. Stable isotopic composition of atmospheric precipitation and natural waters in the vicinity of Barentsburg (Svalbard). *Лёд и Снег, 60*(3), 379-394. https://doi.org/10.31857/S2076673420030046

Snyder, J., Werner, A., & Miller, G., 2000. Holocene cirque glacier activity in western Spitsbergen, Svalbard: sediment records from proglacial Linnévatnet. *The Holocene, 10*(5), 555-563. https://doi.org/10.1191/095968300667351697

Svendsen, J. I., & Mangerud, J., 1997. Holocene glacial and climatic variations on Spitsbergen, Svalbard. *The Holocene, 7*(1), 45-57. https://doi.org/10.1177/095968369700700105

Swann, A. L., Fung, I. Y., Levis, S., Bonan, G. B., & Doney, S. C., 2010. Changes in Arctic vegetation amplify high-latitude warming through the greenhouse effect. *Proceedings of the National Academy of Sciences, 107*(4), 1295-1300. https://doi.org/10.1073/pnas.0913846107

Thomas, E. K., McGrane, S., Briner, J. P., & Huang, Y., 2012. Leaf wax δ^2H and varve-thickness climate proxies from proglacial lake sediments, Baffin Island, Arctic Canada. *Journal of Paleolimnology, 48*(1), 193-207. https://doi.org/10.1007/s10933-012-9584-7

Thomas, E. K., Briner, J. P., Ryan-Henry, J. J., & Huang, Y., 2016. A major increase in winter snowfall during the middle Holocene on western Greenland caused by reduced sea ice in Baffin Bay and the Labrador Sea. *Geophysical research letters, 43*(10), 5302-5308. https://doi.org/10.1002/2016GL068513

Thomas, E., Castañeda, I., McKay, N., Briner, J., Salacup, J., Nguyen, K., & Schweinsberg, A., 2018. A wetter Arctic coincident with hemispheric warming 8,000 years ago. *Geophysical research letters, 45*(19), 10,637-610,647. https://doi.org/10.1029/2018GL079517

Thomas, E. K., Hollister, K. V., Cluett, A. A., Corcoran, M. C., & Briner, J. P., 2020. Reconstructing Arctic precipitation seasonality using aquatic leaf wax δ^2H in lakes with contrasting residence times. *Paleoceanography and Paleoclimatology, 35*(7), e2020PA003886. https://doi.org/10.1029/2020PA003886

Throckmorton, H. M., Newman, B. D., Heikoop, J. M., Perkins, G. B., Feng, X., Graham, D. E., O'Malley, D., Vesselinov, V. V., Young, J., & Wullschleger, S. D., 2016. Active layer hydrology in an arctic tundra ecosystem: quantifying water sources and cycling

using water stable isotopes. *Hydrological processes, 30*(26), 4972-4986. https://doi.org/10.1002/hyp.10883

Tuttle, S. E., Roof, S. R., Retelle, M. J., Werner, A., Gunn, G. E., & Bunting, E. L., 2022. Evaluation of Satellite-Derived Estimates of Lake Ice Cover Timing on Linnévatnet, Kapp Linné, Svalbard Using In-Situ Data. *Remote Sensing, 14*(6), 1311. https://doi.org/10.3390/rs14061311

van der Bilt, W. G., Bakke, J., Vasskog, K., D'Andrea, W. J., Bradley, R. S., & Ólafsdóttir, S., 2015. Reconstruction of glacier variability from lake sediments reveals dynamic Holocene climate in Svalbard. *Quaternary Science Reviews, 126*, 201-218. https://doi.org/10.1016/j.quascirev.2015.09.003

van der Bilt, W. G., D'Andrea, W. J., Bakke, J., Balascio, N. L., Werner, J. P., Gjerde, M., & Bradley, R. S., 2018. Alkenone-based reconstructions reveal four-phase Holocene temperature evolution for High Arctic Svalbard. *Quaternary Science Reviews, 183*, 204-213. https://doi.org/10.1016/j.quascirev.2016.10.006

van der Bilt, W. G., DAndrea, W. J., Werner, J. P., & Bakke, J., 2019. Early Holocene temperature oscillations exceed amplitude of observed and projected warming in Svalbard lakes. *Geophysical Research Letters*. https://doi.org/10.1029/2019GL084384

van Pelt, W. J. J., Kohler, J., Liston, G. E., Hagen, J. O., Luks, B., Reijmer, C. H., & Pohjola, V. A., 2016. Multidecadal climate and seasonal snow conditions in Svalbard. *Journal of Geophysical Research: Earth Surface, 121*(11), 2100-2117. https://doi.org/10.1002/2016jf003999

Vihma, T., Screen, J., Tjernström, M., Newton, B., Zhang, X., Popova, V., Deser, C., Holland, M., & Prowse, T., 2016. The atmospheric role in the Arctic water cycle: A review on processes, past and future changes, and their impacts. *Journal of Geophysical Research: Biogeosciences, 121*(3), 586-620. https://doi.org/10.1002/2015JG003132

Voldstad, L. H., Alsos, I. G., Farnsworth, W. R., Heintzman, P. D., Håkansson, L., Kjellman, S. E., Rouillard, A., Schomacker, A., & Eidesen, P. B., 2020. A complete Holocene lake sediment ancient DNA record reveals long-standing high Arctic plant diversity hotspot in northern Svalbard. *Quaternary Science Reviews, 234*, 106207. https://doi.org/10.1016/j.quascirev.2020.106207

Walczowski, W., & Piechura, J., 2011. Influence of the West Spitsbergen Current on the local climate. *International Journal of Climatology, 31*(7), 1088-1093. https://doi.org/10.1002/joc.2338

Werner, A., 1993. Holocene moraine chronology, Spitsbergen, Svalbard: lichenometric evidence for multiple Neoglacial advances in the Arctic. *The Holocene, 3*(2), 128-137. https://doi.org/10.1177/095968369300300204

Werner, K., Spielhagen, R. F., Bauch, D., Hass, H. C., & Kandiano, E., 2013. Atlantic Water advection versus sea-ice advances in the eastern Fram Strait during the last 9 ka: Multiproxy evidence for a two-phase Holocene. *Paleoceanography, 28*(2), 283-295. https://doi.org/10.1002/palo.20028

Werner, K., Müller, J., Husum, K., Spielhagen, R. F., Kandiano, E. S., & Polyak, L., 2016. Holocene sea subsurface and surface water masses in the Fram Strait–Comparisons of temperature and sea-ice reconstructions. *Quaternary Science Reviews, 147*, 194-209. https://doi.org/10.1016/j.quascirev.2015.09.007

Wickström, S., Jonassen, M. O., Vihma, T., & Uotila, P., 2020. Trends in cyclones in the high-latitude North Atlantic during 1979–2016. *Quarterly Journal of the Royal Meteorological Society, 146*, 762-779. https://doi.org/10.1002/qj.3707

Wilkie, K. M. K., 2012. Compound-Specific Hydrogen Isotopes of Lipid Biomarkers in Lake El'gygytgyn, Ne Russia. *Electronic Doctoral Dissertations for UMass Amherst. Paper AAI3518289*. https://scholarworks.umass.edu/open_access_dissertations/561

Wilkie, K. M. K., Chapligin, B., Meyer, H., Burns, S., Petsch, S., & Brigham-Grette, J., 2013. Modern isotope hydrology and controls on δD of plant leaf waxes at Lake El'gygytgyn, NE Russia. *Climate of the Past, 9*(1), 335-352. https://doi.org/10.5194/cp-9-335-2013

Woo, M. K., Kane, D. L., Carey, S. K., & Yang, D., 2008. Progress in permafrost hydrology in the new millennium. *Permafrost and Periglacial Processes, 19*(2), 237-254. https://doi.org/10.1002/ppp.613

Zhang, X., Walsh, J. E., Zhang, J., Bhatt, U. S., & Ikeda, M., 2004. Climatology and interannual variability of Arctic cyclone activity: 1948–2002. *Journal of Climate, 17*(12), 2300-2317. https://doi.org/10.1175/1520-0442(2004)017<2300:CAIVOA>2.0.CO;2

Østby, T. I., Schuler, T. V., Hagen, J. O., Hock, R., Kohler, J., & Reijmer, C. H., 2017. Diagnosing the decline in climatic mass balance of glaciers in Svalbard over 1957–2014. *The Cryosphere, 11*(1), 191-215. https://doi.org/10.5194/tc-11-191-2017

Supplementary Information for

Holocene precipitation seasonality along a climatic gradient from western Spitsbergen to Nordaustlandet, Svalbard

Sofia E. Kjellman, Elizabeth K. Thomas, Anders Schomacker, Wesley R. Farnsworth, Owen O. Cowling, Lis Allaart, Skafti Brynjólfsson

Contents of this file

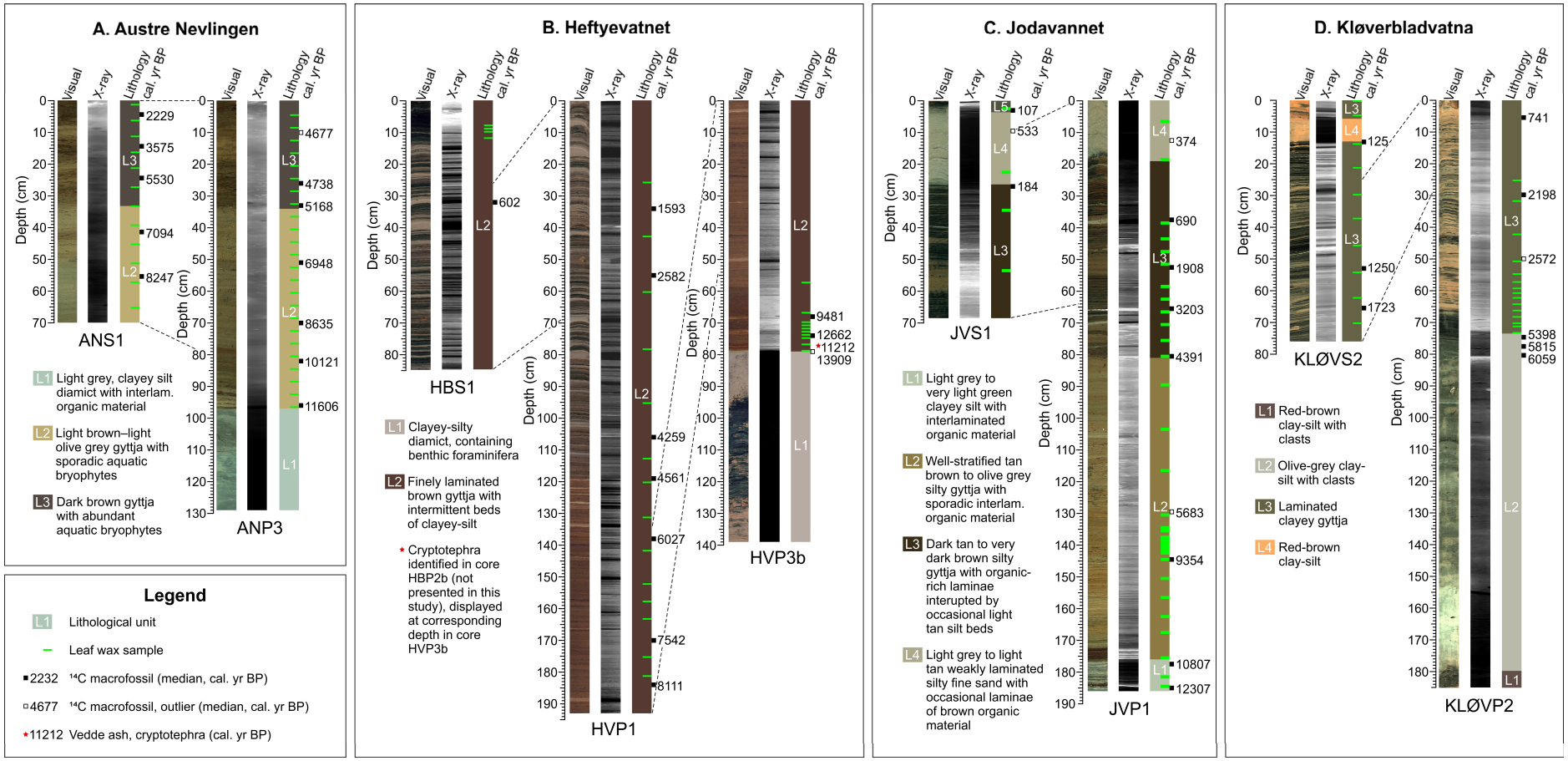

Fig S1. Core overviews for (a) Austre Nevlingen, (b) Heftyevatnet, (c) Jodavannet, and (d) Kløverbladvatna, including core photograph, X-ray image, lithological units, depths for leaf wax samples and calibrated radiocarbon ages and one tephra age. For details on the correlation between the cores, see Fig. S2.

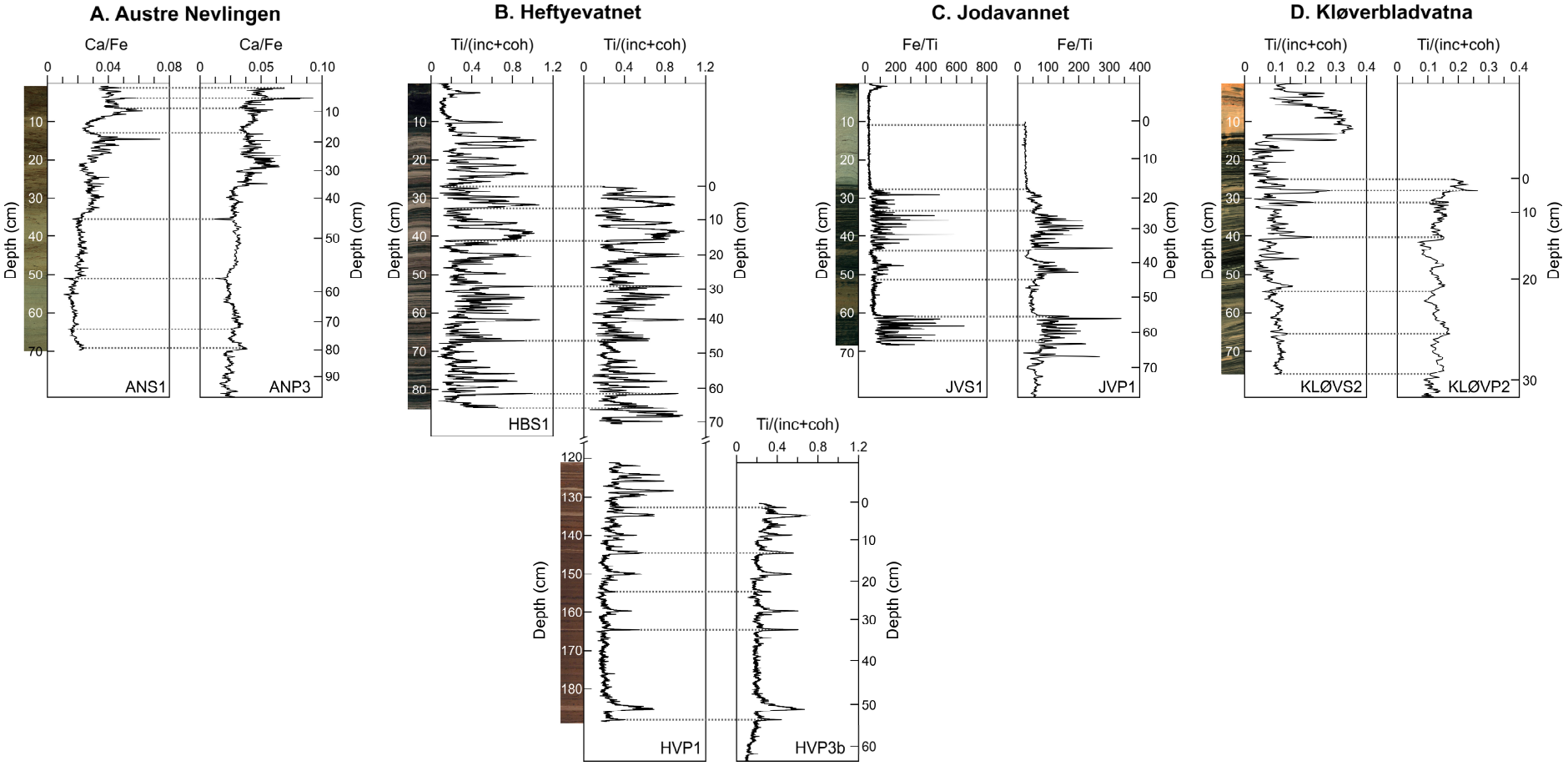

Fig. S2. Stratigraphic correlation of lake sediment cores from (a) Austre Nevlingen, (b) Heftyevatnet, (c) Jodavannet, and (d) Kløverbladvatna, based on X-ray fluorescence (XRF) data and visual similarities in lithology, guided by radiocarbon age constraints. Overlapping cores were aligned in AnalySeries (v. 2.0.8; Paillard et al., 1996), and tie-point in the elemental data were used to construct a composite depth scale. Several elemental ratios and titanium normalized against the incoherent and coherent scatter (Ti/(inc+coh)) were used to correlate each set of cores, with a selection of them displayed in the figure. Depths refer to original core depths.

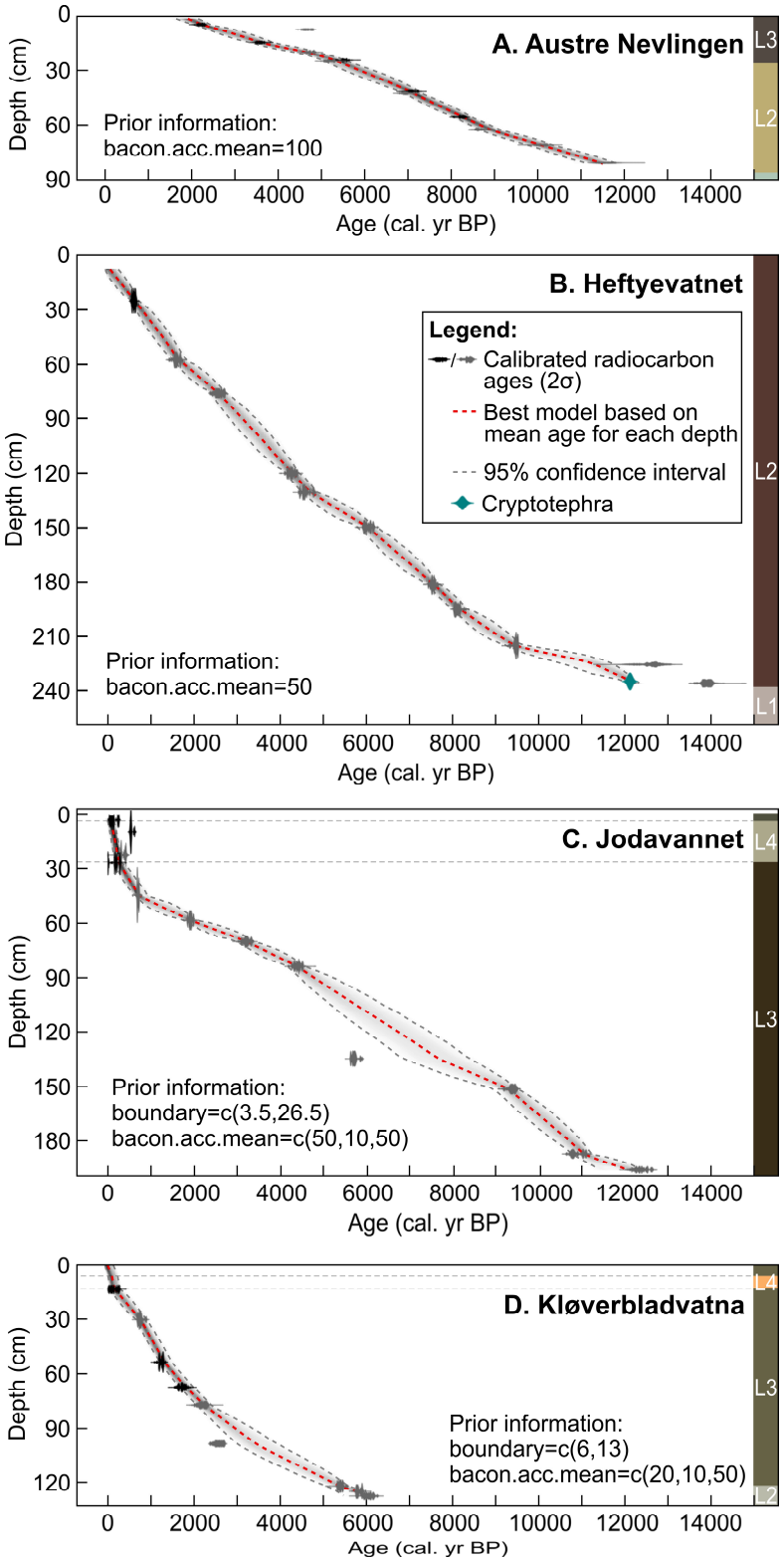

Fig. S3. Bayesian age-depth models for composite records from (a) Austre Nevlingen, (b) Heftyevatnet, (c) Jodavannet, and (d) Kløverbladvatna, generated using Bacon (Blaauw and Christen, 2011) and the IntCal20 calibration curve (Reimer et al., 2020) within the geoChronR package (McKay et al., 2021). Calibrated radiocarbon dates are shown in black for surface cores and grey for piston cores. Details on each radiocarbon age are given in Table S2.

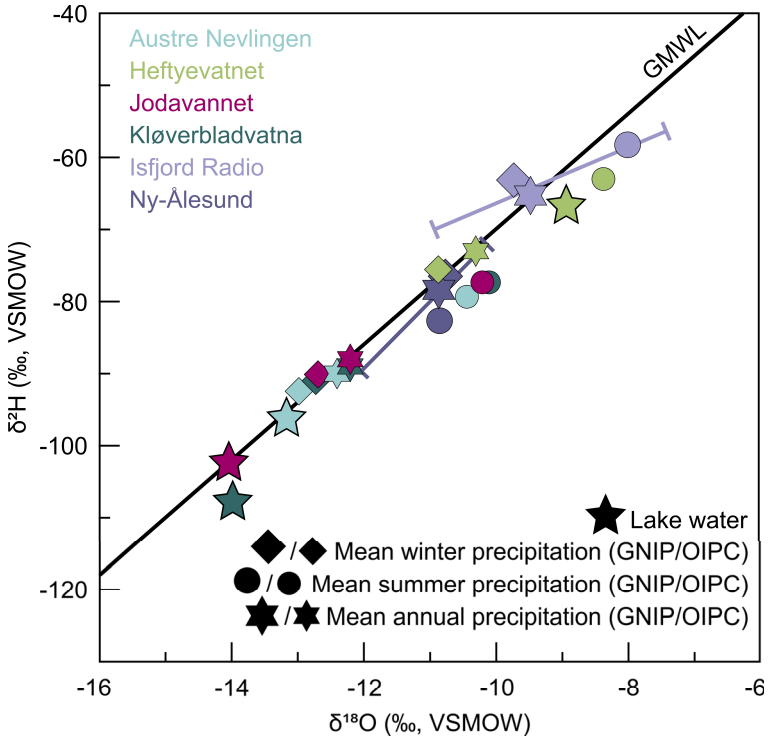

Fig. S4. Co-isotope plot with modern summer (August) lake water values, measured precipitation values from the Global Network of Isotopes in Precipitation (GNIP; IAEA/WMO, 2019) and modelled precipitation values from the Online Isotopes in Precipitation Calculator (OIPC; Bowen et al., 2005; IAEA/WMO, 2019; Bowen, 2021), plotted against the Global Meteoric Water Line (GMWL; $\delta^2H = 8 \times \delta^{18}O + 10$) and local meteoric water lines for Isfjord Radio and Ny-Ålesund.

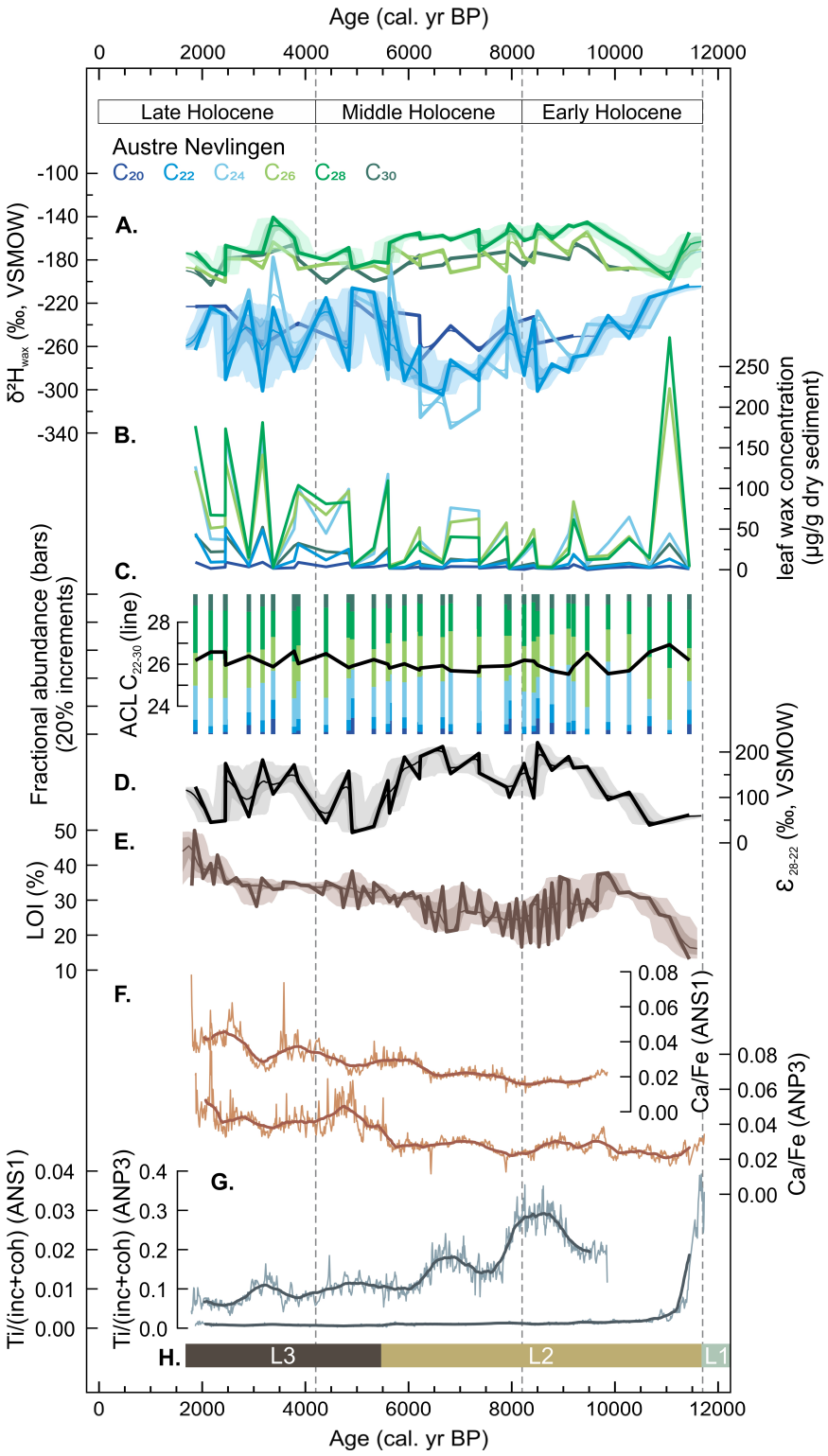

Fig. S5. Selected lake sediment proxies from Austre Nevlingen. Leaf wax δ^2H (a), concentration (b), relative abundance (bars) and average chain length (ACL; line) distribution (c) for even-chain C_{20} to C_{30} *n*-alkanoic acids. (d) Calculated isotope difference between C_{28} and C_{22} (ε_{28-22}). (e) Loss on ignition (LOI). Ca/Fe ratio (f) and Ti normalized by the incoherent and coherent signal Ti/(inc+coh) (g) presented for cores ANS1 and ANP3 separately. (h) Simplified lithology. For details, see Fig. S1. Bold line: measured values plotted on the median age of each sample; fine line: median value of all age model iterations; light and dark shading: 1 and 2 σ age model uncertainty, respectively.

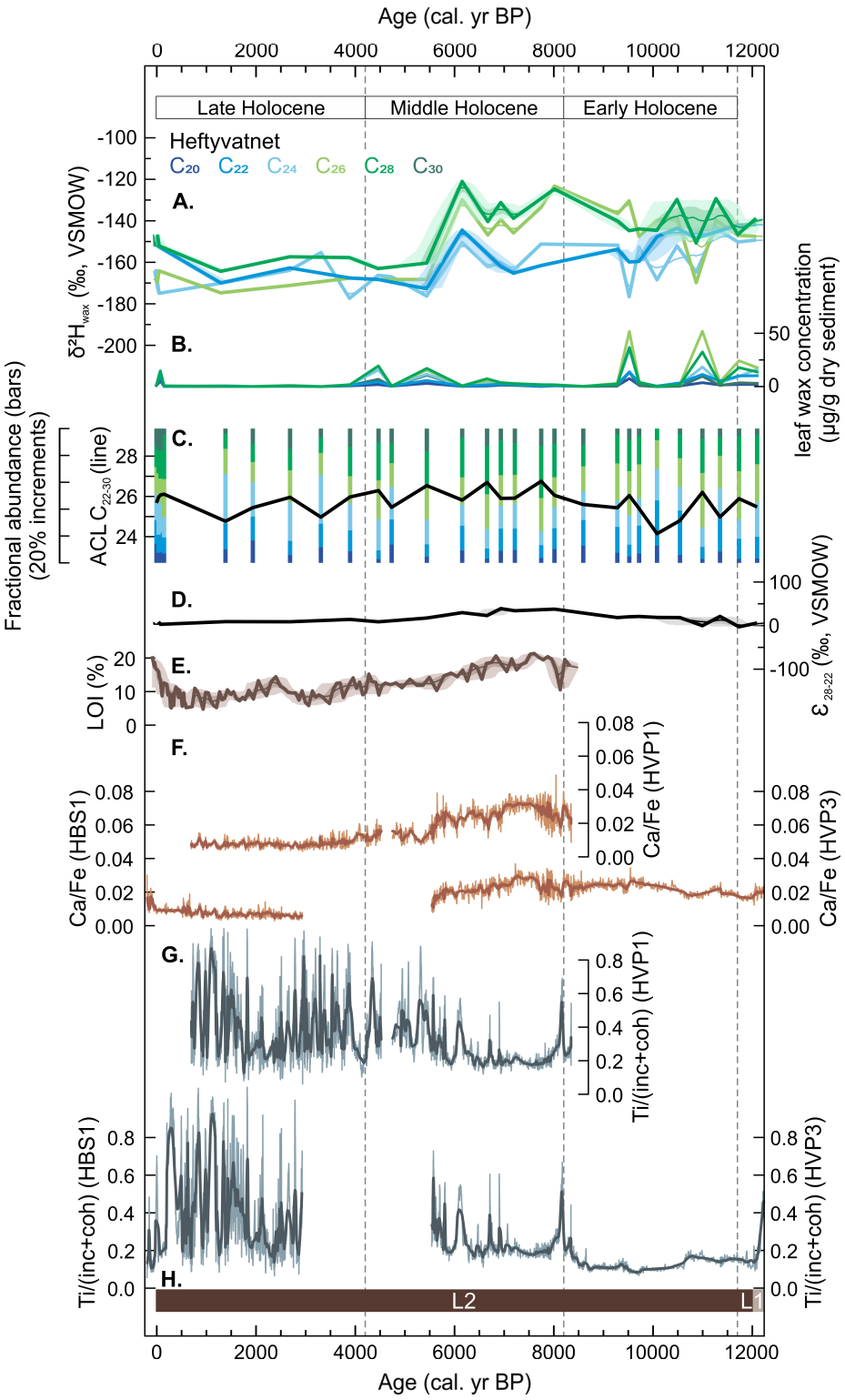

Fig. S6. Selected lake sediment proxies from Heftyevatnet. Leaf wax δ^2H (a) concentration (NB! Normalized to just the sediment mass; b), fractional abundance (bars) and average chain length (ACL; line) distribution (c) for even-chain C_{20} to C_{30} *n*-alkanoic acids. (d) Calculated isotope difference between C_{28} and C_{22} (ε_{28-22}). (e) Loss on ignition (LOI). Ca/Fe ratio (f) and Ti normalized by the incoherent and coherent signal Ti/(inc+coh) (g) presented for cores HBS1, HVP1 and HVP3 separately. Bold line: measured values plotted on the median age of each sample; fine line: median value of all age model iterations; light and dark shading: 1 and 2 σ age model uncertainty, respectively. (h) Simplified lithology. For details, see Fig. S1.

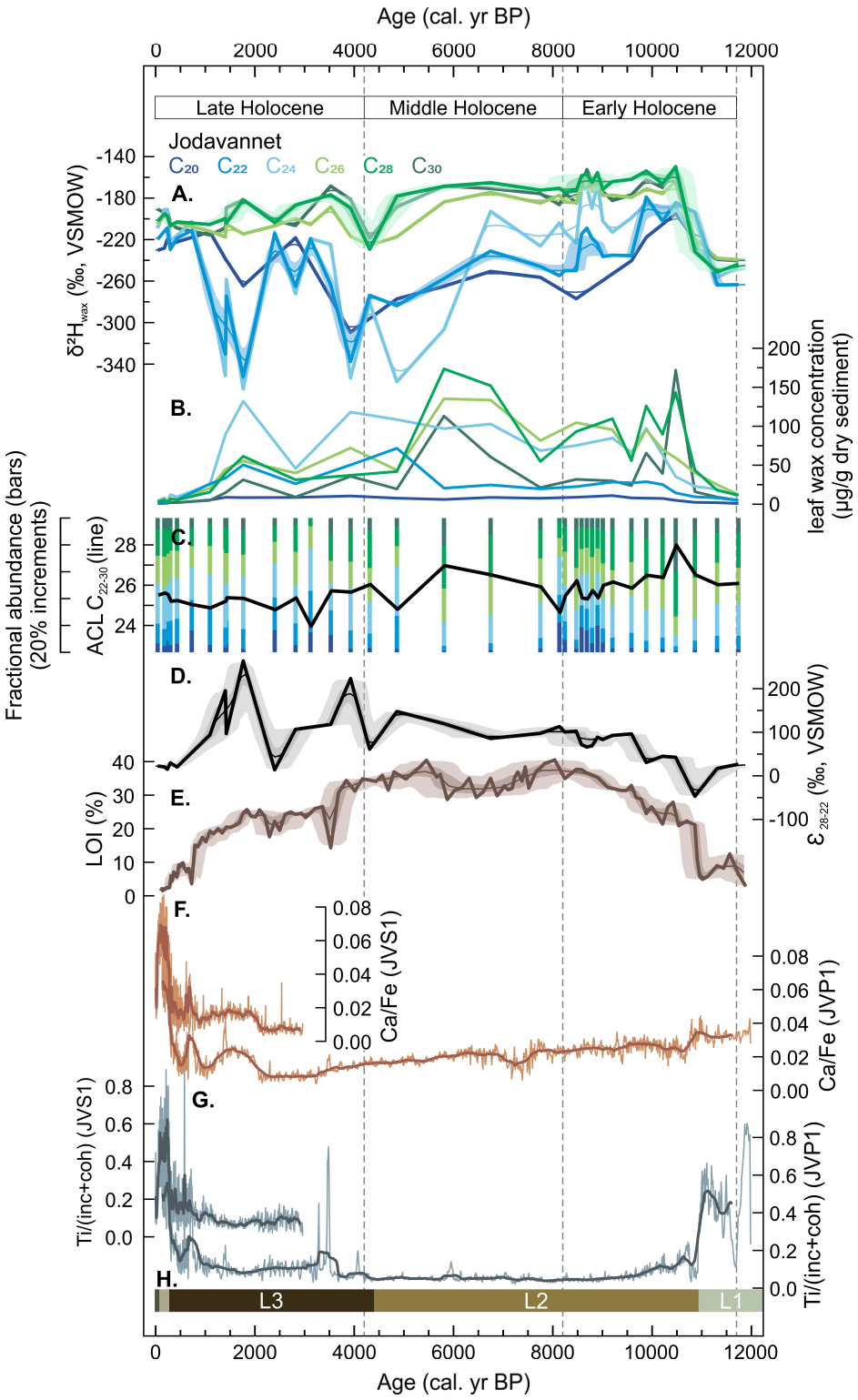

Fig. S7. Selected lake sediment proxies from Jodavannet. Leaf wax δ^2H (a), concentration (b), fractional abundance (bars) and average chain length (ACL; line) distribution (c) for even-chain C_{20} to C_{30} *n*-alkanoic acids. (d) Calculated isotope difference between C_{28} and C_{22} (ε_{28-22}). (e) Loss on ignition (LOI). Ca/Fe ratio (f) and Ti normalized by the incoherent and coherent signal Ti/(inc+coh) (g) presented for cores JVS1 and JVP1 separately. Bold line: measured values plotted on the median age of each sample; fine line: median value of all age model iterations; light and dark shading: 1 and 2 σ age model uncertainty, respectively. (h) Simplified lithology. For details, see Fig. S1.

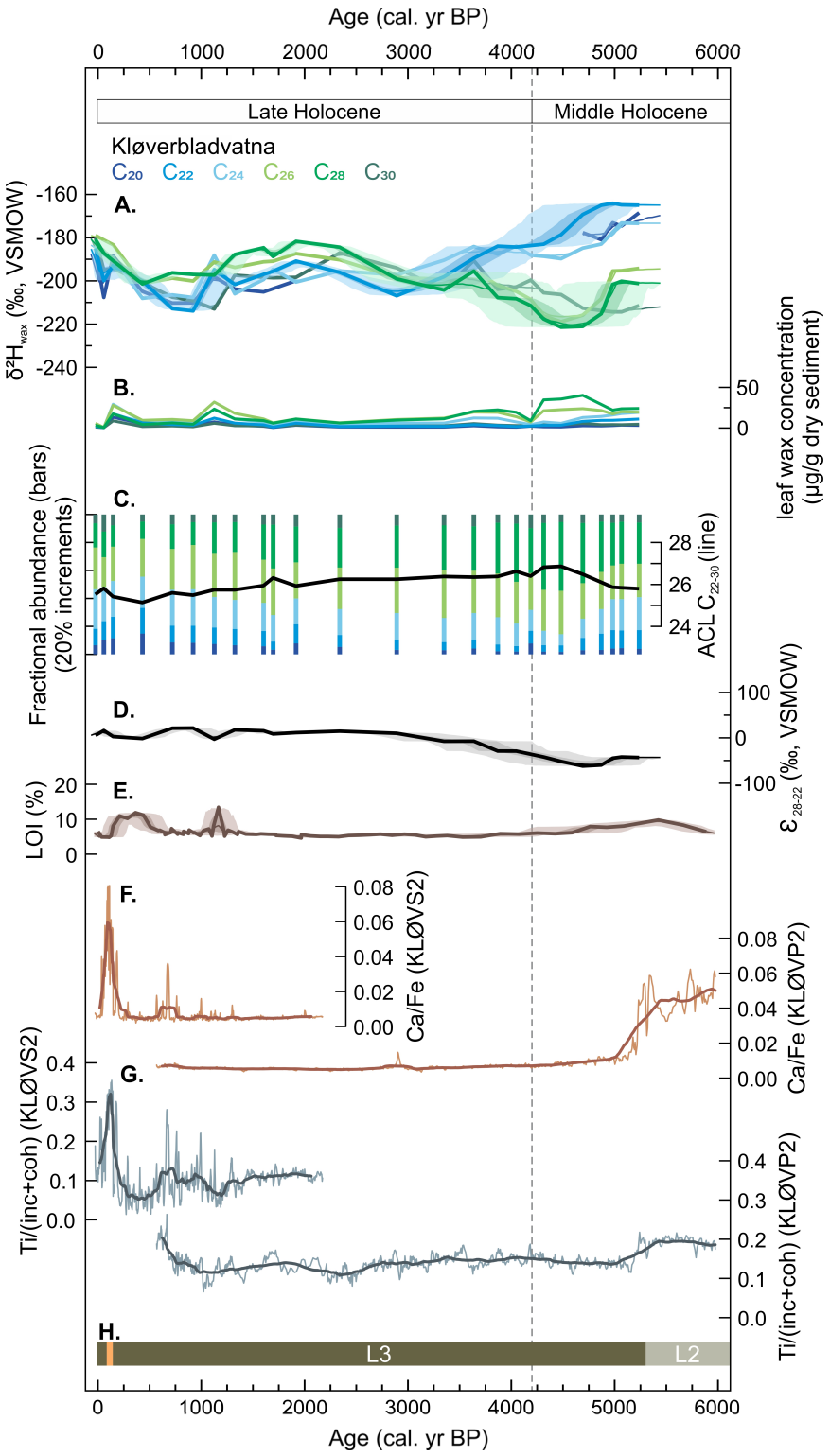

Fig. S8. Selected lake sediment proxies from Kløverbladvatna. Leaf wax δ^2H (a), concentration (b), fractional abundance (bars) and average chain length (ACL; line) distribution (c) for even-chain C_{20} to C_{30} *n*-alkanoic acids. (d) Calculated isotope difference between C_{28} and C_{22} (ε_{28-22}). (e) Loss on ignition (LOI). Ca/Fe ratio (f) and Ti normalized by the incoherent and coherent signal Ti/(inc+coh) (g) presented for cores KLØVS2 and KLØVP2 separately. Bold line: measured values plotted on the median age of each sample; fine line: median value of all age model iterations; light and dark shading: 1 and 2 σ age model uncertainty, respectively. (h) Simplified lithology. For details, see Fig. S1.

Table S1. Calculations of seasonal runoff and residence times for Austre Nevlingen, Heftyevatnet, Jodavannet, and Kløverbladvatna, Svalbard.

	Lake volume (m^3)	**Catchment area (m^2)**	**Total ice-cover season precipitation (October to June) (m)**	**Total ice-free season precipitation (July to September) (m)**	**Runoff during spring melt (m^3)**	**Runoff during ice-free season (m^3)**	**Spring melt residence time (months)**	**Ice-free season residence time (months)**	**% of lake volume replaced during spring melt season**	**% of lake water replaced during ice-free season**
	Calculated from bathymetry measured in the field or Calculated from maximum depth divided by two and the lake surface area	ArcMap 10.5 and DEM from Norwegian Polar Institute (2014)	Svalbard Airport 1991-2020 or Ny-Ålesund 1991-2020 (MET Norway, 2021)	Svalbard Airport 1991-2020 or Ny-Ålesund 1991-2020 (MET Norway, 2021)	Catchment area x Ice-cover season precipitation x 0.5 Assuming 50% of precipitation reaches the lake	Catchment area x Ice-free season precipitation x 0.5 Assuming 50% of precipitation reaches the lake	Lake volume / Runoff Assuming that all winter precipitation melts in 1 month	Lake volume / (Runoff / Ice-free months) Assuming constant precipitation in all summer months	Runoff / Lake volume Assuming 50% of precipitation reaches lake	Runoff / Lake volume Assuming 50% of precipitation reaches lake
Austre Nevlingen										
Median	860737	480084	0.127	0.069	30449	16479	28.3	156.7	4	2
Uncertainty	assume 10%	assume 10%	5^{th} to 95^{th} percentile	5^{th} to 95^{th} percentile	-	-	-	-	-	-
Minimum	774663	432076	0.076	0.028	16345	5966	47.4	389.5	2	1
Maximum	946811	528092	0.202	0.103	53344	27203	17.7	104.4	6	3
Heftyevatnet										
Median	49056	148087	0.323	0.129	23898	9533	2.1	15.4	49	19
Uncertainty	assume 10%	assume 10%	5^{th} to 95^{th} percentile	5^{th} to 95^{th} percentile	-	-	-	-	-	-
Minimum	44150	133278	0.217	0.037	14456	2496	3.1	53.1	33	6
Maximum	53961	162896	0.531	0.202	43264	16482	1.2	9.8	80	31
Jodavannet										
Median	63226	1312671	0.127	0.069	83256	45057	0.8	4.2	132	71
Uncertainty	assume 10%	assume 10%	5^{th} to 95^{th} percentile	5^{th} to 95^{th} percentile	-	-	-	-	-	-
Minimum	56903	1181404	0.076	0.028	44693	16312	1.3	10.5	79	29
Maximum	69548	1443938	0.202	0.103	145856	74381	0.5	2.8	210	107
Kløverbladvatna										
Median	1980370	1642691	0.127	0.069	104188	56385	19.0	105.4	5	3
Uncertainty	assume 10%	assume 10%	5^{th} to 95^{th} percentile	5^{th} to 95^{th} percentile	-	-	-	-	-	-
Minimum	1782333	1478422	0.076	0.028	55929	20413	31.9	261.9	3	1
Maximum	2178407	1806960	0.202	0.103	182526	93081	11.9	70.2	8	4

Table S2. Radiocarbon ages from lake sediment cores from Svalbard. Calibrated ages are median ages within the 2σ age ranges. The samples Ua-64589, LuS 14022, LuS 14023, LuS 14024, Ua-63429, LuS 14025, and LuS 17223 from Heftyevatnet and Ua–55367, Ua–55368, and Ua–55369 from Jodavannet are new to this study. Other ages from Heftyevatnet and Jodavannet are published in Farnsworth et al. (2022) and Voldstad et al. (2020). Ages from Austre Nevlingen are published in Kjellman et al. (2020), and Kløverbladvatna in Schomacker et al. (2019).

Core	Lab ID[a]	Composite depth, midpoint depth (cm)	Original depth (cm)	^{14}C-age (yr BP)	Calibrated age (cal. yr BP)	Calibrated 2σ age ranges (cal. yr BP)	δ^{13}C (‰ VPDB)	Material dated
Austre Nevlingen								
ANS1	Ua–60808	4.5	4–5	2200 ± 33	2229	2325–2120	–25.8	Aquatic bryophytes
ANP3	LuS 12222	7.3	9.5–10.5	4135 ± 45	4677	4824–4529	N/A	Aquatic bryophytes
ANS1	Ua–60809	14.5	14–15	3350 ± 46	3575	3692–3463	–26.6	Aquatic bryophytes
ANP3	LuS 12223	19.9	25.5–26.5	4215 ± 40	4738	4856–4787, 4766–4617	N/A	Aquatic bryophytes
ANS1	Ua–60810	24.5	24–25	4818 ± 62	5530	5660–5445, 5401–5394, 5389–5327	N/A	Aquatic bryophytes
ANP3	LuS 12224	25	32.5–33.5	4545 ± 45	5168	5436–5421, 5322–5046	N/A	Wood
ANS1	Ua–60811	41.5	41–42	6209 ± 56	7094	7255–6957	–26.0	Aquatic bryophytes
ANP3	LuS 12225	42.5	50.5–51.5	6085 ± 50	6948	7157–7103, 7075–6795	N/A	*Salix polaris*
ANS1	Ua–60812	55.5	55–56	7410 ± 52	8247	8364–8163, 8135–8119, 8100–8038	–29.0	*Salix polaris*
ANP3	LuS 12226	62.5	69.5–70.5	7850 ± 45	8635	8975–8956, 8951–8917, 8893–8884, 8862–8831, 8780–8537	N/A	Terrestrial plant macrofossil
ANP3	LuS 12227	71.1	81.5–82.5	8985 ± 70	10121	10254–9892, 9834–9824	N/A	Aquatic bryophytes
ANP3	LuS 12221	81	95.5–96.5	10070 ± 75	11606	11924–11919, 11879–11310, 11293–11283	N/A	Aquatic bryophytes
Heftyevatnet								
HBS1	Ua-64589	31.75	31.5–32	618 ± 40	602	659–545	N/A	Aquatic bryophytes
HVP1	LuS 14022	57.5	34–34.5	1700 ± 45	1593	1710–1516, 1483–1478, 1432–1423	N/A	Aquatic bryophytes
HVP1	LuS 14023	76	55.5–56	2495 ± 40	2582	2729–2422, 2382–2373	N/A	Aquatic bryophytes
HVP1	LuS 14024	120	106–107	3845 ± 35	4259	4405–4151	N/A	Aquatic bryophytes
HVP1	Ua-63429	130.7	118.5–119.5	4072 ± 33	4561	4802–4757, 4698–4674, 4648–4504, 4494–4437	-23.8	*Salix polaris*, aquatic bryophytes
HVP1	LuS 14025	149.7	138–138.5	5250 ± 45	6027	6183–6141, 6120–5920	N/A	Aquatic bryophytes
HVP1	LuS 17223	181.7	170–170.5	6680 ± 55	7542	7661–7636, 7623–7462, 7454–7431	N/A	Aquatic bryophytes
HVP1	Ua-64590	195.4	183.5–184.5	7334 ± 39	8111	8285–8266, 8202–8022	-29.0	*Salix polaris*
HVP3	Ua-64591	215.1	67.5–68.5	8449 ± 38	9481	9535–9420, 9339–9333	-27.2	*Salix polaris*
HVP3	Ua-64592	225.6	73.5–74.5	10705 ± 164	12662	13070–12425, 12402–12101	N/A	*Salix polaris*
HBP2	HBP2_21A	235	40–41	–	12121 ± 57*	–	–	Cryptotephra
HVP1	Ua-63430	236	78.5–79.5	12016 ± 80	13909	14080–13751, 13678–13665, 13626–13615	-29.1	*Salix polaris,* aquatic bryophytes

Jodavannet								
JVS1	Ua–55367	3	2.5–3.5	112 ± 21	107	263–220, 114–25	–29.8	*Salix polaris*
JVS1	Ua–55368	9.5	9–10	519 ± 29	533	623–604, 555–506	–25.0**	*Salix polaris****
JVP1	Ua–55361	22.4	12–13	279 ± 24	374	434–360, 330–287, 164–157	–27.9	*Salix polaris*
JVS1	Ua–55369	27	26.5–27.5	196 ± 21	184	295–263, 220–114, 25–modern	–28.9	*Salix polaris*
JVP1	Ua–55362	44.5	37–38	767 ± 26	690	726–670	–28.3	*Salix polaris*
JVP1	Ua–55363	58.3	52–53	1977 ±25	1908	1990–1959, 1950–1831	–28.6	*Salix polaris*
JVP1	LuS 14000	70.2	65–66	3010 ± 40	3203	3344–3282, 3275–3071	N/A	Aquatic bryophytes
JVP1	LuS 14001	83.9	80–81	3945 ± 40	4391	4520–4465, 4450–4247	N/A	Aquatic bryophytes
JVP1	Ua–55364	134.4	128.5–129.5	4968 ± 34	5683	5852–5828, 5750–5597	–20.3	*Salix polaris****
JVP1	LuS 14002	151.2	144–145	8335 ± 45	9354	9474–9255, 9225–9205, 9176–9143	N/A	Aquatic bryophytes
JVP1	Ua–55365	186.9	177–178	9512 ± 40	10807	11074–10942, 10878–10654, 10619–10598	–29.4	*Salix polaris****
JVP1	Ua–55366	195.6	185–186	10426 ± 42	12307	12605–12539, 12494–12417, 12411–12097, 12083–12077, 12069–12060	–28.0	Aquatic bryophytes
Kløverbladvatna								
KLØVS2	Ua–52330	13.5	13–14	134 ± 36	125	278–172, 153–6	–28.1	*Salix polaris*
KLØVP2	Ua–53787	30.3	6–7	841 ± 40	741	900–871, 797–675	–25*	*Salix polaris*
KLØVS2	Ua–52331	53.5	53–54	1327 ± 39	1250	1304–1176	–27.5	*Salix polaris*
KLØVS2	Ua–53786	67.5	67–68	1821 ± 58	1723	1871–1850, 1843–1570	–25**	*Salix polaris*
KLØVP2	Ua–53788	77.1	28–29	2186 ± 55	2198	2335–2046, 2020–2006	–25**	*Salix polaris*
KLØVP2	Ua–52332	98.6	50.5–51.5	2478 ± 40	2572	2721–2412, 2386–2370	–26.1	*Salix polaris*
KLØVP2	Ua–53789	122.1	74–75	4669 ± 37	5398	5477–5312	–27.6	*Salix polaris*
KLØVP2	Ua–53790	125.1	77–78	5108 ± 33	5815	5928–5844, 5830–5748	–27.9	*Salix polaris*
KLØVP2	Ua–53791	127.6	79.5–80.5	5265 ± 66	6059	6263–6249, 6201–5912	–25**	*Salix polaris*

[a] Ua = Ångström Laboratory, Uppsala University, Sweden; LuS = Lund University Radiocarbon Laboratory, Sweden.
* Vedde Ash in the NGRIP ice core chronology, Greenland (Rasmussen et al., 2006).
** Assumed value.
*** Some small stems from other vascular plants than *Salix polaris* were included to provide enough dateable material.

Table S3. H_3^+ factors, determined at the beginning of each sequence.

Sequence date	Lake	Core	No. of samples	H_3^+ factor
1-3 Nov 2017	Austre Nevlingen	ANP3	16	2.81 ± 0.01
3-5 Nov 2017	Austre Nevlingen	ANP3	3	2.82 ± 0.01
7-8 Nov 2017	Austre Nevlingen	ANP3	5	2.80 ± 0.01
7-9 Dec 2018	Jodavannet	JVS1, JVP1	3, 13	3.57 ± 0.01
11-12 Dec 2018	Jodavannet, Kløverbladvatna	JVS1, KLØVS2, KLØVP2	1, 8, 5	3.61 ± 0.03
13-15 Dec 2018	Jodavannet, Kløverbladvatna	JVP1, KLØVP2	6, 10	3.57 ± 0.02
2-4 Jan 2019	Austre Nevlingen, Kløverbladvatna	ANS1, KLØVS2	12, 2	3.52 ± 0.01
8-10 Dec 2020	Jodavannet, Heftyevatnet	JVP1, HBS1, HVP1, HVP3b	3, 2, 6, 4	2.19 ± 0.02
2-4 Feb 2021	Jodavannet, Heftyevatnet	JVP1, HVP1, HVP3b	6, 3, 4	4.85 ± 0.04
9-10 Feb 2021	Jodavannet, Heftyevatnet	JVP1, HBS1, HVP1, HVP3b	4, 2, 5, 2	5.00 ± 0.04

References

Blaauw, M., & Christen, J. A., 2011. Flexible paleoclimate age-depth models using an autoregressive gamma process. *Bayesian analysis, 6*(3), 457-474. https://doi.org/10.1214/11-BA618.

Bowen, G. J., 2021. OIPC: the Online Isotopes in Precipitation Calculator. Version 3.1. Retrieved from http://www.waterisotopes.org.

Bowen, G. J., Wassenaar, L. I., & Hobson, K. A., 2005. Global application of stable hydrogen and oxygen isotopes to wildlife forensics. *Oecologia, 143*(3), 337-348. https://doi.org/10.1007/s00442-004-1813-y

Farnsworth, W. R., Ingólfsson, Ó., Mannerfelt, E. S., Kalliokoski, M. H., Guðmundsdóttir, E. R., Retelle, M., Allaart, L., Brynjólfsson, S., Furze, M. F., & Hancock, H. J., 2022. Vedde Ash constrains Younger Dryas glacier re-advance and rapid glacio-isostatic rebound on Svalbard. *Quaternary Science Advances, 5*, 100041. https://doi.org/10.1016/j.qsa.2021.100041.

IAEA/WMO, 2019. Global Network of Isotopes in Precipitation. The GNIP Database. Retrieved from https://nucleus.iaea.org/wiser.

Kjellman, S. E., Schomacker, A., Thomas, E. K., Håkansson, L., Duboscq, S., Cluett, A. A., Farnsworth, W. R., Allaart, L., Cowling, O. C., & McKay, N. P., 2020. Holocene precipitation seasonality in northern Svalbard: Influence of sea ice and regional ocean surface conditions. *Quaternary Science Reviews, 240*, 106388. https://doi.org/10.1016/j.quascirev.2020.106388.

McKay, N. P., Emile-Geay, J., & Khider, D., 2021. geoChronR–an R package to model, analyze, and visualize age-uncertain data. *Geochronology, 3*(1), 149-169. https://doi.org/10.5194/gchron-3-149-2021.

MET Norway, 2021. seKlima. Norwegian Meteorological Institute. Available at https://klimaservicesenter.no/observations/.

Norwegian Polar Institute, 2014. Terrengmodell Svalbard (S0 Terrengmodell). https://doi.org/10.21334/npolar.2014.dce53a47.

Paillard, D., Labeyrie, L., Yiou, P., 1996. Macintosh program performs time-series analysis. *Eos, Trans. Am Geophys Union 77*, 379. https://doi.org/10.1029/96EO00259.

Rasmussen, S. O., Andersen, K. K., Svensson, A. M., Steffensen, J. P., Vinther, B. M., Clausen, H. B., ... & Ruth, U. (2006). A new Greenland ice core chronology for the last glacial termination. *Journal of Geophysical Research: Atmospheres, 111*(D6). https://doi.org/10.1029/2005JD006079.

Reimer, P. J., Austin, W. E., Bard, E., Bayliss, A., Blackwell, P. G., Ramsey, C. B., Butzin, M., Cheng, H., Edwards, R. L., & Friedrich, M., 2020. The IntCal20 Northern Hemisphere radiocarbon age calibration curve (0–55 cal kBP). *Radiocarbon, 62*(4), 725-757. https://doi.org/10.1017/RDC.2020.41.

Schomacker, A., Farnsworth, W. R., Ingólfsson, Ó., Allaart, L., Håkansson, L., Retelle, M., Siggaard-Andersen, M.-L., Korsgaard, N. J., Rouillard, A., & Kjellman, S. E., 2019. Postglacial relative sea level change and glacier activity in the early and late Holocene: Wahlenbergfjorden, Nordaustlandet, Svalbard. *Scientific reports, 9*(1), 1-13. https://doi.org/10.1038/s41598-019-43342-z.

Voldstad, L. H., Alsos, I. G., Farnsworth, W. R., Heintzman, P. D., Håkansson, L., Kjellman, S. E., Rouillard, A., Schomacker, A., & Eidesen, P. B., 2020. A complete Holocene lake sediment ancient DNA record reveals long-standing high Arctic plant diversity hotspot in northern Svalbard. *Quaternary Science Reviews, 234*, 106207. https://doi.org/10.1016/j.quascirev.2020.106207.